Genesis and Controls on the Mineralization of the Keglovic Deposit, South-Central Yukon

by

Laurence Pryer

A thesis submitted in partial fulfillment of the requirements for the degree of

Doctor of Philosophy

Department of Earth and Atmospheric Sciences
University of Alberta

Abstract

The mid-Cretaceous Ag-Pb-Zn-Cu-Sn Keglovic deposit, located in the south-central Yukon, is formed by the superposition of an earlier Pb-Zn skarn system with later Keno Hill-style Ag-Pb-Zn veins and is the product of complex regional geological processes, which occur synchronously with mineralization.

The Keglovic deposit is located in the Tay River district, which contains a unique assemblage of mid-Cretaceous (120-90 Ma) igneous rocks belonging to the Omineca Magmatic Belt (OMB). The tectonic setting of plutons in the OMB is controversial. All previous attempts to model the OMB assume that the plutons within it form continental margin-parallel bands, which migrate systematically inboard (away from the margin) with time. This study demonstrates that plutonism in the Tay River district spans a period from 109–90 Ma with no inboard migration, violating this assumption.

Igneous activity in the Tay River district can be divided into three suites. The oldest plutons are 109–104 Ma S-type granites belonging to the Anvil suite, which derived from sediment melting in an exhuming thickened crust. This study uses a novel method to correct discordant U-Pb analyses from xenocrystic zircons from these S-type granites, allowing the identification of the Hyland Group as the protolith for the Anvil suite magmatism. The second suite are 100–96 Ma Tay River I-type felsic rocks, which are derived from lower crustal melting generated by mantle heat input and regional exhumation. The intrusion of the final 96–90 Ma Tombstone suite represents the waning of the thermal pulse and the end of exhumation. Plutonism in the Tay River district terminates at 90 Ma.

A thermochronological study on these three suites indicates that the intrusion of the two older suites occurred synchronously with the exhumation of the Tay River district. The oldest OMB plutonic rocks were emplaced at 12–15 km depth at 107±2 Ma. These rocks cooled below the ^{40}Ar-^{39}Ar closure temperature in biotite (365–395°C), which corresponds to a depth of 5.5–10.5 km, at ~104±2 Ma. They then cooled below the U-Th/He closure temperature in zircon (195-215°C), which corresponds to a depth of 2.5-4.7 km, before ~99.2 ± 3 Ma.

The new definition of suites, based on emplacement age, can be expanded to previously published data from the northern Cordillera to create a new temporal pattern of pluton evolution. The oldest S-type plutons form a core in the regions with the thickest crust and a fertile protolith. Regional I-type plutonism occurs on the peripheries of the Yukon-Tanana terrane. Finally 96–90 Ma plutonism occurs across the whole northern Cordillera. This pattern of plutonism can be explained by delamination of over-thickened lithosphere beneath the Yukon-Tanana terrane. In this model, lithospheric delamination drives regional uplift, as well as creating space for upwelling asthenosphere to transfer heat above the Moho generating lower crustal melts.

The development of mineralization at the Keglovic deposit can now be reexamined within the context of this enhanced regional geological understanding. A Re-Os model age of arsenopyrite from within the vein system yields an age of 100±2 Ma indicating that mineralization occurred synchronously with the exhumation, extensive OMB plutonic activity, and the delamination event. Carbon, oxygen, sulphur and lead isotope analyses suggest a purely crustal origin for the mineralizing fluid with no direct magmatic input and that the same fluid formed both the skarn and the subsequent vein mineralization. The superposition of the mineralization styles is therefore due to telescoping of a single hydrothermal system as a result of regional exhumation. Fluid flow and skarn mineralization were controlled by a fault with

hydrothermal circulation resulting from a high geothermal gradient derived from crustal thickening, intrusive igneous activity and/or delamination-derived lower crustal heating. The change in mineralization style from the skarn to the veins occurred due to a combination of increased volatile content in the fluids – derived from reactions with the host rock - and decreasing pressure due to regional exhumation. In combination, these two effects led to effervescence within the fluid, which promoted deposition of the veins.

In summary, the Keglovic deposit is a product of the regional geological evolution of the Tay River district. Therefore, any future exploration for Keglovic-type deposits will need to consider the broader geological context of the mineralization.

Preface

The concept for the Ph.D. project was developed by Sarah Gleeson (University of Alberta) and Archer, Cathro and Associates (1981) Ltd. The funding for the work came from Archer, Cathro and Associates (1981) Ltd. and a Natural Sciences and Engineering Research Council of Canada Collaborative Research and Development grant (NSERC-CRD) to S. Gleeson. Field work was conducted in the summers of 2013 and 2015. Though I conducted the majority of the field-work and sample collection, many people provided assistance including Dr. Sarah Gleeson, Michael Rogers and Daniel Francis. Fieldwork was only possible with assistance from the Yukon Geological Survey (Rosie Cobbett) and Archer, Cathro and Associates (1981) Ltd. (Dylan Wallinger, Matt Dumala and Heather Burrell). Analytical techniques used as part of this thesis were performed with the assistance of Dr Diane Caird (XRD) and Andrew Locock (EPMA), as well as the authors mentioned below.

Chapter 2 has been submitted to the Geological Society of America Bulletin as Pryer, L., Gleeson, S.A., Johnston, S.T., DuFrance, S.A., Creaser, R.A., Luo, Y. The Evolution of Mid-Cretaceous Omineca Magmatic Belt Granites in the Northern Cordillera: A Product of Mantle Lithosphere Delamination. Regarding author contributions; L.P, S.G and S.J conceived the study. L.P collected the samples and conducted the analytical work with support from S.D.F and Y.L. R.C provided Nd analysis. All authors contributed to data analysis and preparation of the manuscript. L.P wrote the initial manuscript and will oversee every stage of revision and editing.

Chapter 3 will be submitted to Geology as Pryer, L., Gleeson, S.A., Waterton, P., Reimink, J.R., DuFrance, S.A., Creaser, R.A., Waldron. J.W.F. Identifying the source of an S-type granite via xenocrystic zirconology. L.P, S.G, P.W conceived the study. L.P collected the

samples and conducted the LA-ICP-MS dating with S.D.F. R.C provided Nd analysis. J.R developed the code for use in this study. All authors contributed to data analysis and preparation of the manuscript. L.P wrote the initial manuscript and will oversee every stage of revision and editing.

Chapter 4 will be submitted to Tectonics as Pryer, L., Gleeson, S.A., Johnston, S.T., Reiners, P.W., Spell, T.L. Thermochronology of Omineca Magmatic Belt granites in the Selwyn Basin: Evidence for Mid-Cretaceous exhumation of the central Yukon and passage of the northern Cordillera over the Yellowstone Hotspot in the Late Cretaceous. L.P, S.G and S.J conceived the study. L.P collected the samples and conducted U-Th/He work in conjunction with P.R at the University of Arizona, Tuscon. T.S (Nevada Isotope Geochronology Laboratory, University of Nevada, Las Vegas) provided the Ar-Ar analysis. All authors contributed to discussion of results and their implications, as well as manuscript preparation. L.P wrote the initial manuscript and will oversee every stage of revision and editing.

Chapter 5 will be submitted to Economic Geology as Pryer, L., Gleeson, S.A., Creaser, R.A. The Keglovic Deposit: A telescoped Ag-Pb-Zn skarn and vein deposit, Central Yukon, Canada. L.P and S.G conceived the study. L.P collected the samples and performed the majority of the analyses. R.C provided the Re-Os dating. Steve Taylor of the University of Calgary provided the carbon, oxygen and sulphur isotope analysis. All authors contributed to discussion of results and their implications, as well as manuscript preparation. L.P wrote the initial manuscript and will oversee every stage of revision and editing.

The ideas presented within this thesis are my own, although discussion with co-authors has developed and refined them. All the writing, figures and tables within this thesis are my own, as are any errors, mistakes or omissions.

Acknowledgements

This section is too short to recognize all the people who deserve acknowledgement for their contribution to this thesis and the quality of my life in Canada. Firstly, and most importantly, Sarah Gleeson for her patience with my punctuation and personality. The time she put into fostering my scientific development made this thesis what it is, and anything that can be coherently taken away from reading it is dominantly attributable to her editorial skills.

Secondly, the many people who provided assistance in the field during the summer of 2013 and 2015. The sample collection we performed was incredibly strenuous and would not have been successful without the assistance of Rosie Cobbett and Lee Piagage of the Yukon Geological Survey; Matthew Dumala, Dylan Wallinger, Heather Burrell and Liz Smith of Archer Cathro Ltd; as well as various field assistants including Michael Rogers, Levi Knapp, Mark Alban, Anatole, Tuzlak, Daniel Francis and Crystal Chung.

In addition there are many University of Alberta staff and faculty members who aided the collection of data and guided my scientific ramblings into this thesis. These include, but are not limited to, Dr. Jeremy Richards, Dr. Tom Chacko, Dr. Andrew Locock, Dr. Grahem Pearson, Dr. Rob Creaser, Dr. Andy DuFrance, Dr. Stephen Johnston, Dr. John Waldron, Dr. Richard Stern, Dr. Karlis Muelhenbachs, Mark Labbe, Martin Von Dollen, Igor Jakob and Dr. Yan Luo. Fellow graduate students also assisted with laboratory work and discussion including Robert Dokken, Kevin Byrne, Merilie Reynolds, Devon Smith, Neil Beaton and Joe Magnall.

From a financial angle this study would not have been possible without financing from Silver Range Resources Ltd. and an NSERC CRD- awarded to S. Gleeson. While, two Society of Economic Geologists Canada Foundation (SEGCF) awards (2015 and 2016) given to L. Pryer

allowed additional lab work to take place and the Presidents International Doctoral Scholarship from the University of Alberta made PhD life a lot more enjoyable.

Finally, I would be remiss not to Thank a few people who have made Canada home for me. Alanna Poole for averaging 4 years of Type 2 fun. Team sufferfest for 4 years of adventures; especially Robert Emberson who taught me to use semi colons. As well as Lily Jensen, Trent Grey, Natasha Barrett and Sierra Poole who have all shared a roof with me during the PhD.

Table of Contents

List Of Tables

List Of Figures

Chapter 5

Chapter 1: Introduction

The vast and remote Yukon Territory in northern Canada represents one of the great frontiers for global mineral exploration and has been the focus of prospecting since 1896 when Skookum Jim Mason discovered gold in Bonanza Creek and sparked the Klondike Gold Rush (Adney 1994). To this day gold exploration contributes significantly to the economy of the Yukon with current estimates of available hard rock gold reserves of ~25 million ounces for the territory (Yukon Government 2014). As well as gold, the Yukon Territory contains a number of significant deposits of other commodities, especially within the Paleozoic and Mesozoic basinal sediments that comprise the Selwyn Basin (Figure 1.1; Gordey 2013, Nelson et al. 2013). Deposit types found within the Selwyn basin include: the Anvil, Howard's pass and Macmillan type stratiform sediment-hosted massive sulphide occurrences (Goodfellow 2007, Goodfellow and Lydon 2007); the Marg volcanogenic massive sulphide deposit (Holbek and Copeland 2000); the Mactung and Cantung tungsten skarns (Dick and Hodgson 1982); the Keno Hill Ag bearing veins (Beaudoin and Sangster 1992); and a plethora of skarns, veins and porphyries with variable metallogenic signatures (Deklerk and Traynor 2005).

In the central Yukon, the Anvil district sediment-hosted massive sulphide deposits were discovered to the North of the town of Faro in the 1950's and 1960's (Tempelman-Kluit 1972, Jennings and Jilson 1986). Their discovery led to extensive exploration in the area, and the initial discovery of a small base metal prospect about 45 km to the north of the Anvil district called the Keglovic deposit. However, the Keglovic prospect contained sulphides in veins and skarn/carbonate altered rocks, and so was of limited interest to prospectors focused on finding another SHMS deposit (Cathro 1967, Eaton 2011, Dumala 2013). Interest in this region was re-

kindled in 2010 when Silver Range Resources amalgamated an 1100 km^2 staked area containing ~22 mineralized zones into the "Keg Property" (Figure 1.1). The Keglovic (or "Keg") deposit is the largest of the known mineralized zones on the Keg Property, with an inferred resource of 39.8 million tonnes of 30.25 g/t Ag, containing metal estimates of 38.7 million ounces of Ag, 675 million lbs of Zn, 228 million lbs of Pb, and 131 million lbs of Cu (Dumala 2013). Preliminary work on the deposit also reported anomalously high In, Sn and Cd (Brand 2011). However, advanced exploration on the Keglovic deposit in the summers of 2010 to 2013, including 69 drill holes, was unable to produce a coherent descriptive or genetic model for the mineralization observed. Key questions that could not be answered included: the source of the fluids involved in the mineralization; the number and style of mineralization events; and the nature and age of the causative intrusion. Without fully understanding the genesis of the Keglovic deposit it is impossible to effectively exploit it or explore for similar types of mineralization elsewhere. This project aimed to answer these questions and to create a genetic model for Keglovic style mineralization that can act as a guide to future exploration efforts.

Constraining the genesis of mineralization at the Keglovic deposit requires a detailed understanding of the regional geology, tectonic setting, and associated magmatism at the time of deposit formation. The Tay River district, which surrounds and contains the Keg property, is underlain by one of the highest densities of mid-Cretaceous igneous rocks in Yukon (Figure 1.1; Pigage 2004, Gordey 2013). The district also contains up to 38 km diameter calderas, representing the only known mid-Cretaceous extrusives in the Yukon (Gordey 1988). These intrusive and extrusive igneous rocks belong to the Omineca Magmatic Belt (OMB), an enigmatic and poorly understood band of plutons that extend along the length of the northern Cordillera (Figure 1.1). Numerous tectonic models have been proposed for the genesis of the

OMB, including formation due to a flat-slab, back arc extension or a cryptic western dipping subduction zone (Mortensen et al. 2000, Hart et al. 2004, Mair et al. 2006, Johnston 2008, Rasmussen 2013).

As well as containing a unique mid-Cretaceous igneous rock assemblage the Tay River district has experienced a complex Mesozoic tectonic evolution, including >10 km of regional uplift synchronous with the OMB plutonism, which led Smith and Erdmer (1990) to describe the region as "*atypical of the Cordillera"* with potentially *"a unique tectonic history or position in the orogen* [northern Cordillera]*"*. However, as the plutons in the Tay River district have traditionally been thought to be uneconomic or barren, the region has received little attention academically or economically (Pigage and Anderson 1985, Pigage 2004, Cobbett 2015).

Without a complete understanding of the igneous and tectonic evolution of the Tay River district it is impossible to understand the mineralization at the Keglovic deposit. Therefore, in this thesis I aimed to constrain the nature of OMB plutonism and volcanism in the Tay River district as a function of the complex tectonic evolution the region experienced in the mid-Cretaceous. Only once this regional framework had been created did I attempt to explain the mineralization observed at the Keglovic deposit.

Throughout this thesis I hope to convince the reader the Keglovic deposit is a product of the complex regional tectonic and igneous evolution, which occurred synchronously with the deposit formation. Therefore, in future exploration efforts the geological evolution of a region and environment of mineral formation needs to be considered, not just the age or geochemistry of the surrounding igneous rocks.

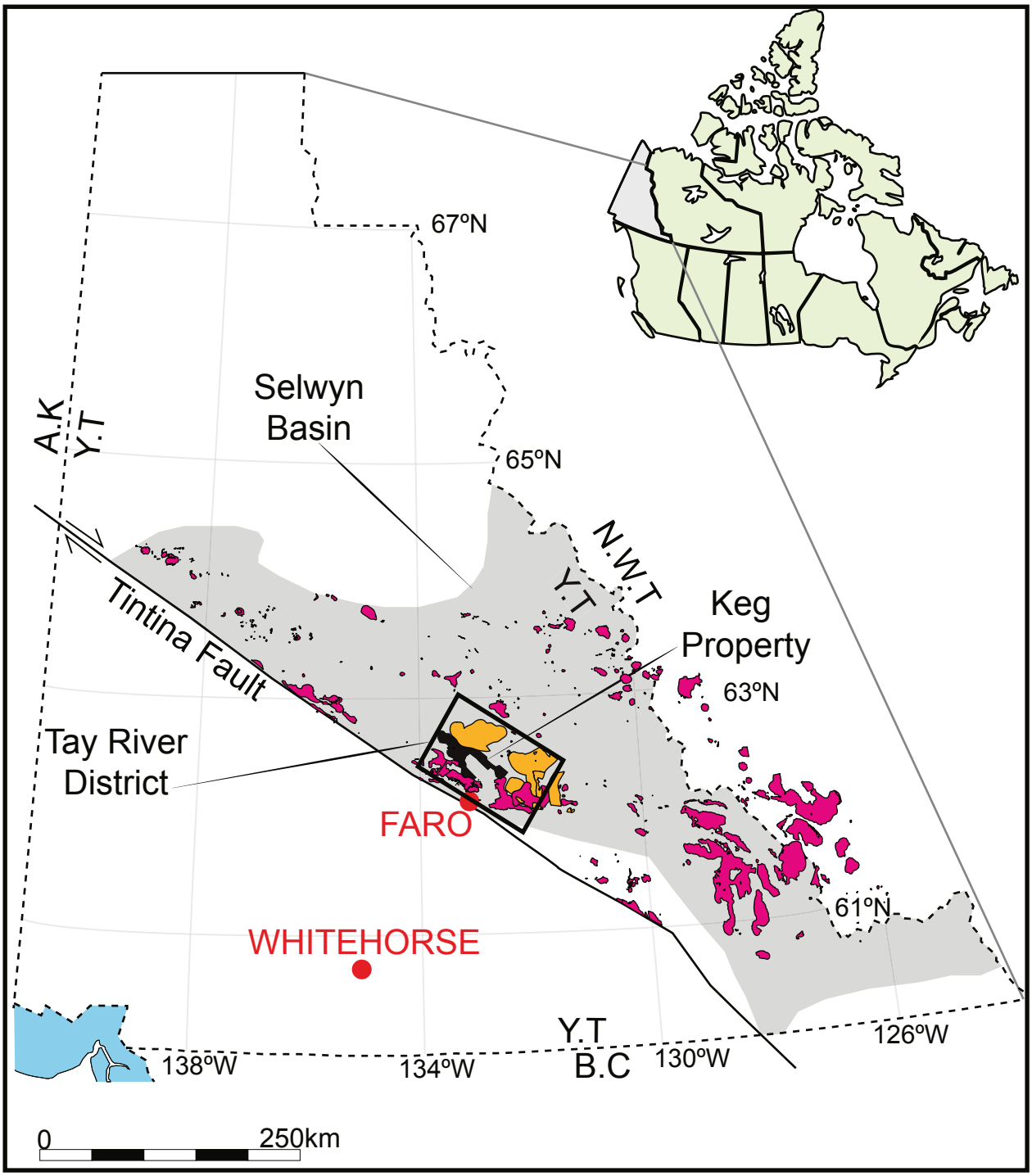

Figure 1.1: Map of Yukon showing key geographical and geological features. Selwyn basin extents from Nelson et al. (2013). OMB bodies within the Selwyn Basin (intrusives in pink and extrusives in orange) from Rasmussen (2013).

Outline of the thesis

This thesis contains 4 main chapters (Chapter 2 to 5), each addressing a fundamental question pertaining to the evolution of the OMB and the Keglovic deposit. Chapter 6 concludes the thesis. A summary of the main topics addressed by Chapters 2-5 is given below.

Chapter 2- *The Evolution of Mid-Cretaceous Omineca Magmatic Belt Granites in the Northern Cordillera: A Product of Mantle Lithosphere Delamination*- provides a detailed study of the mid-Cretaceous rocks within the Tay River district. This chapter uses petrography, U-Pb geochronological data, whole rock geochemical data, zircon chemistry and isotope chemistry generated during this PhD project. This data is integrated with compilations of existing data allowing for the sub-division of the OMB rocks in the district into suites based on time of emplacement. The petrogenesis of the igneous rocks in the Tay river district is discussed and the newly outlined pluton sub-divisions are expanded across the northern Cordillera. Finally a brief descriptive tectonic model is created to explain the newly developed pattern of OMB plutonism within the Tay River district and across the northern Cordillera.

Chapter 3- *Identifying the source of an S-type granite via xenocrystic zirconology*- provides a novel method for identifying the source of an S-type granite from U-Pb LA-ICP-MS analyses of inherited zircon grains. The method uses the software produced by Reimink et al. (2016) to correct for Pb loss in the inherited zircons and extract the inherited zircon age spectra from an S-type granite. By statistically comparing the extracted age spectra to those from regional sedimentary rocks it is possible to identify the sedimentary melt sources of an S-type granite. This method is applied to an S-type granite from the Tay River district.

Chapter 4- *Thermochronology of Omineca Magmatic Belt granites in the Selwyn Basin: Evidence for Mid-Cretaceous exhumation of the central Yukon and passage of the northern*

Cordillera over the Yellowstone Hotspot in the Late Cretaceous- provides a detailed study of the thermal and exhumational history of the Tay River district. This chapter uses U-Pb geochronological data combined with Ar-Ar and U-Th/He analyses to accurately constrain a previously hypothesised period of uplift that affected the Tay River district in the mid-Cretaceous.

Finally, based on the understanding of the mid-Cretaceous Tay River district generated by Chapters 2 to 4, Chapter 5- *The Keglovic Deposit: A telescoped Ag-Pb-Zn skarn and vein deposit, Central Yukon, Canada*- provides a descriptive and genetic model for mineralization at the Keglovic deposit. This chapter uses petrography, isotope studies, Re-Os geochronological data, microthermometry and whole rock geochemical data to accurately describe the evolution of mineralization at the Keglovic deposit.

Chapter 2: The Evolution of Mid-Cretaceous Omineca Magmatic Belt Granites in the Northern Cordillera: A Product of Mantle Lithosphere Delamination.

INTRODUCTION

The northern Cordillera of the Yukon Territory, Canada and Alaska, USA contains multiple phases of igneous activity associated with the complex amalgamation of terranes during the Mesozoic. Mid-Cretaceous (120-90 Ma) plutons in the northern Cordillera are considered one of the most important magmatic episode in the Cordilleran orogenic belt due to their diverse nature, regional abundance, and the varied economic resources associated with these magmatic phases (Hart et al., 2004). Two belts of mid-Cretaceous plutonism have been identified (Armstrong, 1988): the Coast Plutonic Belt (CPB), which is derived from the dehydration of an east dipping subducting plate (Woodsworth et al., 1991), and the more enigmatic, inboard, Omineca Magmatic Belt (OMB). This study focuses on the origin of the northern portion of the less well-understood OMB. Numerous models have been proposed for the formation of the plutons in the northern OMB including flat-slab, back arc extension and a cryptic western dipping subduction zone (Rasmussen, 2013; Mortensen et al., 2000; Hart et al., 2004; Mair et al., 2006; Johnston, 2008). All previous models have been based on the assumption that the mid-Cretaceous plutons form arc-margin parallel bands, which systematically young inboard.

In this paper, we propose a new model for OMB magmatism focusing on mid-Cretaceous constraints for granite genesis in the Tay River district, to the north of Faro, central Yukon. By defining plutonic suites by time of emplacement, we then expand this model to the scale of the

northern Cordillera using literature data and propose a new formation mechanism for OMB magmatism.

Geology Of The Northern Cordillera

The northern Cordillera represents the complex amalgamation of multiple terranes and basins onto the western margin of the North American craton (Figure 2.1). The eastern most, parautochthonous, sedimentary rocks were deposited in the Selwyn Basin, which formed during Proterozoic rifting along the ancestral North American passive margin. The basement to the Selwyn Basin is likely rifted older crust and cratonic rocks from the North American continent (Gordey and Anderson, 1993; Lund, 2008). The Selwyn Basin is bound to the north and east by carbonate-dominated platforms (the Ogilvie and Mackenzie platforms respectively). Sediment deposition in the Selwyn Basin occurred in three stages. The initial deep-water Selwyn Basin sedimentary assemblage was deposited from the Late Proterozoic to Middle Devonian. The deep-water rocks are unconformably overlain by Devono-Mississippian turbidities and conglomerates of the Earn Group. The final stage of sediment deposition in the Selwyn Basin occurred from the Mississippian to the middle of the Mesozoic, forming an assemblage of clastic shelf rocks (Gordey, 2013). Sediment deposition in the Selwyn Basin terminated in the Early to Middle Jurassic with the onset of the Sevier-Columbian orogeny and amalgamation of exotic terranes onto the western margin of North America (Nelson et al., 2013; Nelson and Colpron, 2007). The amalgamation of terranes appears to have occurred in two stages. “Intermontane” terranes (which consist of the Yukon-Tanana and Slide Mountain terranes in Alaska and the northern Yukon, and the Cache Creek, Stikinia and Quesnellia terranes in the southern Yukon and northern British Columbia) were initially accreted to the North American margin in, or pre-, the Early Jurassic (Colpron et al., 1996; Mihalynuk et al., 1994; Hildebrand, 2014; Beranek and

Mortensen, 2011). Intermontane terrane accretion was followed by the accretion of the "Insular" terranes. Current studies in the northern Cordillera do not agree upon the timing of Insular terrane accretion. The majority of the literature supports Insular terrane accretion in the Early to mid-Cretaceous (Evenchick et al., 2007; Nelson et al., 2013), however, there are a number of studies that indicate Insular terrane accretion occurred post-Late Cretaceous, in the early Cenozoic period (Hults et al., 2013; Johnston and Canil, 2007). The Intermontane terranes comprise a set of arcs, remnants of marginal seas and oceanic basins, and continental fragments that ringed the North American craton in the late Permian to Early Triassic (Nelson et al., 2006). The close proximity of the Intermontane terranes to the North American craton throughout their evolution is not generally accepted, with some studies suggesting that the Cache Creek terrane was derived 1000's of km from the western North American margin in the Tethys ocean (Monger and Ross, 1971; Johnston and Borel, 2007). The Yukon Tanana Terrane (YTT) represents a Paleozoic arc built onto a continental fragment, which was rifted away from the North American craton during the late Devonian to Permian. The rocks of the Slide Mountain terrane are the remnants of the rift generated oceanic crust that separated the YTT from North America in the Paleozoic. Closure of the Slide Mountain Ocean was driven by west dipping subduction beneath the YTT initiated in the Permian (Creaser et al., 1997; Mortensen, 1992; Grant, 1997) with the accretion of the YTT with ancestral North American occurring possibly as early as the late Permian, resulting in the Klondike orogeny (Beranek and Mortensen, 2011). The timing and nature of YTT accretion is not universally agreed upon; paleomagnetic data and Permian fauna suggest the Slide Mountain Ocean was not continuous with North America and did not obduct until the Middle Jurassic (Richards et al., 1993), while other studies suggest the

Late Permian collision represents accretion between an exotic carbonate platform (Cassiar platform) and the YTT far from the North American margin (Hildebrand, 2009; Johnston, 2008).

The Insular terranes evolved during the Paleozoic, distal to the North American margin, in the Arctic realm (Colpron et al., 2007). In the Yukon, compressive tectonics and terrane accretion terminated in the Early to mid-Cretaceous transforming in the Late Cretaceous into a transtensional stress regime, which was characterized by a number of orogen-scale dextral strike-slip faults (Nelson et al., 2013). The Tintina fault is the most easterly of these faults. The Tintina fault accommodated 430km of motion during the early Cenozoic. The more westerly Denali fault added another 350km of displacement beginning in the early Paleogene (Gabrielse et al., 2006).

Tectonic Setting Of The Mid-Cretaceous Omineca Magmatic Belt

In the generally accepted model for the northern Cordillera, east-directed subduction of the Farallon plate initiates around the Middle Triassic with the subducting oceanic plate conveying terranes into the continental margin (Beranek and Mortensen, 2011; Nelson et al., 2013; Evenchick et al., 2007). During the Early Cretaceous, this continued east-directed subduction, under the western most accreted terranes, at the continental margin forms the CPB. The oldest, most westerly, plutons of the CPB were emplaced into the Insular terranes between 160-140 Ma (Gehrels et al., 2009; Nelson et al., 2013). However, recent seismic tomography work by Sigloch and Mihalynuk (2013) and Sigloch (2012) suggests west dipping subduction occurred at the North American margin until at least the mid-Cretaceous, with terrane accretion occurring as the western margin of North America is overridden by upper plate volcanic archipelagos and subduction complexes. In this model, subduction occurs beneath the long-lived archipelagos in almost stationary intra-oceanic trenches.

Inboard of the CPB arc complex, the previously accreted allochthons had begun to ride up over the edge of the North American craton, during the Early to mid-Cretaceous periods (Sevier-Columbian orogeny; Hildebrand, 2009), along a number of NW-vergent thrusts. Lower crustal detachments between the advancing terranes and the continental basement allowed upper crustal shortening above the basement, forming 60 km thick crust under and involving the YTT in the core of the orogen (Pavlis et al., 1993; Staples et al., 2014, 2016, 2013).

Initiation of plutonism in the OMB coincided with a change in tectonic regime. It is generally thought the change was from sinistral to dextral transpression, at the western margin of cratonic North America, triggered by a change in relative plate trajectory between the North American and Pacific plate at ~110 Ma (Nelson et al., 2013; Elston et al., 2002). However, Kent and Irving (2010) suggest there were actually two changes in relative plate motion around the time of initiation of plutonism in the OMB: an earlier change from dextral to sinistral transpression in the Early Cretaceous followed by a return to dextral transpression in the Late Cretaceous through Eocene. The change in tectonic regime established a large dextral fault system between 115 and 95 Ma in the Teslin region, South Yukon (includes the Teslin and Cassiar faults; Nelson et al., 2013; Gallagher, 1999; Gabrielse, 1998). This dextral system extended into the Selwyn Basin propagating into a number of thrusts (Tombstone, Dawson and Robert Service thrusts; Mair et al., 2006) at the north and eastern contacts of the Selwyn Basin strata with the epicratonic rocks in the Ogilvie and Mackenzie platforms. Total displacement on this system was around 250km (Gabrielse et al., 2006). The OMB therefore, formed in a region of previously thickened crust escaping from the center of the Sevier-Columbian orogen, to the north, in a dextral tectonic regime (Pavlis, 1989; Staples et al., 2016; Angen et al., 2014) with plutons intruded during, and in part accommodating, syn-magmatic dextral shearing (Johnston, 1999).

Escape tectonics lead to rapid exhumation and extension in the core of the orogeny, with YTT rocks showing 14-18 km of vertical uplift between ~118 and 105 Ma (Dusel-Bacon et al., 2002; Staples et al., 2013, 2016; Berman et al., 2007). The rate of erosion kept up with vertical uplift at this time, leading to the removal of >10 km of the crustal section in the YTT, and neighboring Selwyn Basin, between ~115-100 Ma (Smith and Erdmer, 1990; Pavlis et al., 1993). Large volumes of sediment deposited, between ~115-100 Ma, in hinterland and foreland basins in Interior Alaska (including 5-8 km thick sections of sediments in the Yukon-Koyukuk basin and 12 km thick sections in the Kuskokwim basin), were presumably derived from this rapid erosion (Miller and Hudson, 1991; Underschultz and Erdmer, 1991; Patton and Box, 1989). The amphibolitic rocks of the YTT represent exhumed deeply buried continental crust (Pavlis et al., 1993; Miller and Hudson, 1991). Core complexes exhumed during the mid-Cretaceous have been identified in the YTT. These complexes show northwest to southeast extension (Mortensen, 1990; Staples et al., 2014; Hansen and Dusel-Bacon, 1998). At the north and northeast edges of the Selwyn Basin and YTT, the structural overlap generated by exhumation and extension was accommodated on the Tombstone, Dawson and Robert Service thrust faults. Movement on these faults ended at 104-100 Ma (Mair et al., 2006), synchronous with the proposed end of regional vertical uplift of the YTT. Post 100 Ma, dextral displacement in the northern Cordillera was focused onto a number of crustal scale faults with movement on the Tintina Fault beginning in the early Cenozoic (Gabrielse et al., 2006). Extension in the core of the OMB continued after 100 Ma with around 60 km of extension between the Tombstone thrust and the McEvoy platform, parallel to the Tintina fault, occurring between 100 Ma and 67 Ma (Gabrielse et al., 2006).

Summary Of The Mid-Cretaceous Igneous Rocks In The OMB

The OMB consists of a band of Cretaceous plutons emplaced mainly between 118 to 90 Ma (mid-Cretaceous) inboard of the North American continental margin. OMB magmatism follows a near complete magmatic lull from 135 to 125 Ma in western North America (Woodsworth et al., 1991; Armstrong, 1988), which Ross et al. (2005) equate with a period of tectonic quiescence. Plutons of the OMB extend along the whole length of the N. American Cordillera; this study will focus on the plutons within the Yukon and central Alaska (Figure 2.3).

Previous studies on the OMB have divided the diverse mid-Cretaceous igneous activity into suites representing regional groupings of plutons with similar emplacement ages, mineral assemblages and geochemical signatures. To avoid confusion with the temporal division of suites that will be defined in this paper, the spatial divisions of plutons will be termed *"plutonic regions"*. Previous analysis has identified greater than 25 separate plutonic regions (grouped into 13 larger belts) in the Yukon and eastern Alaska, covering both the CPB and the OMB (Figure 2.3; Mortensen et al., 2000; Rasmussen, 2013; Hart et al., 2004; Heffernan, 2004).

Mortensen et al. (2000) concluded that pluton emplacement in the OMB appears to step northeast, with time, in bands parallel to the western margin of the Cordillera, and that the oldest plutons in the OMB (114-98 Ma) occur near the Tintina fault within the Yukon-Tanana Uplands, Anvil, Cassiar and Hyland regions. Inboard - 98-96 Ma - younger plutons (and associated volcanics) occur within the Tay River and Fairbanks-Salcha regions. The furthest inboard, and youngest, (98-90 Ma) plutons occur within the Tombstone-Tungsten Belt (TTB), which includes the Tombstone, Tungsten and Mayo regions (Hart et al., 2004; Rasmussen, 2013; Morris and Creaser, 2008). Hart et al. (2004) used iron speciation in plutons to make genetic inferences about pluton formation. Their study tracked an inboard younging trend from the oldest-

outboard, magnetite series, metaluminous plutons through a band of younger ilmenite series, slightly peraluminous, plutons to the most inboard- youngest, magnetite series, alkalic plutons.

The mid-Cretaceous plutons of the OMB extend further inboard than any other intrusive rocks in the Cordillera except for very minor Eocene plutons.

Geology Of The Tay River District

The Tay River district is the focus of this study as it contains one of the highest concentrations of OMB plutons, and one of the rare examples of OMB volcanic rocks preserved in the northern Cordillera. The study area encompasses the Tay River and Anvil plutonic regions as identified by previous workers (Figure 2.3), and appears to have been affected by minimal tectonic activity since the mid-Cretaceous, with less than 1 km of denudation and less than a five degrees change in bed dip of mid-Cretaceous volcanic flows in the last 100 Ma (Smith and Erdmer, 1990; Gordey, 2013), meaning that the OMB igneous rocks have maintained their relative position since their emplacement. This allows for an accurate assessment of the relationship between igneous rocks of different ages.

The Tay River district is contained within the Omineca belt, which separates the cratonic foreland belt from the Intermontane belt (Monger et al., 1982). The district is located to the northeast of the most easterly allochthonous terranes. The study area is bound to the south by the Inconnu thrust that places the Slide Mountain and YTT against the North American margin sediments. The Tintina Fault lies to to the areas southwest (Gordey and Irwin, 1987). The Tay River district strata consist of deformed sediments of the parauthochthonous North American passive margin. These sediments have undergone regional lower greenschist facies metamorphism and have been imbricated and intensely folded during the Mesozoic Sevier-Columbian orogeny (Pigage, 2004). Thrust imbrication of the sediments has occurred on a

number of faults, including the Two Pete and Tay River thrusts, which show >2350 m stratigraphic overlap (Gordey, 2013). Mid-Cretaceous plutonic and volcanic rocks intrude Precambrian to Triassic Selwyn Basin strata in ~25% of the region (Gordey, 2013). Large mid-Cretaceous intrusive bodies in the area include the Anvil, Orchay and Marjorie batholiths (Figure 2.4). The South Fork volcanics occur in 8 calderas ranging from 6 to 55 km across, which contain volcaniclastic deposits up to 1 km thick (Gordey, 1988, 2013).

Previous studies on the regional mid-Cretaceous igneous rocks have divided the area into a number of suites (Pigage and Anderson, 1985; Gordey, 2013; Pigage, 2004; Gordey, 1988; Smith and Erdmer, 1990). Pigage and Anderson (1985) mapped the Anvil Batholith as containing three phases, including the muscovite- biotite bearing Mount Mye and two hornblende-biotite bearing phases (the Orchay and Marjorie). Gordey (2013) mapped all mid-Cretaceous intrusive phases as part of the Selwyn Plutonic suite which contained three rock types based on mineralogy: 1. Granitic rocks with common hornblende; 2. Granitic rocks dominated by biotite with rare hornblende; and 3. 2-mica (biotite and muscovite) bearing granites. Pigage (2004) simplified the classification using the scheme of Mortensen et al. (2000); the Anvil suite contains the two mica granites dated at 109-104 Ma and all other intrusive phases, containing biotite ± hornblende, belong to the Tay River suite (98-96 Ma). The South Fork volcanics are the extrusive equivalent of the Tay River suite. This study will build upon the previous work done in the region, and aims to map the temporal changes in the multiple styles of igneous activity within the Tay River district.

STUDIED SAMPLES AND ANALYTICAL TECHNIQUES

In order to test regional theories on OMB development thirty-four representative samples of granitic rocks (G1 to G34; Table A1) were collected from a mapping project carried out on the

Tay River district (Figure 2.4). To remove the post-crystallization affects of alteration petrographic studies identified the least altered samples for analysis. Unless otherwise reported, all analyses were conducted at the Canadian Centre for Isotopic Microanalysis at the University of Alberta, Edmonton, Canada.

U-Pb Zircon Geochronology

Zircons were separated from 10 granitic samples (G1, 3,4,10,11,12,18,20,22,27) using standard gravimetric and magnetic techniques. From the heavy mineral separate we selected ~ 60 zircons that were subsequently annealed for 48 hours at 1000°C. The annealed zircons, along with two grains from a reference material (Zircon 94-35), were mounted in epoxy and then imaged in secondary electron, cathodoluminescent and backscattered light using a Zeiss Evo-MA-15 scanning electron microscope (SEM). U-Pb dating was carried out by in situ LA-ICP-MS spot analysis on approximately thirty grains per sample. Laser ablation sites were selected from the CL images to avoid mixing -between zircon growth during OMB magmatism and inherited cores - and to pick parts of the magmatic grain with favourable uranium concentrations.

U-Pb analyses were carried out using a New Wave UP-213 laser coupled to a NuPlasma Multi-Collector ICP Mass Spectrometer using procedures modified from Simonetti et al (2005). The laser was operated at 4 Hz pulse rate with a beam spot size of 40 μm and a fluence of ~3 J/cm^2. On peak gas and acid blanks (30s) were measured prior to a set of 10 unknown analyses for each sample, bracketed by analysis of two zircon reference materials: GJ-1 (Jackson et al., 2004), and 94-35 (Klepeis et al., 1998). Unknowns were normalized to the zircon reference material GJ-1. Reproducibility of the primary reference GJ-1 is estimated to be ~1% 2 RSD for $^{207}Pb/^{206}Pb$ and 2-3% 2 RSD for $^{206}Pb/^{238}U$. The secondary reference (94-35) yields a weighted regression intercept of 55.96 ± 0.51 Ma (MSWD 0.18, n =37) in Tera Wasserburg

space. The errors reported in Table A2 are a quadratic combination of the within run standard error and the external reproducibility of the primary reference GJ1 in terms of standard deviation. However, there is a growing body of literature (i.e. Marillo-Sialer et al., 2016) that indicate that the total uncertainty in an *in situ* U-Pb age measurement is closer to 1-2% even if the intercept regression errors or weighted average errors are < 1%. Therefore, real uncertainties on the ages reported in this study are more likely closer to 1-2 Ma, rather than 0.58-1 Ma suggested by the weighted regression intercept age. Rarely, data points with a large amount of common lead or where an inclusion had been analyzed were discarded (one point from G10, G18, G22 & G27). All other data points were plotted on a Tera-Wasserburg plot using the Isoplot software of Ludwig (2003).

Major And Trace Element Chemistry

Eleven samples of intrusive rocks covering the range of observed granitic rock compositions and textures in the Tay River district were analyzed for major, trace and rare earth element (REE) concentrations at Bureau Veritas Mineral laboratories, Vancouver, Canada (Table A3). Major and selected trace elements were analyzed by X-ray Fluorescence spectroscopy. Trace elements, including REE, were analyzed by ICP-MS following an aqua regia digestion. As well as the procedures employed by Bureau Veritas, we submitted: a crush split duplicate of sample G18, silica blanks and known standards for external quality assurance procedures. The known standards (OREAs 131a and 134a from the Ore Research and Exploration PTY LTD and Green River Shale SGR-1 from the USGS) returned values within the accepted limits of published values for all reported elements. The crush split of G18 showed reproducibility of better than 10% for all elements above the practical lower detection limit. Additional geochemical data from

mid-Cretaceous igneous rocks in the Tay River district were incorporated from Gordey (2013), Pigage (2004), Pigage & Anderson (1985) and Rogers (2017).

Zircon LA-ICP-MS Trace Element Chemistry

Twenty eight trace elements were analyzed on annealed mounted zircon separates from five samples (G1,4,10,18 & 20; Table A4) by laser ablation inductively coupled plasma mass spectrometry (LA-ICP-MS). The laser used was a RESOlution M-50 193nm excimer laser system connected, via Nylon tubing, to a sector-field ICP-MS Thermo Element XR2. The laser was operated at a repetition rate of 8 Hz, energy density 4J/cm^2, and with a spot size of 50 μm. An analysis comprised 40 s of background gas collection, followed by 60 s of ablation. Ablated aerosols were entrained in a He (1000 ml/min) and Ar (0.8 ml/min) cell gas flow, prior to entering the ICP-MS torch. The ICP-MS was operated at 1300 W and a torch depth of 3.8 mm. Argon and He gas flow, torch position and focusing potentials were optimized in order to achieve optimal (Co, La and Th) signals and low oxide production rates (ThO/Th<0.2%). Calibration was performed using NIST SRM 612 and NIST SRM 610 in conjunction with internal standardization using Zr (Wiedenbeck et al., 1995; Hoskin and Schaltegger, 2003; Belousova et al., 2002). All data were reduced offline using Iolite v3 (Paton et al., 2010, 2011). The results of the secondary standard (zircon 91500) agree with the reference values within relative uncertainties of typically 5-10% or better, at the 95% confidence level. The detection limits are below 0.1 ppm for most elements. Ten to fifteen spots were recorded per sample. The SEM images were used to ensure no inherited core component of the zircons was ablated.

Pb, Sr And Nd Isotope Studies

Lead isotopes were measured from primary magmatic K-feldspar grains from three 150μm uncoated petrographic slides of the Anvil suite (Table A5). The slides are described in Rogers (2017). The three slides used were taken from the same drill core section as G18. The set up was analogous to the U-Pb measurements; ablation was performed with a New Wave UP-213 laser and measured on a NuPlasma Multi-Collector ICP Mass Spectrometer. The laser was operated at 20 Hz pulse rate with a beam spot size of 80-100 μm and a fluence of ~10 J/cm^2. The solution was doped with 8 ppb Tl. NBS SRM981was used as a solution/ aspiration standard and returned values of $^{208}Pb/^{204}Pb$ equal to 36.69±0.01, $^{207}Pb/^{204}Pb$ equal to 15.490±0.005, $^{206}Pb/^{204}Pb$ equal to 16.935±0.005 and $^{207}Pb/^{206}Pb$ equal to 0.9146±0.0001 (accepted values Todt et al., 1996:$^{208}Pb/^{204}Pb$ =36.70, $^{207}Pb/^{204}Pb$=15.489, $^{206}Pb/^{204}Pb$=16.936 and $^{207}Pb/^{206}Pb$= 0.9146). NIST 612 glass was used as an ablation standard and returned average analysis of $^{208}Pb/^{204}Pb$ equal to 36.98±0.02, $^{207}Pb/^{204}Pb$ equal to 15.507±0.007, $^{206}Pb/^{204}Pb$ equal to17.093±0.009 and $^{207}Pb/^{206}Pb$ equal to 0.9071±0.0002 (accepted values Woodhead and Hergt, (2001): $^{208}Pb/^{204}Pb$ =37.00, $^{207}Pb/^{204}Pb$=15.51, $^{206}Pb/^{204}Pb$=17.09 and $^{207}Pb/^{206}Pb$= 0.9076).

Strontium and neodymium isotope analysis methods are described by Creaser et al. (2004) and D'Souza et al. (2016). Ten unweathered granite samples, which had been ground to a fine powder in an agate mill (G1,3,4,10,11,18,20,21,22 & 27) were dissolved in HF and HNO_3, and Rb, Sr, Sm and Nd purified by standard chromatographic methods. Accuracy was monitored by use of the SRM987 Sr isotope standard and ShinEtsu Nd isotope standard, and the Sr and Nd isotope data are presented relative to a value of 0.710245 for Sr and 0.512107 for ShinEtsu. Based on the U-Pb ages of the granites, time corrections were applied to calculate the $^{87}Sr/^{86}Sr_i$ and εNd_T of each sample, representing the isotopic ratios at the time of granite crystallization.

The depleted mantle model age (T_{DM}) gives an estimate of crustal residence time and is calculated for each sample (after Goldstein et al., 1984; Nelson and DePaolo, 1984; Arndt and Goldstein, 1987).

RESULTS

Petrography combined with U-Pb dating defines three distinct suites of plutonic rock present in the Tay River district. The suites are correlated with the Anvil and Tay River suites as defined by Pigage (2004) and a newly identified and defined Tombstone suite. Note that in previous studies, the Tombstone-Tungsten Belt (TTB) (Figure 2.3) collectively referred to the most inboard regional divisions of plutons in the Selwyn Basin (Tungsten, Mayo & Tombstone regions) (Rasmussen, 2013), which show highly variable geochemical characteristics and mineralogies. However, all three suites in the TTB were emplaced between 96- 90 Ma. Therefore, in this study we use the term '*Tombstone suite'* to define the plutons identified in the Tay River district in this temporal range.

Results are presented in three groups corresponding to the three plutonic suite classifications. Since the South Fork volcanics are the extrusive equivalent of the Tay River suite, results from the volcanic rocks are presented with the Tay River suite. Previous geochemical data, obtained from plutons in the Tay River district, are reclassified based on U-Pb age or, when a U-Pb age is not available, mineralogy (Pigage, 2004; Pigage and Anderson, 1985; Gordey and Irwin, 1987; Gordey, 1988, 2013). Previously published U-Pb dating on zircons and monazite are included in the definition of the suites. Other dating methods - K-Ar, Rb-Sr and Ar-Ar - are not considered due to the susceptibility of these systems to open system behavior in regions where post emplacement thermal/ hydrothermal alteration may have occurred.

Anvil Suite

Petrography

The Anvil suite consists of seriate hypidiomorphic biotite-muscovite (two mica) phanerocrystalline granites. The mineralogy of the plutonic suite is homogenous in all samples analyzed. Samples G1 - G3, G5, G8, G9, G14 - G16, G28, G29, G32 and G34 belong to the Anvil suite. The rocks are observed in the field as a number of small plugs and laccoliths commonly elongated in a northwest to southeast orientation. Roof pendants are common. Granite sills occur in the metasedimentary host rock close to the main intrusive bodies. The cores of Anvil suite bodies are massive but foliations are present in the granite near the margins. The presence of coexisting primary magmatic muscovite and biotite defines this plutonic suite. Biotite forms primary subhedral-euhedral laths, showing strong pleochroism between a pale tan brown-yellow and a red-brown colour (Figure 2.5B). Pigage (2004) notes that biotite in the host schists is identical to the grains seen in the Anvil suite. Muscovite occurs as both primary isolated euhedral magmatic grains (Figure 2.5A) and as secondary anhedral aggregates. The primary biotite and muscovite grains commonly contain zircon and monazite inclusions and associated radiation damage haloes. Quartz, microcline, albite and oligoclase make up the equigranular to seriate groundmass of the samples, occurring as up to 1 cm crystals. K-feldspar grains form orientated oikocrystic megacrysts (up to 15 cm, commonly 5-8 cm) in some samples. Myrmekite grains are common (Figure 2.5C) and are diagnostic of this plutonic suite. Allanite and tourmaline are the last phases to crystallize in highly fractionated samples (Pigage and Anderson, 1985). Highly peraluminous minerals (garnet and cordierite) are not observed in these samples but have been reported by other authors in the Anvil suite (Pigage and Anderson, 1985; Smith, 1989). However, the presence of these peraluminous phases is hypothesized for some

samples due to rare circular clots of dense highly un-orientated fibrolite and sericite. Foliation in marginal samples of the Anvil suite is defined by interstitial mica aggregates, coplanar with recrystallized quartz subgrains. The effect of strain during crystallization is seen in bent muscovite grains and undulose extinction of quartz subgrains. Chlorite and epidote alteration is minimal. Secondary hydrothermal biotite, fibrolite and sericite occur rarely on grain boundaries.

U-Pb Dating

Samples G1 & G3 from the Anvil suite were dated. Greater than 95% of zircons separated from the Anvil suite samples contain inherited cores. In sample G1 the cores are commonly spheroidal with diameters ranging from 40 to 220 μm. Cores typically make up 25±10% (range of 7 to 51%) of the zircon grain by volume. Magmatic rims on the zircons display well-defined regular zoning in cathodoluminescent light. The U-Pb data from G1 define a line intercepting the Tera-Wasserburg curve at 108.14 ± 0.97 Ma (2σ, MSWD=1.3, n=30; Figure 2.6A). Inherited cores dominate the zircon volume of sample G3, making it impossible to avoid sampling both domains during *in situ* analysis and so we do not provide an estimation of emplacement age here. Previous monazite U-Pb ages for the Anvil suite range from 109.3 to 103.9 Ma (Pigage, 2004). No other zircon ages exist for the Anvil suite.

Tay River Suite and South Fork Volcanics

Petrography

The Tay River suite consists of porphyritic to seriate, phaneritic to aphanitic biotite-hornblende bearing granites and granodiorites. Considerable textural and mineralogical heterogeneity exists within this plutonic suite. Samples G4, G11, G13, G17 - G19, G22, G23, G27 and G32 belong to the Tay River suite. The rocks are observed in the field as isolated batholiths and also as dykes

and sills cutting the Anvil suite. These dykes and sills are commonly elongate in an east to northeast direction (Pigage, 2004). Coexisting euhedral phenocrysts of biotite and hornblende define this plutonic suite. Hornblende grains are euhedral and show strong absorption colours ranging from pale green to olive and brown-greens (Figure 2.5E). Biotite phenocrysts are pleochroic in shades of dark-chocolate brown to pale-straw brown (Figure 2.5F). The suite is characteristically porphyritic (around 75% of samples analyzed) containing phenocrysts of biotite, alkali feldspar, plagioclase feldspar, hornblende and quartz in a fine-grained aphanitic groundmass of quartz and feldspars (Figure 2.5D). Clinopyroxene, associated with hornblende phenocrysts, is rare. Euhedral phenocrysts are commonly 0.3-0.8 cm, and rarely up to 2 cm in size. The other 25% of samples display a seriate hypidiomorphic texture with similar phenocryst sizes, but a microcrystalline groundmass (Figure 2.5E). Myrmekite is absent. Microperthite exsolution is observed in feldspar phenocrysts.

There is no evidence of a foliation in any of the samples studied or observed in the field. The only evidence for strain seen in the Tay River suite samples is rare undulose extinction in quartz grains of the seriate samples. Alteration is more common than in the Anvil suite. The Tay River suite has chlorite- epidote aggregates altering the hornblendes. Chlorite, carbonates and sericite (saussuritization) alteration of plagioclase forms turbid phenocrysts. Alteration of hornblende and plagioclase phenocrysts is more pronounced in the dykes and sills of the Tay River suite than the isolated batholiths. In the samples taken from dykes and sills, hornblende and plagioclase phenocrysts have undergone complete hydrothermal alteration to fine grained mineral aggregates.

The South Fork volcanics consist of intermediate composition extrusive rocks. The volcanic rocks are thought to have previously been regionally extensive, but erosion has removed

these deposits with only ~1 km thick caldera fills remaining (Gordey, 1988). Samples G20, G21 and G24 - G26 are examples of the South Fork volcanics. The South Fork volcanics consist of tuffs, crystal-lithic lapilli tuffs and rare lapillistones interlayered with sparse andesitic composition lava flows. The South Fork volcanics have the same phyric content as the Tay River suite (hornblende, biotite, quartz, feldspars and rare pyroxenes) ranging from 0.5 to 5 mm. The subrounded to rounded crystals commonly form polyminerallic glomerocrysts which are hosted in a tuffaceous felsic matrix compromising 35 to 60% of the rock. Bent and broken crystal grains are common (Figure 2.5G). Development of weak eutaxitic textures and fiamme are seen in some samples (Figure 2.5H). Angular to subround lithic fragments make up less than 5% of the volcaniclasts consisting of argillites and cherts (Figure 2.5I). Alteration is pervasive with chlorite-epidote aggregates altering biotite, hornblende and feldspars pyroclasts.

U-Pb Dating

Samples G4, G11, G18, G22 and G27 from the Tay River suite were dated. For each sample 30 spots were measured from the rims of 30 zircon grains. The zircons separated from the Tay River suite samples contain no evidence of inheritance in SEM images. Regular magmatic zoning is seen throughout the zircon crystals, which commonly form prismatic to elongate euhedral grains. The five intercept ages range from 98.00 ± 0.62 Ma (G18; 2σ, MSWD=0.65, n=30) to 99.57 ± 0.77 Ma (G27; 2σ, MSWD=1.11, n=30; Figure 2.6B & 2.6C). The average age is 98.7 ± 0.8 Ma. Cobbett & Crowley (Pers. Comms) independently dated sample G32 at 95.37 ± 0.03 Ma. Four published U-Pb dates on the Tay River suite range from 96.74 ± 0.03 to 99.3 ± 1 Ma (Gordey, 2013; Pigage, 2004; Cobbett, 2015)

Sample G20 of the South Fork volcanics was dated and the U-Pb data define a line intercepting the Tera-Wasserburg curve at 98.81 ± 0.83 Ma (2σ, MSWD=1.07, n=30; Figure

2.6C). Five published U-Pb zircon dates on the South Fork volcanics range from 96.8 ±1 Ma to 97.7 ± 0.3 Ma (Gordey, 2013).

Tombstone Suite

Petrography

The Tombstone suite in the Tay River district is characterized by biotite-bearing granites and granodiorites. Samples G10, G12, G30, G31 and G33 belong to the Tombstone suite. Rocks are observed in the field as small, commonly rounded, plugs displaying no elongation. No internal foliation of the Tombstone suite is observed. The Tombstone suite rocks display equigranular hypidiomorphic phaneritic textures dominated by (>90%) crystals of microcline, Ca-rich plagioclase and quartz. Subhedral- anhedral microcline forms characteristic tartan (polysynthetic) twinning with euhedral to subhedral anorthite grains displaying Carlsbad twins. Quartz grains are characteristically equigranular and anhedral (Figure 2.5J). Primary biotite occurs as interstitial, euhedral, laths with characteristic straw-yellow to black-brown pleochroism (Figure 2.5K&L). The biotite laths commonly form monominerallic aggregates, which are not seen in the other plutonic suites. Primary magmatic muscovite is absent. Hornblende is rare to absent from most Tombstone suite samples (<1%). Hydration of primary magmatic and hydrothermal biotite to chlorite is common within the Tombstone suite rocks as is the breakdown of feldspars to form turbid plagioclase.

U-Pb Dating

Samples G10 and G12 from the Tombstone suite were dated in this study. For each sample between 27 and 30 spots were measured from the magmatic rims of the zircon grains. In sample G10 the U-Pb data points define a line intercepting the Tera-Wasserburg curve at 91.68 ± 0.58

Ma (2σ, MSWD=1.15, n=27; Figure 2.6D). Sample G12 gave an intercept age of 94.82 ± 0.72 Ma (2σ, MSWD=0.49, n=30; Figure 2.6D) Cobbett & Crowley (Pers Comms) independently dated sample G33 at 96.61 ± 0.03 Ma. Pigage (2004) previously dated a monazite from a sample in the western Anvil Batholith at 95.3 ± 1.3 Ma, but did not recognize it as being from the Tombstone suite.

Major And Trace Element Geochemistry

On the TAS plutonic diagram (Figure 2.7A; Middlemost, 1994) the intrusive rocks of the Tay River district range from granite to diorite with rare quartz monzonites (60 to 75 SiO_2 wt%). A decrease in SiO_2 wt% is seen with time from the felsic granites and quartz monzonites of the Anvil suite to the more mafic granodiorites and diorites of the Tay River suite. The Tombstone suite samples spread over the whole geochemical range recorded in the region. The South Fork volcanics cover TAS (Figure 2.7B; Le Maitre, 1989) compositions ranging from andesitic to dacitic, overlapping with the range seen for the Tay River suite.

The mid-Cretaceous granitic magmas in the Tay River district range from calc-alkaline to high-K calc-alkaline (Figure 2.7C; Rickwood, 1989) and have a peraluminous aluminum saturation index (ASI, i.e. A/CNK>1; Barton and Young, 2002). The Anvil suite rocks are generally strongly peraluminous and high K calc-alkaline. The Tay River suite is weakly peraluminous and calc alkaline to high-K calc alkaline in composition. Chondrite normalized REE patterns (McDonough and Sun, 1995) for the different plutonic suites (Figure 2.7D) display significant variations. The rocks of the Anvil suite have LREE enrichment, a minor negative Eu anomaly and strong HREE depletion. The REE pattern for the Tay River suite and South Fork volcanics form a listric shape with MREE depletion and minor HREE depletion and a pronounced negative Eu anomaly. The Tombstone suite samples have REE patterns identical to

the Tay River suite. All granitic rocks possess very analogous minor element concentrations (Figure 2.7E), similar to that found in average upper crustal rocks with U and Th concentration 100 times those found in the average lower crust/MORB and 10,000 Chondrite (Pearce, 1982; McDonough and Sun, 1995). Table 2.1 shows a number of geochemical parameters for each suite with Figure 2.7 F-I showing plots of these parameters.

Zircon Chemistry

Titanium thermometry based on the Ti concentration in zircons was conducted on each suite following the methods of Ferry and Watson (2007). Silica and titanium activities were assumed to be equal to one due to the presence of solid quartz and rutile in the rocks sampled. Maximum uncertainties of 60-70°C at 750°C are introduced to zircon thermometry by unconstrained a_{SiO2} and a_{TiO2} (Ferry and Watson, 2007). Rutile inclusions occur rarely in zircon crystals of sample G4, G10 and G18. When these inclusions were ablated anomalously high titanium concentrations, and therefore temperatures, were recorded. These data points were not included in the average (Table A6). The Anvil suite (G1) gave the lowest average crystallization temperature estimates of 620±40°C. The Tay River suite samples (G4 and G18) gave higher average crystallization temperature estimates of 710±45°C, similar to the Tombstone suite sample (G10) which returned a value of 730±110°C. South Fork volcanics zircons gave temperatures of 760±100°C (Figure 2.8).

Uranium and thorium concentrations were measured in zircons from each plutonic suite and the South Fork volcanics (Figure 2.9). The Anvil suite zircons have high uranium concentrations ($\bar{x}$ =3700±700 ppm). The Tay River and Tombstone suites have lower U but higher Th than the Anvil suite. The zircons of the Tay River suite are not as enriched in U ($\bar{x}$ =400±150 ppm) or Th. The zircons of the Tombstone suite have minor enrichments in U ($\bar{x}$ =1410±600 ppm) and

Th concentrations up to 750 ppm. The Anvil, Tay River and Tombstone suite zircons all contain <10 ppm Pb. The REE patterns of all the zircon crystals have the same shape; a steeply rising slope from LREE to HREE with positive Ce anomalies and negative Eu anomalies. Large variations in chemistry within the grains of an individual sample are seen. Table 2.2 shows the range of chemistries of each igneous suite for some common parameters of zircon chemistry (Hoskin and Schaltegger, 2003; Hoskin and Ireland, 2000).

Isotope Chemistry

Whole rock Sr and Nd isotopes, corrected to the age of pluton emplacement (εNd_t and $^{87}Sr/^{86}Sr_i$) both change systematically with time (Figure 2.10; Table 2.3). The Anvil suite gave highly negative values of εNd_{110Ma} equal to -20±1 and high $^{87}Sr/^{86}Sr_{110Ma}$ (0.7378-0.7393). The average depleted mantle model (T_{DM}) age for the Anvil suite is 2.20±0.04 Ga. Lead isotopes from the K-feldspars of the Anvil suite gave average values of $^{208}Pb/^{204}Pb$ equal to 39.33±0.02, $^{207}Pb/^{204}Pb$ equal to15.727±0.006 and $^{206}Pb/^{204}Pb$ equal to 19.337±0.007. These lead values are just above the values expected for an upper crustal sediment in the Selwyn Basin at 110 Ma calculated from the Shale curve ($^{208}Pb/^{204}Pb$=37.083, $^{207}Pb/^{204}Pb$=15.551 and $^{206}Pb/^{204}Pb$=17.264; Godwin and Sinclair, 1982; Andrew et al., 1984).

Tay River suite, South Fork volcanics and Tombstone suite samples give εNd_{100Ma} values ranging from -16.3 to -13.9. $^{87}Sr/^{86}Sr_i$ values for the younger suites cluster around 0.717±0.02. Depleted mantle model ages average at 2.1±0.2 Ga (range 1.73 to 2.32 Ga).

DISCUSSION

Regional Distribution Of Suites

Petrography, combined with U-Pb dating, on the granitic rocks of the Tay River district has identified three plutonic suites: the 109-104 Ma Anvil suite, the 100-96 Ma Tay River suite (and coeval South Fork volcanics) and the 96-90 Ma Tombstone suite (Figure 2.6E). The suite interfingering, seen in the Tay River district, does not show any systematic inboard younging direction (Figure 2.11). Therefore, here we present a new model for OMB magmatism focusing on granite genesis constraints in the Tay River district. We then expand this model to the scale of the northern Cordillera using literature data.

Genesis Of Plutonic Suites In The Tay River District

The peraluminous nature of all igneous rocks in the Tay River district, along with the highly evolved Nd, Sr and Pb isotopic ratios, suggest they all formed from crustal melting, rather than from primary, mantle-derived, melts.

No isotopic evidence for mixing of mantle and crustal melts is seen in the Tay River district and there are no mafic intrusives associated with mid-Cretaceous plutonism in the Tay River district. The zircon REE patterns and presence of inherited cores also indicate a crustal, rather than mantle, melt source (Table 2.2). A single, assimilating, and fractionally crystallizing pluton cannot explain the general TAS trend, to more mafic rocks with time. This general trend combined with the 20 Myr range of intrusion ages in the Tay River district, means that the source, origin and tectonic history of each suite is likely to be different and the three suites are not all derived from the same magmatic system.

Anvil Suite

The 109-104 Ma Anvil suite comprises coexisting biotite and primary-magmatic muscovite bearing granites and quartz monzonites. Subduction appears to have played no role in the formation of the Anvil suite as the "subduction signature" is nearly absent (Table 2.1); this is a useful indicator of a granite's source, because granites lacking LILE enrichment compared to HFSEs (Ba/Ta_N) are derived from a source that has never undergone subduction processes (Morris and Creaser, 2008). The lack of LILE/HFSE enrichment in the Anvil suite, therefore, indicates a crustal source for the melt of the Anvil suite. Geochemistry can be used to constrain the protolith for the Anvil suite. Sylvester (1998) used CaO/Na_2O versus Al_2O_3/TiO_2 of peraluminous post collisional granites as an indicator of both temperature (Al_2O_3/TiO_2 decreases with temperature) and chemistry of the melting crust (Figure 2.7F). CaO/Na_2O of experimental melts derived from pelites is <0.3, greywackes is >0.3 and meta-igneous rocks (tonalities) and psammites equals ~1. The results for the Anvil suite (see Table 2.1) suggest melting from a greywacke at low temperatures. The εNd_{110Ma} and $^{87}Sr/^{86}Sr_i$ values measured from the Anvil suite (-20±1 and 0.7378-0.7393 respectively) indicate a highly evolved, upper crustal, source rock. The Anvil suite values overlap with the average values for $^{87}Sr/^{86}Sr_{100Ma}$ and εNd_{100Ma} of Proterozoic sedimentary rocks in the Selwyn Basin (0.765 and -17.9 to -22.7, respectively; Ghosh and Lambert, 1989; Driver, 1998; Garzione et al., 1997; Boghossian et al., 1996). The crustal residence age (T_{DM}) for the Anvil suite is similar to those reported for cratonic North America (2.8-2.5 Ga; Theriault and Ross, 1990), suggesting a sedimentary upper crustal source derived from the craton. Pb isotopes in K- feldspars in the Anvil suite suggest the Pb is derived from a crustal unit enriched in U and Th compared to the average Selwyn Basin sedimentary rocks (Godwin and Sinclair, 1982).

The isotopic and geochemical results from the Anvil suite, along with the large inherited zircon component, suggest that the granite originates from low temperature melting of a pelite or greywacke. Minimum temperatures required for fluid absent melting via muscovite and biotite dehydration range from 800 to 875°C for pelitic rocks (Vielzeuf and Montel, 1994; Patiño Douce and Johnston, 1991). Pelites melt at lower temperatures (850±20°C) than metagreywackes (950±30°C) at 1000 MPa (Searle et al., 2009; Vielzeuf and Montel, 1994). Wet melting is not considered a possibility as H_2O saturated conditions do not occur in the mid- to deep crust (Patiño Douce and Johnston, 1991).

The aureoles of plutons assigned to the Anvil suite contain andalusite, staurolite, garnet, biotite, muscovite, quartz and plagioclase with local sillimanite (fibrolite) and cordierite forming concentric isograds to the intrusive rocks (Smith and Erdmer, 1990; Smith, 1989; Pigage and Anderson, 1985). The aureole mineralogy, combined with the lack of kyanite and the presence of primary magmatic muscovite, constrains the emplacement depth to 3.5 to 4 kbars, or around 12-15 km, of overburden. The emplacement temperature can be constrained from the aureole mineralogy to be 600-620°C (Smith and Erdmer, 1990), consistent with the emplacement temperature of 620 ± 40°C suggested by the Ti concentration of zircons from sample G1.

Pigage (2004) mapped numerous roof pendants in the southeast portion of the Anvil batholith with mineralogy similar to the aureole, indicating that the present level of exposure is near the top of the pluton and that 12 to 15 km of overlying crust has been eroded since emplacement. Burial to ~4 kbars is supported by the broad greenschist facies alteration of the Tay River district (Gordey, 2013; Pigage, 2004). Adding this amount of denudation to the current crustal thickness in the Tay River district of 40 ± 5 km, as shown from the SNORCLE lithoprobe survey line 3 (Cook et al., 2004), gives a paleo- mid-Cretaceous crustal thickness of

50-60 km agreeing with estimates for the proximal YTT (Pavlis et al., 1993; Staples et al., 2016). The high $(La/Yb)_N$ and $(Sm/Yb)_N$, combined with HREE depletion, seen in the Anvil suite suggests garnet in the source and, therefore, supports the presence of thick crust during the formation of the Anvil suite (Figure 2.7 D, G-H; Kay and Mpodozis, 2001; Kay et al., 1991; Haschke and Günther, 2003). The high U concentration of the Anvil suite zircons and highly radiogenic K- feldspar lead ratios suggest a sedimentary rock enriched in heat producing elements was involved in the genesis of the Anvil suite. This sedimentary layer, present in thickened crust, would generate the heat required to melt the metasedimentary source rocks in 30 to 50 Myr following attainment of maximum tectonic thickening (Bea, 2012; Patiño Douce et al., 1990), which fits with mid-Cretaceous (~115-110 Ma) melt initiation following crustal thickening derived from accretion of the Intermontane terranes to the western North American margin, which was complete by the Middle (Mihalynuk et al., 1994; Colpron et al., 1996) to Early Jurassic (Hildebrand, 2014). Uplift recorded proximal to the Tay River district, in the YTT starting at ~118 Ma, may have caused decompression melting contributing to Anvil suite formation (Staples et al., 2013; Dusel-Bacon et al., 2002; Pavlis et al., 1993). Mantle heat input is not required to generate the earliest mid-Cretaceous melts in the Tay River district, but a contribution from an external heat source cannot be ruled out.

Marginal samples of the Anvil suite show a strong foliation with minor regions of granite mylonite. This fabric is interpreted to be due to regional shear stresses during the emplacement of the Anvil plutonic suite (i.e. D2 as defined by Jennings and Jilson, 1986; Pigage, 2004). The plutons appear to be associated with major crustal scale (reverse) faults.

In conclusion, the oldest style of mid-Cretaceous plutonism in the Tay River district, represented by the Anvil suite, is emplaced prior to 100 Ma and derived from low temperature

melting of sedimentary rocks with upper crustal geochemical signatures (enriched in radiogenic elements). Internal heating by radiogenic elements in a previously thickened crust, can generate the heat required to melt the protolith. Concurrent exhumation in the Tay River district, between ~118 and 105 Ma, could have enhanced melting through decompression. The Anvil suite rocks are characterized by primary magmatic muscovite, 12-15 km emplacement depths, geochemistry consistent with derivation from a sedimentary protolith and high-grade metamorphic aureoles. Plutons are commonly associated with crustal-scale dextral transpressional (reverse) faults. Marginal igneous rocks in Anvil suite plutons commonly show a well-defined foliation. Isotopic ratios are consistent with derivation from an upper crustal sedimentary source (εNd_T=-16±4, $^{87}Sr/^{86}Sr_i$=0.7350±0.005 and $^{206}Pb/^{204}Pb$ = ~19.3; $^{207}Pb/^{204}Pb$ = ~15.70).

Tay River Suite and South Fork Volcanics

The 100-96 Ma amphibole-biotite bearing diorites, granodiorites and granites that characterize the Tay River suite and coeval South Fork volcanics, show a mineral assemblage, significant "subduction signature", I-type geochemical character, MREE depletion and $^{87}Sr/^{86}Sr_{100Ma}$ ratio consistent with melting of an amphibolite facies igneous source rock (Table 2.1; Clemens, 2003). These results fit with the evidence that I-type felsic rocks form from amphibolite facies melting of lower crustal rocks (Chappell and Stephens, 1988), although Miller (1986) noted that I-type granites can be derived from melting of a juvenile sediment composed of felsic igneous components.

There is no evidence for the input of mantle melts, so it is not likely that the Anvil suite source rock mixed with primitive mantle melts during the mid-Cretaceous to form the Tay River suite melts. Instead the Nd and Sr isotope data indicates an evolved crustal source, potentially, a mafic peraluminous meta-tonalite, which can contain up to ~30% biotite and muscovite making

them ideal for the production of granitoid magmas (Patiño Douce and Johnston, 1991). A tonalitic source fits with the CaO/Na_2O of the Tay River plutonic suite. Borg and Clynne (1998) showed that felsic calc-alkaline rocks, dominated by amphibole ± biotite phenocrysts and with a strong MREE depletion, were produced from relatively high $f(H_2O)$ ($P[H_2O]$~2 kbar), but still water under-saturated melting of amphibolitic lower crustal rocks at ~900°C. Amphibolite melting is proposed to occur via biotite dehydration at the amphibolite to granulite facies transition, where biotite, plagioclase and quartz breakdown to form orthopyroxene, garnet, K-feldspar and melt (Patiño Douce and Beard, 1994). Nair and Chacko (2002) report conditions of 875-1025°C required to stabilize orthopyroxene under middle to lower crustal depths (5-15 kbars) and water under-saturated conditions. Higher temperatures involved in the formation of the Tay River suite are supported by the high Al_2O_3/TiO_2 ratio of the whole rocks and the zircon titanium thermometry (710±45°C). However, temperatures of ~900°C are not achieved even at the base of extremely (>70 km) thickened crust (England and Thompson, 1986; Thompson and Connolly, 1995). Therefore, an external heat source is required to generate the melts that formed the Tay River suite. External heat can be derived either directly, via conduction from the mantle to the crust, or through the addition of mantle melts to the lower crust. The high temperatures required to melt amphibolite are unlikely to be found in the upper crust, so lower crustal amphibolite facies metatonalite melting, or melting of a juvenile metasediment sourced dominantly from a metatonalite, are the most probably sources for the Tay River suite magmas.

Potential sources for the Tay River suite and South Fork volcanics could be either a unit in the lower crust of cratonic North America or the proximal YTT (Morris and Creaser, 2008). For example, the amphibole facies quartz phyllites and mica-quartz schists of the Nisultin assemblage in the YTT, which have an average εNd_{100Ma} of -12±4 (range-3.8 to -19.3) and a τ_{Dm}

of 1.2 to 2.4 Ga (Grant, 1997). The Nisultin assemblage rocks are composed of the eroded components of an igneous rock generated from mixing of subduction derived basalt with North American continental rocks; such a source would explain the geochemical and isotopic compositions of the Tay River suite (Creaser et al., 1997; Mortensen, 1992). However, as significant horizontal flow of melt is not common in granitic systems (Petford et al., 1994, 2000; Clemens and Mawer, 1992), the source for the Tay River suite must underlie the Tay River district, which would require underplating of the YTT. Currently, no evidence for underthrusting of the Tay River district has been identified, although it cannot be ruled out, as subcretion within the Cordillera is supported by the work of Johnston and Canil (2007), Pavlis et al. (1993) and Staples et al. (2016). Until evidence for subcretion is identified, we suggest that amphibole-bearing rocks in the lower cratonic crust, underlying the Tay River district, are the more likely melt source for the Tay River suite.

The Tay River suite was emplaced at shallow crustal levels, as shown by the plutons close association with the South Fork volcanics, hornsfelsed aureole (<500 m, typically 200 m) and characteristic porphyritic nature. The Anvil suite and Tay River suite are on the same stratigraphic level. Therefore, the exhumation of the Anvil suite, from 12-15 km, must have been complete by the emplacement of the Tay River suite (Smith and Erdmer, 1990), implying exhumation at >1 $kmMa^{-1}$ between 110 Ma and 100 Ma. Exhumation rates and magnitudes identical to those seen in the Tay River district have been proposed in the proximal YTT (Staples et al., 2013; Dusel-Bacon et al., 2002; Pavlis et al., 1993) suggesting a large area of exhumation. In contrast to the Anvil suite, no foliation or mineral alignment is observed in the Tay River suite samples, which may indicate a lack of shear stress during Tay River suite emplacement. Dykes of the Tay River suite, intruded into the Anvil suite, are elongate parallel to north to northeast

trending Cretaceous normal faults in the Tay River district (Pigage, 2004; Cobbett, 2015), indicating a syn-genetic origin for the two features. However, the emplacement of the Tay River suite appears controlled by the same regional crustal-scale reverse faults that controlled the emplacement of the Anvil suite.

The large-scale calderas (up to 55 km maximum diameter; Gordey, 2013) filled by the explosive extrusive deposits of the South Fork volcanics, indicate shallow (<5 km) large volume ($>10^2$ km^3) magma chambers in regions of thick continental crust (Lipman, 1984). Caldera formation is also associated with regions with high geothermal gradients and extensional settings (Jellinek and DePaolo, 2003). The long crustal residence times of magma chambers required to generate large calderas suggest the eruption of South Fork volcanics occurred post exhumation.

To summarize, the 100-96 Ma Tay River suite rocks are characterized by amphibole phenocrysts, a commonly porphyritic texture, I-type geochemistry and associated volcanics. Tay River suite and coeval South Fork volcanics are derived from high temperature melting of a lower crustal, likely amphibolite facies, metatonalite. The heat required to melt the amphibolitic source rock was derived from the mantle. Decompression during regional exhumation could have aided melting, contributing to the large volume of Tay River suite observed. Pluton emplacement is associated with the same style of structures that control Anvil suite pluton emplacement, but Tay River suite plutonism occurred at shallower crustal levels in an extensional setting. The typical isotopic values for the Tay River suite plutons in the Tay River district cluster around εNd_T values equal to -10±5 and $^{87}Sr/^{86}Sr_i$ values equal to 0.715±0.01. However regionally, as isotopic ratios derive from the melt source they are highly varied; for example a Tay River-type melt derived from melting of the mafic Cache Creek terrane would

have a εNd_T value equal to 3±1.5 and a $^{87}Sr/^{86}Sr_i$ value equal to 0.7035 (Morris and Creaser, 2008).

Tombstone Suite

The plutonism that makes up the 96-90 Ma Tombstone suite appears to share characteristics with the Anvil and Tay River suites, however a paucity of samples limits this study. The large spread in geochemical characteristics (Figure 2.7I) and isotopic composition displayed by the Tombstone suite samples suggests a significant period of crustal residence time leading to assimilation, fractionation, and crustal contamination (AFC processes). Tombstone suite plutons, resembling Anvil suite style sedimentary protolith melting and Tay River suite style igneous protolith melting are both documented. Temperatures derived from zircons have a wider spread than the other plutonic suites, indicating that Tombstone suite pluton emplacement, or crystallization, occurred over a wider temperature range. Amphibole is rare to absent from the Tombstone suite. This may suggest a lower temperature melt source than the Tay River suite, or that amphibole settled as cumulates in lower crustal magma chambers. Rare earth element patterns and isotopic composition are identical to those of the Tay River suite, indicating the Tombstone suite may represent fractionation of magma similar to the Tay River suite ± crustal contamination ± sediment anatexis derived melt. Regionally compared to the Anvil and Tay River suites, the Tombstone suite plutons are characteristically low volume, round plugs. Less than 500 m wide hornfels facies aureoles, composed of biotite, andalusite and K-feldspar in pelites (Mair et al., 2006), suggest emplacement at shallow depths (<1 to 2 kbar, Spear and Cheney, 1989). Based on spatial associations, the emplacement of Tombstone suite plutons in the Tay River district appears to be controlled by normal faults, rather than the thrust faults that control the previous two plutonic styles (Cobbett, 2015).

Rare, late-stage, cross-cutting (shoshonite) lamprophyres are reported to occur in association with the Tombstone suite across the Selwyn Basin (Rasmussen, 2013), although lamprophyres were not seen in the Tay River district. These late stage dykes are proposed to indicate the involvement of primary mantle melts due to continued continental extension and rifting, during and post the emplacement of the Tombstone suite. However, Rasmussen (2013) reports highly evolved isotopic ratios for the lamprophyres - εNd_{100Ma}=-8±1, $^{87}Sr/^{86}Sr_{100Ma}$=0.712±0.02 and τ_{Dm}=1.8 to 2.1 Ga- indicating significant crustal contamination of the primary mantle melts or the presence of a highly irregular, radiogenic, mantle during their emplacement.

To summarize, the final stage of OMB plutonism in the Tay River district, represented by the 96-90 Ma Tombstone suite, constitues the waning stages of the external thermal pulse that formed the Tay River suite. Melts may have been generated by melting of an upper crustal sedimentary source, a lower crustal igneous source, or by continued fractionation of Tay River suite melts. The inferred long crustal residence times, round shape of the plutonic bodies and lack of foliation implies a lack of significant syn-intrusive stress. However, the regional association with late stage lamprophyre dykes and the close association of Tombstone suite plutons with upper crustal normal faults shows that continental crustal extension was occurring during the emplacement of the Tombstone suite. In summary, the Tombstone suite is characterized by: round low-volume plutonic bodies, absence of both muscovite and hornblende, and common spatial association with normal (extensional) faults in the upper crust. Isotope ratios are non-diagnostic. Mainly, Tombstone suite plutons are identified by U-Pb zircon and monazite ages of younger than 96 Ma.

Reclassifying Regional Plutonism

The aim of this section is to determine if plutons of the northern OMB can all be broadly classified as belonging to one of the three plutonic suites defined in this study, and if so to map out the spatial distribution of each suite. To achieve this, key characteristics of each suite are compared with descriptions of plutons in the literature (USGS, 2015; Yukon Geological Survey, 2014; Hart et al., 2004; Rasmussen, 2013; Dilworth et al., 2007; Heffernan, 2004; Gordey and Anderson, 1993; Gordey and Irwin, 1987; Joyce, 2002; Morris and Creaser, 2008; Bacon et al., 1990; Driver et al., 2000; Hudson, 1994; Selby et al., 1999; Aleinikoff et al., 2000; Solie et al., 2014; Mortensen et al., 2000; Hart, 1995). Using Nd and Sr isotopic ratios to reclassify regional plutonism is complicated if the plutons derive from crustal anatexis, as these plutons inherit an isotopic signature from their protolith. Due to this ambiguity, U-Pb ages, geochemical characteristics, and mineral assemblages of plutonic rocks are primarily used for reclassification (Figure 2.13) with isotopic ratios, structural associations, aureole mineral assemblages, and pluton emplacement depths as secondary controls.

Anvil-type two mica granites are associated with the center of the northern OMB in the Yukon-Tanana Uplands, Anvil, Cassiar and Hyland regions. Plutons of the Anvil-type igneous bodies have been identified in the Cassiar batholith (Driver et al., 2000), Hyland batholith (Rasmussen, 2013) and at the Square Lake pluton within the Yukon Tanana inlier to the northeast of the Tintina Fault (Hudson, 1994). The extent of S-type plutonism may be greater than seen in outcrop as the batholiths of this suite are emplaced at mid-crustal levels and these mid-crustal levels may not have been regionally exhumed.

Across the northern Cordillera, the > 150 U-Pb dates analyzed show the same quiescence in plutonism between Anvil-type and Tay River-type pluton emplacement (104-100 Ma) as

observed in the Tay River district (Figure 2.13 and Figure 2.6E). An exception is a minor number of emplacement ages in the Tanacross-Dawson Range region that occurs during this time.

Large volumes of 100-96 Ma Tay River-type plutons form the dominant components of the Tay River, Fairbanks-Salcha, Yukon Tanana Uplands and Tanacross-Dawson Range regions. Tay River-type plutons occur with Anvil-type intrusive rocks within the Anvil, Cassiar, Yukon-Tanana Uplands and Hyland regions. Close spatial association of Anvil and Tay River-type igneous rocks have previously been reported in the following: Anvil batholith (Pigage and Anderson, 1985), Cassiar batholith (Driver et al., 2000), Big Salmon & Nisultin batholiths (Morris and Creaser, 2008) and the Billings batholith (Rasmussen, 2013). Explosive volcanism is not only seen in the Tay River district, but occurs in ca. 93Ma (K-Ar age) felsic calderas (Sixty Mile Butte, Dennison, Middle Fork & West Fork) in the Yukon Tanana Uplands region of Alaska (Bacon et al., 1990).

Post 96 Ma, Tombstone-type plutonism monopolizes the Tok-Tetlin and TTB (Tungsten, Mayo and Tombstone) regions. The Livengood region is also assumed to contain multiple intrusions of the Tombstone style however; no U-Pb dates are currently available for this area of Alaska. The plutonism in the Tungsten region (part of the TTB) likely reflects highly fractionated magmas of the Tay River suite (Heffernan, 2004). Dates indicating the presence of Tombstone style plutons are recorded in the Tanacross- Dawson Range, Yukon-Tanana Uplands, Anvil, Tay River and Cassiar regions alongside Anvil and Tay River-type plutons. Tombstone-type plutons may be even more widespread in the OMB than identified in this study; as the small volume of the Tombstone suite intrusive bodies, in comparison to older plutons, may have

prevented their identification in less well-studied regions (i.e. Fairbanks-Salcha and Hyland regions).

The 124 to 106 Ma (Morris and Creaser, 2008) Whitehorse plutonic region is commonly considered as part of the OMB (Figure 2.3), however, in this study it is not correlated with any of the types of plutonism seen in the Tay River district. The Whitehorse region is geographically isolated from other mid-Cretaceous plutonism. To the east the Teslin fault separates the Whitehorse region from the Cassiar region and to the north a 150-200 km region with no cogenetic pluton exposures separates the Whitehorse and Tanacross-Dawson Range regions. The Whitehorse plutonic region has previously been interpreted as the easternmost representation of mid-Cretaceous arc magmatism (Hart et al., 2004). A mantle derivation for plutons in the Whitehorse region is indicated by: primitive isotopic ratios (εNd_{100Ma}=+2.3 to -1.2 and $^{87}Sr/^{86}Sr_{100Ma}$ averages 0.705), metaluminous chemistry, presence of contemporaneous gabbros and association with Cu mineralization in the Whitehorse Copper Belt (Hart, 1995; Morrison et al., 1979). The associated volcanism of the Mount Nansen group is also proposed to be arc related (Rasmussen, 2013). Therefore, the reclassification of regional OMB plutonism does not include the Whitehorse region. However, Morris & Creaser (2008) suggest that two plutons within the Whitehorse region (Surprise Lake batholith and Hayes Peak pluton) lack the "subduction signature" and show isotopic ratios (εNd_{100Ma}=+1.4 to +3.8 and $^{87}Sr/^{86}Sr$=0.7035) consistent with a derivation from melting of mafic crust possibly in the Slide Mountain or Cache Creek terrane with no arc mantle input. Therefore, plutons in the Whitehorse region may be Tay River-type and generated from lower crustal anatexis. However, for this study it is assumed plutons of the Whitehorse region are arc related and, therefore, not part of the northern OMB.

Restoring Eocene dextral displacement on the Tintina Fault (Figure 2.12) demonstrates that the temporal subdivisions of plutons do not form margin parallel bands as previously proposed (Figure 2.3). Instead the plutonic suites form a concentric pattern approximately surrounding the YTT and Intermontane terranes. The two regions of explosive volcanism correlate geochemical and spatially, but are separated by over 200 km across the YTT (Figure 2.12). Plutons also show symmetry around the YTT i.e. the ~100 to 96 Ma Dawson Ranges batholith (Joyce, 2002), which correlates geochemically and mineralogical with the Tay River suite in the Tay River district.

Plutons in the core of the OMB (i.e. in the Yukon-Tanana Uplands, Anvil, Cassiar and Hyland regions) consist of all three suites and have ages ranging over the whole mid-Cretaceous magmatic episode (115-90 Ma) (Figure 2.12 & 2.13) i.e. the Goodpaster Batholith in the Yukon-Tanana Uplands region which shows igneous rocks ranging from a 109-107 Ma biotite-muscovite bearing granite (Anvil-type) to 95.4-93.7 Ma diorite (Tombstone-type; Dilworth et al., 2007). Plutonic regions on the peripheries of the Yukon-Tanana inlier show the Tay River and Tombstone styles of igneous activity with U-Pb ages ranging from 100-90 Ma. The most distal plutonic regions on both sides of the YTT (TTB, Livengood & Tok-Tetlin regions) are dominated by Tombstone style plutonism and are characterized by ages mainly between 96 and 90 Ma. Therefore, rather than a systematic migration of plutonism inboard (as previously proposed), the OMB appears to reflect a sequential increase in the area affected by mid-Cretaceous igneous activity over time.

Tectonic Model

The regional distribution of plutonism outlined above is the basis for a new tectonic model for the OMB. The symmetry of plutonism around the YTT and Intermontane terranes suggests these terranes were a primary factor controlling the distribution of plutonism across the whole OMB.

Accretion of Intermontane terranes to North America, ended 30-70 Myr before OMB plutonism began (Johnston, 2008; Nelson et al., 2013; Colpron et al., 1996; Hildebrand, 2014). The accreted terranes formed up to 60 km thick crust in the core of the YTT and neighboring terranes during the Early to mid-Cretaceous (Pavlis et al., 1993; Staples et al., 2016). The amphibolitic rocks of the YTT represent deeply eroded continental crust (Pavlis et al., 1993; Miller and Hudson, 1991) and record a significant thermal event occurring between 116-112 Ma (Mair et al., 2006; Day et al., 2002; Mortensen, 1990), followed immediately by ~115- 105 Ma rapid exhumation (Dusel-Bacon et al., 2002; Staples et al., 2014; Berman et al., 2007) and the onset of felsic volcanism (Hudson, 1994).

Model For Anvil-Type Plutonism In The OMB

The three primary controls on the generation of Anvil-type granites are: 1.The presence of 50-60 km thick crust; 2.The presence of a fertile upper crustal protolith (likely a deeply buried arkosic rock); and 3. Related exhumation to promote upper crustal melting via decompression (Figure 2.14A).

Anvil-type granites occur down the core of the Columbia orogen in the Anvil, Cassiar, Hyland and Yukon-Tanana Uplands regions (Figure 2.14B) dominantly within Selwyn Basin strata. Emplacement of the Anvil suite occurred during a period of regional dextral shear with syn-plutonic deformation creating orogen parallel crustal pathways (dextral transpressional faults) for pluton emplacement (Nelson et al., 2013; Johnston, 1999) i.e. the Cassiar fault which

is coeval with the Cassiar Batholith. The regional distribution of Anvil-type plutons may be wider than is currently exposed, as mid-crustal levels have not been regionally exhumed.

The cessation of magmatism between 104 and 100 Ma is proposed to be due to a decrease in the rate of regional exhumation. A change in tectonism at this time is also demonstrated by the termination of movement on the Robert service thrust between 103-100 Ma (Mair et al., 2006).

Model For Tay River And Tombstone-Type Plutonism In The OMB

OMB magmatism between 100 and 90 Ma represents the development and death of a thermal pulse affecting the upper and lower crust across a region of 300 km by 500 km combined with the termination of regional exhumation and continued continental extension and rifting.

External sources of heat that can provide the temperatures necessary to melt amphibolite facies igneous rocks in the lower crust could derive from basaltic magma injection (Dufek and Bergantz, 2005) or asthenosphere upwelling (Houseman et al., 1981; Wang and Currie, 2015; Collins, 1994). Basalt injection is unlikely to explain the Tay River magmatism as indicated by the lack of contemporaneous mafic rocks and the evolved isotopic signatures of ~100 Ma to 96 Ma melts.

Regional uplift and exhumation followed by lower crustal melting in the northern Cordillera can be explained by delamination. The convective removal and subsequent foundering of previously thickened lithosphere allows asthenosphere to upwell into contact with the lower crust (Göğüş and Pysklywec, 2008a; Farmer et al., 2002), yielding a temperature increase at the Moho and regional uplift due to isostatic rebound (Göğüş and Pysklywec, 2008b; Bao et al., 2014; Garzione et al., 2006). Tectonic and erosional denudation of the uplifting region produces exhumation (Ring et al., 1999). Isostatic rebound derived uplift occurs synchronously with the delamination event (Figure 2.14A), while the thermal anomaly can take up to 20 Myr to cause a

significant (>100°C) temperature increase above the Moho (Figure 2.14C; Wang and Currie, 2015).

The radial nature and scale of the plutonism fits with the convective removal of over-thickened lithosphere, via delamination, beneath the YTT (Figure 2.14D; Wang and Currie, 2015; Wang, 2015). This suggests that the lithosphere beneath the YTT was unique compared to the lithosphere underneath the rest of the Cordillera. Preferential delamination of the YTT lithosphere could have been controlled by edge driven convection, where the YTT lithosphere met the cratonic lithosphere (Hardebol et al., 2012) or due to eclogitization of the lithosphere beneath the YTT (Krystopowicz and Currie, 2013). Both of these models differ from the generally accepted thin-skinned view of the northern Cordillera (Figure 2.2; Cook et al., 2004) by implying that until the mid-Cretaceous the YTT overlay, and was connected to, its own unique patch of lithosphere.

Delamination causes a local tensile stress field which, when not opposed by tectonic stress induced at the proximal plate boundary, gives rise to crustal extension and exhumation (Ranalli et al., 1986; Bardoux and Mareschal, 1994). The mid-Cretaceous period was defined by a change in tectonic regime from a compressional stress regime to orogen parallel extension triggered by a change in relative North American plate trajectory at ~110 Ma (Elston et al., 2002; Kent and Irving, 2010; Staples et al., 2016). Orogen parallel extension, combined with the local stress regime derived from delamination, would have allowed exhumation and extension to proceed at the rapid rates recorded in the Tay River district. Exhumation appears to have lasted ~15 Myr (between 115-100 Ma) corresponding to timescales seen in other areas where delamination is proposed (Bardoux and Mareschal, 1994; Ducea, 2011). Regional extension

continued beyond the end of isostatic uplift at 105 Ma, terminating in the Late Cretaceous (Gabrielse et al., 2006).

Tombstone-type plutons represent the terminal stages of exhumation and the thermal pulse derived from delamination. The volume of magma decreases significantly at around ~96 Ma (Figure 2.14E). The Tombstone-type plutonism occurs in the same regions as the previous two stages, as well as in locations distal to the center of delamination and the exhuming YTT (Figure 2.14F). These plutons have previously only been largely identified in the distal parts of the system due to their small volumes compared to the 100-96 Ma plutons. However, multiple dates of ~94±2 Ma have been measured across Yukon.

Across the OMB voluminous mid-Cretaceous plutons are linked to regions where exhumation and decompression melting have occurred. The inboard limit of plutonism corresponds with thrust faults (i.e. Robert Service and Tombstone thrusts to the northeast of the OMB) where exhumation and extension did not occur (Mair et al., 2006). To the south of the OMB the limit of magmatism corresponds to the southern limit of the delaminating lithosphere.

In the OMB, igneous activity ceased at ~90 Ma due to the end of the enhanced geothermal gradient derived from delamination, termination of regional uplift and exhumation and perhaps slowing of regional extension as tectonic forces change towards a purer strike-slip regime.

Outside The Bounds Of This Study

In previous work, the mid-Cretaceous plutonism assigned to the OMB has been mapped across a larger area than identified in this study. However, we propose that plutons outside of the area in this study do not possess the same genetic history as the plutons displayed in Figure 2.3 & 2.12. To the south of the Yukon border, and south of the proposed limit of the thermal

perturbation, the density of mid-Cretaceous plutons decreases significantly (see Hildebrand 2009, Figure 2.13). Throughout northern British Columbia (B.C), mid-Cretaceous plutonism defines a thin band parallel to the major dextral faults in the northern Cordillera (Johnston, 1999). Therefore, we suggest only Anvil-type plutons exist in northern B.C, as the region was not affected by a thermal perturbation. High densities of mid-Cretaceous magmatism exist straddling the U.S. -Canada border, however, the separation between the southern B.C plutonism and this study mean they are unlikely to be derived from the same thermal event.

To the north of the study area, OMB plutonism has previously been mapped in a band stretching across northern Alaska from the hinterland of the Brooks Range, towards the Seaward Peninsula, and out to St. Lawrence Island (Hart et al., 2004). While this plutonism is cogenetic with the igneous activity in this study we suggest it may be related to a different set of tectonic events to those outlined for the central Yukon. The tectonic events forming the northern Alaska belt involve Late Devonian to Mississippian closure of the Angayucham Ocean by south dipping subduction, followed by Late Jurassic compression, then north vergent deformation and extension of the Brooks Range between 145 and 112 Ma (Moore et al., 1994; Nelson et al., 2013; Fuis et al., 2008), potentially due to opening of the Amerasian basin (Grantz and May, 1983; Strauss et al., 2013). Therefore, while the genesis of plutons in this region could also be derived from delamination of overthickened lithosphere created due to terrane accretion, it is unlikely that the same event generated the plutonism seen in this study. Different genetic origins for the two clusters of plutonism is supported by an over 100 km gap in plutonism between the two regions of mid-Cretaceous igneous flair up seen when Eocene fault displacement is corrected (see Hart et al. 2004, Figure 2.8).

Implication For Future Regional Metallogenic Exploration

The OMB hosts a number of significant mineral deposits, which show a large variation in metallogeny (Figure 2.15). However, the dominant deposit styles are W skarns, Au deposits (both intrusion-related and orogenic-lode systems), distal Ag-Pb-Zn veins and rarer Sn occurrences (Gordey and Anderson, 1993; Nelson et al., 2013). The new model proposed has three key implications for exploration.

1. For deposit types linked to a certain intrusion age or style, our new distribution of the plutonic styles changes the areas over which exploration for these deposits should occur. For example intrusion related gold systems (IRGS) in the Tintina Gold Belt are strongly associated with 92 ± 2 Ma plutons of the Tombstone style (Goldfarb et al., 2000; Hart et al., 2004; Lang and Baker, 2001). The model presented in this paper suggests that Tombstone style plutonism occurs, not only in the TTB but also across the whole OMB (Figure 2.15). The genetic link between Tombstone style plutonism and IRGS means that wherever 92±2 Ma plutons occur there is the potential for gold deposits.
2. For deposit types associated with a unique tectonic regime, our model has the potential to change the exploration methodology. For example, W and Sn deposits are associated with plutons showing high degrees of fractionation and crystallization (Lehmann, 1994; Newberry and Swanson, 1986), so are more likely to be associated with post exhumation plutons like those found in the Tungsten region (Heffernan, 2004; Figure 2.15).
3. Our proposal of mantle heating from below and coeval regional uplift and exhumation implies a high geothermal gradient during OMB magmatism. A high geothermal gradient will promote the development of magmatic-hydrothermal systems and could explain pluton distal deposits and deposits with no genetic link to coeval plutonism (Beaudoin

and Sangster, 1992; Robb, 2005). For example, the Keno Hill Ag-Pb-Zn veins are proposed to form from a prolonged hydrothermal cell, but a direct genetic link to a causative pluton has not been found (Lynch, 1989; Hantelmann, 2013). In our model, the high regional geothermal gradient would promote the development of large, prolonged, hydrothermal cells. Orogenic-lode gold deposits, that lack a direct connection to intrusive rocks, could be similarly explained (Sillitoe and Thompson, 1998). Deposits linked to the flow of metamorphic fluids (i.e. distal base metal veins and orogenic gold deposits) would be expected to occur in areas with the highest geothermal gradients (Figure 2.15).

CONCLUSIONS

1. In the Tay River district there are three plutonic suites defined by time of emplacement: the (110-104 Ma) Anvil, (100-96 Ma) Tay River and (96-90 Ma) Tombstone. All three plutonic suites are derived from crustal anatexis. The Anvil suite represents upper crustal melting of a fertile sedimentary protolith due to internal heating by radiogenic elements in a significantly thickened crust. Concurrent exhumation occurring in the region between ~118 and 105 Ma caused decompression melting. The Tay River suite and coeval South Fork volcanics result from mantle derived heat, which caused high temperature melting of a lower crustal metatonalite. The Tombstone suite represents the waning stages of the thermal pulse. Plutonism in the Tay River district occurs from 110 Ma to 90 Ma with younger suites intruding the older suites. Therefore, the previously hypothesized inboard migration and younging of plutonic suites for the Selwyn Basin does not apply in this region of the northern Cordillera.

2. Mid-Cretaceous plutonism in the northern OMB can be reclassified into the three suite temporal framework identified in the Tay River district. When Eocene dextral fault displacements are restored the OMB plutons show a concentric pattern around the YTT. All

three plutonic styles occur in the core of the OMB. Areas on the peripheries of the YTT comprise the Tay River and Tombstone-type plutons. Areas distal to the YTT contain only the younger Tombstone-type plutons. The regional concentric U-Shaped pattern around the YTT shows a sequential increase in the area affected by mid-Cretaceous igneous activity over time and that the YTT was a primary control on OMB formation.

3. Delamination of over-thickened lithosphere explains the rate and timing of regional uplift and the distribution of plutons across the OMB. The delamination event occurred at ~115 Ma. The foundering lithosphere allowed asthenosphere to upwell into contact with the lower crust. The less dense asthenosphere caused instantaneous isostatic rebound and uplift of the OMB. Tectonic and erosional denudation occurred synchronously with the uplift leading to exhumation. Anvil-type plutonism occurred at this time. The upwelling asthenosphere also transferred heat across the Moho, causing lower crustal melting around 10-15 Myr after the delamination event generating the Tay River-type melts. As the thermal pulse wanes volumes of melt decrease. OMB plutonism terminates at ~90 Ma due to re-equilibration of the mantle derived thermal pulse.

4. Our pattern of OMB plutonism is consistent with delamination of lithosphere beneath the YTT. Region specific delamination implies region specific lithosphere, indicating that the YTT was above unique lithosphere in the mid-Cretaceous. This finding implies that the transition to thin skinned tectonics in the northern Cordillera did not occur until post the mid-Cretaceous delamination event. Preferential removal of YTT lithosphere could occur due to eclogitization or edge driven convection. The pattern of OMB plutonism also indicates that all terranes covered by the plutonism were accreted to each other prior to the mid-Cretaceous since the suites of plutons span terrane boundaries.

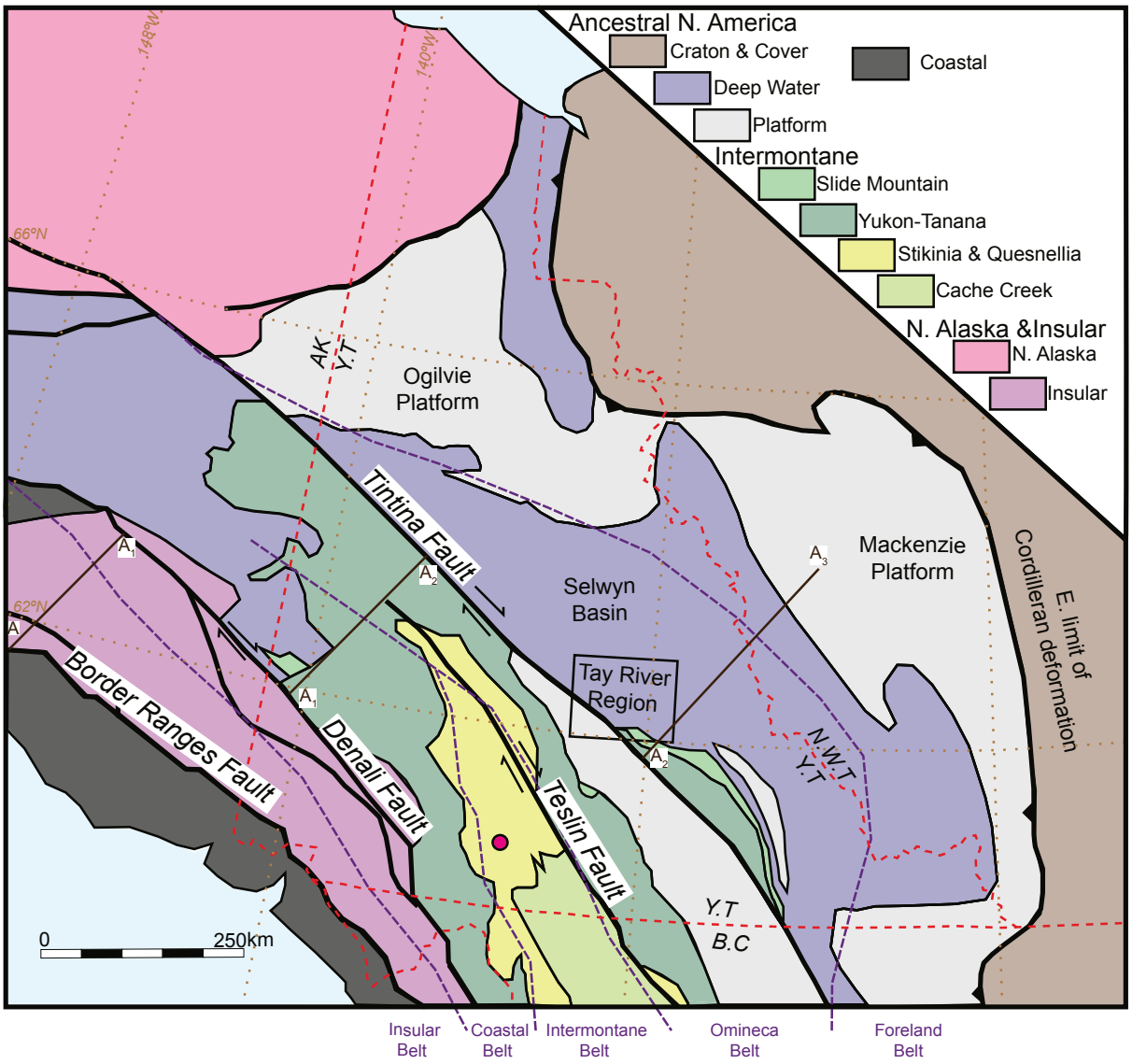

Figure 2.1: Modern terranes, major structures (black) and morphological belts (purple) of the northern Cordillera adapted from Nelson et al. (2013). Terranes are grouped in the legend according to paleogeographic affinities. Cross section line for Figure 2.2 shown by dark-brown line A-A_1-A_2-A_3. Red dot indicates location of Whitehorse City.

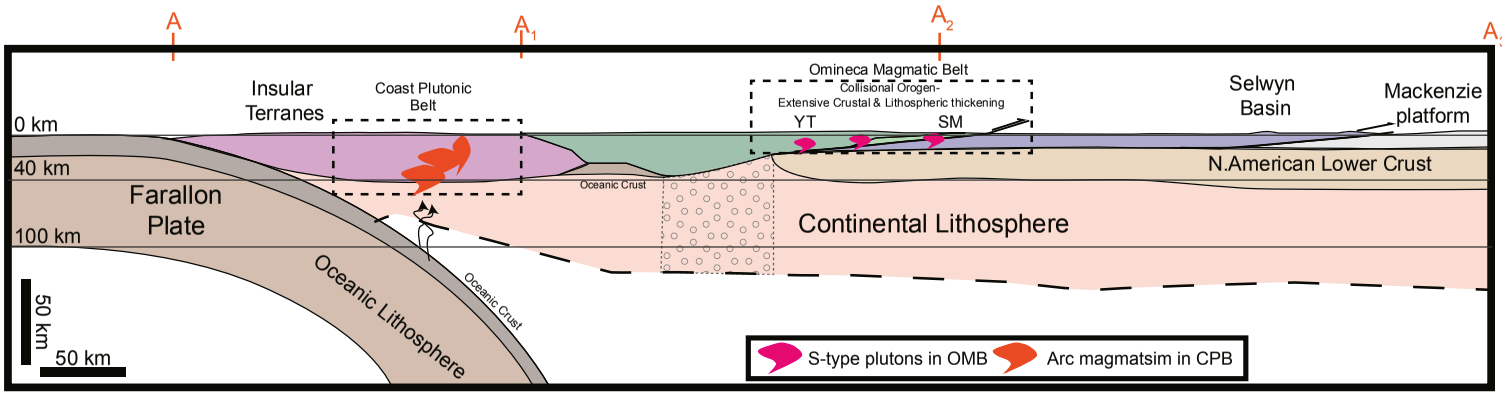

Figure 2.2: Schematic cross section across the mid-Cretaceous northern Cordillera showing the positions of the two magmatic belts. No vertical exaggeration. Adapted from Mair et al. (2006) and Evenchick et al. (2007). Points A, A1 and A2 correlate to Figure 2.1.Terrane colours are the same as in Figure 2.1.Dotted area represents proposed region of delamination see Figure 2.14.

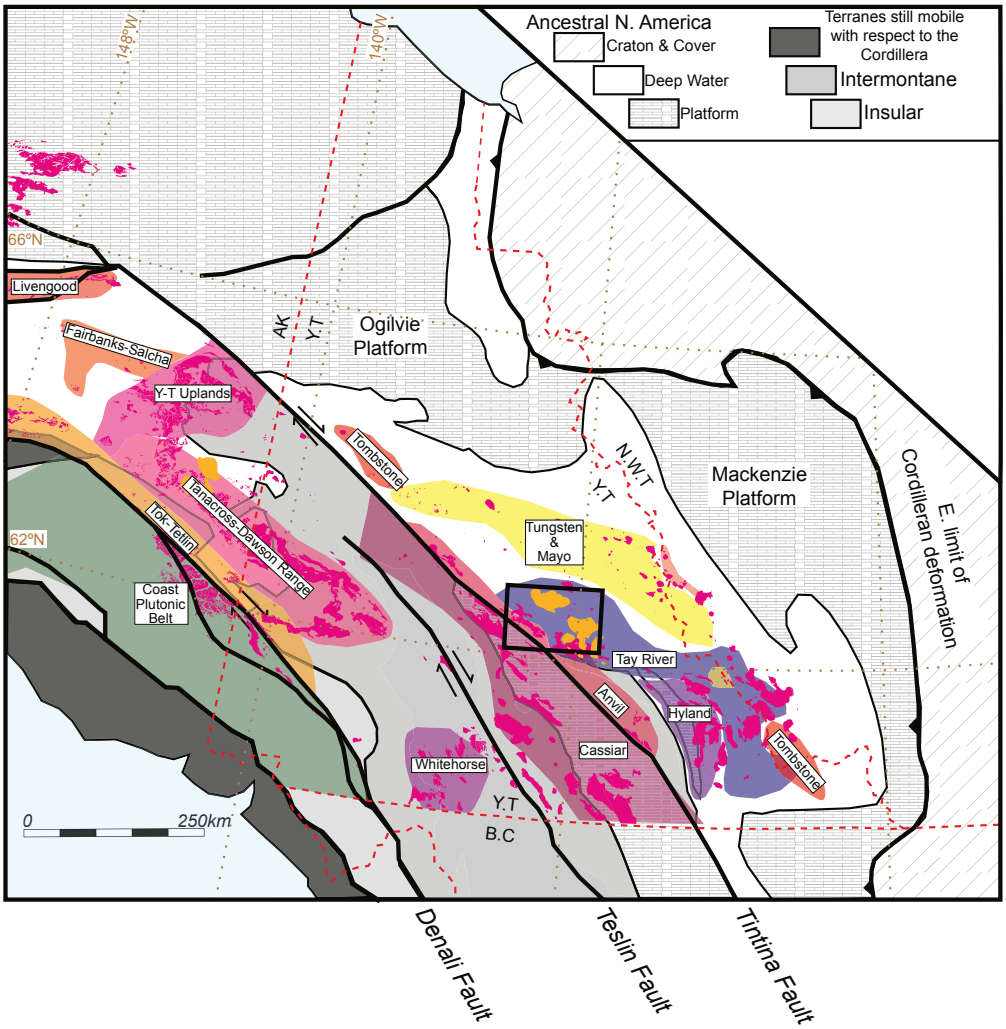

Figure 2.3: Location of the plutonic regions of the OMB identified from Mortensen et al. (2000), Hart et al. (2004) and Rasmussen (2013). Generalized tectonic elements and major structures simplified from Figure 1. Tay River district identified by the black rectangle within the Selwyn Basin.

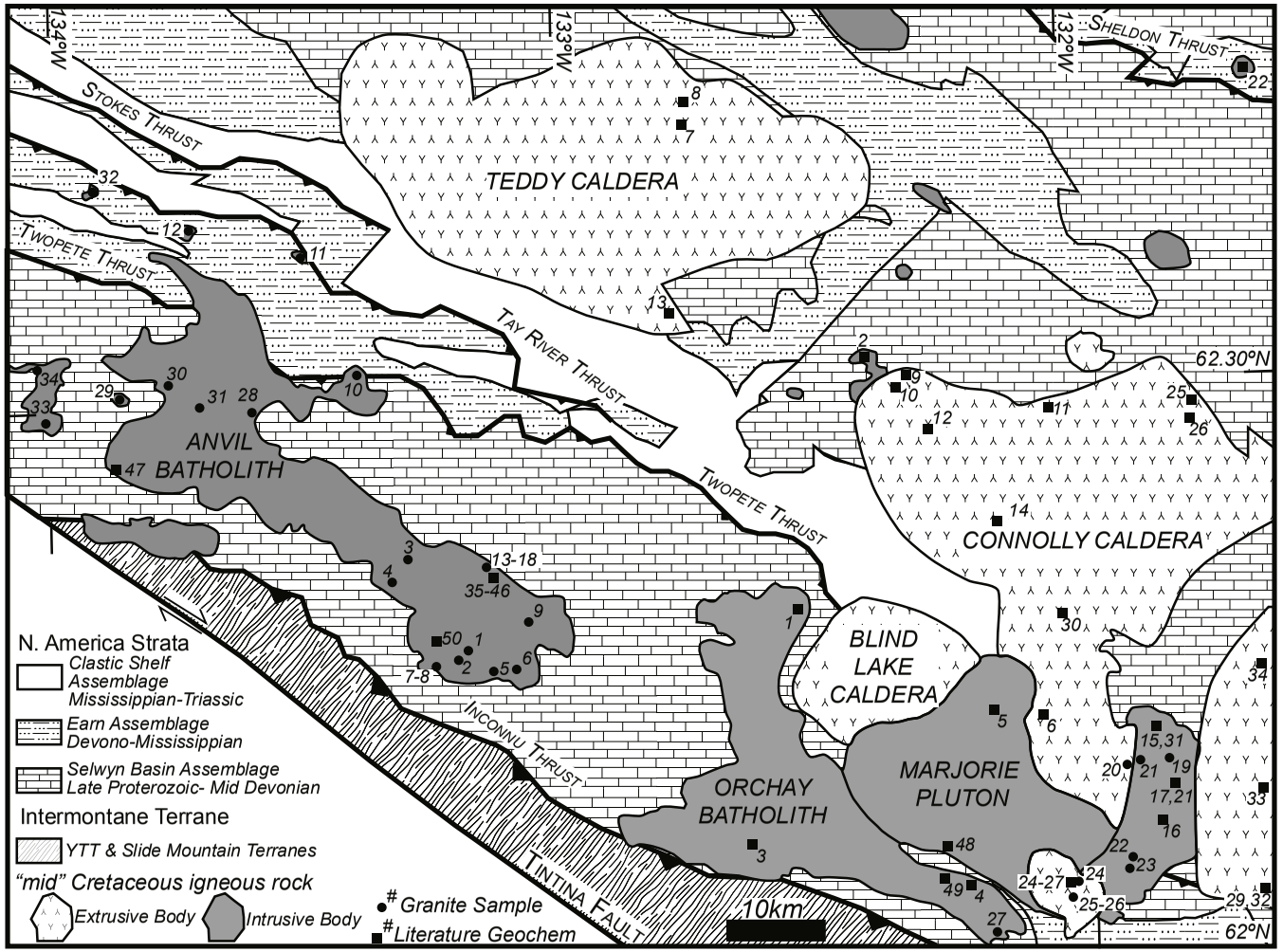

Figure 2.4: Simplified bedrock geological map of the Tay River district adapted from Cobbett (2015), Gordey (2013) and Yukon Geological Survey (2017). Positions of granite samples from this study and literature data are shown. Major thrust faults created during Mesozoic orogeny and major mid- Cretaceous igneous bodies are labeled.

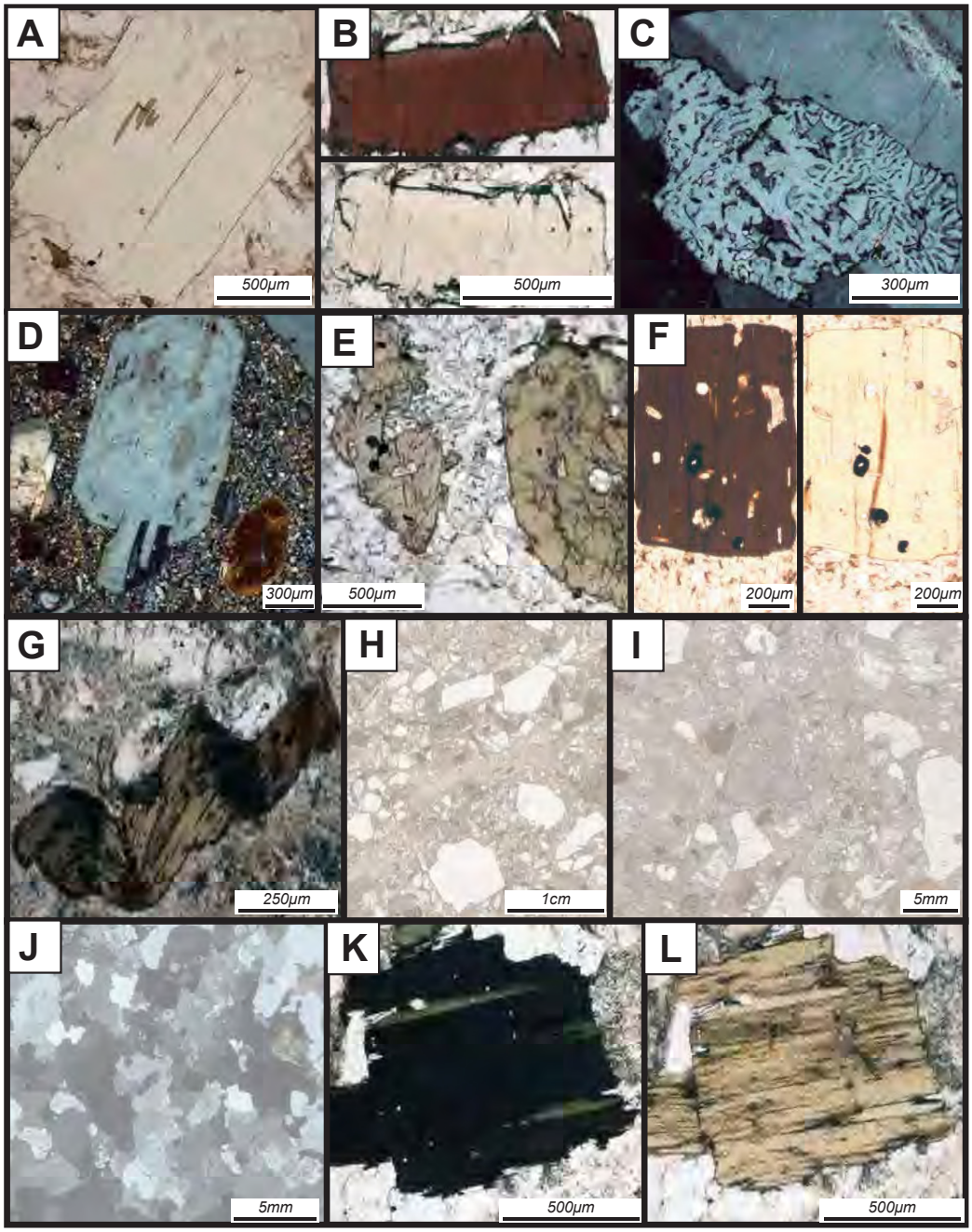
A
500µm
B
500µm
C
300µm
D
300µm
E
500µm
F
200µm
200µm
G
250µm
H
1cm
I
5mm
J
5mm
K
500µm
L
500µm

Figure 2.5 (Previous Page): Key petrographic features of plutonic and volcanic suites as seen in thin sections.
Anvil plutonic suite (A-C). A- Primary magmatic muscovite in plane-polarized light (PPL). B-Biotite pleochroism (PPL). C. Myrmekite in cross-polarized light (XPL).
Tay River Suite (D-F). D. Typical porphyritic samples (PPL). E. Typical seriate sample (PPL). F. Biotite pleochroism (PPL).
South Fork Volcanics (G-I). G. Deformed crystals (PPL). H. Fiamme (PPL). I. Lithic Fragment (PPL).
Tombstone Suite (J-L). J. Typical Tombstone suite sample (XPL). K. Biotite pleochroism (PPL). L. Biotite pleochroism (PPL).

Figure 2.6 U-Pb Dating (Next 2 pages): A to D: Tera-Waserburg diagrams for samples dated in this study separated by suite.
E: Compilation of all U-Pb ages of Mid-Cretaceous plutons from the literature (outlined boxes) and this study (shaded boxes). Divided based on plutonic suites identified in this study. V indicates extrusive samples. (Gordey, 2013; Pigage,2004; Cobbett, 2015).

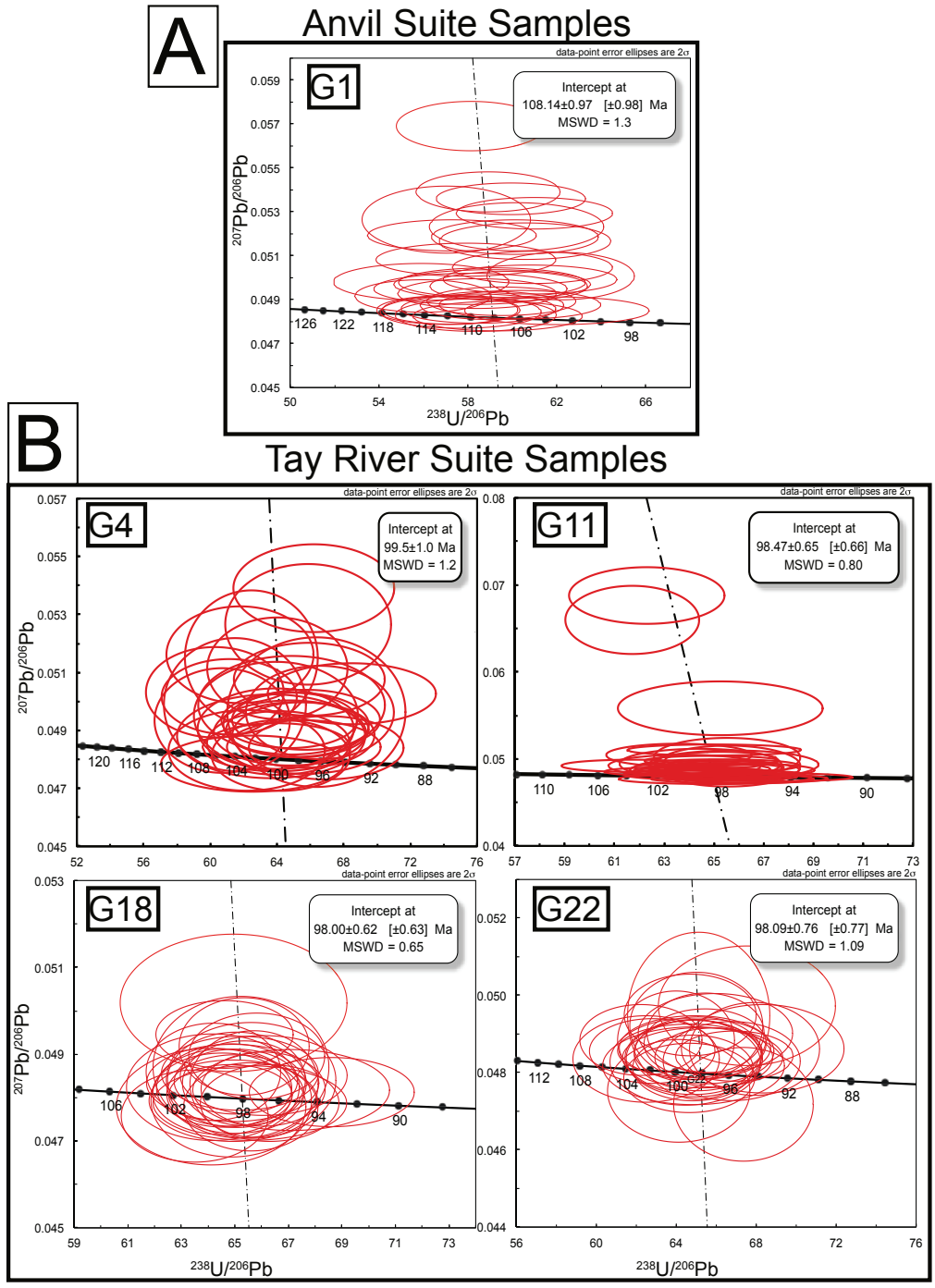
A
Anvil Suite Samples
data-point error ellipses are 2σ
G1
Intercept at
108.14±0.97 [±0.98] Ma
MSWD = 1.3
$^{207}Pb/^{206}Pb$
$^{238}U/^{206}Pb$
B
Tay River Suite Samples
G4
Intercept at
99.5±1.0 Ma
MSWD = 1.2
G11
Intercept at
98.47±0.65 [±0.66] Ma
MSWD = 0.80
G18
Intercept at
98.00±0.62 [±0.63] Ma
MSWD = 0.65
G22
Intercept at
98.09±0.76 [±0.77] Ma
MSWD = 1.09

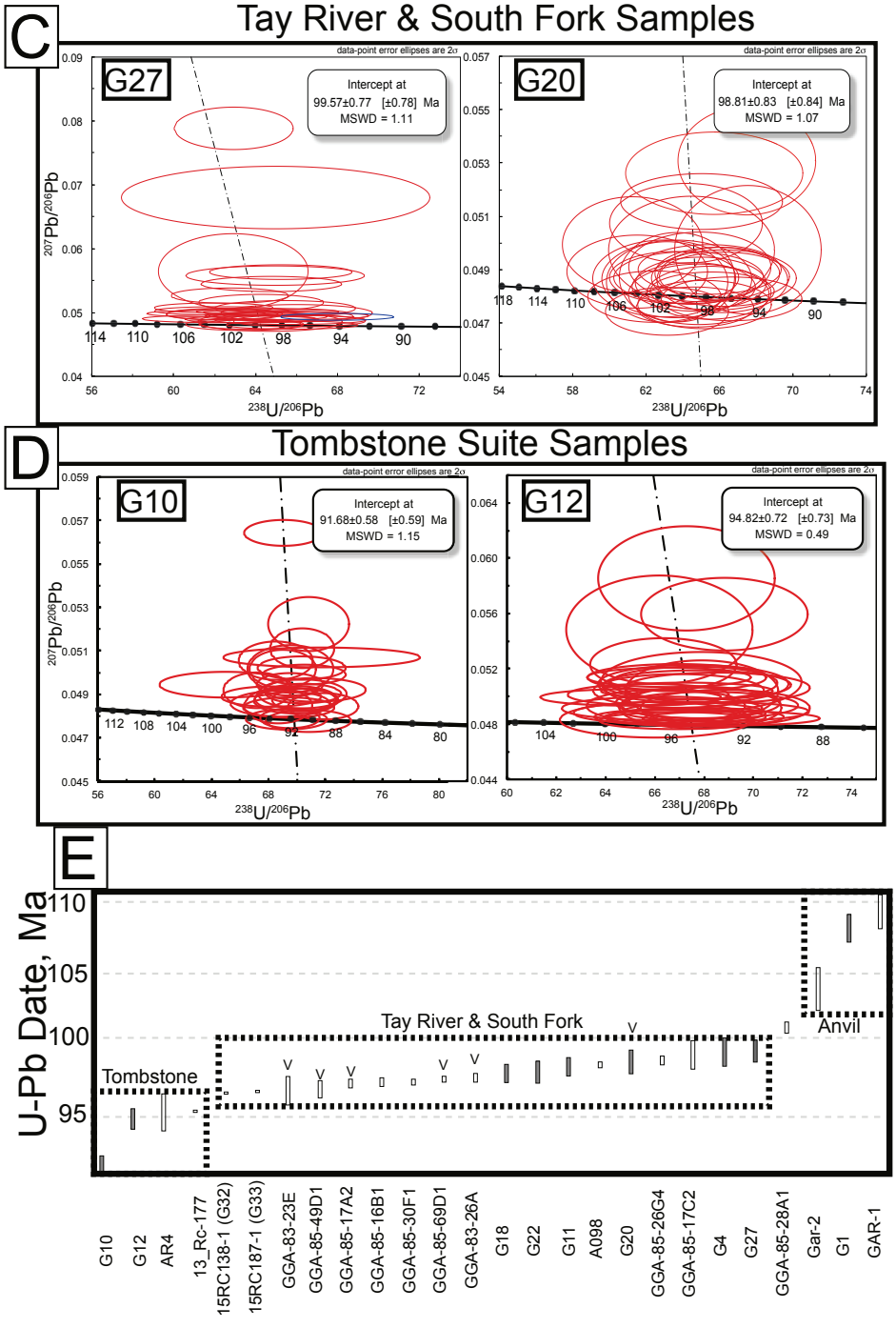
C
Tay River & South Fork Samples
G27
Intercept at
99.57±0.77 [±0.78] Ma
MSWD = 1.11
G20
Intercept at
98.81±0.83 [±0.84] Ma
MSWD = 1.07
data-point error ellipses are 2σ
$^{207}Pb/^{206}Pb$
$^{238}U/^{206}Pb$
D
Tombstone Suite Samples
G10
Intercept at
91.68±0.58 [±0.59] Ma
MSWD = 1.15
G12
Intercept at
94.82±0.72 [±0.73] Ma
MSWD = 0.49
E
U-Pb Date, Ma
Tombstone
Tay River & South Fork
Anvil
G10
G12
AR4
13_Rc-177
15RC138-1 (G32)
15RC187-1 (G33)
GGA-83-23E
GGA-85-49D1
GGA-85-17A2
GGA-85-16B1
GGA-85-30F1
GGA-85-69D1
GGA-83-26A
G18
G22
G11
A098
G20
GGA-85-26G4
GGA-85-17C2
G4
G27
GGA-85-28A1
Gar-2
G1
GAR-1

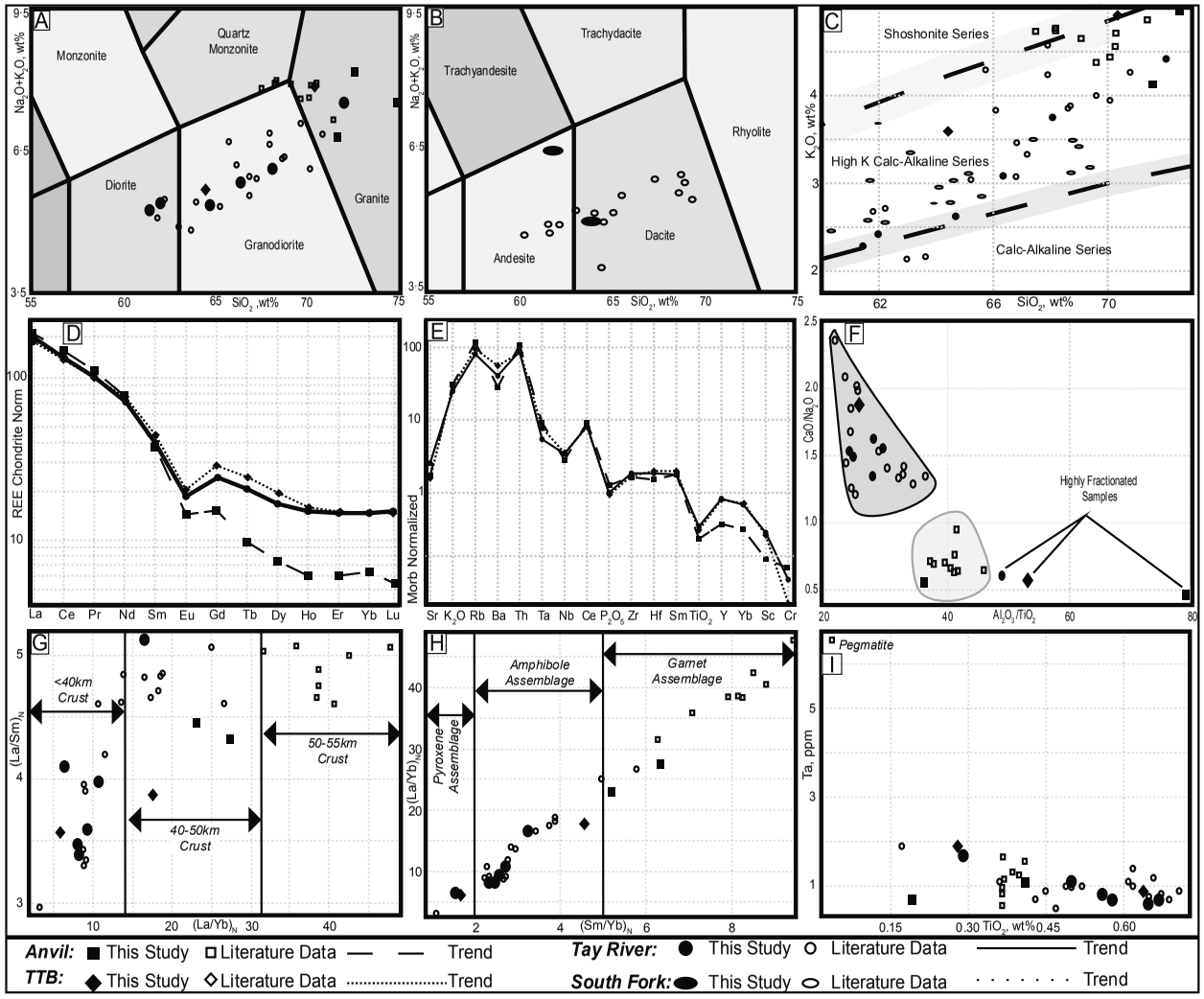
A
Monzonite
Quartz Monzonite
Diorite
Granite
Granodiorite
Na2O+K2O, wt%
SiO2, wt%
B
Trachydacite
Trachyandesite
Rhyolite
Andesite
Dacite
C
Shoshonite Series
High K Calc-Alkaline Series
Calc-Alkaline Series
K2O, wt%
SiO2, wt%
D
REE Chondrite Norm
La Ce Pr Nd Sm Eu Gd Tb Dy Ho Er Yb Lu
E
Morb Normalized
Sr K2O Rb Ba Th Ta Nb Ce P2O5 Zr Hf Sm TiO2 Y Yb Sc Cr
F
CaO/Na2O
Highly Fractionated Samples
Al2O3/TiO2
G
<40km Crust
40-50km Crust
50-55km Crust
(La/Sm)N
(La/Yb)N
H
Pyroxene Assemblage
Amphibole Assemblage
Garnet Assemblage
(La/Yb)N
(Sm/Yb)N
I
Pegmatite
Ta, ppm
TiO2, wt%
Anvil: This Study Literature Data Trend
TTB: This Study Literature Data Trend
Tay River: This Study Literature Data Trend
South Fork: This Study Literature Data Trend

Figure 2.7 (Previous Page): Various geochemical discrimination diagrams for the bulk whole rock geochemistry of igneous rocks in the Tay River district. A: Plutonic samples plotted on the TAS plutonic diagram from Middlemost (1994). B: Volcanic samples plotted on the TAS volcanic diagram from Le Maitre (1989). C: K_2O (wt%) versus SiO_2 (wt%) binary plot of all samples. Field boundaries from Le Maitre (1989). D: Average Chondrite normalized REE plots for the plutonic suites. E: Average MORB normalized minor elements plots for the plutonic suites. F: CaO/Na_2O versus Al_2O_3/TiO_2 binary plot for plutonic samples adapted from Sylvester (1998). G: Chondrite normalized $(La/Sm)_N$ versus $(La/Yb)_N$ binary plot for plutonic samples. Proposed crustal thickness associated with $(La/Yb)_N$ variation shown from Kay et al. (1991) and Haschke and Günther (2003). H: Chondrite normalized $(La/Yb)_N$ versus $(Sm/Yb)_N$ binary plot for plutonic samples. Showing proposed mineral assemblages in equilibrium with melts associated with $(Sm/Yb)_N$ variation from Kay and Mpodozis (2001). I: Ta (ppm) versus TiO_2 (wt%) binary plot for plutonic samples.

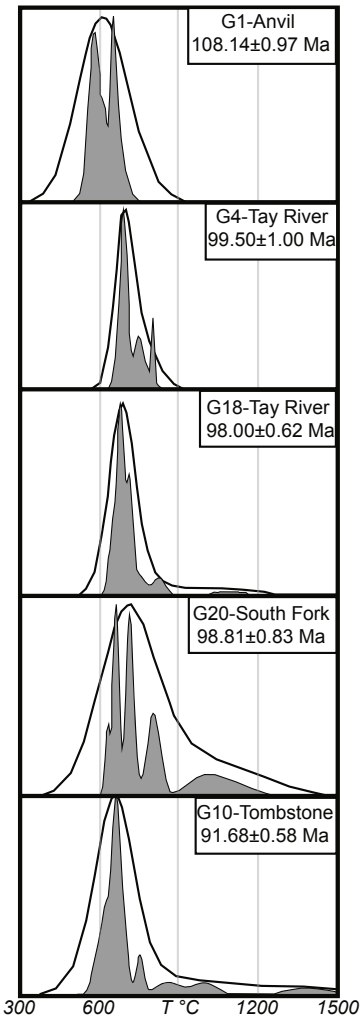

Figure 2.8: Probability density plots (shaded) and kernel density envelopes (outline) for temperatures calculated by titanium thermometry on zircon grain separates from five samples.

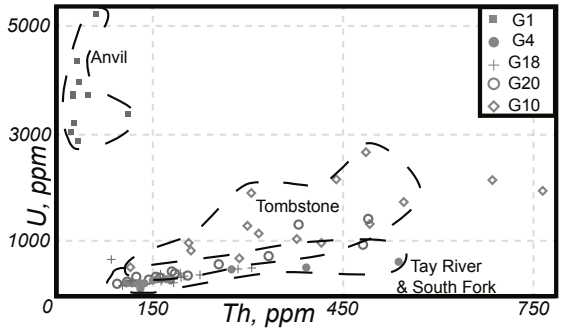

Figure 2.9: Binary plot of U (ppm) versus Th (ppm) of zircons from five samples. Dotted lines show the range of individual suites identified in this study.

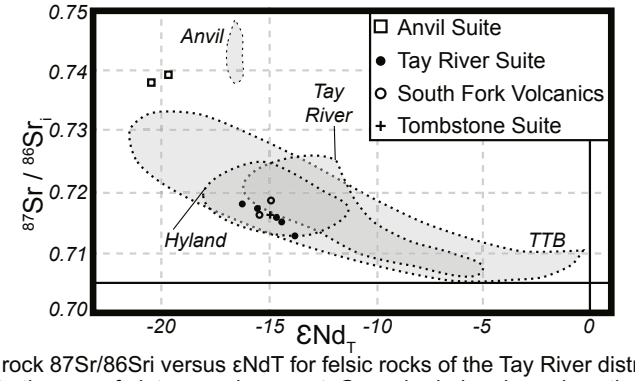

Figure 2.10: Whole rock 87Sr/86Sri versus εNdT for felsic rocks of the Tay River district separated by suite and corrected to the age of pluton emplacement. Grey shaded regions show the range of compiled isotope data for Cretaceous Selwyn Basin plutons - corrected to 100 Ma - subdivided based on plutonic region. Regional isotopic data from Rasmussen (2013) and references therein. Black lines represent the Bulk Earth composition (CHUR) relative to Nd and Sr.

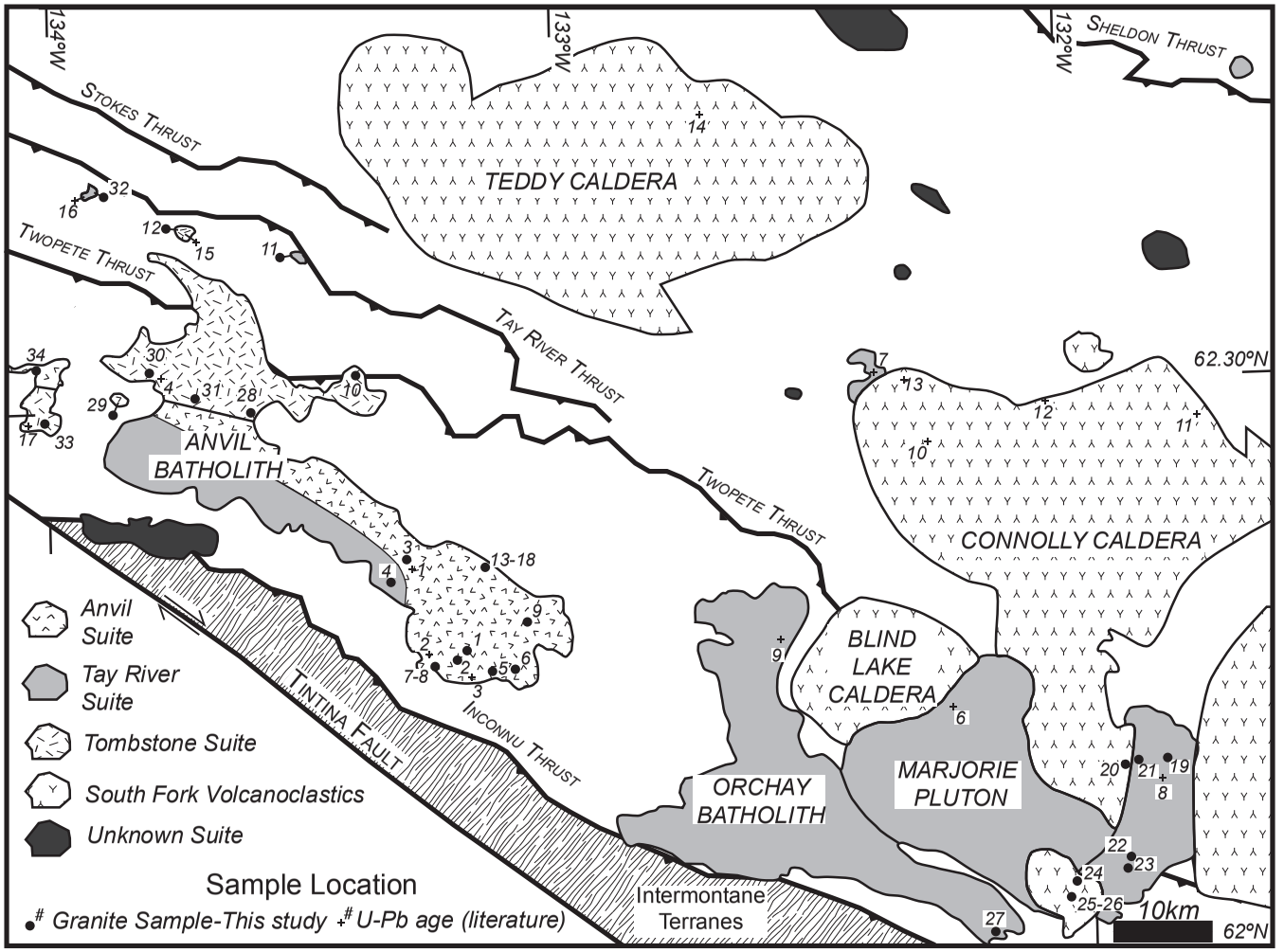

Figure 2.11: Distribution of the three plutonic suites identified in this study within the Tay River district. Simplified major structures and outlines of large Mid-Cretaceous bodies from Gordey (2013) and Yukon Geological Survey (2017). Positions of U-Pb age locations from this study and literature data are shown (Pigage, 2004; Gordey, 2013; Cobbett, 2015).

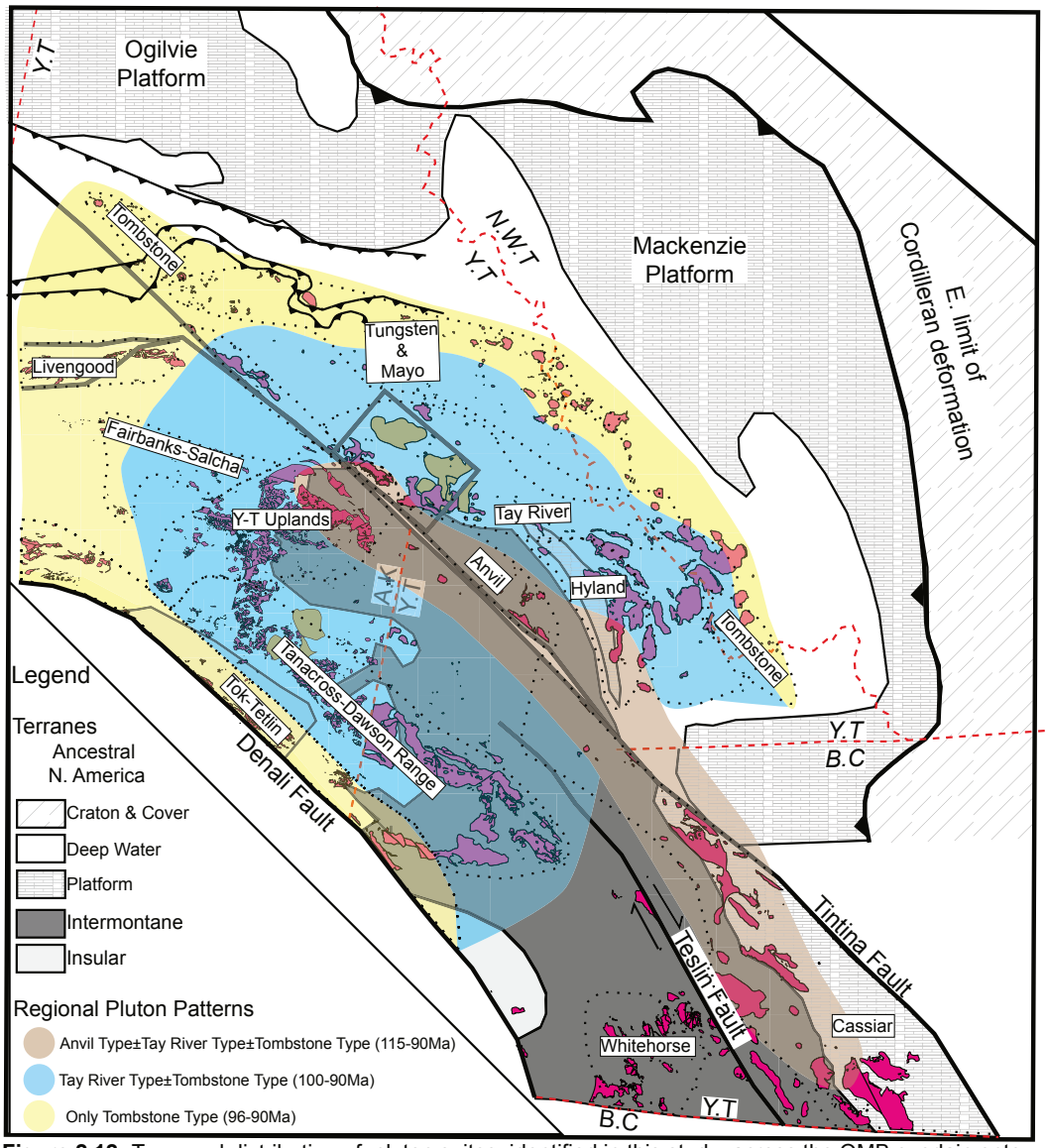

Figure 2.12: Temporal distribution of pluton suites, identified in this study, across the OMB overlain onto a schematic representation of major tectonic elements with restoration of 430km of dextral movement on the Tintina fault (modified from the reconstructions of Heffernan, 2004 and Gabrielse et al. 2006). Plutonic regions shown from Figure 2.3 and tectonic terranes divided by paleogeographic affinity from Figure 2.1. Position of Robert Service, Tombstone and Dawson thrusts from Mair et al. (2006). Mid-Cretaceous intrusive (pink) and extrusive bodies (orange) taken from Yukon and Alaskan Geological Surveys.

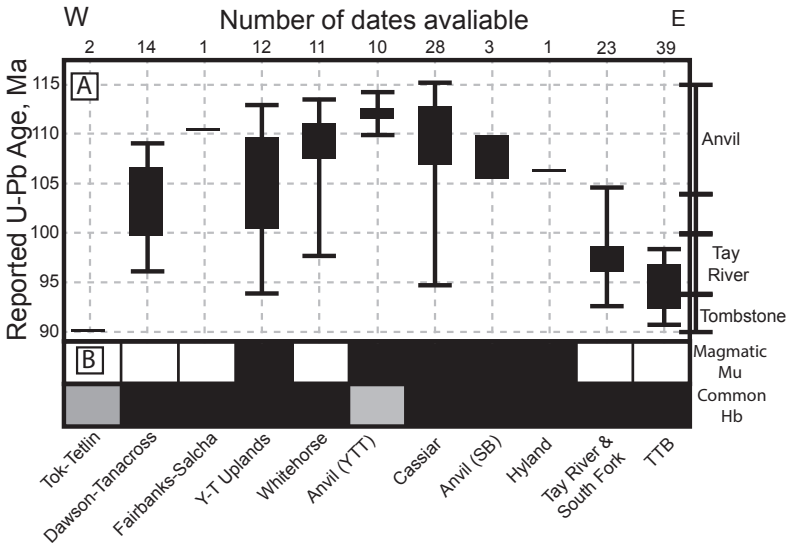

Figure 2.13: Compilation of U-Pb dates and mineralogical description of igneous rocks present in each plutonic region (see references in text). A: Dates divided based on temporal suites identified in Tay River district and a distinct amagmatic period between 104-100Ma. B: Identification of regions where magmatic muscovite and/ or common hornblende are definitely present (black), potentially present (grey) and not reported (white).

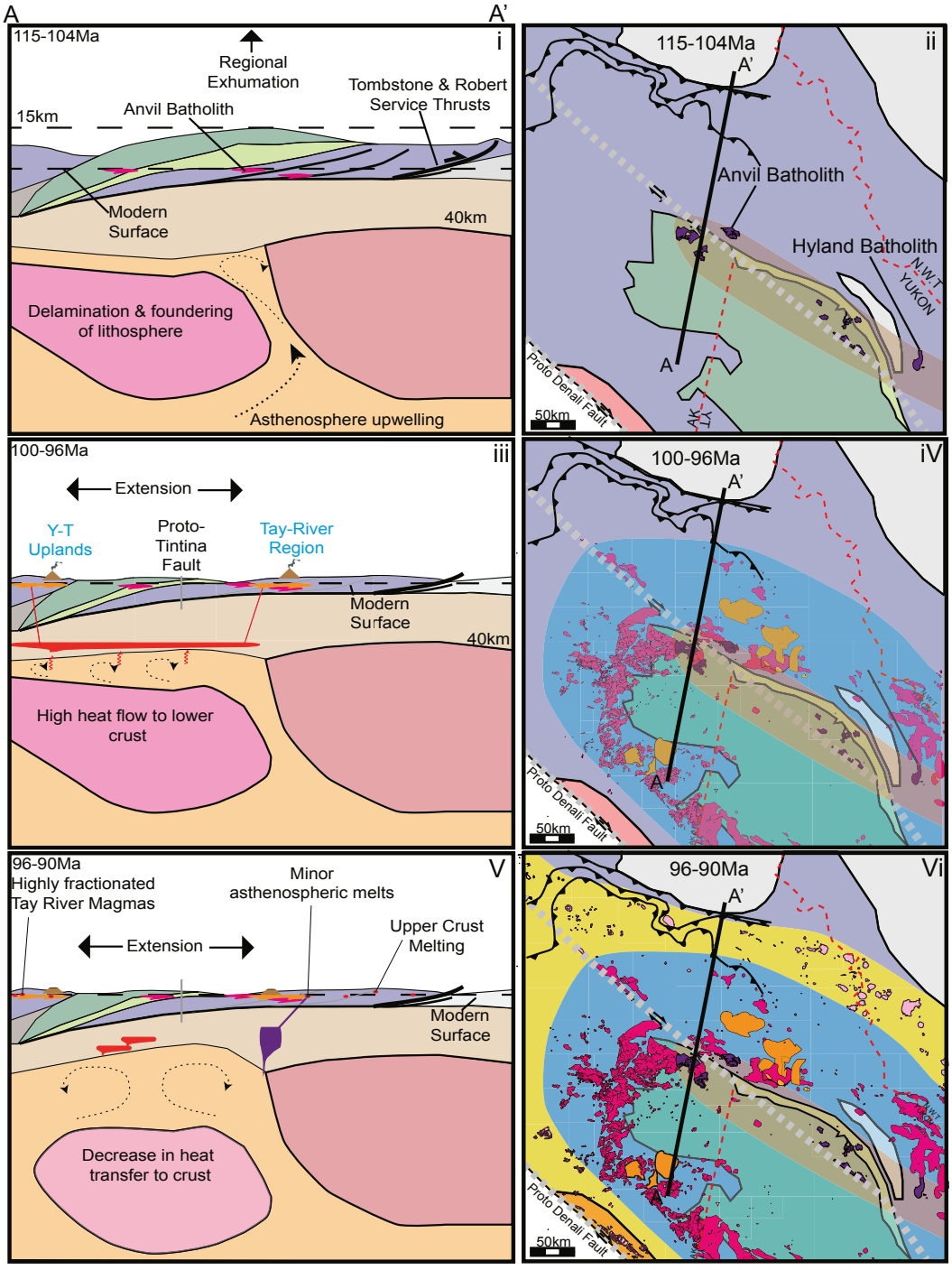
A
A'
115-104Ma
i
Regional
Exhumation
Tombstone & Robert
Service Thrusts
Anvil Batholith
15km
Modern
Surface
40km
Delamination & foundering
of lithosphere
Asthenosphere upwelling
115-104Ma
ii
A'
Anvil Batholith
Hyland Batholith
NWT
YUKON
A
Proto Denali Fault
50km
100-96Ma
iii
Extension
Y-T
Uplands
Proto-
Tintina
Fault
Tay-River
Region
Modern
Surface
40km
High heat flow to lower
crust
100-96Ma
iV
A'
A
Proto Denali Fault
50km
96-90Ma
Highly fractionated
Tay River Magmas
V
Minor
asthenospheric melts
Extension
Upper Crust
Melting
Modern
Surface
Decrease in heat
transfer to crust
96-90Ma
Vi
A'
Proto Denali Fault
50km

Figure 2.14 (Previous Page): i, iii and V: Cross sections across the OMB between 115-90Ma. ii, iV and Vi: Schematic aerial views of pluton distribution for the time periods corresponding to i, iii and V. Tintina fault restoration based on Figure 2.12. Terrane boundaries and colours from Figure 1. i: 115-104 Ma: Delamination of thickened cordilleran lithosphere below the Yukon-Tanana terrane creates space for asthenosphere to upwell into contact with the lower crust. This causes immediate isostatic rebound and regional exhumation. Decompression melting occurs in radiogenic element enriched sedimentary layers in already thickened crust forming Anvil-type plutons. Exhumation stops at ~105 Ma. At the northeast of the OMB vertical exhumation is taken up on the Tombstone and Robert Service thrusts. ii: Anvil-type granites form in the center of the orogeny including parts of the Anvil, Hyland and Cassiar batholiths. iii: 100-96 Ma: Asthenosphere has gradually heated the lower crust over the past 10 Myr leading to melting of lower crustal igneous rocks forming Tay River-type melts. Exhumation has slowed and regional extension continues. Lower crustal melts rise through the crust rapidly pooling in shallow magma chambers (Tay River-type plutons) which occasionally erupt causing catastrophic caldera formation (South Fork-type volcanics). iv: Tay River-type plutons occur in the same regions as the Anvil-type but also occur in a concentric pattern proximal to the YTT. Distribution is strongly controlled by the scale of the delaminating lithosphere. Plutons include the Dawson Range, Orchay and Marjorie batholiths. v: 96-90 Ma: Lithosphere foundering continues but the thermal perturbation begins to wane as asthenosphere in contact with the crust cools. This leads to lower volume lower crustal melts. A lack of exhumation increases crustal residence times leading to high degrees of crustal contamination seen in Tombstone-type plutons. Contin-ued extension leads to the intrusion of rare lamprophyres assumed to derive from asthenosphere melts. vi: Tombstone pluton emplacement occurs across the whole OMB associated with the previous two plutonic styles and as isolated plutons in the most distal parts of the OMB.

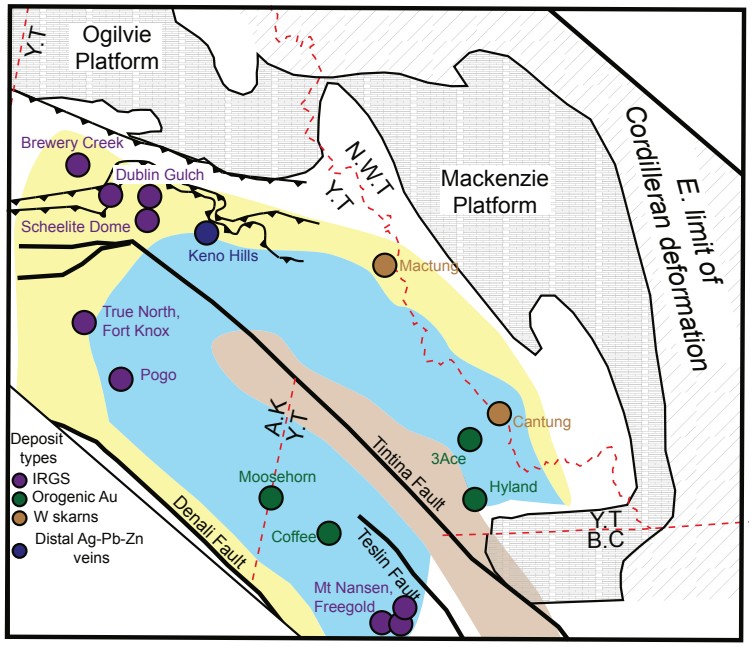

Figure 2.15: Reproduction of Figure 2.12 showing a selection of major Mid-Cretaceous mineral deposits of the OMB from Nelson et al. (2013). Deposits are colour coded based on type.

Table 2.1. Geochemical Parameters from Whole Rock Bulk Analysis of Granitic Samples

	A/CNK				ASI (A/NK)				$(Eu/Eu^*)_{CN}$				$(La/Yb)_{CN}$				$(Ba/Ta)_{MN}$				Dy/Dy*			
	X	±σ	Max	Min	X	±σ	Max	Min	X	±σ	Max	Min	X	±σ	Max	Min	X	±σ	Max	Min	X	±σ	Max	Min
Anvil	1.5	0.1	1.8	1.4	1.9	0.1	2.2	1.8	0.55	0.07	0.73	0.49	36	7	48	23	7	3	13	4	0.11	0.02	0.16	0.09
Tay River	1.6	0.1	1.7	1.5	2.6	0.4	3.4	1.9	0.60	0.12	0.79	0.40	13	6	27	6	11	4	19	4	0.24	0.06	0.33	0.14
Tombstone	1.6	0.1	1.7	1.6	2.4	0.7	2.9	1.9	0.56	0.01	0.57	0.55	12	8	18	6	11	8	17	6	0.30	0.07	0.35	0.25
South Fork	1.6	0.1	1.7	1.5	2.9	0.3	3.5	2.5	0.57	0.08	0.70	0.44	12	3	20	8	12	3	25	9	0.26	0.04	0.32	0.17

	CaO/Na_2O				Al_2O_3/TiO_2				$(Sm/Yb)_{CN}$				$(Nb/Ta)_{CN}$				$(La/Sm)_{CN}$			
	X	±σ	Max	Min	X	±σ	Max	Min	X	±σ	Max	Min	X	±σ	Max	Min	X	±σ	Max	Min
Anvil	0.7	0.1	0.9	0.5	40	2	42	36	7.58	1.33	9.42	5.18	13	3	18	8	4.8	0.3	5.1	4.3
Tay River	1.5	0.4	2.4	0.6	28	4	38	22	3.06	0.95	5.77	1.55	18	5	34	11	4.2	0.6	5.1	3.3
Tombstone	1.2	0.9	1.9	0.6	39	19	53	26	3.1	2.0	4.5	1.7	15	9	22	13	3.7	0.2	3.9	3.6
South Fork	1.9	0.4	3.0	1.3	26	4	33	22	2.82	0.37	3.76	2.33	20	7	46	13	4.1	0.6	5.5	3.4

Table 2.2. Geocehmical Parameters from Zircon LA-ICP-MS

Suite	*Ce/Ce**	*Eu/Eu**	*Σ REE (ppm)*	*$(Sm/La)_N$*	*$(Lu/Gd)_N$*	*Th/U*
Anvil	1-6	0.003-0.015	760-1660	0.4-72.5	31-134	0.01-0.03
Tay River	1-67	0.007-0.014	660-1990	0.5-320	11-41	0.13-1.2
Tombstone	1-10	0.003-0.038	665-2600	1.5-440	12-52	0.16-0.43
South Fork	1-81	0.003-0.014	390-1280	0.4-17	12-49	0.29-0.59
REFERENCE VALUES						
Mantle Affinity*	1-10	~1	<40	<50	~1-10	--
Crustal Affinity*	1-100	<<1-<1	1500-2000	57-547	16-74	--
Igneous Zircon*	--	--	--	--	--	0.4-1.0
$Meta^m$ Zircon*	--	--	--	--	--	0.01-0.08

* Typical values from Hoskin and Schaltegger (2003) and Hoskin and Ireland (2000).

Table 2.3. Isotopic Results from OMB Granites in the Tay River District

Sample #	T (Ma)	Sm (ppm)	Nd (ppm)	$^{147}Sm/^{144}Nd$	$^{143}Nd/^{144}Nd_0$	±2σ	$^{143}Nd/^{144}Nd_T$	εNd_T	T_{DM} (Ga)	Rb (ppm)	Sr (ppm)	$^{87}Rb/^{86}Sr$	$^{87}Sr/^{86}Sr$	±2σ	$^{87}Sr/^{86}Sr_i$
G1	108	4.74	28.14	0.1018	0.511574	0.000008	0.511502	-19.4	2.16	139	167	2.427	0.74300	0.00005	0.73927
G3	108	3.85	22.77	0.1023	0.511517	0.000015	0.511444	-20.6	2.24	105	143	2.135	0.74104	0.00003	0.73777
G4	100	4.95	24.99	0.1197	0.511876	0.000008	0.511798	-13.9	2.08	110	314	1.016	0.71400	0.00003	0.71256
G10	92	1.78	6.26	0.1723	0.511853	0.000010	0.511750	-15.0	N/A	214	83	7.457	0.72564	0.00003	0.71593
G11	98	3.86	19.94	0.1169	0.511751	0.000011	0.511675	-16.3	2.22	119	232	1.486	0.71969	0.00003	0.71762
G18	98	5.10	26.04	0.1183	0.511842	0.000011	0.511766	-14.5	2.10	71	296	0.696	0.71587	0.00003	0.71490
G20	99	4.45	24.30	0.1106	0.511787	0.000008	0.511716	-15.5	2.03	145	222	1.892	0.71861	0.00003	0.71595
G21	99	5.42	34.75	0.0944	0.511804	0.000006	0.511743	-15.0	1.73	127	416	0.885	0.71963	0.00003	0.71838
G22	98	4.42	24.49	0.1092	0.511782	0.000010	0.511712	-15.6	2.01	82	367	0.647	0.71796	0.00002	0.71706
G27	100	4.51	21.47	0.1270	0.511838	0.000007	0.511755	-14.7	2.32	145	161	2.600	0.71946	0.00003	0.71578

Chapter 3: Identifying the source of an S-type granite via xenocrystic zirconology.

Clastic sedimentary rocks commonly contain detrital mineral grains like zircons that resist destruction during erosion and diagenesis. The population of detrital zircon grains in a sedimentary unit is typically derived from multiple sources with different ages that reflect the provenance of the rock. Therefore, U-Pb dating of a suite of detrital grains can be used to produce an age spectrum that can be characteristic of a given sedimentary unit (Fedo et al. 2003). S-type granites are peraluminous felsic rocks, which form as the result of the partial melting of metasedimentary rocks in the crust. These granites inherit a chemical and isotopic signature (e.g., Nd, Sr), as well as zircons from their sedimentary source rocks (Chappell and White 1974). However, magmatic processes, such as crustal contamination, crystal fractionation and magma mixing (Clemens 2003), make it challenging to precisely identify the melt source (s) of S-type granites.

Here, we use U-Pb dating of inherited zircons in an S-type granite to accurately identify the sedimentary protolith. This approach has previously proven difficult (Keay et al. 1999) as inherited zircons commonly have discordant $^{206}Pb/^{238}U$ and $^{207}Pb/^{235}U$ ages, having lost Pb during the melting process. Recently, however, Reimink et al., (2016) published a new method enabling the extraction of robust ages from a population of discordant zircon analyses. In this study, we apply this method to discordant U-Pb analyses from xenocrystic zircons extracted from an S-type granite, in conjunction with Nd-isotope analyses of the granite. Using these data we are able to accurately constrain the sedimentary protolith that partially melted, and show that

inherited zircons from this Cretaceous S-type granite preserve a record of multiple rock cycles dating back to the Archean.

Geological Background

The Anvil region in the central Yukon, Canada provides an ideal natural laboratory for testing this method: the regional stratigraphy has been well constrained (Pigage 2004, Gordey 2013); detrital zircon spectra (Gehrels et al. 1999, Ross et al. 2005, Hadlari et al. 2009, 2012, Leslie 2009, Lane and Gehrels 2014) and Nd-isotope compositions (Boghossian et al. 1996, Garzione et al. 1997) are documented for the sedimentary units in the region; and the study area contains a large and accessible S-type granite, the Anvil batholith (Pigage and Anderson 1985, Smith and Erdmer 1990).

The crystalline basement in this part of western Canada is the cryptic Nahanni terrane (Hoffman 1989, Ross 1991a), which is proposed to comprise 2400 –1850 Ma rocks (Hildebrand et al. 1987, Villeneuve et al. 1991). A package of supracrustal units, including three sedimentary Proterozoic supergroups (Wernecke, Delaney 1981, Thorkelson et al. 2001, Furlanetto and Thorkelson 2009; Mackenzie Mountain, Heaman et al. 1992, Narbonne and Aitken 1995, Rainbird et al. 1996; and Windermere, Ross 1991b, Narbonne et al. 1994, Nelson et al. 2013) were deposited on the crystalline basement. These Proterozoic strata are not found in the Anvil region, but outcrop in the northeastern Yukon (Young et al. 1979, Young 1984) (Figure 3.1). As paleocurrent data demonstrate that Proterozoic Canadian passive margin sedimentation was sourced from the east or northeast (Cecile et al. 1997, MacNaughton et al. 2000, Hadlari et al. 2009, 2012) the sedimentary source regions, and consequently the detrital zircon signatures, of the northeastern Yukon Proterozoic outcrops and unexposed crust in the Anvil region are likely analogous. These outcropping units described in previous studies (Young et al. 1979, Narbonne

and Aitken 1995, Leslie 2009) can, therefore, be used to estimate the detrital grain contents of the unexposed rocks in the Anvil region.

The Proterozoic supergroups are covered by the deep-water sedimentary rocks of the Selwyn Basin, which were deposited onto the passive western margin of the North American craton between the late Proterozoic and Jurassic (Pigage 2004, Gordey 2013). The Hyland group, which is correlative with the upper Windermere Supergroup, was deposited during the initiation of rifting that formed the Selwyn Basin (Nelson et al. 2013). The Gull Lake and Rabbitkettle formations overlie the Hyland Group (Figure 3.1). The Gull Lake Formation is the oldest unit that outcrops in the Anvil region (Pigage 2004). A shift in $\varepsilon Nd_{(T)}$ values, from -10 to -20 for Cambrian and older strata, to -5 to -10 for Early Ordovician to Permian samples (Boghossian et al. 1996, Garzione et al. 1997) marks a change in the source region of Selwyn basin sediments after the deposition of the Gull Lake Formation. Sediment deposition in the Selwyn Basin continued throughout the Paleozoic, ending in the Jurassic due to the onset of the northern Cordilleran orogeny (Nelson et al. 2013). Finally, intrusions in the Anvil region were emplaced in the Cretaceous in a syn- to post-orogenic setting (Hart et al. 2004, Rasmussen 2013).

This study presents zircon and Nd-isotope data from the Anvil plutonic suite (APS), which forms the southeastern end of the Anvil batholith (Pigage and Anderson 1985) a Cretaceous plutonic body hosted within the Cambrian sediments of the Gull Lake Formation. The APS predominantly consists of a peraluminous muscovite-biotite S-type granite (Pigage and Anderson 1985). U-Pb dating of monazite records crystallization ages of 109–104 Ma (Pigage 2004). The melt that formed the APS is thought to derive from partial melting of a sedimentary protolith (Smith and Erdmer 1990, Rasmussen 2013) within the unexposed crust of the Selwyn Basin; however the melt source units(s) have not been identified. By identifying the age

distribution of the inherited zircons in the APS we can identify not only the source for the S-type granite, but also show that the APS retains information on the provenance of the zircon grains and the history of multiple rock cycles in North America.

Decrypting the inherited zircon age spectra of the Anvil plutonic suite

Zircons were separated from two unaltered samples of APS granite and then analyzed using cathodoluminescence imaging on a scanning electron microscope (Figure A1). Of the 150 imaged zircons, 149 contained inherited cores, interpreted to represent the inherited remnants of the detrital zircon grains from the clastic sedimentary melt source. The inherited zircon cores were commonly overgrown by younger rims during magmatic zircon growth. The cores are commonly round with diameters ranging from 40 to 220 μm. Assuming the cores are spheroidal, they typically make up 25±10% (1SD; range of 7 to 51%) of the zircon grain by volume. U-Pb dating of 108 inherited cores was conducted via laser ablation- inductively coupled plasma-mass spectrometry (LA-ICP-MS; Appendix 3). Analyzing such small cores with laser ablation has traditionally proved difficult, as the size of the analytical volume sampled by the laser can be larger than the zircon core, leading to mixing between core and rim domains, ultimately creating a discordant U-Pb analysis that has proven difficult to interpret.

The majority of the 108 U-Pb analyses collected from the inherited zircon cores yield discordant analyses (Figure 3.2A), and only 20 of the analyses are <10% discordant, a typical filter in detrital zircon studies (Fedo et al. 2003). However, the modelling methodology of Reimink et al. (2016) can be used to calculate the most probable lower intercept age for the discordant zircon analyses from the APS (Figure 3.2B). Using this method, the highest probability for the lower intercept age from the 108 zircon cores analysed is calculated to equal

~110 ± 4 Ma, which within analytical uncertainty is indistinguishable from the age of emplacement of the APS (Pigage 2004).

Using this fixed lower intercept age, the upper intercept age spectra (interpreted as the crystallization ages for the inherited zircons), with associated errors, can be calculated from the modeling output of Reimink et al. (2016). The 2σ errors in individual discordant zircon analyses are combined with the ±4 Myr error in the lower intercept to produce a conservative error envelope (Figure 3.3). The corrected zircons display dominant age-abundance peaks at ~1830 and ~1920 Ma, with secondary peaks at ~1100, ~1200 and ~2700 Ma. Minor peaks are present at ~1550 and ~2350 Ma. These peaks represent common ages seen in age spectra from sedimentary samples in western Canada (Leslie 2009, Lane and Gehrels 2014).

In order to evaluate the similarity of potential sedimentary sources and the APS inherited zircon spectra with some statistical rigor, we used the Kolmogorov-Smirnov (K-S) goodness-of-fit test. However, the continuous age spectra produced by the modeling output are not suitable, as the K-S test requires discrete input data. Therefore, we recalculated the upper intercept ages for each grain by solving the simultaneous equations that describe the discordia lines and the concordia polynomial (Appendix 3). Analyses proximal to the lower intercept ($^{206}Pb/^{238}U<0.05$ or $^{207}Pb/^{235}U<0.5$) were not corrected as these samples are dominated by lead-loss or magmatic rim overprinting and therefore, would require large extrapolations to calculate the upper intercept, resulting in large errors. Seventy-one out of the 108 analyses were corrected back onto the concordia curve. The age spectrum calculated in this way is nearly identical to the spectrum produced by the modeling procedure of Reimink et al. (2016), but the modeling procedure is able to more robustly account for uncertainty.

To assist in identifying the sedimentary source we also analyzed two whole-rock samples of unaltered APS granite for their Sm-Nd-isotope composition (Appendix 3). These analyses returned $\varepsilon Nd_{(110\ Ma)}$ values of -19.4 and -20.6 for the two APS samples.

Identifying the melt source of the Anvil plutonic suite

The corrected age-probability curve of the APS zircon cores can be compared to the detrital zircon age distributions from sedimentary rocks present in the region in order to identify the magma source(s). Three additional constraints can be placed on the age of the APS melt source:

1. The youngest detrital zircon age in a sedimentary unit yields a probable maximum age for that host unit (Nelson 2001, Fedo et al. 2003). Since the APS zircons are inherited from their source, that source was deposited after the youngest inherited core age (in this case 1032 ± 40 Ma).
2. The sedimentary melt source is assumed to be stratigraphically below the middle to late Cambrian sedimentary rocks (Pigage 2004) within which the Anvil Batholith is currently emplaced. The Gull Lake Formation, which hosts the APS, has been metamorphosed to greenschist to mid-amphibolite grade (Smith and Erdmer 1990, Pigage 2004, Gordey 2013), indicating the host strata never attained the temperatures necessary to generate the volume of melt required to form the APS (Nair and Chacko 2002). As there is no evidence for tectonic imbrication of sediments around the Anvil Batholith (Pigage 2004), the protolith for the APS must be Cambrian or older.
3. The sedimentary melt source must have highly evolved $\varepsilon Nd_{(110\ Ma)}$, similar to the APS, requiring a Cambrian or older protolith (Figure 3.1).

Therefore, the protolith for the APS was deposited between ~1000 and ~500 Ma. Consequently, the Rabbitkettle Formation and Wernecke Supergroup cannot be the protoliths for the APS. This leaves the Mackenzie Mountains Supergroup (MMSG), Windermere Supergroup, and the correlative Hyland Group, or the Gull Lake Formation as potential protoliths.

The detrital zircon age spectra from potential protoliths is summarized in Figure 3.4 (Gehrels et al. 1999, Leslie 2009, Hadlari et al. 2012, Lane and Gehrels 2014). The major peaks at ~1830 and ~1920 Ma in the APS zircon cores are missing from both the MMSG samples, precluding the MMSG Supergroup from being the dominant APS protolith (Leslie 2009). The sample equivalent to the Gull Lake Formation displays the ~1830 Ma peak, but contains peaks at 719 Ma and 790 Ma (Lane and Gehrels 2014), which are not seen in the APS zircons. The Gull Lake-equivalent also does not display the minor peak at 2350 Ma seen in the APS zircons. However, strata from the Windermere Supergroup (Hyland Group and Keele Formation) are similar in their detrital zircon populations to the APS with close matches in relative peak heights and abundances of ages.

The K-S test can be used to explore the relationship between zircon age spectra by identifying if there is a statistically significant difference between two distributions, removing the subjective bias of a visual comparison. To run the K-S test the 71 discrete corrected data points (without errors) from the APS can be compared to raw data from both individual sedimentary units and mixtures of multiple sedimentary units in the region. Possible populations of zircons derived from more than one lithology were generated by combining random Monte-Carlo populations from mixtures of zircons in sequential sedimentary units (Table A13).

K-S test comparisons of zircon ages from combinations of the sedimentary units with the APS, confirm that most of the zircon populations (individual or mixed) cannot be potential

sources (p-value> 0.1) for the APS. The K-S test shows that only the Windermere Supergroup (p-value = 0.880; d-statistic=0.11), or mixed zircon populations dominated by zircons from the Windermere Supergroup and Gull Lake Formation (average p-value from multiple runs=0.34) have a statistical likelihood of sharing a zircon population with the APS.

Furthermore, the Nd-isotope values measured on the APS ($\varepsilon Nd_{(110\ Ma)}$= -20±0.6) overlap with the ratios measured in the Windermere Supergroup ($\varepsilon Nd_{(110\ Ma)}$= -21±2; Boghossian et al. 1996, Garzione et al. 1997) supporting the Precambrian sediment as the dominant contributor to the APS melt.

Therefore, whereas mixing between the Windermere Supergroup/Hyland Group, and other sedimentary units cannot be ruled out, the Nd isotopic values and remarkable correlation between the Windermere Supergroup and APS zircons suggests that the Hyland Group is the most probable source for the APS melt.

The story of a continent in a hand specimen

This study demonstrates that correcting discordance in U-Pb analyses of inherited zircon cores from an S-type granite allows the identification of the source sedimentary unit that partially melted, constraining that part of the rock cycle. However, the corrected zircon ages reveal more than just the last stage in which the Hyland Group melted to form an S-type granite; this granite plug contains a record of events affecting the North American continent over the last 3 billion years. The peaks at 2870 and 2700 Ma represent growth periods within Archean cratons (Hoffman 1989), likely derived from the Slave or Hearne provinces (Leslie 2009). Paleoproterozoic peaks at 2350, 1920 and 1830 Ma derive from the accretionary and continental orogenies (Villeneuve et al. 1993) that brought together these Archean cratons to form the core of present day North America. Mesoproterozoic peaks represent zircon grains sourced from the

east of the North American continent by a river system that transported grains 3000 km, from their source in the Grenvillian orogen (Rainbird et al. 1992, 1997, Ross and Villeneuve 2003) to the western passive margin of the North American continent. Grains sourced from across North America were then deposited in the late Proterozoic as the Hyland Group within the Selwyn Basin. Basin inversion during the Mesozoic Columbian orogeny (Wheeler and Gabrielse 1972) buried the Hyland Group to >15 km (Smith and Erdmer 1990) until the clastic sedimentary rocks reached temperatures that induced partial melting. The melt generated from the Hyland Group migrated from within the >3 km thick sequence of clastic sediments (Gordey and Anderson 1993, Gordey 2013) into the overlying Gull Lake Formation where the magma cooled and solidified to form the S-type APS, thus completing the rock cycle. The S-type granite was gradually exhumed to the surface in the Cretaceous (Gordey 2013) where it presently outcrops as a felsic intrusion containing the history of nearly 3 billion years of the rock cycle in North America.

Implications for granite petrology

The ability to identify the exact melt source of an S-type granite has the potential to solve a number of controversial problems (Clemens 2003) in granite petrology. Applying the method outlined in this study to identify the sources of other granites could clarify the thermal conditions of the crust at the time of partial melting (Miller et al. 2003, Kemp et al. 2005), the nature of the heat sources causing anatexis (Petford and Gallagher 2001), the processes that control the compositional diversity of granites (Clemens and Stevens 2012), and the kinetics of granitic plumbing systems within sedimentary basins (Petford et al. 2000). Identifying the melt source of an S-type granite could also be used to identify the nature of unexposed crust beneath the igneous body and map the variability of buried, sedimentary, units across a region.

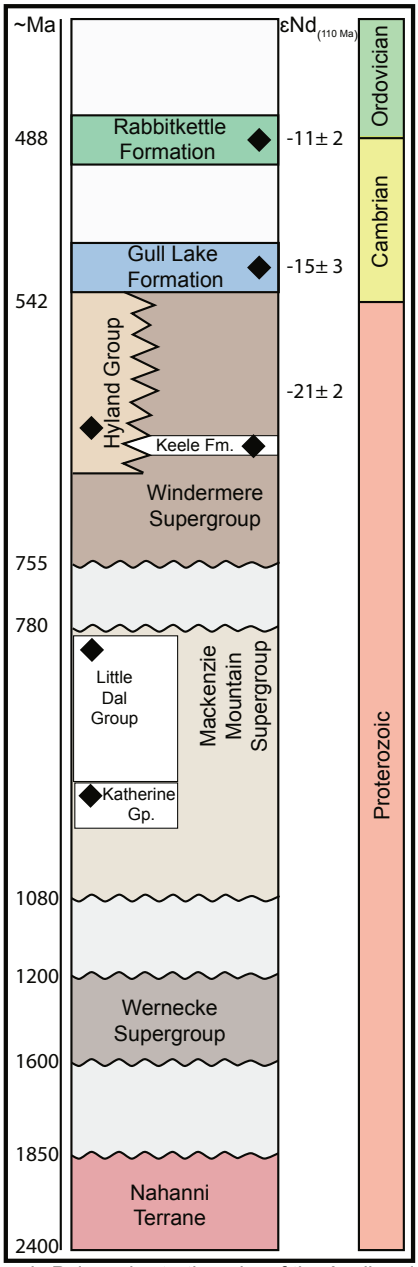

Figure 3.1: Proterozoic and early Paleozoic stratigraphy of the Anvil region (modified from Lane & Gehrels, 2014). Ages of units are taken from references in the text. Black diamonds show sedimentary sample locations. The white boxes show the approximate stratigraphic position of selected formations and groups discussed in the text. Average $\varepsilon Nd_{(110\ Ma)}$ values for Paleozoic sediments are from Garizone et al. (1997) and Boghossian et al. (1996).

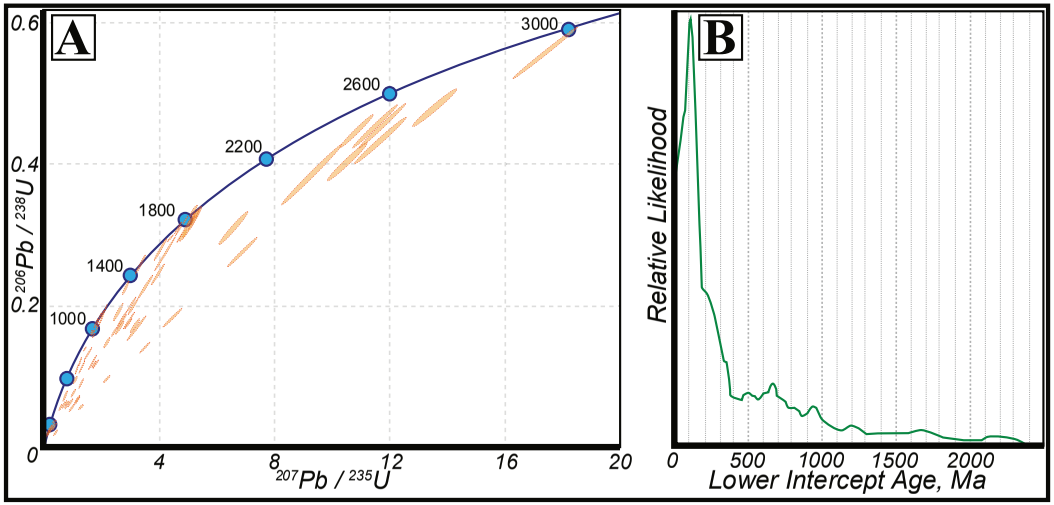

Figure 3.2: A. U-Pb concordia plot of data from APS inherited detrital zircon cores. B. Graph showing likelihood of each lower intercept age for the APS zircons, calculated using the modeling procedure of Reimink et al. (2016). The peak in probability occurs at 110±4 Ma.

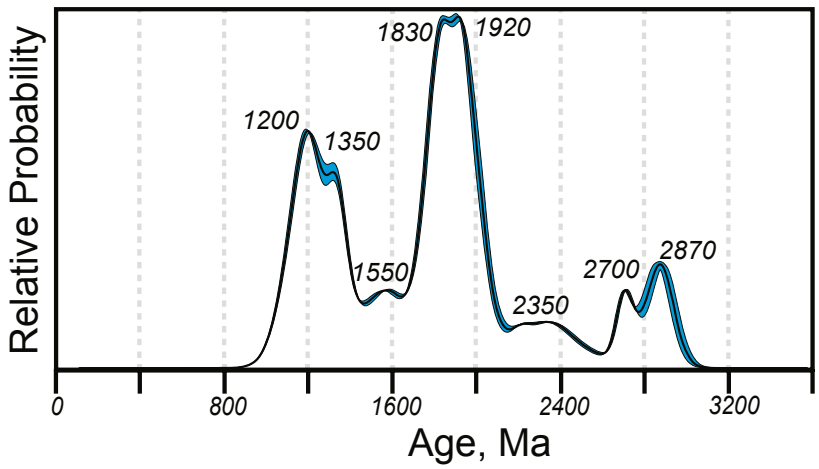

Figure 3.3: Zircon age probability curve showing the corrected results from the APS cores. The conservative error envelope (blue) shows the variation in age spectra derived from a ±4 Ma error in the lower intercept and 2σ errors in U-Pb data.

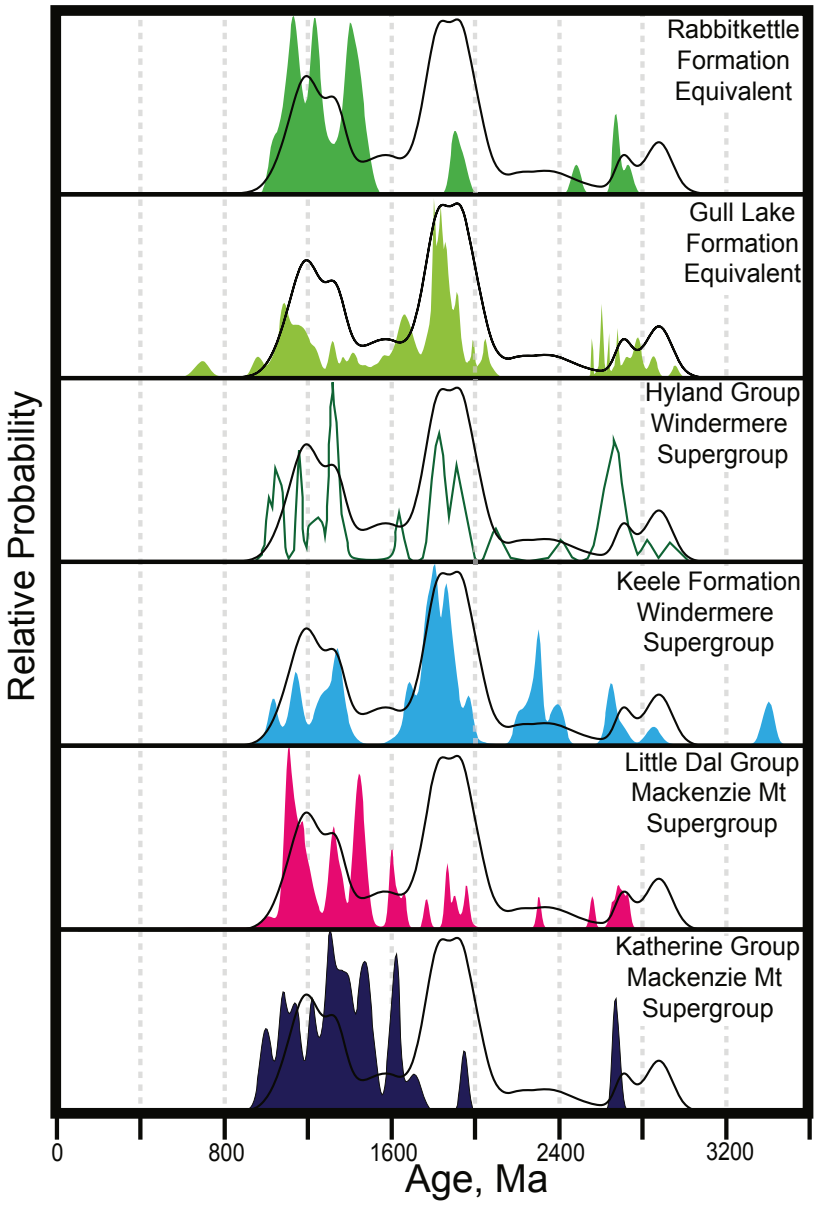

Figure 3.4: Zircon age probability density curves from sedimentary rock equivalents of the units identified in the Anvil region from Leslie (2009), Lane and Gehrels (2014), Gehrels et al. (1999) and Ross et al. (2005) plotted using DensityPlotter (Vermeesch, 2013). The black line shows the APS zircon age spectra calculated in this study. The Hyland Group spectrum is not filled, as the raw data could not be located; the age probability distribution for the Hyland Group come from Leslie (2009)

Chapter 4: Thermochronology of Omineca Magmatic Belt granites in the Selwyn Basin: Evidence for Mid-Cretaceous exhumation of the central Yukon and passage of the northern Cordillera over the Yellowstone hotspot in the Late Cretaceous.

Introduction

The geology to the north of Faro (Tay River district) in south-central Yukon records a complex series of events during the late Mesozoic associated with the transition from the compressional phase of the Sevier-Columbia orogeny to a post-orogenic period. In the Tay River district this is manifested by the mid-Cretaceous (Aptian to Cenomanian) emplacement of one of the largest volume pulses of plutonism and volcanism seen in the northern Cordillera (Gordey 2013). It has been suggested by previous workers that synchronously with the igneous activity the area underwent rapid-exhumation of greater than 10km (Smith and Erdmer 1990, see Chapter 2). Here, we add to the understanding of the geological evolution of the Tay River district in the late Mesozoic by using low temperature thermochronology on plutons to constrain the Cretaceous thermal history of the region. Using these data we derive the nature of, and potential driving forces responsible for this period of exhumation and igneous activity in the Tay River district. These regional-scale dynamics have implications for the evolution of the northern Cordillera and post-compressional orogenies worldwide.

Geological Setting

Regional Setting

The bedrock geology of the Tay River district (Figure 4.1) comprises sedimentary rocks originally deposited between the Precambrian and late Triassic in the Selwyn Basin on the rifted, western passive-margin of cratonic North America (Pigage 2004, Lund 2008, Gordey 2013). The dominantly deep-water sediments of the Selwyn Basin are flanked to the north, west and east by coeval carbonates formed on shallow marine platforms (Gordey and Anderson 1993). Sediment deposition in the Selwyn Basin had terminated by the Jurassic to Cretaceous, due to allochthonous terrane accretion to the western margin of North America and the subsequent onset of the Sevier-Columbia orogeny (Mihalynuk et al. 1994, Nelson et al. 2013, Hildebrand 2014). This Mesozoic orogeny is dominantly thought to be thin skinned (Cook et al. 2004, Cook and Erdmer 2005), with the allochthonous terranes overriding the North American margin, and is interpreted to have resulted in crustal thickening (Pavlis et al. 1993), exhumation of previously deeply-buried crust (Colpron et al. 1996), and the formation of a fold and thrust belt at the eastern margin of the orogen (Ross et al. 2005, Nelson et al. 2013). The strata of the Tay River district were structurally imbricated and folded during the orogeny (Figure 4.2; Pigage 2004, Gordey 2013, Cobbett 2015, Yukon Geological Survey 2017).

Mid-Cretaceous Igneous Rocks

Mid-Cretaceous plutonic rocks outcrop across the whole northern Cordillera in two distinct belts (Armstrong 1988, Woodsworth et al. 1991): the outboard Coastal Plutonic Belt (CPB) and the inboard Omineca Magmatic Belt (OMB). The plutons within the Tay River district form part of the OMB; an enigmatic group of plutons that intruded inboard of the

continental margin, in a post-orogenic setting. Researchers do not agree on the formation mechanism for the OMB plutons and there are numerous models for their genesis (Rasmussen, 2013; Johnston, 2008; Hart et al., 2004; see Chapter 2).

The Tay River district contains one of the highest densities of OMB plutons, and some of the only preserved outcrops of OMB volcanic rocks (Figure 4.2). In Chapter 2 it was shown that the mid-Cretaceous plutons in the Tay River district were emplaced continuously from 110 to 92 Ma and that these plutons can be divided into three suites based on their age, geochemistry and petrology**.** The oldest suite in the Tay River district is the Anvil, followed by the Tay River and finally the Tombstone suite. Descriptions of each suite can be found in Mortensen et al., (2000); Hart et al., (2004);Rasmussen, (2013) and in Chapter 2.

Significant exhumation within the Tay River district concurrent with the emplacement of these plutons has been hypothesized (Tempelman-Kluit 1972, Pigage and Anderson 1985). The first constraint on exhumation is constrained by the aureole and intrusive rock mineralogy of the oldest plutons in the region, the 109-104 Ma Anvil suite (Pigage 2004). This aureole consists of pelitic schists containing an assemblage of andalusite-staurolite-garnet-biotite-muscovite-quartz and plagioclase with local fibrolite and cordierite, but lacking kyanite (Pigage and Anderson 1985, Smith 1989), indicating emplacement at less than 4 kbar. Some authors (Tempelman-Kluit 1972) have previously argued that the isograds in the pelitic schists are truncated by plutons of the Anvil suite and, therefore, the mineralogy reported above was the result of regional Devonian metamorphism rather than Anvil suite emplacement. However, Smith and Erdmer (1990) mapped biotite, andalusite, staurolite, garnet, and sillimanite isograds within the schists, concentric to an Anvil suite pluton, consistent with the formation of the mineral assemblage in the mid-Cretaceous. The Anvil suite igneous rocks contain primary magmatic muscovite (see

Chapter 2) indicating that mica was a primary magmatic phase in the magmas and, therefore, emplacement of the Anvil suite occurred at >3.5 kbar. Overall, the aureole mineralogy- combined with the lack of kyanite and the presence of primary magmatic muscovite- constrains the Anvil suite emplacement to between 3.5 - 4 kbar, which corresponds to depths of 12-15 km (Pigage 2004). The intrusion of the Anvil Batholith is believed to coincide with the beginning of exhumation due to the regional lower greenschist grade, consistent with burial of the Tay River district to a maximum depth of around 12-15 km (Pigage 2004), and due to comparison with Staples et al. (2016).

The second geological constraint on the exhumation comes from the 100-96 Ma Tay River suite and the cogenetic South Fork volcanics (Gordey 1988). The Tay River suite was emplaced at shallow levels (<1-2 km), as shown by the close spatial association between Tay River suite plutons and coeval extrusive caldera volcaniclastics (Smith and Erdmer 1990, Pigage 2004 and see Chapter 2). The shallow level of Tay River suite intrusion is supported by an association with hornfels (Pigage 2004) and the coeval-proximal deposition of sub-aerial coarse clastic rocks dated by dinosaur prints (Long et al. 2001). However, the Tay River suite and Anvil suite currently outcrop at the same stratigraphic level and the two suites interfinger within a number of batholithic bodies. This means that between the Anvil suite emplacement (109-104 Ma) and the Tay River suite emplacement (100-96 Ma), the Anvil suite was exhumed from ~13±2 km to 1.5±0.5 km. This corresponds to a 12±2 km exhumation in 8±4 Ma at a rate of between ~1 and >3 km/Ma.

After the emplacement of the Tay River suite, the Tombstone suite was intruded across the Tay River district, between 96-90 Ma (see Chapter 2). Round, small volume, Tombstone suite plutons are surrounded by hornsfels facies aureoles composed of biotite, K-Feldspar and

andalusite bearing pelites. This association is consistent with emplacement at shallow crustal levels (<1- 2 km; Spear and Cheney 1989, Mair et al. 2006). In the 90 Ma after the intrusion of OMB plutons, the Tay River district appears to have undergone very little geological change: the 100-96 Ma South Fork volcanic flows are still approximately horizontal (Gordey 1988, 2013) and 1km thick tuffaceous deposits still remain within the calderas, which based on typical North American caldera fill thicknesses (Lipman 1984) suggests only ~1km of denudation has occurred since the Turonian (Smith and Erdmer 1990).

The mid-Cretaceous exhumation rates seen in the Tay River district are high, but consistent with erosional denudation keeping pace with tectonic uplift (Reiners and Brandon 2006). In Chapter 2, both the period of uplift and changes in pluton style could be explained via a delamination model, proposing that foundering of lithosphere caused uplfit due to isostatic rebound. Modern studies on asthenosphere flow during post-glacial rebound demonstrate that this method could produce the uplift rate observed in the Tay River district (Sigmundsson 1991). However, the magnitude of exhumation seen in the Tay River district (>10 km) is unlikely to derive from only delamination driven isostatic rebound (Krystopowicz and Currie 2013) and requires synchronous tectonic exhumation and denudation via brittle and/or ductile thinning of the crust.

This chapter aims to further constrain the details of the mid-Cretaceous exhumation in the Tay River district using accurate low temperature thermochronology on the igneous rocks of the region. Thermochronology is the study of the thermal history of rocks based on a number of radiogenic isotope systems that display open system behavior above a defined temperature range - termed the effective closure temperature (T_C; Hodges 2003, Reiners and Brandon 2006). The date recorded by a thermochronometer indicates the time the system cooled below T_C. Therefore,

dating a rock via a number of systems with different closure temperatures can elucidate the thermal history (temperature versus time path; Tt) of that rock. For this study, we have combined new ^{40}Ar-^{39}Ar dates from biotite or hornblende and U-Th/He dates from zircon separated from OMB plutons in the Tay River district, with U-Pb zircon ages previously reported in Chapter 2. The typical approximate effective closure temperatures at cooling rates experienced within a range of geological environments of these three systems respectively are: 325-375°C, 200-150°C and 800- 900°C (Figure 4.3; Hodges 2003, Reiners 2005, Reiners and Brandon 2006). Therefore, combining the three systems will yield a Tt path for the OMB plutons passage through the upper crust during mid-Cretaceous exhumation.

Methods

To examine the Cretaceous regional exhumation of the Tay River district, nine samples of unaltered granitic rock characterizing representative samples of each of the Anvil, Tay and Tombstone suites were selected for analyses (Figure 4.2; Table 4.1). The geological context of the samples is provided in Chapter 2. Unless otherwise reported, all analyses were conducted at the Canadian Centre for Isotopic Microanalysis at the University of Alberta, Edmonton, Canada.

Mineral Separation and Imaging

Zircons

Zircons were separated from the samples using standard gravimetric and magnetic settling techniques to isolate a heavy mineral separate composed of dominantly zircon grains. Imaging of representative mounted grains from each sample was conducted to characterize parent nuclide (U) zonation within individual zircon grains. The imaging was conducted in secondary electron,

cathodoluminescent (CL) and backscattered light, using a Zeiss Evo-MA-15 scanning electron microscope. While not possible to image the exact grains that are measured for U-Th/He ages, the imaging of >60 zircons per sample allowed effective characterization of U zonation for the zircon population of each sample.

Biotite

Biotite was hand picked from crushed samples of eight of the granitic rocks. Sample G18 did not contain any separable biotite so hornblende was isolated. Contamination of samples, by secondary (hydrothermal) biotite was a concern. However, detailed petrography carried out on all samples indicated that primary-magmatic grains displayed a strongly euhedral crystal form in contrast to the anhedral- "shreddy" form displayed by the secondary-hydrothermal biotite grains. Petrography also revealed that the primary biotite of each suite displays characteristic colours in hand specimen and transmitted light (Table 4.1; Figure 2.5). Therefore, primary-magmatic biotite could be isolated from each sample based on both colour and crystal form. Petrography also revealed that alteration of primary biotite grains was minimal in each sample. However, the hornblende phenocrysts in Sample G18 had been extensively replaced by hydrothermal chlorite, meaning pure hornblende samples could not be isolated. Therefore, the $^{40}Ar/^{39}Ar$ data from the hornblende samples will include Ar degassed from the younger chlorite grains making any $^{40}Ar/^{39}Ar$ dates obtained minimum age estimates (Little et al. 1995).

LA-ICP-MS methodology

In order to further characterize the zonation of parent nuclides within zircon grains, U and Th concentrations were measured on mounted zircon separates from zircons from an Anvil suite sample (G1). Measurements were carried out by laser ablation inductively coupled plasma mass spectrometry (LA-ICP-MS) using a Resonetics M-50 LR laser ablation system coupled to a

Thermo Neptune Plus Multicollector inductively coupled plasma mass spectrometer following the methods outlined in Chapter 2.

^{40}Ar-^{39}Ar methodology

$^{40}Ar/^{39}Ar$ analysis was carried out on eight biotite and one hornblende separate (Table 4.2) at the Nevada Isotope Geochronology Lab (NIGL), University of Nevada, Las Vegas using their in-house laboratory procedures - described below. At least 100 mg of pure mineral separate was included for each sample.

During the irradiation stage Ar induced interferences from K and Ca were corrected by repeated analysis of synthetic K-glass and CaF_2 within the irradiation packages. Measured $(^{40}Ar/^{39}Ar)_K$ values were 7.13 (± 9.38 %) x 10^{-3}. Ca correction factors were $(^{36}Ar/^{37}Ar)_{Ca}$ = 2.31 (± 0.29 %) x 10^{-4} and $(^{39}Ar/^{37}Ar)_{Ca}$ = 6.27 (± 0.08%) x 10^{-4}. Biotite fluence was monitored by standard GA-1550, which was assigned an age of 98.50 Ma (Spell and McDougall, 2003). Excellent reproducibility (0.3 to 0.8 %) of the single crystal GA-1550 biotite fluence monitor along the length of the irradiation tube indicates that there were no significant neutron fluence gradients present within individual crystal packets. Total neutron fluence variation along the length of the irradiation package was <4%.

The furnace step heating method was carried out in an ultrahigh vacuum furnace (Staudacher et al. 1978), with final measurements of the Ar ratio performed in a MAP 215-50 mass spectrometer. Systematic errors in the mass spectrometer were calibrated via multiple analysis of atmospheric argon aliquots, which yielded $^{40}Ar/^{36}Ar$ ratios of 305.28 ± 0.08% (accepted value 295 ± 5 (Nier 1950)) during this work. Therefore, a correction factor of 0.9680 (4 AMU) was applied to measured isotope ratios. The sensitivity of the mass spectrometer was ~6 x 10^{-17} mol mV^{-1} with the multiplier operated at a gain of 36 over the Faraday. Line blanks

averaged 3.07 mV for mass 40 and 0.03 mV for mass 36 for laser fusion analyses and 15.45 mV for mass 40 and 0.06 mV for mass 36 for furnace heating analyses.

U-Th/He methodology

U-Th/He analyses were carried out on separated zircons from all nine samples at the Arizona Radiogenic Helium Dating Laboratory (ARHDL), University of Arizona, Tuscon. Three to four single zircon crystal aliquots were measured per sample. Three steps are involved in the collection of U-Th/He data: Step 1- selection, characterization and preparation of grains, Step 2- ^{4}He extraction and measurement, and Step 3- U-Th measurement (Reiners 2007).

Step 1 involves the collection of grain morphology and size measurements, based on the methods and terminology of Hourigan et al. (2005). These measurements allow for the calculation of an α- ejection correction, as well as grain volume and mass, for each individual grain. Grain picking was biased towards large-euhedral crystals that lacked inclusions, visible staining, and fractures. Individual selected grains were placed in 1-mm Nb tubing to prevent volatilization of parent nuclides during direct lasing (Reiners 2005).

Step 2 involves He extraction following the method outlined in Reiners (2005; 2007). Around 15 grains at a time were placed in a Cu planchet that also included 1 blank (empty Nb tube) and 3-4 Nb packets containing the standard Fish Canyon Tuff zircon interspersed evenly throughout the unknowns. A CO_2 laser, run at between 5-15 W, was used to heat samples to between ~1000-1300°C for 15 minutes under ultrahigh vacuum ($<10^{-8}$ Torr). Twenty-minute re-extracts were performed on all zircons (often multiple times) until ^{4}He on the re-extract yielded less than 1-2% of the accumulated ^{4}He volume. Hot blanks gave ^{4}He values of <0.1 fmol.

Step 3 involves the measurement of the concentration of parent nuclides (U and Th) in the zircons via isotope dilution ICP-MS, following the methods of Reiners and Nicolescu (2006). Precision on measured U-Th ratios was better than 0.5%.

The internal standard used across all 3 steps was the Fish Canyon Tuff zircon. Analyzes on 5 grains of the Fish Canyon Tuff zircon during this study returned an average mean U-Th/He date of 28.0 ± 0.73 Ma; the accepted value is 28.3 ± 0.26 Ma (Reiners et al. 2002).

Results

Imaging of zircons

SEM imaging of 60 to 80 zircons from each sample demonstrated remarkable homogeneity of the zircon morphology within each sample and each plutonic suite. However, the zircon morphologies from differing plutonic suites vary significantly (Figure 4.4). Of the 150 imaged zircons from granites of the Anvil suite (sample G1 & G3), 149 contained inherited cores surrounded by rhythmically oscillatory-zoned rims; the cores are commonly round with diameters ranging from 40 to 220μm. Assuming the cores are spheroidal, they typically make up 25±10% (range of 7 to 51%) of the zircon grain by volume. The zircons from the Tay River (sample G4, G11, G18, G22 and G27) and Tombstone suite (G10 and G12) are rhythmical-oscillatory zoned. Changes in the width of zoning occur in the grains but no significant internal heterogeneity of zircon morphology was observed.

LA-ICP-MS

Based on the SEM imaging, we used LA-ICP-MS to analyze both the rims and cores of Anvil suite sample (G1). Mean U concentrations (± 1σ) from the Anvil rims and cores,

respectively are 3700±700 ppm and 1400±800 ppm. Mean Th concentrations (± 1σ) from the Anvil rims and cores respectively are 40±25 ppm and 150±80 ppm.

^{40}Ar-^{39}Ar

The argon produced in each heating step had a high radiogenic yield, thus, there was not enough spread in the data to create an isochron for any of the samples. Furthermore, the samples also did not return reliable plateau ages (defined as when 3 or more consecutive steps are indistinguishable in age at the 2 sigma level and comprise >50% of the total ^{39}Ar released; Dalrymple and Lanphere 1974, Lee et al. 1991). Samples G1, G3, G4, G11, G12 and G27 form pseudo-plateaus, allowing age interpretation to be extracted by averaging the step ages within the pseudo-plateau (Figure 4.5); the interpreted ages for each sample with 1σ errors are respectively: 103.5±2.1 Ma, 104.3±2.1 Ma, 98.8±1.7 Ma, 94.9±1.8 Ma, 93.4±1.8 Ma and 103.0±2.2 Ma. These apparent ages are calculated assuming that the initial argon is atmospheric and, therefore, provide maximum constraints for the actual age, which would be lower if excess argon was present. Argon dating of samples G10, G18 and G22 was unsuccessful because the isotopic ages did not plateau during the stepwise heating of the sample (Figure 4.5).

U-Th/He

U-Th/He was measured from three to four single zircon- grain aliquots for each sample (Table 4.2). Replicate U-Th/He ages from the same sample yield a 2 sigma standard deviation of ~6-10%, which is greater than the ~3-4% error from analytical processes in U, He, Th and Sm measurement (Hourigan et al. 2005). The grains from samples G3, G4, G11 and G18 report a consistent date at the 2 sigma level of reproducibility; the dates with 1σ errors are respectively:

68±4 Ma, 90±4 Ma, 77±3 Ma and 68±3 Ma. The three-grain aliquots from sample G1 overlap at ±10%, producing a date of 85±8 Ma. The grain aliquots from sample G10, G12, G22 and G27 do not yield a reproducible date at either ±2σ or ±10% overlap conditions. The alpha ejection correction applied to calculate the U-Th/He dates relies on homogenous U and Th distribution within all zircons analyzed. SEM imaging combined with LA-ICP-MS analyses shows that for certain samples, heterogeneous parent nuclide zonation exists, and this must be corrected for in order to extract reliable U-Th/He dates (Orme 2015).

Correcting for heterogeneity within grains

Zircon grains from sample G1 and G3 possess inherited cores. The cores have brighter CL than the rims, suggesting that the cores have suffered less damage due to lower radiogenic element concentrations, as amorphisation suppresses broad-band CL emission (Nasdala 2003). The LA-ICP-MS work confirms that the cores have significantly lower effective U content (eU=U+0.235Th) than the overgrown magmatic rims. The rim thickness (approximately perpendicular to the c axis) measured from 2D CL images of 57 zircons from the Anvil suite averages 8±6 μm with a range of 34 to 1 μm. Approximating the Anvil suite grains to a circular morphology (Farley et al. 1996) gives an average grain radius of 75±18 μm with a rim width of 30±10 μm. An effective spherical radius cannot be accurately calculated from the 2.D imaging as only one a_x axis dimension is known and in zircons a_1 does not commonly equal a_2.

Assuming heterogeneity in parent nuclide distribution instead of homogeneity in eU in a single grain leads to an underestimate of the α-ejection correction, as the high eU rim results in more He rejection than is calculated and therefore, is an overestimate of bulk He retention (Hourigan et al. 2005). In the Anvil suite zircons the ~2.5 factor rim enrichment can lead to a

maximum age inaccuracy of about ~10% for typical crystal radii, which occurs when the rim effective spherical radius equals ~10 μm (Orme 2015). Based on the average rim radii, zircon crystal size and rim to core eU enrichment recorded from the Anvil suite zircons, it is expected that on average the U-Th/He dates measured will be between 5 and 8% too young (Hourigan et al. 2005). Therefore, a 6.5±1.5% correction is applied to the Anvil suite (G1 & G3) zircons (Table 4.3).

Discussion

Evidence for Exhumation

The simplest explanation of the thermochronological data is that the Ar-Ar and U-Th/He ages reflect the time at which the pluton cooled below the effective closure temperature of each mineral system (T_c; Figure 4.3). The effective closure depth (Z_c) - the depth at which T_C occurs for each mineral system - can be modeled in the upper crust at fixed exhumation rates using a two step process. First we calculate the geotherm for a region of exhuming crust. The exhuming crust is approximated as a one dimensional thermal field of finite thickness, L, with fixed, constant, temperatures at the surface and base, T_S and T_L respectively, and a uniform internal heat production H_T. A more detailed explanation of the modeling procedure can be found in Reiners and Brandon (2006). We assume that horizontal velocities do not significantly affect the model (Batt and Brandon 2002). Material moves through this one-dimensional layer at a constant speed, equal to the rate of exhumation, $\dot{\varepsilon}$. This model calculates temperature as a function of depth, T(z), giving geotherms for constant exhumation rates. In models with a rapid constant exhumation rate the geotherms move to shallower depths, causing the effective closure temperature of each radiogenic system to shallow (Figure 4.6). Parameters for the model were

based on typical convergent orogens, as reported by Reiners and Brandon (2006). The thickness of the layer (L) was set to 40 km based on the current crustal thickness identified in the Lithoprobe SNORCLE Line 3 (Cook et al. 2004), which transects through the eastern corner of the study area (Figure 4.1). This Moho thickness is consistent with the global average Moho depth from Christensen and Mooney (1995). The model was calculated for erosion rates from 0 to 10 km Ma^{-1}. Step two involves calculating T_c, and subsequently Z_c, for each mineral system based on the modeled geotherms. Closure temperature depends on cooling rate (Figure 4.4). Cooling rate for the modeled geotherms can be found by multiplying the change in geothermal gradient (dT/dz) by the exhumation rate. The T_c and Z_c are then extracted by solving the Dodson equation (Dodson 1973) for each mineral system, based on the calculated cooling rate variation with depth. Repeating this for many closely spaced exhumation rates allow the effective T_c and Z_c paths of each mineral system to be calculated (See Chapter 4 Appendix; colored lines on Figure 4.6).

The model results indicate that in a region exhuming at between 1 and 3 km Ma^{-1} the Z_c of U-Th/He in zircon is between 2.5 and 4.7 km (T_c range of 195 to 215°C) and the Z_c of Ar-Ar in biotite is between 5.5 and 10.4 km (T_c range of 365 to 395°C).

^{40}Ar-^{39}Ar

The U-Pb and $^{40}Ar/^{39}Ar$ dates from the Anvil suite are different (G1 and G3; Table 4.2; Figure 4.5) reflecting the exhumation of the plutonic rock from emplacement at ~12 km depth at ~107±2 Ma, through the $^{40}Ar/^{39}Ar$ T_c and Z_c at 104±2 Ma. The majority of Tay River and Tombstone suite samples (G4, G12, G27) have indistinguishable U-Pb and $^{40}Ar/^{39}Ar$ ages, indicating emplacement of the plutons at crustal levels shallower than the $^{40}Ar/^{39}Ar$ Z_c. This observation is consistent with previously established geological constraints on exhumation based

on aureole mineralogy and U-Pb dating of plutons in the Tay River district. One Tay River sample (G11) shows a difference between the measured U-Pb and $^{40}Ar/^{39}Ar$ ages. Sample G11 is from a small plug that outcrops in a thrust sheet bound by two regional Jurassic to Cretaceous thrust faults (Figure 4.2). The difference in the two ages may suggest that the timing or the magnitude of the exhumation was variable across the thrust faults. However, a broader spread of data points would be needed to confirm this relationship. An alternative explanation is that the biotite in G11 was heated during intrusion of proximal Tombstone suite rocks (G12; Figure 4.2) at 94.8±0.7 Ma causing partial or full argon loss and, therefore, the $^{40}Ar/^{39}Ar$ date of sample G11 records this event rather than initial cooling. Partial argon loss in biotite occurs at temperatures within the partial retention zone (PRZ) of the $^{40}Ar/^{39}Ar$ system (275 - 350°C for a hold time of 1 Ma; Figure 4.7), which could be achieved in the aureole of an intruding felsic pluton.

U-Th/He

The U-Th/He data are not consistent with the simple exhumation model outlined above. Geological constraints (Smith and Erdmer 1990, Pigage 2004, Gordey 2013) place the outcrops sampled in this study at crustal levels shallower than the U-Th/He Z_c during the emplacement of the (99-96 Ma) Tay River and (96-90 Ma) Tombstone suites. However, the zircons from the Tay River district commonly have U-Th/He dates from the end of the Cretaceous and early Paleogene periods. This indicates that the zircons in the study area have experienced some form of He loss significantly after initial cooling. The spread of ages indicate that resetting (due to He loss) was not complete and suggest a reheating event to temperatures within the U-Th/He system PRZ (100 - 180°C for typical hold times; Baldwin and Lister 1998, Wolf et al. 1998; Figure 4.7). The spread in U-Th/He dates between samples cannot be explained by the elevation of the samples, as the spread in outcrop elevation is minimal (range of 800 m from 980 to 1786 m.a.s.l; Table

4.1). Elevation also cannot explain the significant inter sample single grain aliquot U-Th/He date variation.

Variations in grain size and/ or radiation damage could explain the significant dispersion seen in U-Th/He dates of the Tay River district. There is no clear relationship between U-Th/He date and zircon grain effective spherical crystal radius (ESR; the radius of a sphere with an equivalent surface-to-volume ratio for each zircon grain; Farley 2002) in the collected data (Figure 4.8). Therefore, grain size is not a primary control on the U-Th/He date dispersion in the Tay River district. The primary control on U-Th/He date dispersion in the Tay River district is most likely variable radiation damage.

Guenthner et al. (2013) developed a parameterization for the effect of radiation damage on He diffusivity. These authors interpreted the amount of radiation damage to correlate to the α-dose experienced by each grain. They observed a dramatic decrease in He diffusivity with increasing radiation damage at low α-doses (less than ~2 $x10^{18}$ α/g; Guenthner et al. 2013), which corresponds to a T_c increase with α-dose (from 140 to 220°C between damage amounts of ~$1x10^{16}$ α/g and ~1 $x10^{18}$ α/g; Guenthner et al. 2014a). Above a certain degree of radiation damage (corresponding to an α-dose greater than ~2 $x10^{18}$ α/g) He diffusivity begins to increase with increasing radiation damage, leading to a decrease in T_C with increasing radiation damage above this critical value. This behavior was explained by a model that describes the tortuosity of a He particle's escape from a zircon crystal and comparison to studies on apatite (Flowers et al. 2009), which is assumed to act the same as zircon (Guenthner et al. 2013). At α-doses less than ~2 x 10^{18} α/g a decrease in diffusivity occurs with increasing α-dose - caused by increasing areas of damage, which increases the tortuosity of a He particles, diffusion from the grain (Flowers et

al. 2009). However, above α-doses of ~2 x10^{18} α/g the He diffusivity begins to increase due to the interconnection of fast diffusing damage zones (Flowers et al. 2009, Guenthner et al. 2013).

The total accumulated radiation damage can be approximated by the eU of each grain. Given the maximum age (110 Ma) and maximum eU (3200 ppm) of the zircons from the Tay River district, all samples can be modeled as having accumulated a total α-dose of less than 2x10^{18} α/g.

There is a positive correlation between U-Th/He date and eU in all the zircons from the Tay River district (Figure 4.9). A positive correlation in zircons with low radiation damage can result from a thermal pulse reaching maximum temperatures within the zircon U-Th/He PRZ (Figure 9 from Guenthner et al. 2013). The zircon grains with higher radiation damage (approximated by higher eU) have higher T_c, so they experience less He loss than grains with lower eU. Therefore, the highest eU grains yield the least disturbed (oldest) U-Th/He ages and, provide the best approximation for the initial time at which the system cooled through the zircon U-Th/He T_C and Z_c. The oldest U-Th/He date measured in the Tay River district, corrected for grain heterogeneity, is from a zircon grain from the Anvil suite, which gave a U-Th/He date of 99.2±3 Ma. This date places a minimum age constraint on the time that the Tay River district was exhumed through the zircon U-Th/He Z_c, consistent with the geological constraint that the Anvil suite was at shallow crustal levels (<1-2 km) by the time of intrusion of the Tay River suite (99-96 Ma).

Combining the geological constraints from the Anvil and Tay River suites and U-Pb ages of each plutonic suite from Chapter 2 with the $^{40}Ar/^{39}Ar$ and U-Th/He conclusions from this study allows an accurate model Tt path for mid-Cretaceous exhumation of the Tay River district to be constructed (Figure 4.10). The constructed Tt path demonstrates that exhumation rates and

magnitude are consistent with tectonic uplift coupled with erosional denudation; this is consistent with a model in which the Tay River district was experiencing extensional collapse in the mid-Cretaceous after the termination of compressional tectonics.

Modeling of U-Th/He data

The U-Th/He data indicate that the Tay River district experienced a complex thermal history, this study has identified a significant thermal event, which affected the intrusive rocks of the study area after their initial cooling and exhumation. Properties of the thermal pulse can be studied by using the ZDRAAM kinetics (zircon radiation- damage and annealing model) developed by Guenthner et al. (2013, 2014a, 2014b), which are part of the HeFty thermal modeling software program (Ketcham 2005). The ZDRAAM model combines the damage-diffusivity parameterization discussed above with a damage annealing model to calculate the date – eU correlations generated by an individual Tt path (Guenthner et al. 2013).

To study the thermal pulse that affected the Tay River district, a forward-model based approach was used, which involved inputting specific Tt paths and comparing the output to the measured Tay River district U-Th/He data, then iteratively altering the Tt paths to achieve the best fit between modeled and observed date-eU correlation. For each forward model the inputs are a Tt path, the ESR of the zircon, and the eU of each grain. The constructed forward models are based around a Tt path, which fits the geological constraints in the Tay River district. In all input Tt paths initial exhumation derived cooling of the Tay River district below the U-Th/He T_c occurs at ~100 Ma. This is then followed by thermal equilibration with the surface (20°C) at 90 Ma; then by a single thermal pulse reaching a maximum temperature T, which affected the Tay River district beginning at time t, and persisted for time Δt (Figure 4.11A). The thermal pulse is modeled as a rectangle for simplicity, and as it was found that models varying the shape of the

thermal pulse in Tt space caused only minor variations in the output date-eU correlation compared with the variations generated by varying T and Δt. The ESR of all zircons is set to 50 μm, based on the mean average of all zircons analyzed in the Tay River district (48±10 (1σ) μm; range of 37 to 82μm). To account for secondary scatter derived from grain size variation, 5 date-eU paths were generated for each Tt path, based on the mean grain ESR ± one standard deviation and using the total range of ESR measured in the Tay River district. These curves encompass the predicted date variation derived from radiation damage combined with the observed grain size variation. The grain eU was varied from 0 to 3500 ppm to cover the range displayed by Tay River zircons (250 to 3200 ppm).

Heterogeneous intergranular eU zonation derived from inherited cores - as seen in the Anvil suite zircons- is likely to cause further secondary scatter in the measured Tay River district U-Th/He ages (Hourigan et al. 2005, Guenthner et al. 2013). However, we lack the necessary observations and understanding of how radiation damage is annealed during inherited zircon assimilation to magma to quantify this scatter. In our forward models we do not consider inherited helium (Guenthner et al. 2014b, Powell et al. 2016) from the xenocrystic zircon cores of the Anvil, as assimilation of the inherited older zircon cores into the Anvil suite magma occurred at temperatures well above the U-Th/He T_C.

Forward models were generated for a range of Tt paths by varying T, t and Δt. These models showed that varying the time of pulse initiation, t, had negligible influence on the date-eU correlation (Figure 4.11D) and that the dominant factors affecting the date-eU correlation are changes in T and Δt (Figure 11B,C and E); there is a negative feedback between T and Δt. The longer a thermal pulse persists (longer Δt) the lower the pulse temperature needs to be to generate the observed date-eU correlation.

Our model provides an end-member simplest solution that ignores geological complexities. For example, samples proximal to crustal scale faults (e.g. G10) may experience an enhanced (hydro-) thermal pulse compared to samples from a dyke (e.g. G4), which may be insulated by encasement in low-porosity granite. Therefore, a range of t, T and Δt that best fit the observed data are suggested, rather than a specific individual Tt path and inverse modeling was not attempted. The best fit for the observed U-Th/He data is generated from Tt paths involving a thermal pulse originating in the Late Cretaceous to early Paleocene (t best fit range 80 to 65 Ma), lasting (Δt best fit range) 5-15 Ma and reaching a maximum temperature (T best fit range) of 150 to 170°C.

The Big Flush

The modeling carried out in ZDRAAM indicates that the intrusives in the Tay River district were thermally perturbed in the Late Cretaceous to early Paleocene. Either burial or significant intrusion of igneous rocks at this time could potentially cause this regional reheating. However, in the Tay River district neither of these scenarios seems likely. There is no Late Cretaceous magmatism documented in the Selwyn basin (Rasmussen 2013) except for the volumetrically minor 67 to 64 Ma McQuesten plutonic suite, which outcrops in the far north of the Selwyn Basin (Figure 4.12; Murphy 1997, Thiessen et al. 2016). Paleogene volcanism is recorded in the Tay River district as small-volume rounded Eocene (55-53 Ma) porphyries (Pigage 2004), however, these intrusions are emplaced after the modeled thermal pulse and are too small volume to have thermally perturbed the entire Tay River district. Burial also appears geologically improbable as 5-7 km of burial would be required to heat the Tay River district to

~150°C and there is no evidence for this amount of post mid-Cretaceous sediment deposition or the faults required to generate a basin this large (Pigage 2004, Gordey 2013).

In the Late Cretaceous a large thermal event that affected most of central and southern Yukon, was coeval with eruption of the Carmacks Group flood basalts, which were extruded across 100,000 km^2 of the southwest to central Yukon between the Tintina and Denali fault (Figure 4.12; Johnston et al. 1996, Wynne et al. 1998) between 72 to 69 Ma (Grond et al. 1984, Lowey et al. 1986, Hart 1995). Widespread resetting of K-Ar ages (Hart 1995) and remagnetization of older rocks (Wynne et al. 1998) at this time indicate that an extensive thermal/hydrothermal system was active during Carmacks Group extrusion. Wynne et al. (1998) termed this regional hydrothermal event the Big Flush. The Carmacks Group volcanics and the Big Flush have been linked to the passage of North America over the Yellowstone hotspot in the Late Cretaceous (Johnston et al. 1996). Neither the Carmacks Group volcanics or their thermal signature have been previously reported north of the Tintina fault (Rasmussen 2013). However, when Eocene movement on the Tintina fault is restored outcrops of the Carmacks group (and coeval volcanics in Alaska) are seen within <50 km of the Tay River district (Figure 4.12). Therefore, we suggest the coincidence between the known thermal event in the central Yukon and the pulse recorded by the U-Th/He data in the Tay River district are cogenetic; this would imply that the Big Flush hydrothermal system affected the Tay River district. It is possible that the Carmacks Group flood basalts could also have extended north of the Tintina fault but have subsequently been removed by erosion. However, as the thermal pulse reached only 150 to 170°C in the Tay River district it is more likely a distal lower temperature periphery of the hotspot activity. Data on the scale of hydrothermal alteration associated with continental flood basalts (CFBs) does not exist. However, global CFBs (Deccan, Karoo, Columbia River;

Rampino and Stothers 1988, Courtillot and Renne 2003) typically cover equant areas of 2000-2500 km across, and are proposed to be underlain by thermal anomalies with diameters of the same order of magnitude (White and McKenzie 1989, Campbell and Griffihs 1990). CFBs are proposed to develop at the initiation of a plume with subsequent evolution to a narrower - ~200 km wide - chain of volcanic activity as the plume declines (Campbell and Griffihs 1990, Kumagai et al. 2008). Based on the current outcrop width the Carmacks Group appears to represent the second stage of the plume's life.

Late Cretaceous resetting of chronometers by a magmatic hydrothermal event is identified by Bineli Betsi et al. (2012) within the central Dawson range, to the south of the Teslin fault (Figure 4.12), who reported a chlorite-altered dyke with zircon U-Pb age of 109 Ma, whole rock Ar-Ar age of 76 Ma and zircon U-Th/He ages ranging from 89 to 66 Ma. Late Cretaceous Zircon U-Th/He single grain ages (78 to 72 Ma) are also reported in the Mount Adami Pluton, in the McQuesten Area, to the southwest of the Tintina Fault (Knight et al. 2013; Figure 4.12). A resetting event was not identified in this study, due to averaging dispersed U-Th/He dates from individual aliquots into a single mean date for each sample (i.e a Monzogranite sample 09RAYJR175A, which showed a spread in 5 single grain Zircon U-Th/He dates from 140 to 78 Ma and was assigned a mean age of 113 Ma). However, a Late Cretaceous thermal pulse fits the observed data.

Therefore, the passage of the Yellowstone hotspot proximal to the Tay River district in the Late Cretaceous fits with the observed thermal perturbation observed in the ZDRAAM modeling. As Carmacks Group volcanics are not observed in the Tay River district we suggest the thermal pulse was linked to the Big Flush hydrothermal system created by the hotspot at this time.

Conclusions

Low temperature thermochronology on the mid-Cretaceous rocks of the Tay River district, in the Selwyn Basin, constrain a period of exhumation. The Anvil suite was exhumed rapidly from the emplacement site at 12-15 km depth between 109-104 Ma, through the Ar-Ar closure depth (5.5-10.4 km) at 104±2 Ma and above the zircon U-Th/He closure depth (2.5-4.7 km) before 99.2±3 Ma. This is consistent with previously established geological constraints based on aureole mineralogy and U-Pb dating of plutons in the Tay River district (Pigage and Anderson 1985, Smith and Erdmer 1990 and see Chapter 2). The magnitude and rate of exhumation is consistent with the extensional collapse of previously thickened crust in the mid-Cretaceous, implying that the Sevier-Columbia orogeny had terminated and the core of the northern Cordillera was beginning to collapse by the Late Mesozoic.

However, the zircon U-Th/He systematics are complicated by a partial resetting due to a loss of He after initial cooling in the Late Cretaceous to early Paleogene. Modeling based on the ZDRAAM kinetics (Guenthner et al. 2013) allows us to conclude that partial resetting of the U-Th/He dates is due to a thermal pulse with a maximum temperature of 150-170°C that affected the Tay River region for 5-15 Ma in the Late Cretaceous to Paleocene. This modeled thermal pulse fits with the proposed passage of the northern Cordillera across the Yellowstone hotspot in the Late Cretaceous, which led to the extrusion of the Carmacks Group flood basalts across the southwest-central Yukon between 72-69 Ma. Significant regional resetting of thermally sensitive systems has been attributed to a big flush generated by the Yellowstone hotspot. This study represents the most inboard recognition of the big flush and, therefore, has implications for the distribution of hotspot derived thermal/hydrothermal alteration.

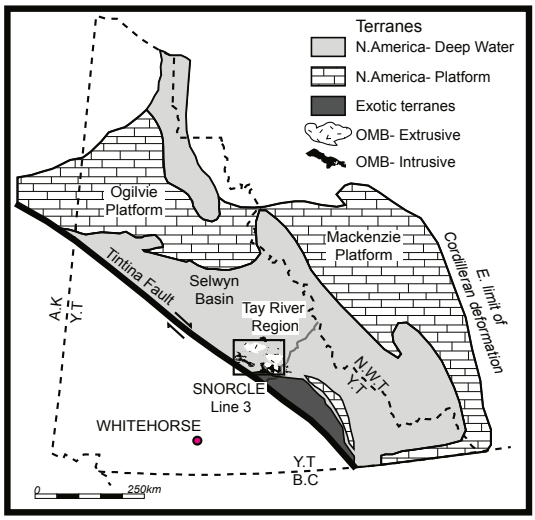

Figure 4.1: Simplified geological map of the Yukon showing modern terrane geology north of the Tintina fault based on Nelson et al. (2013) . Tay River district identified by the black rectangle. Extent of OMB igneous rocks within the Tay River district from Gordey (2013). SNORCLE line 3 shown north of the Tintina fault from (Cook and Erdmer 2005).

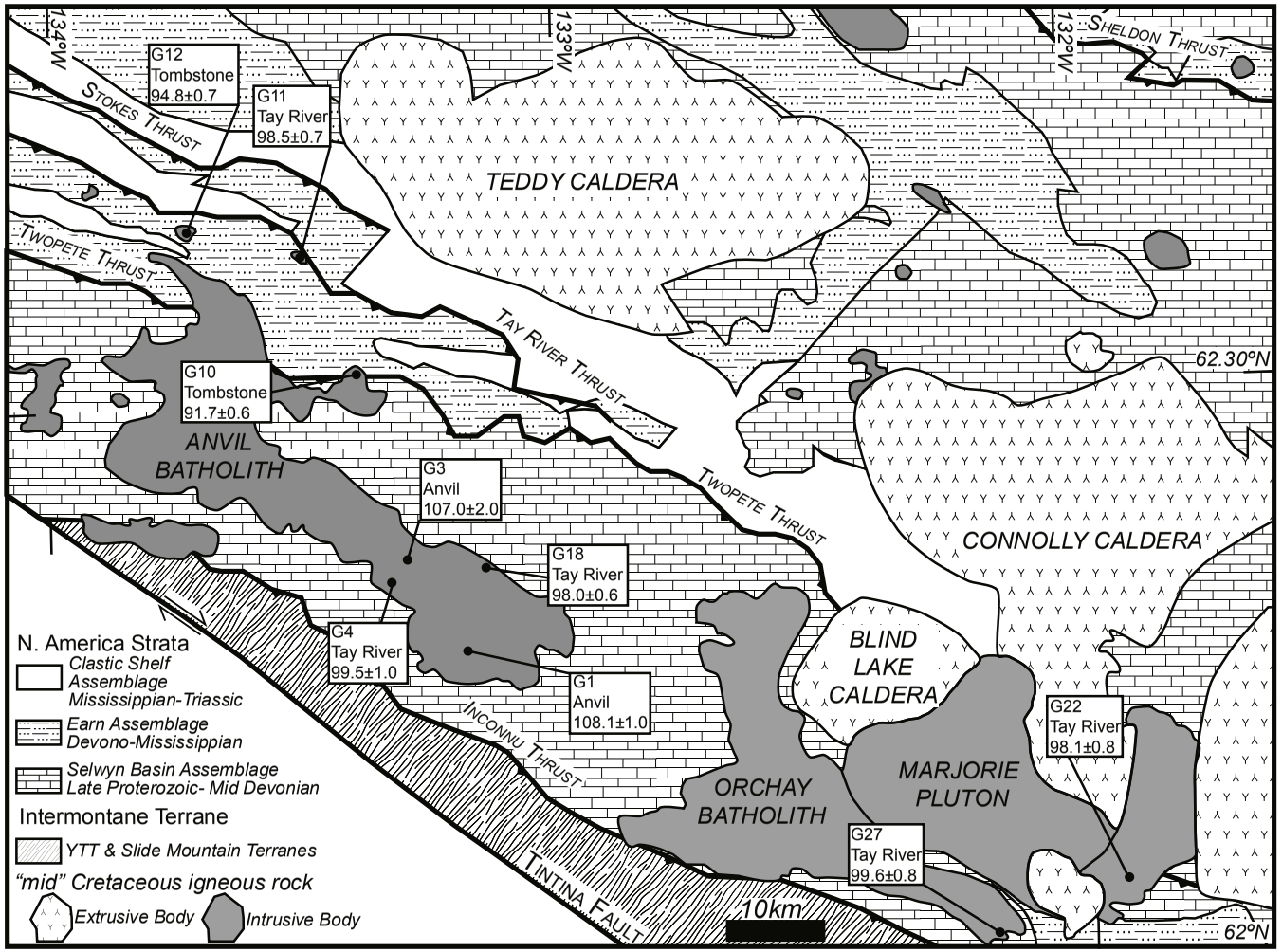

Figure 4.2: Simplified geological map of the Tay River district adapted from Yukon Geological Survey (2017), Gordey (2013) and Cobbett (2015) and Chapter 2. Samples referenced in this study identified by black dots labeled with: sample I.D, plutonic suite and U-Pb age from Chapter 2. Major thrust faults formed during the Sevier-Columbia orogeny and major OMB igneous bodies are labeled.

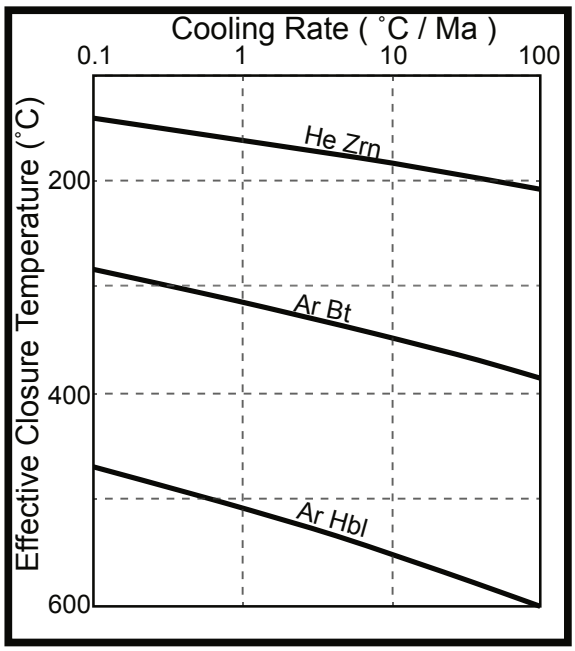

Figure 4.3: Effective closure temperature (T_C) as a function of cooling rate for the thermochronometers applied in this study. Calculated lines are from the CLOSURE program (Brandon et al. 1998, Ehlers 2005, Reiners and Brandon 2006). Effective spherical radius of zircons is 60 μm and cylindrical radius of biotite and hornblende is 500 μm.

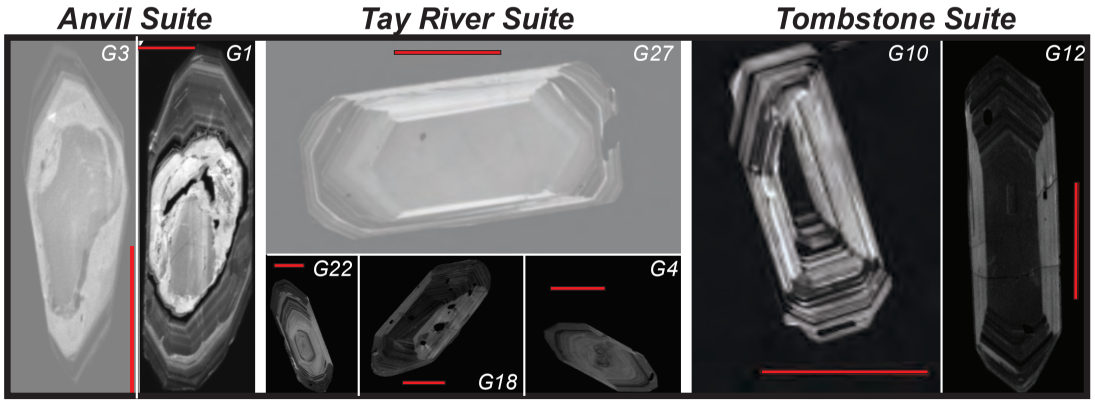

Figure 4.4: CL images of representative zircons from each sample, subdivided by plutonic suite.

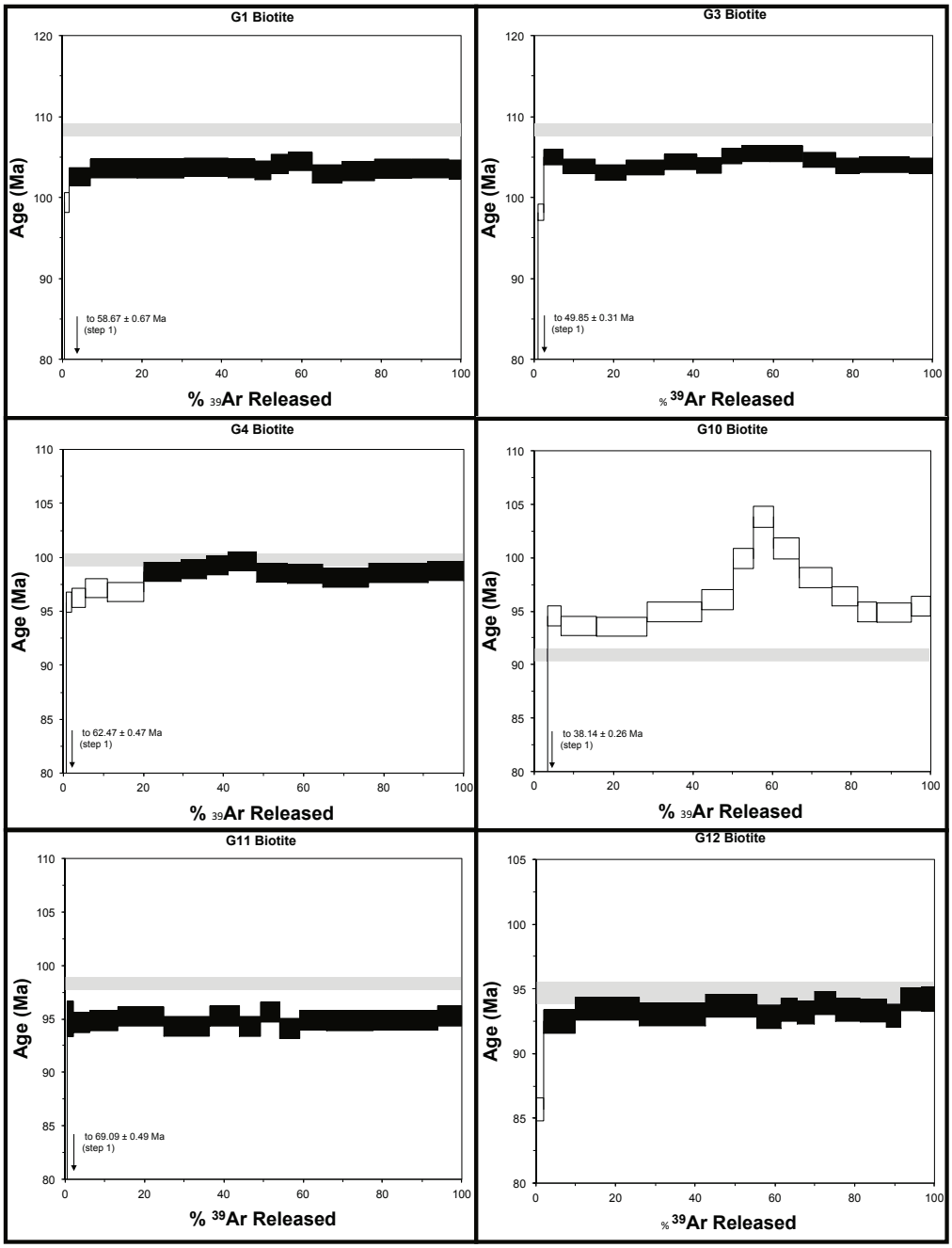
G1 Biotite
Age (Ma)
% 39Ar Released
to 58.67 ± 0.67 Ma
(step 1)
G3 Biotite
Age (Ma)
% 39Ar Released
to 49.85 ± 0.31 Ma
(step 1)
G4 Biotite
Age (Ma)
% 39Ar Released
to 62.47 ± 0.47 Ma
(step 1)
G10 Biotite
Age (Ma)
% 39Ar Released
to 38.14 ± 0.26 Ma
(step 1)
G11 Biotite
Age (Ma)
% 39Ar Released
to 69.09 ± 0.49 Ma
(step 1)
G12 Biotite
Age (Ma)
% 39Ar Released

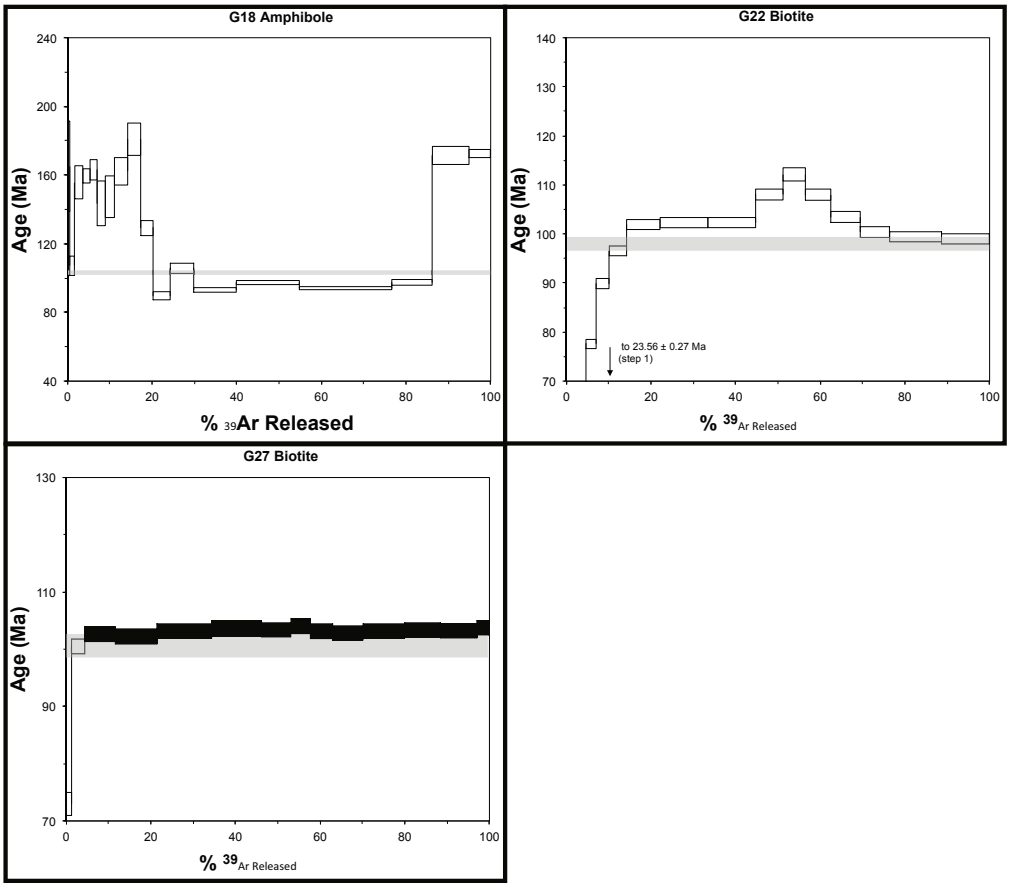

Figure 4.5 (2 pages from previous): $^{40}Ar/^{39}Ar$ age spectra for samples from the Tay River district with one sigma error. Pseudo - plateau steps are shown in black. U-Pb date with one sigma error from Chapter 2 shown by the grey rectangle.

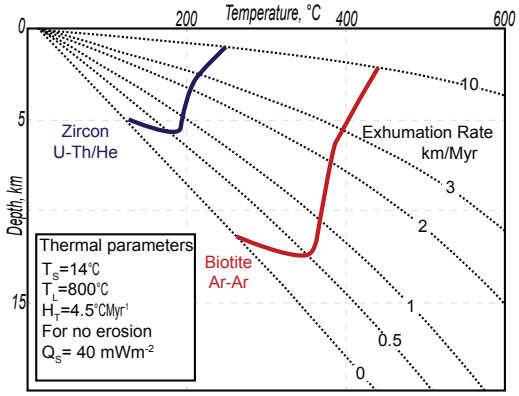

Figure 4.6: Thermal profiles derived from a steady- state solution for a one dimensional 40 km thick layer undergoing a constant exhumation rate, modeled by a fixed steady vertical velocity through the layer. Thermal parameters are shown on the figure generalized from a typical convergent orogen (Reiners and Brandon 2006). Colored lines show the continuous closure temperature paths of the thermochronometers in this study, based on the variable erosion rates modeled and solved to yield effective closure depths at each erosion rate.

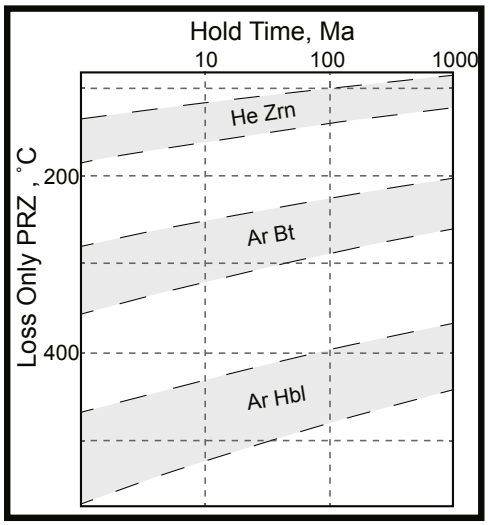

Figure 4.7: Loss-only partial retention zones (PRZ) for the thermochronometers used in this study calculated using the CLOSURE program. The PRZ is defined by the steady-state temperatures associated with 10% and 90% retention for a specified hold time (Brandon et al. 1998, Ehlers 2005, Reiners and Brandon 2006).

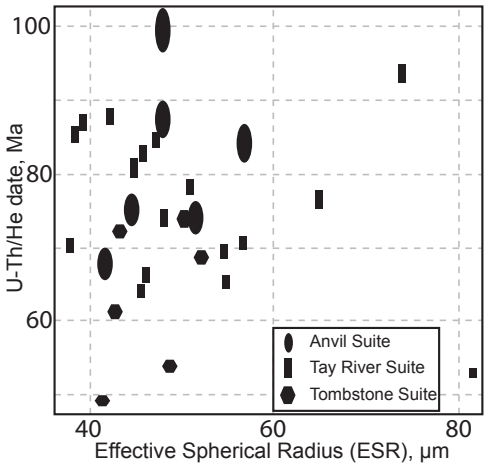

Figure 4.8: U-Th/He date - effective spherical radius (ESR) plot for zircons analyzed in the Tay River district. U-Th/He dates from Anvil suite are corrected for heterogenous eU. Vertical extents of the point reflects 1σ error in the U-Th/He date.

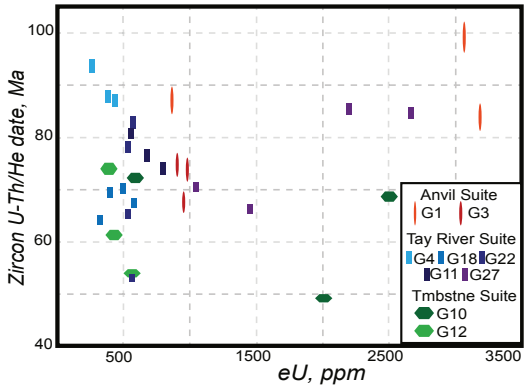

Figure 4.9: U-Th/He date- eU plot for zircons from OMB plutons in the Tay River district. U-Th/He dates from Anvil suite are corrected for heterogenous eU. Vertical extent of points indicates the 1σ error of the U-Th/He date.

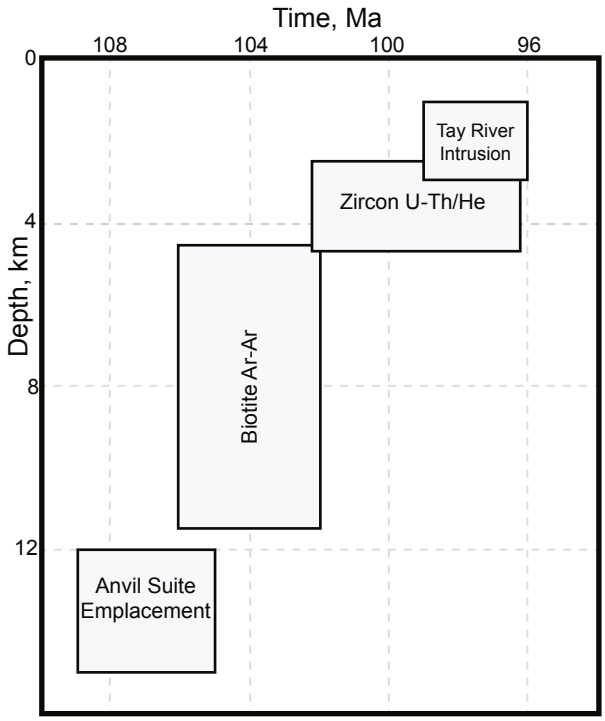

Figure 4.10: Depth versus time graph showing constraints on the exhumation of the Anvil suite preceding shallow crustal intrusion of the Tay River suite. Boxes represent range of possible depths and one-standard deviation errors in age.

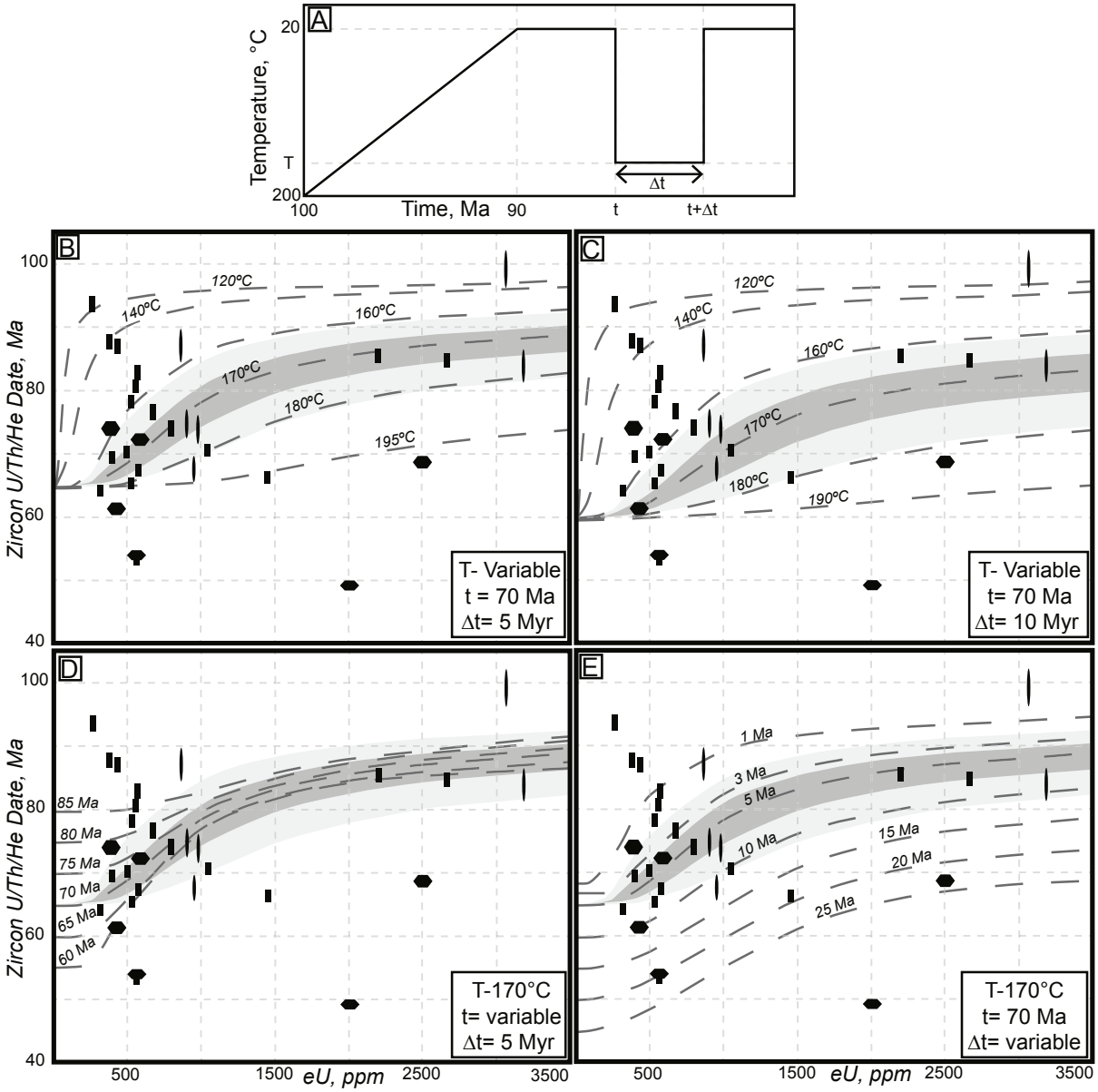

Figure 4.11: A- Variable Tt path showing initial cooling upon exhumation, followed by a thermal pulse of temperature T, duration Δt and initial onset at t. Thermal pulse is assumed to have instantaneous heating and cooling (rectangular shape) as shape of pulse was shown to have little effect on outputs.

B-E- ZDRAAM forward results (Guenthner et al. 2013) modeled in HeFty (Ketcham 2005) based on varying the Tt path in A. Black data points are from Figure 10 divided based on suite: Ellipses- Anvil, Rectangle- Tay River and Hexagon-Tombstone. The fixed and variable parameters are labeled for each plot. Grain size is set at 50 μm. Envelopes show the effect of varying grain size on the 170°C maximum temperature model that initiates at 70 Ma and has a hold time of 5 Myr (B,D,E) or 10 Myr (C). The dark grey envelope represents the same model at ±10 μm while the light grey envelope represents dispersion due to grain sizes varying from 30 to 80 μm.

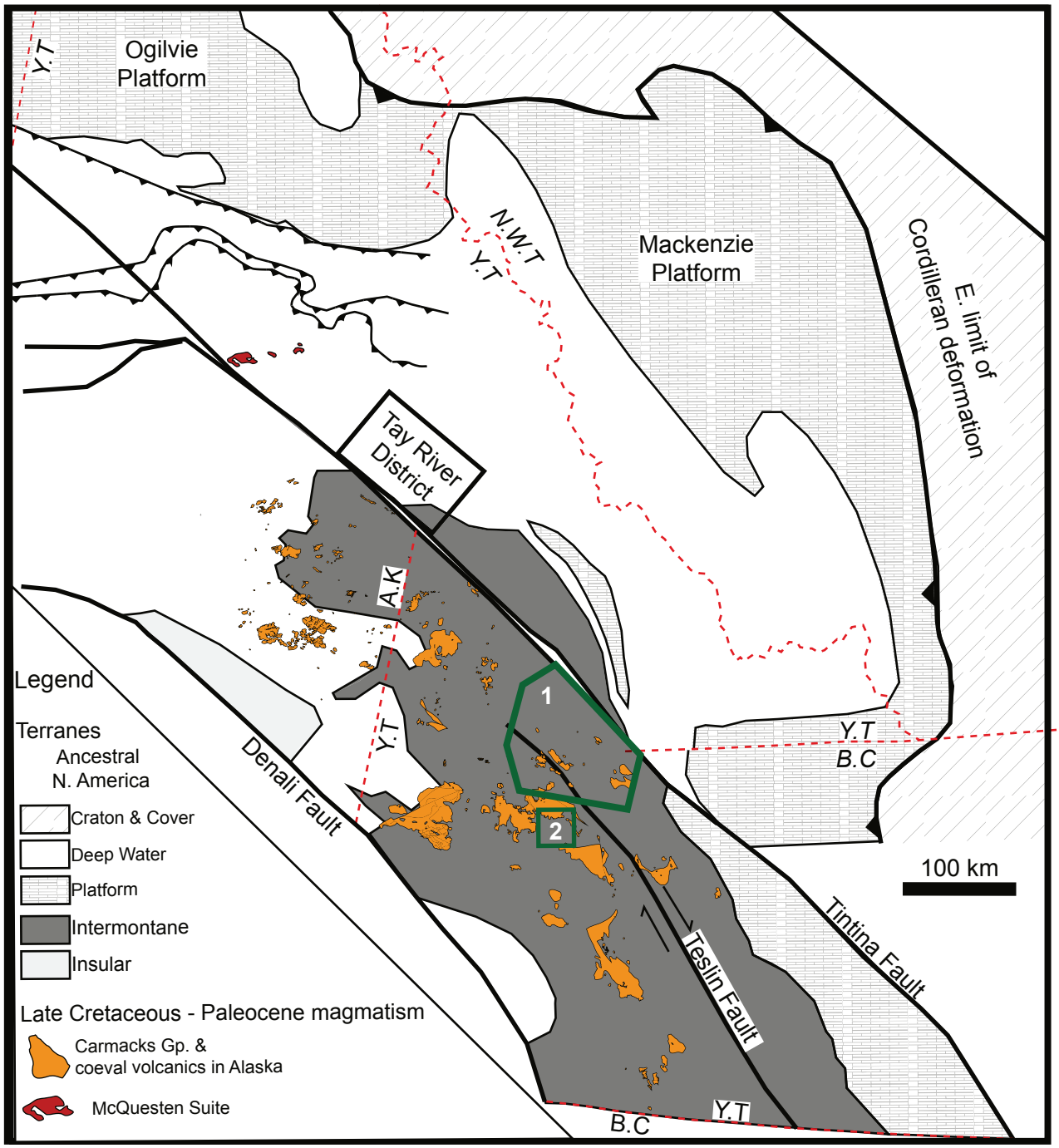

Figure 4.12: Distribution of Late Cretaceous and Paleocene magmatism relevant to this study overlain onto a schematic representation of major tectonic elements with restoration of 430km of dextral movement on the Tintina fault (adapted from Figure 2.12) McQuesten and Carmacks Group distribution within the Yukon from Yukon Geological Survey (2017). Distribution of Late Cretaceous-Paleocene volcanics within Alaska from Alaska Geological Survey. Green shapes show extents of previous U-Th/He studies. 1: Knight et al. 2013 and 2: Bineli Betsi et al. 2012.

Table 4.1. Brief geological description and location information for samples from Chapter 2

Sample I.D	Plutonic Suite	UTM E	UTM N	UTM Zone	Elevation (m)	Igneous Body	Rock Type	Biotite Pleochroic colours
G1	***Anvil***	593582	6909787	8	1556	Anvil Batholith	Ms-Bt phanerocrystalline granite	Light red-brown/ tan-yellow
G3		587557	6918824	8	1511	Anvil Batholith	Ms-Bt phanerocrystalline granite + Afs megacrysts	
G4	***Tay***	586071	6916583	8	1495	Anvil Batholith	Hbl-Bt porphyritic granodiorite	Dark chocolate brown/ pale yellow
G11		576538	6948979	8	1786	Minor Plug	Hbl-Bt phanerocrystalline granodiorite	
G18		595522	6918027	8	1614	Anvil Batholith	Hbl porphyritic diorite	
G22		348143	6890689	9	980	Marjorie Pluton	Hbl-Bt phanerocrystalline granodiorite	
G27		646969	6881669	8	1051	Orchay Batholith	Bt phanerocrystaline granite	
G10	***Tombstone***	584712	6934088	8	1200	Anvil Batholith	Bt phanerocrystaline granite	Black-Brown/ Dark Straw-Yellow
G12		565363	6951516	8	1663	Minor Plug	Bt phanerocrystaline granodiorite	

Table 4.2. Results of the Ar-Ar and U-Th/He work compared to U-Pb ages

Sample		U-Pb (Zrn)*		Ar-Ar (Bt or Hbl)			U-Th/He (Zrn)							
							Grain 1		Grain 2		Grain 3		Grain 4	
I.D	Plutonic Suite	Age (Ma)	±1σ (Ma)	Mineral	Date (Ma)	±1SD (Ma)	Corrected Date (Ma)	±1σ (Ma)	Corrected Date (Ma)	±1σ (Ma)	Corrected Date (Ma)	±1σ (Ma)	Corrected Date (Ma)	±1σ (Ma)
G1	***Anvil***	108.1	0.5	Bt	103.5	2.1	78.8	1.2	81.8	1.3	93.2	1.4	--	--
G3	***Anvil***	107	1	Bt	104.3	2.1	70.1	1.1	63.5	1.0	69.3	1.1	--	--
G4	***Tay***	99.5	0.5	Bt	98.8	1.7	93.8	1.3	87.8	1.1	87.0	1.2	--	--
G10	***Tmbst***	91.7	0.3	Bt	--	--	72.2	1.0	68.7	1.0	49.2	0.8	--	--
G11	***Tay***	98.5	0.4	Bt	94.9	1.8	76.6	1.2	74.0	1.2	80.9	1.3	--	--
G12	***Tmbst***	94.8	0.4	Bt	93.4	1.8	74.0	1.2	53.9	0.9	61.3	1.0	--	--
G18	***Tay***	98.0	0.3	Hbl	--	--	67.4	1.0	64.1	0.9	70.3	1.0	69.5	1.0
G22	***Tay***	98.1	0.4	Bt	--	--	53.0	0.7	82.8	1.2	78.2	1.1	65.4	0.9
G27	***Tay***	99.6	0.4	Bt	103	2.2	85.5	1.1	70.7	1.0	84.7	1.1	66.3	1.0

*From Chapter 2

Table 4.3. Anvil suite grain uncorrected and corrected U-Th/He dates

Sample		***Assuming Homogenous eU***		***Assuming Heterogenous eU***	
I.D	**Grain Number**	***Date (Ma)***	**±1σ (Ma)**	***Date (Ma)***	**±1σ (Ma)**
G1	***1***	78.8	1.2	83.9	2.6
	2	81.8	1.3	87.1	2.6
	3	93.2	1.4	99.2	3.0
G3	***1***	70.1	1.1	74.7	2.3
	2	63.5	1.0	67.6	2.1
	3	69.3	1.1	73.8	2.3

Chapter 5: The Keglovic Deposit: A telescoped Ag-Pb-Zn skarn and vein deposit, Central Yukon, Canada.

Introduction

The polymetallic Keglovic advanced exploration project located in central Yukon, Canada (Figure 5.1), has an inferred mineral resource of 39.8 million tonnes of 30.25 g/t Ag - with contained metal estimates of 38.7 million ounces of Ag, 675 million lbs of Zn, 228 million lbs of Pb, and 131 million lbs of Cu (Dumala 2013). Preliminary mineralogical work on the deposit also reported unusually high concentrations of In, Sn and Cd (Brand 2011). The Keglovic deposit is the largest of at least 22 mineralized occurrences that form two northwest trending, parallel arrays on the 1100 km^2 Keg property (Eaton 2011; Figure 5.1 and 5.2A). The northern Tay trend, which hosts the Keglovic deposit, contains a linear array of mineralized zones hosted by metasedimentary rocks, which trend sub-parallel to the major regional thrust faults. The southern trend is termed the Mount Mye trend and consists of a number of epithermal and epigenetic veins, mineralized breccias and endo-skarns, hosted almost entirely within plutonic rocks (Mortensen and Ballantyne 1992, Eaton 2011, Dumala 2013). The Hammer showing, the largest known mineralization in the Mount Mye trend, was recently studied in detail by Rogers (2017). The Keglovic deposit is by a substantial margin the largest known mineralized showing in either trend and has been the focus of an advanced exploration program, which included 69 drill holes (from 2010 to 2013) and the calculation of the inferred mineral resource given above. The Keglovic deposit is split into two domains (Main and East). The large ore body identified at Keglovic Main has not been identified at Keglovic East.

Silver-Pb-Zn mineralization in the Selwyn Basin has previously been mined at the Anvil Range SEDEX deposits (10 to 45 km south of the Keg property; Shanks and Woodruff 1987) and in the Keno Hill silver district (Boyle et al. 1970, Lynch 1989, Beaudoin and Sangster 1992). The Keglovic deposit shares some characteristics with these mineral deposit types, however, the Keglovic mineralization is sufficiently different and as a result previous authors have reported it to be unique within Yukon (Brand 2011, Eaton 2011, Dumala 2013). Preliminary geological and petrographic studies have suggested the Keglovic deposit mineralization occurs both as lenticular skarns, confined to carbonate-rich horizons and in veins in the host units (Brand 2011), and that this mineralization formed from multiple mineralizing events (Brand 2011, Dumala 2013). This study was undertaken to test these hypotheses. Petrography was used to establish the presence of the multiple mineralization events that are superimposed to form the Keglovic deposit. Once the events have been defined, the fluid chemistry, temperature of formation, mineralogy, and relative age of each will be characterized. This allows us to describe the evolution of the mineralization and fluid chemistry at the deposit through time, and to produce a genetic deposit model for the Keglovic mineralization. This study also aims to date the mineralization at the Keglovic deposit and to try to identify why significant mineralization has not been found at Keglovic East.

Regional Geology and Tectonic Setting of the Keg property

The Keg property is hosted by Paleozoic to early Mesozoic sedimentary units imbricated during the Jurassic-Cretaceous Columbia-Sevier orogeny (Hildebrand 2009, Gordey 2013; Figure 5.2B). The sedimentary rocks belong to three broad assemblages: the Selwyn Basin, Earn, and Clastic Shelf (Figure 5.3; Gordey 2013). The Precambrian to Middle Devonian deep water sedimentary rocks that comprise the Selwyn Basin assemblage were deposited onto the western passive-margin of North America (Gordey and Anderson 1993). Rifting in the Devono-

Mississippian caused an abrupt change in depositional regime and the deposition of the Earn assemblage within fault bounded basins (Gordey and Irwin 1987, Gordey 2013). Rocks of the Earn assemblage consist of coarse-clastic strata and turbiditic sediments (Campbell 1967). The Earn assemblage rocks were succeeded by Mississippian to Triassic sediment deposition on a shallow-marine shelf, forming the Clastic Shelf assemblage. The Clastic Shelf assemblage comprises three Formations: the Mississippian Tay (MT); the Carboniferous to Permian Mount Christie (CPMC); and the Triassic Jones Lake. These three formations consist of marl-rich siliciclastics interbedded with limestone, cherts and shales.

Sediment deposition on the Clastic Shelf terminated in the early to mid-Mesozoic due to northwest directed compression (Colpron et al. 2007), the convergence of exotic allochthons with North America (Mair et al. 2006) and the subsequent formation of a fold and thrust belt within the regional strata (Ross et al. 2005, Nelson et al. 2013). The imbrication of sedimentary rocks currently observed in the study area formed during this orogeny along a number of transcrustal thrust faults (Cobbett 2015), which led to significant crustal thickening at this time (Pavlis 1989, Staples et al. 2016).

Middle Cretaceous uplift and extension have been documented within the Selwyn Basin, Yukon-Tanana and Alaska (Pavlis et al. 1993, Hudson 1994, Staples et al. 2013, 2016, Chapter 4) associated with post-orogenic collapse of the previously thickened crust. Extensive plutonism and volcanism occur within the Omineca Magmatic Belt (OMB) synchronous with this tectonic collapse (Chapter 2). The OMB igneous activity occurs inboard of the continental margin (Coastal Plutonic Belt arc complex) in the parauthochthonous and autochthonous North American margin strata between ~118-89 Ma (Hart et al. 2004, Rasmussen 2013). The formation mechanism and tectonic setting for OMB plutonism and volcanism is disputed. Current theories

include OMB development due to delamination of over thickened lithosphere (as proposed in Chapter 2) or due to a flat slab, back arc extension or a cryptic western dipping subduction zone (Mortensen et al. 2000, Mair et al. 2006, Johnston 2008, Rasmussen 2013).

Following the Sevier-Columbia orogeny, Late Cretaceous to Eocene regional dextral strike slip motion initiated on the Tintina Fault, which currently displays ~430km of offset (Gabrielse et al. 2006).

Local Geology and Field Relationships at the Keglovic Deposit

The large ore body identified at Keglovic Main has not been identified at Keglovic East. As such this study will focus on the mineralization at the Keglovic Main deposit (KMD), which consists of stratified, massive, skarn beds, ranging from 10 cm to >1 m thick, surrounded and cross-cut by stockworks of vein/fracture fills, mineralized breccias and disseminated sulphides (Brand 2011).

Previous studies of the Keglovic deposit have suggested that the mineralization may have a magmatic-hydrothermal origin and that a large plutonic body may underlie the KMD (Brand 2011, Dumala 2013). However, no evidence for any such plutonic body has been identified in either drill core or via Airborne Z-Tipper Axis Electromagnetic and Magnetic Surveys conducted over the Keg property (Dumala 2013). The closest outcrops of intrusive rock to the KMD are ~4 km to the southwest (Figure 5.2B) and belong to the Anvil Batholith, an OMB pluton emplaced between ~109 – 90 Ma, which consists of three distinct plutonic suites as summarized in Chapter 2. These suites are the 109 – 104 Ma Anvil, 99 – 96 Ma Tay River and 96 – 90 Ma Tombstone. In Yukon, the Anvil and Tay River suites are generally thought to lack significant mineralization while the Tombstone suite is associated with a number of intrusion-related gold deposits (Goldfarb et al. 2000, Mortensen et al. 2000, Hart et al. 2004, Rasmussen 2013). The

emplacement of the Anvil Batholith created a >5 km metamorphic halo of dominantly greenschist facies conditions with minor amphibolite grade zones proximal to the intrusion (Pigage and Anderson 1985, Smith and Erdmer 1990, Pigage 2004). The KMD is also 10 km south of the 38 km diameter Teddy Caldera (99 – 96 Ma; Figure 5.2B), which is genetically related to the intrusive Tay River suite (Gordey 1988). Minor 69-65 Ma rhyolite plugs exist on the Keg property (Gordey 2013) but they are volumetrically insignificant in comparison to the mid-Cretaceous plutons and calderas. Based on the overall volume of OMB plutons surrounding the KMD and association of mineralization with Jurassic-Cretaceous thrust faults it is believed that the KMD mineralization formed in the mid-Cretaceous (Brand 2011); however, no dating of the mineralization has previously been attempted.

The region around the KMD experienced significant exhumation during the mid-Cretaceous, as demonstrated by Chapter 4, which outlines a low temperature thermochronology study that constrained a period of ~10 km vertical exhumation to between ~105 and ~100 Ma at a rate of between 1 and 3 km Ma^{-1}. To accurately understand the mineralization at the KMD the affect of this exhumation on the style of mineralization needs to be considered.

Methods

Field Mapping and Drill Core logging

Deposit-scale mapping and sampling of the Keglovic deposit (1:5000 scale) was conducted in the summers of 2013 and 2015. Twenty-five drill holes were re-logged and sampled, including two approximately perpendicular drill hole transects (Figure 5.4 A).

Petrography and mineralogy

Over 750 hand specimens and 125 thin sections from the Keglovic deposit were analyzed using thin section petrography, bench-top cathodoluminescence (CL) and X-ray Diffraction (performed on an Rigaku Powder X-Ray diffractometer at the University of Alberta) in order to constrain a paragenesis for mineralization.

Electron microprobe analyses (EPMA; with the Jeol 8900 at the University of Alberta) allowed for accurate mineral identification and characterization based on relative elemental abundance using electron dispersive spectrometry (EDS). Wavelength dispersive spectrometry (WDS) was also performed to identify the major and minor chemistry of the silicate minerals (garnet and diopside) and sulphide minerals within the KMD. For the WDS the EPMA beam was operated at an accelerating voltage of 20 kV, a probe current of 20 nA, and a beam diameter of 1μm. The concentrations of specific elements were calibrated for the sulphides using in house standards: galena for Pb and S; silver metal for Ag; indium arsenide for In; gallium arsenide for As; antimony metal for Sb; sphalerite for Zn; copper metal for Cu; cadmium selenide for Cd and Se; tin metal for Sn; bismuth telluride for Bi and Te; and iron metal for Fe. For the quantitative analysis of the silicate minerals, the in house standards used were: rutile for Ti; chromium (III) oxide for Cr; diopside or grossular for the Si; grossular for the Al and Ca; diopside for the Mg; sanidine for K; albite for Na; fayalite for Fe; and rhondite for Mn.

The trace and REE element chemistry of the sphalerite from all styles of mineralization observed at the KMD was analyzed via Laser Ablation ICP-MS at the Arctic Resources Laboratory, University of Alberta using a RESOlution M-50 193nm excimer laser system connected to a sector-field ICP-MS Thermo Element XR2. Calibration, accuracy and precision were calculated using the NIST SRM 612 and 610 standards. Sphalerite analyses followed

methods outlined in Cook et al. (2009). Zinc and iron concentrations measured independently on the EPMA were used for internal standardization. USGS BCR 2G was measured as a secondary reference standard. All data were reduced offline using Iolite v3 (Paton et al. 2010, 2011). Analytical accuracy based on comparison of the secondary standards with known reference values is typically 5-20% or better, at the 95% confidence level.

Isotopes: C, O, S and Pb

Carbon and oxygen stable isotopic analyses on carbonates (22 calcite separates) and sulphur stable isotopic analysis on sulphides (22 separates) were both performed at the Isotope Science Lab, Department of Physics and Astronomy, University of Calgary. For the C and O isotopes, standards NBS- 18 and 19 and IAEA CO- 1,8 and 9 were analyzed. Precision and accuracy for both $\delta^{13}C$ and $\delta^{18}O$ values are reported as 0.2 ‰ (1σ). Sulphur isotope analyses followed methods adapted from Giesemann et al. (1994). Lab standards IAEA S 1,2 and 3 were analysed. The precision and accuracy of the $\delta^{34}S$ values are within 0.3 ‰ (1σ).

Pb isotopic analyses were performed on 11 galena separates at the Canadian Center for Isotopic Microanalysis at the University of Alberta. Galena crystals were dissolved in HCl and HNO_3 and the Pb isotope composition was measured on a Nu Plasma Multi-collector ICP-MS in static analyses mode. Instrumental bias was corrected with the $^{203}Tl/^{205}Tl$ spike (Belshaw et al. 1998). The lab standard was NIST SRM981, which has shown 6 month absolute values of ^{206}Pb / $^{204}Pb = 16.9373 \pm 0.0027$, ^{207}Pb / $^{204}Pb = 15.4901 \pm 0.0022$, ^{208}Pb / $^{204}Pb = 36.6921 \pm 0.0061$ (accepted values from Todt et al. 1996: ^{206}Pb / $^{204}Pb = 16.9356$; ^{207}Pb / $^{204}Pb = 15.4891$; ^{208}Pb / $^{204}Pb = 36.7005$). Reproducibility of Pb isotopes for the SRM981 standard is better than 0.02%. The standard deviations of the measured Pb isotope values are reported in Table 5.5a. Lead isotopes from unaltered whole rock samples of sedimentary rocks surrounding the Keglovic

deposit were analyzed at Bureau Veritas Mineral laboratories, Vancouver Canada via ICP-MS analysis of a sample after modified Aqua Regia digestion. Precision of the whole-rock lead isotopes is low with typical standard deviations in the $^{207}Pb/^{204}Pb$ and $^{206}Pb/^{204}Pb$ values of 0.6.

Re-Os dating

Precise Re-Os dating on an arsenopyrite separate from the KMD was attempted at the crustal Re-Os Geochronology Laboratory, University of Alberta following the procedures outlined in Morelli et al. (2010). The one point obtained did not allow for the calculation of an isochron age. However, a model age was constructed by assuming an initial $^{187}Os/^{188}Os$ ratio, which can range from 0.12 for the mantle to 1.0 for the upper crust (Luck and Allègre 1991). The model age was calculated using the full range of initial Os values.

Microthermometry

Fluid inclusion microthermometry was performed on a Linkam THMSG600 heating/freezing stage (with a working range of -200 to +600°C) mounted on an Olympus BX50 microscope. Calibration was performed before and after analyses using SynFlinc synthetic fluid inclusions. Accuracy below 0°C was ±0.2°C and, above 0°C accuracy was ±2°C.

Whole Rock Analysis

Thirty-nine samples, representing the relevant lithologies, alteration styles, and mineralization styles were analyzed by Bureau Veritas Mineral laboratories, Vancouver, Canada for major and minor element chemistry (Aqua Regia 250 Extended Package and the Liquid Fusion 200 package). Major and selected trace elements were analyzed by X-ray Fluorescence spectroscopy. Trace elements, including REE, were analyzed by ICP-MS following an aqua regia digestion. As well as the procedures employed by Bureau Veritas, two internal reference

materials, a blank and a duplicate sample, were analyzed for quality assurance. The known standards (OREAs 131a and 134a from the Ore Research and Exploration PTY LTD and Green River Shale SGR-1 from the USGS) returned values within the accepted limits of published values for all reported elements. The crush split duplicate showed reproducibility of better than 10% for all elements above the practical lower detection limit.

The whole rock analyses conducted in this study were supplemented by the extensive drill core assays (7950 3m intervals) provided by Archer, Cathro and Associates Ltd. which include measured concentrations of Ag, As, Au, Cu, Fe, In, Mo, Pb, Sb, Sn and Zn. These drill core samples were analyzed at the ALS minerals laboratories, Vancouver, Canada. All elements, except Au, were analyzed by ICP-MS following an aqua regia digestion (package ME-MS41). Au was analyzed using Fire Assay ICP-MS (package Au-ICP21;Eaton 2011, Dumala 2013).

3D Distribution of the Mineralization

Three-dimensional modeling of the distribution of mineralization at the KMD was carried out in Leapfrog Geo using the interpolation model included in the software. The geological model was created from drill core logging of fault zones and changes in lithology. The extensive drill core assays allowed 3D modeling of the distribution of Ag, As, Au, Cu, Fe, In, Mo, Pb, Sb, Sn and Zn concentrations.

Results

Field Mapping and Drill Core logging

Host Rock

Lithological logging of the KMD drill holes (Figure 5.4) and 1:5000 scale mapping (Figure 5.2A) - conducted as part of this study- identified units of the Earn and Clastic Shelf

assemblages (Figure 5.3). Locally the Earn Group consists of foliated, non-calcareous, variably graphite and organic-rich, black siltstones and minor cherts, interbedded with chert-rich mudstones and massive siltstone beds. Rare turbiditic sediments including graded arkosic, sandstone beds and chert-pebble conglomerates are also present.

The Earn Group is overlain by black to dark-grey coloured, variably organic-rich silty-limestone, and carbonaceous siltstone of the MT. Interbeds of organic-rich black siltstone occur on cm to m scales. Evidence of bioturbation, including burrows, and soft sediment deposition, including flame structures, convolute bedding and sole markings are commonly observed within beds of the MT. Fine-grained pyrite occurs as euhedral cubes within the MT (Figure 5.5A); framboidal pyrite was not observed. Bedding varies from 10 cm to ~2 m. The CPMC unconformably overlies the MT and consists of bedded cherts with characteristic maroon and lime-green colours. No carbonate is associated with this unit. Laminated black siltstones occur in the chert units bedded on cm to m scales. Laminations within the siltstone are typically planar and occur on sub mm scales, although, regions with lenticular laminations and cross-stratification are found throughout the CPMC.

The youngest strata in the region, from the Triassic Jones Lake Formation, are lithologically identical to the MT and can only be distinguished by stratigraphic position relative to the CPMC cherts. Regionally all of the sedimentary units have experienced greenschist facies alteration (Pigage 2004, Gordey 2013).

Relogging of drill holes on two approximately perpendicular transects shows that the mineralization at the KMD is hosted predominantly within the carbonate-bearing rocks of the MT, with minor mineralization in the chert bearing-lithologies of the CPMC. No ore mineralization is observed within the Earn Group rocks although calcite-quartz-pyrite filled

fractures do occur. The fractures within the Earn Group do not intersect the main mineralization at the KMD. Therefore the relative age of these fractures, or whether they are the same age as the KMD ore, could not be confirmed. The lithological logs also indicate that the Earn, CPMC and MT units have been imbricated along three thrust faults (Figure 5.4B-C). The top and bottom thrust faults (Fault-1 and -3 on Figure 5.4 B-C) have been mapped at the surface during this study and by Gordey (2013) and Cobbett (2015). The middle fault (Fault-2 on Figure 5,4 B-C) does not break the surface and is interpreted from the drill core logs. However the surface-trace of this fault has previously been inferred by the presence of a syncline-anticline pair within the CPMC (fault propagation fold) with fold axis sub-parallel to the surface thrust fault exposures (Cobbett 2015; Figure 5.2A). The vergence of all three faults was inferred from the orientation of the syncline-anticline pair associated with Fault-2. The vergence of the faults at the Keglovic deposit is consistent with regional thrust fault vergence (Gabrielse et al. 2006). This middle fault (Fault-2) is associated with nearly all the logged stratified sulphides (Figure 5.4). Mineralization is bounded by the upper and lower thrust faults (Figure 5.4).

Keglovic Calc-Silicate (KCS)

The KMD mineralization is associated with the extensive decalcification of the MT, which converts silty-limestone beds into calc-silicate and carbonate-silicate beds, via silication and silicification (Figure 5.5B-C). The alteration can be observed in surface outcrops in an area of 5 km by 1.5 km area (Figure 5.2B) and at depths from 100 to >400 m in drill cores (stratigraphic orientation unknown). The KCS typically occurs as a blue-grey to white-pink rock. Sedimentary structures can be preserved in the less altered beds but in the areas of most significant alteration, the beds and lithologies have been totally recrystallized. The KCS is very

fine-grained with a sucrosic texture created by micro- to crypto-crystalline silicification. It was observed in the field that the carbonate content of the KCS decreases with increasing alteration (based on reaction of the rock with HCl). However, complete decalcification is rarely observed; even the most pervasively altered limestone beds showing minor reaction with HCl resulting in a carbonate-silicate rock (Rosen et al. 2007). When visible, the contact with the unaltered rock is gradational across 1-3 m. A transect across a gradational metasomatic front between KCS and MT was sampled (Transect 1). Transect one involves 10 samples from drill hole 11-12 ranging from 357-387m depth with a visible contact between the two lithologies occurring at 369 m. The contact appears sharp in hand specimen, although bands of visually unaltered MT (.i.e sample 11-12 357) appear within the KCS indicating the gradational - non-complete - nature of the metasomatic replacement. Transect one displays a gradual decrease in silica, increase in carbonate and darkening of the hand specimen colour towards the visibly unaltered MT.

Wollastonite bands occur within the KCS. These bands form linear topographic highs ~2.5 m tall and 3-4 m wide, which trend ~north to south (range 330 to 030) and can be mapped for up to 200 m. The rock within these bands appears to be >95% wollastonite with <5% by volume quartz and K-feldspar. The CPMC is less altered than the MT, but displays bleaching around fractures.

Petrography and Paragenesis

Keglovic Mineralization

Based on the detailed hand specimen and thin section descriptions conducted in this study, the mineralization at the KMD can be split into four mineralogically and texturally distinct paragenetic stages, defined by clear crosscutting relationships or the replacement and alteration of earlier phases (Figure 5.6).

Stage 1: The first mineralization event in the paragenetic sequence involves the pervasive replacement of the carbonate-silicate beds within the host-rock KCS by an assemblage of diopside-1, garnet-1, quartz-1, K-feldspar-1, pyrrhotite-1, galena-1, chalcopyrite-1 and arsenopyrite-1. This mineral assemblage dominantly replaces the carbonate-rich beds in stratabound bodies or is found in rare, discrete 1-3 cm veins that crosscut the silt-rich beds in the KCS. Sulphides dominate this assemblage with ubiquitous, subhedral to anhedral, galena-1 and pyrrhotite-1 occurring in massive intergrowths commonly associated with chalcopyrite-1 and arsenopyrite-1 (Figure 5.5D). Arsenopyrite-1 typically occurs as 300 to 500 μm in diameter, euhedral, grains that display angular crystal boundaries when in contact with galena-1 and pyrrhotite-1 (Figure 5.5D); therefore these phases are interpreted to be in textural equilibrium and are considered to be coeval in the paragenetic sequence. All silicates are typically euhedral (Figure 5.5E-F) with representative grain diameters of 0.5-1 mm. Galena-1, pyrrhotite-1 and chalcopyrite-1 form an oikocryst around the euhedral arsenopyrite-1 and silicates; suggesting that these sulphides crystallized later in this mineral assemblage (Figure 5.5E). The veins associated with this stage are curvi-linear features with planar walls. Euhedral diopside-1, quartz-1 and garnet-1 grains nucleate on the wall rock and grow into the centre of the vein with a comb texture (Figure 5.5G). Stage 1 sulphides are not seen within the veins. The centres of the veins are filled with minerals from the later paragenetic stages (see below).

There appears to be a spatial zoning within the replacement Stage 1 mineralization; samples containing garnet-1 and diopside-1 contain more chalcopyrite-1 than samples with only diopside-1. Rare stage-1 samples have only galena-1, pyrrhotite-1 and quartz with no calc-silicate minerals or chalcopyrite-1. The zoning appears linked to regions of fault breccia development, with garnet-1 and chalcopyrite-1 occurring in samples proximal to certain faulted

regions, although the complexity of the structures in a single drill core does not allow for conclusive assessment of the spatial zoning to be made.

EPMA analyses on calc-silicate minerals in the replacement beds and veins identified garnet-1 as having a grandite composition (range of grossular$_{70\text{-}87mol\%}$, andradite$_{13\text{-}30mol\%}$) and suggest diopside-1 has an average composition of 59% diopside, 36% hedenbergite and 5% johannsenite (ranges of Di$_{42\text{-}77mol\%}$, Hd$_{20\text{-}53mol\%}$, Jo$_{1\text{-}8mol\%}$). Galena-1 hosts the silver in this stage (0 to 1.22wt%; although the lower values occur in grains retrograded by later mineral assemblages) and also has high Se (up to 3.2 wt%) and Bi (up to 2.92 wt%) concentrations. The Ag and Bi concentrations of galena-1 are positively correlated (Table 5.1) suggesting a coupled substitution mechanism. Pyrrhotite-1 and arsenopyrite-1 have end-member compositions with negligible trace element concentrations. Chalcopyrite-1 also has a near end-member composition but EPMA analyses show up to 0.3wt% Sn and 0.16 wt% Ag, likely due to microscopic intergrowths within the chalcopyrite crystals.

Overall, this stage is associated with Ag and Pb in galena-1, As in arsenopyrite-1, Cu and Fe in chalcopyrite-1 and Fe in pyrrhotite-1.

Stage 2: a). sulphide formation event b). sulphide retrograding event: Stage 2a consists of a mineral assemblage of quartz-2, calcite-1, diopside-2, sphalerite-1, chalcopyrite-2, stannite-1 and pyrite-1. Stage 2a overgrows and rims the Stage 1 mineral assemblage, as well as infilling the centre of veins lined with the Stage 1 mineral assemblage (Figure 5.5G). The mineralization is characterized by anhedral sphalerite-1, which co-precipitates ubiquitously with chalcopyrite-2 and commonly with stannite-1 (Figure 5.5H). When sphalerite-1 is in contact with arsenopyrite-1 the arsenopyrite does not display a euhedral-angular crystal form (Figure 5.5D) indicating

textural disequilibrium; this is interpreted as suggesting that sphalerite-1 belongs to a later paragenetic stage than arsenopyrite-1. Diopside-2 occurs as <50 μm grains pervasively overgrowing Stage 1 sulphides and silicates. EPMA analyses identified the range of pyroxene compositions as being identical to diopside-1. Radial aggregates of diopside-2 grains are seen in the surrounding wall-rock up to 50 cm beyond the sulphide mineralization. Calcite-1 crosscuts and fractures garnet-1 and diopside-1 but appears in textural equilibrium with sphalerite-1 (Figure 5.5G). Stage 1 and 2a combine to form beds of near complete massive-sulphide replacement (and sparser vein infills).

EPMA measurement on sphalerite-1, indicate that this sulphide contains significant Fe (10.8 to 12.8 wt%), minor Mn (up to 0.62 wt%) and minor Cd (up to 1.06 wt%; Table 5.2a). The trace element chemistry of sphalerite-1 was also analyzed via LA-ICP-MS (Table 5.2b), which indicated that sphalerite-1 contains a trace amount of In (200 ppm average). Chalcopyrite-2 and stannite-1 associated with this mineral assemblage appear to have end-member compositions from the EPMA analyses. Overall Stage 2a is associated with Zn, Fe and minor In in sphalerite-1, minor Cu and Fe in chalcopyrite-2 and Sn and Fe in stannite-1.

Stannite-sphalerite geothermometry based on Fe-Zn cation exchange was performed on pairs of sphalerite-1 and stannite-1 grains that appeared to display textural equilibrium (Table A20; Shimizu and Shikazono 1985, Bortnikov et al. 1990, Scott and Barnes 1971). Multiple Fe and Zn concentrations from pairs of intergrown minerals were measured on the EPMA. The average concentration data from each stannite-sphalerite pair was used to calculate a partition coefficient and then a temperature of mineral deposition based on the equations in Shimizu and Shikazono (1985). This method gave an average temperature for sphalerite-1 and stannite-1 deposition of 300±25 °C.

Stage 2b consists of quartz-3, apatite and numerous hydrous silicates including clinochlore, epidote, clinozoisite, tremolite, talc and hornblende. This mineral assemblage destructively overprints the sulphides deposited in Stage 1 and 2a (Figure 5.5J). Tremolite, talc, hornblende and clinozoisite occur as up to 5mm acicular needles overprinting sphalerite-2 (Figure 5.5J). Clinochlore, epidote and apatite form fine-grained mats intergrown with anhedral quartz rimming and overgrowing the margins of sulphides from Stage 1 and 2a.

Stage 2b is not associated with significant new sulphide deposition, but records the alteration of previously deposited sulphides and redistribution of some elements. For example, galena-1, in contact with Stage 2b minerals, has exsolved bismuth inclusions (Figure 5.5K) and a complex assemblage of exsolved sulfosalts. The exsolved sulfosalts, identified by EPMA, include many Ag-bearing phases such as freibergite-1, stephanite, pyrargyrite and cervellite (Figure 5.5L). EPMA work on the galena-1 suggests that this exsolution leads to a decrease in the silver content of galena-1. During this stage pyrite-1 is also observed overprinting pyrrhotite-1.

Overall Stage 2b does not introduce any new metals to the Keglovic deposit but leads to the redistribution of Ag from the galena lattice to As, Sb and Sn bearing sulfosalts.

Stage 3a to 3c: Stage 3 occurs in discrete 2-25 cm fracture- and void-fills and mm-scale breccias, which crosscut the KCS and rarely intersect the mineralization generated in Stage 1 to 2b. The fractures are most numerous in the non-carbonate bearing, calc-silicate beds of the KCS.

Stage 3a consists of a mineral assemblage of calcite-2, quartz-4, pyrrhotite-2, chalcopyrite-3 and pyrite-2. Stage 3a is characterized by acicular calcite-2 infilling breccias and voids (Figure 5.7A-C). Rare iron sulphides occur at the margins of the carbonate filled fractures

(Figure 5.7C) indicating deposition prior to calcite-2. Pyrrhotite-2, pyrite-2 and chalcopyrite-3 all have end-member compositions and contain negligible trace elements on the EPMA.

This stage does not contribute significantly to the metal budget at the Keglovic deposit.

Stage 3b consists of a mineral assemblage of quartz-4, calcite-3, galena-2, pyrite-3, arsenopyrite-2, stibnite-1, freibergite-2 and hocartite. Stage 3b is dominated by euhedral quartz-4 grains, with minor euhedral arsenopyrite-2 and subhedral to anhedral galena-2 and pyrite-3, which are deposited within planar, discrete, fractures (Figure 7 D-E). Stibnite-1 is associated with arsenopyrite-2 in large fractures (Figure 5.7F). Stibnite-1 and arsenopyrite-2 display angular grain boundaries in contact with quartz-4 and galena-2, which are inferred to be in textural equilibrium and, therefore, coeval in this paragenetic stage. Freibergite-2 grains occur on the contact between galena-2 and other sulphides in this stage. Calcite-3 is minor, occurring on grain boundaries and is therefore interpreted to crystallize late in this stage. Galena-2 has the same chemistry as galena-1 with high Se concentrations (up to 1.25 wt %; Table 5.1) and variable Ag (up to 1.15 wt%) and Bi (up to 2.68 wt%) content. However, galena-2 appears to crystallize in equilibrium with silver bearing fahlore minerals in Stage 3b, which is not observed in Stage 1. Arsenopyrite-2, pyrite-3 and stibnite-1 have end-member compositions. Freibergite-2 is typically a silver-rich tetrahedrite containing 28 wt% Sb and 22 to 30 wt% Ag but no measurable As.

Overall, Stage 3b is associated with Ag and Pb in galena-2, As in arsenopyrite-2, Sb in stibnite-1, and Ag and Sb in the freibergite-2.

Stage 3c consists of sphalerite-2, chalcopyrite-4, cubanite-1 and stannite-2. This mineral assemblage is observed as intergrowths of the sulphides, infilling the final primary spaces in the fractures (Figure 5.7G-I). Minor calcite-3 and quartz-4 occur associated with the sulphides.

Sphalerite-2 contains similar Fe concentrations (6.8 to 11.4 wt%) but typically lower concentrations of Mn (0.18 to 0.48 wt%) and Cd (0.53 to 0.78wt%) than sphalerite-1 (Table 5.2a). The In concentration of sphalerite-2 measured by LA-ICP-MS is ~3 times lower than recorded in sphalerite-1 (70 ppm average compared to 200 ppm average; Table 5.2b). Cubanite-1 and stannite-2 contain near pure compositions. Chalcopyrite-4 contains up to 0.2 wt% Sn and up to 0.3 wt% Ag likely as microscopic inclusions.

Stannite-sphalerite geothermometry conducted on pairs of intergrown sphalerite-2 and stannite-2 displaying equilibrium textures (via the same method outline in Stage 2) gives an average temperature of 280±10°C for the deposition of these mineral pairs. (Table A20).

Overall Stage 3c is associated with Zn and Fe in sphalerite-2, Cu and Fe in cubanite and chalcopyrite, and Sn, Cu and Fe in stannite-2.

Stage 4 consists of quartz-5, calcite-4 and zeolite. This mineral assemblage occurs in late undulose <1 cm fractures which cross-cut all previous mineralization (Figure 5.7J -L). Within the fractures, mineral grains are typically <0.5 mm and euhedral, suggesting this stage infills late voids. No sulphide deposition was observed. However, where fractures intersect sulphides, pyrite-4 replaces pyrrhotite-1 and 2. Iron oxide staining of silicates is also associated with these late-stage fractures.

Isotopes: C, O, S and Pb

Carbon, oxygen, sulphur and lead isotopes were measured on mineral separates from each of the paragenetic stages to track the evolution of the mineralizing fluid, metal source and deposition mechanism(s) with time. Carbon and oxygen isotope data from the visibly unaltered

carbonates of the MT and separates of calcite-1, 2, 3 and 4 are displayed in Table 5.3 and Figure 5.8. The MT samples have the highest $\delta^{18}O_{SMOW}$ and $\delta^{13}C_{PDB}$ values recorded in the study; ranging from 13.8 to 21.0 ‰ and -0.5 to -2.4 ‰ respectively. $\delta^{18}O_{SMOW}$ and $\delta^{13}C_{PDB}$ values for the calcite-1 separates range from 9 to 13.6 ‰ and -4.3 to -7.3 ‰ respectively. $\delta^{18}O_{SMOW}$ and $\delta^{13}C_{PDB}$ values for the calcite-3 and 4 separates are similar to calcite-1, with the $\delta^{18}O_{SMOW}$ and $\delta^{13}C_{PDB}$ values of calcite-3 ranging from 13.1 to 14.2 ‰ and -4.7 to -6.3 ‰ and calcite-4 ranging from 12.9 to 13.6 ‰ and -5.6 to -7.1 ‰ respectively. Calcite-2 has different $\delta^{18}O_{SMOW}$ and $\delta^{13}C_{PDB}$ values than the other three calcite phases, with values ranging from 1.7 to 7.9 ‰ and -2.6 to -6.1 ‰ respectively

Sulphur isotope data is presented in Table 5.4 and Figure 5.9. Galena-1 was separated from Stage 1 mineralization. Sphalerite-1 was separated from Stage 2 mineralization. Pyrite-2, pyrrhotite-2, chalcopyrite-3, pyrite-3, galena-2, arsenopyrite-2 and sphalerite-2 were separated from Stage 3 mineralization. Stage 1 and 2 minerals have $\delta^{34}S_{CDT}$ values ranging from -1.0 to 0.1 ‰ and 0.4 to 5.1 ‰ respectively. Sulphide separates from Stage 3 returned $\delta^{34}S_{CDT}$ values ranging from -2.8 to 9.8 ‰.

The Pb isotope results are shown in Table 5.5a and 5.5b and Figure 5.10. Lead isotopes were measured on galena-1 and galena-2 from Stage 1 and Stage 3 mineralization respectively. Galena-1 has $^{208}Pb/^{204}Pb$ ranging from 39.179 to 39.196, $^{207}Pb/^{204}Pb$ ranging from 15.699 to 15.703 and $^{206}Pb/^{204}Pb$ ranging from 19.273 to 19.281. Galena-2 has average $^{208}Pb/^{204}Pb$ ranging from 39.129 to 39.197, $^{207}Pb/^{204}Pb$ ranging from 15.694 to 15.706 and $^{206}Pb/^{204}Pb$ ranging from 19.255 to 19.278. Present day lead isotopes from unaltered samples of the Earn Group, CPMC and MT are indistinguishable and have average $^{208}Pb/^{204}Pb$ ~41, $^{207}Pb/^{204}Pb$ ~16 and $^{206}Pb/^{204}Pb$ ~ 20 (Table 5b). The precision associated with these measurements is low (typical one standard

deviation error in $^{207}Pb/^{204}Pb$ and $^{206}Pb/^{204}Pb$ of 0.6) and is not sufficient to distinguish between the different units.

Re-Os dating

Arsenopyrite-2 from Stage 3b was successfully dated using the Re-Os technique. Results are shown in Table 5.6. An isochron could not be constructed for arsenopyrite-2 as only one Re-Os analyses was successful. Therefore, a model age was calculated by varying the $[^{187}Os/^{188}Os]_i$ from 0.12 (upper mantle value) to 1.0 (crustal value), which encompasses the entire possible variation in initial osmium natural reservoir values (Luck and Allègre 1991). This method returned a model age of 100±2 Ma for arsenopyrite-2.

Microthermometry

Microthermometric analyses were performed on fluid inclusion assemblages (FIAs) in quartz-1, garnet-1, quartz-2 and quartz-4. Fluid inclusions were categorized based on their room temperature phase assemblages and also their timing relative to the mineral growth. Inclusions were classified as primary (P), pseudo-secondary (PS) or secondary (S; Roedder 1984). Inclusions that displayed very irregular shapes or appeared necked were not analyzed due to potential post-entrapment modification. FIA data are presented in Tables 5.7 and 5.8 and Figure 5.11, and are discussed in the following section based on paragenetic stage.

Stage 1: Rare primary fluid inclusions are observed within euhedral garnet-1 and quartz-1. The grandite garnets show growth zones in pleochroic light, allowing primary fluid inclusions to be easily identified. For quartz-1, no discernible growth zones could be seen and inclusions were

assigned as primary on the basis of their isolation, random orientation (i.e. not forming linear arrays), size and negative crystal shape. Primary inclusions typically occur as 15 to 30 μm isolated inclusions in quartz-1 and garnet-1 (Figure 5.12A-C).

Primary FIAs from quartz-1 and garnet-1 had identical microthermometric properties and will, therefore, be discussed together in this section. Primary FIAs from both minerals contained two-phase aqueous inclusions (~70% liquid water and ~30% vapour by volume at room temperature). No evidence for CO_2 was detected in any of these primary inclusions.

First melting temperatures (T_{melt}) from Stage 1 primary FIAs had a range from -20 to -41°C suggesting the dominant solute is NaCl, but some inclusions also contain $MgCl_2$ and/or $CaCl_2$ (Davis et al. 1990). The final ice melting temperature (T_{ice}) for these inclusions ranged from -3.5 to -1.8°C. These T_{ice} measurements can be used to calculate salinities (wt% $NaCl_{Equiv}$) using the equation of Bodnar (1993). Calculated salinities for Stage 1 primary FIAs in garnet-1 and quartz-1 are low, averaging 4.0±0.9 wt% $NaCl_{Equiv}$ (1SD; range 3.1 to 5.7 wt% $NaCl_{Equiv}$). Homogenization temperatures (T_H) for Stage 1 FIAs average 347±17°C (1SD; range 318 to 364°C).

Trails of tiny (typically 1-5 μm) secondary inclusions (~95% liquid water and ~5% vapour by volume at room temperature; Figure 5.12C) crosscut the quartz grains; due to the size of these secondary inclusions, no data could be collected. Rare, larger, FIAs in secondary trails have similar average salinities (4.3 wt% $Nacl_{equiv}$) to the primary inclusions but have a significantly lower average T_H (165 °C).

Stage 2: Stage 2 FIAs occur within quartz-2 associated with sphalerite-1. Primary fluid inclusions are typically isolated and occur in the center of quartz grains (Figure 5.12D-E). Rare

growth zones with high fluid inclusion densities are also observed (Figure 5.12F). Primary FIAs in quartz-2 contained two-phase aqueous inclusions (~90% liquid water and ~10% vapour by volume at room temperature). No evidence for CO_2 was detected in any fluid inclusion hosted in quartz-2.

All primary FIAs from quartz-2 displayed T_{melt} values of ~21°C indicating that the Stage 2 inclusions can be modeled as an H_2O-NaCl fluid. These inclusions had T_{ice} values ranging from -3.0 to -2.4°C and have an average salinity of 4.3±0.3 wt% $NaCl_{Equiv}$ (1SD; Range 4.0 to 4.9 wt% $NaCl_{Equiv}$). Homogenization temperatures for the Stage 2 primary FIAs range from 251 to 292°C.

Secondary inclusions (~95% liquid water and ~5% vapour by volume at room temperature) are common in quartz-2 crystals occurring as trails crosscutting the grain. Microthermometric measurements identify two populations of secondary inclusions; one with a lower average salinity (~2wt% $NaCl_{Equiv}$) and a higher average T_H (255°C), and a second with higher salinity (ranging from ~3-5wt% $NaCl_{Equiv}$) and lower T_H (ranging from 100-150°C).

Stage 3: Primary FIAs in Stage 3 occur predominantly within quartz-4 as high-density regions of randomly orientated inclusions within growth zones, although very rare isolated primary inclusions may be observed (Figure 5.12G-L). At room temperature, FIAs containing liquid water + vapour; liquid water + carbonic liquid; and liquid water + carbonic liquid + solid halite are all observed within quartz-4 within the same growth zones.

Upon freezing liquid water + carbonic acid inclusions, solid CO_2 was formed. This phase melted within error of -56.6°C, consistent with near pure CO_2, although minor depression (to -57.6°C) may indicate the presence of N_2 or CH_4 (Jacobs and Kerrick 1981). The primary liquid

water + carbonic liquid inclusions have T_{ice} values ranging from -6.6 to -1.5°C (which are typically lower then the T_{ice} expected for a pure CO_2-H_2O system; Brown and Lamb 1989, Diamond 2001, Hedenquist and Henley 1985, Wilkinson 2001).

Clathrate melting (Tm_{Clath}) and carbonic liquid homogenization (Tm_{Car}) were measured in some primary FIAs from quartz-4, although it was extremely difficult to observe in most cases. Clathrate melting temperature was accurately measured in 12 of 16 carbonic liquid bearing FIAs. Carbonic liquid homogenization was also accurately measured in 12 of 16 carbonic liquid bearing FIAs. Clathrate melting temperatures range from 7.2 to 11.9°C. The salinity of the H_2O-CO_2-NaCl bearing inclusions was calculated from Tm_{clath} data using the equation of Diamond (1992) to give salinities of less than 5wt% $NaCl_{equiv}$ based on the least ambiguous observations. Some clathrate melting temperatures are above +10°C indicating the presence of another gas as well as CO_2 in the inclusion (Brown and Lamb 1989, Diamond 1992, Bakker 1997). Homogenization of the carbonic phase (Tm_{car}) occurs at temperatures as low as +13°C (range 13 to 24°C) indicating the presence of CH_4 within these FIAs (Hollister and Burruss 1976).

Upon further heating these carbonic liquid bearing primary FIAs commonly decrepitated (at a temperature T_D) before total homogenization occurred. When total homogenization (T_H) was observed around 50% of the carbonic liquid bearing primary FIAs displayed total homogenization to a gas phase, making it difficult to observe the true homogenization temperature. Consequently, a large spread in T_H and T_D from 195 to 350°C is reported.

Primary liquid-rich inclusions containing liquid water + water vapour are observed in the same FIAs with the vapour-rich aqueo-carbonic liquid bearing inclusions. No evidence for CO_2 was detected in these inclusions, however, its presence in trace amount cannot be ruled out. These inclusions have T_{melt} ranging from -42 to -21.1°C suggesting the aqueous fluid contains

NaCl as the major solute with some divalent cations (Mg^{2+}or Ca^{2+}). Final ice melting temperatures from these aqueous inclusions range from -6.1 to -1.4°C indicating salinities ranging from 2.4 to 9.3 wt% $NaCl_{equiv}$ based on the calculation of Bodnar (1993), although the presence of any CO_2 would cause these salinity values to be an overestimate (Hedenquist and Henley 1985). These primary aqueous inclusions display total homogenization (T_H) to a liquid phase at temperatures ranging from 162-337°C.

Far less abundant inclusions containing carbonic liquid + liquid water + solid halite were rarely observed in FIAs with carbonic liquid + liquid water and liquid water + water vapour inclusions. In these halite bearing inclusions first melting of the solid CO_2 was within error of -56.6°C with final ice melting occurring at an average value of -24.5±0.2°C.

Homogenization of the non-solid phases within the halite bearing inclusions occurred at temperatures ranging from 233 to 255°C. Halite was still present at this temperature. Decrepitation of the inclusion occurred before halite dissolution in every case, so the salinity of these inclusions could not be obtained.

Secondary trails of typically <5μm inclusions are observed crosscutting growth zones within quartz-4. The small size of these inclusions did not permit microthermometric measurements to be made. Rare, larger, secondary inclusions contain aqueous water + water vapour and have T_{melt} ranging from -42 to -21.1°C, T_{ice} ranging from -3.6 to -1.4°C and total homogenization temperatures ranging from 158 to 161°C.

Whole Rock Analysis

Bulk rock analysis results are split into major-oxide elements (Table 5.9) and minor and trace elements (Table A21). Elements that returned values below the limit of quantification (three times the limit of detection) for all samples were removed from the results. Two transects

across fronts of alteration were sampled. Transect one (see Host Rock section) spans a gradational metasomatic contact between MT and KCS. At the contact SiO_2, Al_2O_3 and Fe_2O_3 decrease from the KCS to MT (from: ~70 to ~35 wt%; ~8 to ~3 wt%; and ~3 to ~1 wt% respectively), while organic carbon content and CaO concentrations increase (from: ~0 to ~6wt %; and ~9 to ~30 wt% respectively). The second transect involves 4 samples from 20 cm of drill core from hole 11-12 at a depth of 234 m. Transect two spans a sharp contact between the KCS and skarn mineralization. Sample 234-a and -b are from the skarn, while sample 234-c and –d are from the proximal KCS. SiO_2 values (average 65 wt%) are consistent with typical KCS values throughout transect-2 indicating KCS alteration occurred before skarn mineralization. CaO decreases into the skarn (from ~12 to ~6 wt%) while most metallic (Cu, Sn, Pb, Zn. Ag) elements and total S increase into the mineralized zone. Indium, Cd, Se and Bi are all more concentrated within the skarn mineralization compared to the KCS (from: ~0 to ~50 ppm; ~12 to ~750 ppm; ~5 to ~ 65 ppm; and ~5 to ~130 ppm).

3D Deposit Analysis

The distribution of "anomalously high" element concentrations (Ag, Pb, Zn, Sn and Sb) at the KMD is shown in Figure 5.13 relative to the large scale thrust faults logged in the region. Anomalously high is defined as representing the top 6-10 % of concentrations from the 7950 drill core assays available. The solid- coloured regions on Figure 5.13 represent regions where these high assay concentrations are inferred to occur based on interpolation of the drill core assay data generated using the interpolation software built into Leapfrog Geo. For the interpolation models the boundary was set to enclose the 3D space covered by the drill core assays. Drill hole collars are regularly spaced in a grid across the KMD so inter hole compositing was not necessary. The data was processed using down-hole compositing on a length of 10 m and

minimum coverage of 30%. These values were chosen to ensure that any 3 m assay interval containing mineralization was not excluded from the interpolant. The fine scale of compositing is necessary due to the fine-scale of the mineralization hosted within cm- scale veins and m- scale beds. The resulting interpolants (Figure 5.13) show that high concentration of Ag, Pb, Zn and Sn are controlled by the large fault in the region (Fault-2). In comparison high Sb grades occur at a single depth- horizon.

Discussion

Characteristics of the host-rocks

Logging of the drill hole transects at the Keglovic deposit (Figure 5.4) illustrates that mineralization is hosted dominantly within the MT with minor mineralization in the CPMC, and that both formations have been altered prior to mineralization. The very different chemical and rheological properties of the two sedimentary units present at the KMD have played a primary role on the distribution and style of mineralization observed.

Half of the carbon and oxygen isotopic data obtained from visually unaltered carbonaceous MT, yield $\delta^{13}C_{PDB}$ and $\delta^{18}O_{SMOW}$ values consistent with typical Mississippian marine carbonates (expected range $\delta^{13}C_{PDB}$ 0 to +2 ‰, $\delta^{18}O_{SMOW}$ +20 to +23 ‰; Veizer et al. 1999; Figure 5.8). However, in the whole data set from the host-rocks there is a trend in carbon and oxygen isotope values to more negative compositions (Figure 5.8). This suggests that some samples have been affected by post-depositional alteration of the primary MT by an unidentified source rich in ^{12}C and ^{16}O. The isotopically altered samples are indistinguishable in hand-specimen and thin section from the unaltered samples. The isotopic alteration is unlikely to be diagenetic due to the systematic correlation between the $\delta^{13}C$ and $\delta^{18}O$ values, which suggest

equilibration with another fluid reservoir. The altered MT values have $\delta^{13}C$ and $\delta^{18}O$ values between typical marine carbonates and calcite-1, suggesting that the fluid that was involved in the formation of calcite-1 (discussed below) may have affected rocks up to 200 m outside the zone of visible KCS alteration.

The lead isotopes measured from unaltered, bulk rock samples of the MT, CPMC and Earn Group have values consistent with typical upper crustal lithologies in the Selwyn Basin. Lead isotopes in the upper crustal sedimentary units of the Selwyn Basin are modeled on the shale-curve, which gives expected values at the present day of $^{208}Pb/^{204}Pb$ ~39.8, $^{207}Pb/^{204}Pb$ ~15.7 and $^{206}Pb/^{204}Pb$ ~ 19.5 (Godwin and Sinclair 1982).

Origin of Keg Calc-Silicate alteration

Around the Keglovic deposit mineralization the MT has been regionally altered to form the KCS rock. The alteration is also seen to a lesser extent within the CPMC. Alteration has affected at least 2.2 km^3 of host rock around the KMD. The most pervasive alteration, which leads to the destruction of sedimentary textures, occurs proximal to faults and fractures within the KCS. The bands of wollastonite observed in the field indicate high degrees of alteration as a result of fluid flow along approximately north to south trending fractures, which cut discordantly across the regional strata. Alteration also appears to have occurred along beds with KCS alteration of more permeable beds in the host rock (e.g. silty-limestone beds in the MT) occurring up to 25 m away from visible fractures.

The clear structural control on the alteration and scale of altered rocks suggests the alteration is metasomatic rather than metamorphic in origin, and that the KCS is the product of regional-scale hydrothermal circulation that focused up faults and fractures within the crust before flowing along permeable bedding horizons in the host rock.

Bulk rock analyses on alteration transect 1 indicates that the metasomatism of the MT is associated with a relative increase in Si, Al oxide and Fe oxide concentrations, and with an associated decrease in carbonate and organic C content. This suggests both silication and silicification occurred to form the KCS from the MT. The large volumes of Si in this hydrothermal system could derive from juvenile Si of magmatic origin or Si which has been leached from underlying or surrounding rocks by circulating hydrothermal solutions (Lovering 1962). Isotopic studies on the Keglovic mineralization (discussed below) will help constrain the origin of the Si.

Descriptive model for Keg Deposit Mineralization

There are two styles of mineralization in the KMD: an early phase of skarn and carbonate replacement mineralization (Stage 1 and 2) followed by high-grade vein-hosted Ag-Pb-Zn mineralization (Stage 3). In this section we will discuss the metal source, temperature, environment of formation, and fluid origin for each mineralization event.

Stage 1 and 2: Ag-Pb-Zn-Cu-Sn skarn

Stage 1 mineralization occurs, dominantly, as pervasive replacement of the metasomatized carbonate-silicate beds within the KCS and, in minor fractures, in less carbonate rich calc-silicate horizons. The presence of grandite and diopside-hedenbergite suggests the mineralization formed by metasomatism in a skarn environment (Meinert 1992). Lithological logging (Figure 5.4) illustrated that the stratiform sulphides occur predominantly associated with the central fault (Fault 2; Figure 5.4), but are not associated with either of the other faults. This is confirmed by the 3D modeling performed in Leapfrog Geo, which suggests a strong association between the areas of high Zn, Pb and Ag concentrations (elements associated with Stage 1 and 2

mineralization) with the central fault (Fault 2; Figure 5.13). The correlation between the central fault (Fault-2) and mineralization suggests the flow of the mineralizing fluid was controlled by this structure. Why this structure played a primary role on fluid flow but the other faulted areas did not remains unclear, although a tectonic reconstruction (Figure 5.14) suggests this middle fault (Fault-2) may represent a fault with less stratigraphic throw than the other two faults (Fault-1 and Fault-3; Figure 5.4 and Figure 5.14) mapped in drill core, potentially leading to larger permeability in the later central feature (Caine et al. 1996, Sheldon and Micklethwaite 2007).

Based on the observed mineral changes in the skarn, a zonation of mineralization is hypothesised away from the central fault. Garnet and chalcopyrites are found proximal to the central fault, then pyroxene dominated skarns and finally carbonate replacement style deposits (CRD; Meinert, 1987) distal to the fault. This zoning represents a gradation from proximal fluid reaction with the carbonate rocks to distal transport and fluid evolution prior to complete fluid exhaustion away from the transcrustal fault, and is typical for this type of deposit (Table 5.10; Einaudi et al. 1981, Meinert 1987, Megaw et al. 1988, Lynch 1989).

Stage 1 and 2 mineralization could not be radiometrically dated but occurred prior to the 102-98 Ma deposition of arsenopyrite-2 (discussed below).

The Pb isotopes indicate a predominantly upper crustal origin for Pb in galena-1 (Figure 5.10; Godwin and Sinclair 1982) but some mixing between an upper crustal Pb reservoir and a second Pb reservoir cannot be ruled out, as the galena-1 Pb isotopes fall below the upper crustal shale curve (Beaudoin 1992). This second lead reservoir could be lower-crustal or igneous in origin. The evolution of lower-crustal lead isotopes in the northern-Cordillera is modeled by the Bluebell curve (Andrew et al. 1984), which produces expected lead isotope values for the lower crust at 100 Ma of 18.199 for $^{206}Pb/^{204}Pb$ and 15.525 for $^{207}Pb/^{204}Pb$ (Figure 5.10A). The granites

of the Tay River district show a bimodal distribution of lead isotopes. Lead isotopes from K-feldspar in the Anvil plutonic suite (see chapter 2) have present day $^{206}Pb/^{204}Pb$ values ranging from 19.328 to 19.350 and $^{207}Pb/^{204}Pb$ values ranging from 15.720 to 15.741; these values fall above the shale curve and therefore cannot explain the lead isotopes in the KMD mineralization (Figure 5.10A). In contrast, the Tay River and Tombstone suites have $^{206}Pb/^{204}Pb$ values ranging from 19.033 to 19.429 and $^{207}Pb/^{204}Pb$ values ranging from 15.686 to 15.727 (Rasmussen 2013), which overlap with lead isotope values obtained from the Keglovic galena (Figure 5.10A). However, Stage 1 and 2 mineralization occurred before the intrusion of the 96-90 Ma Tombstone suite (see Chapter 2) emplacement. Stage 1 and 2 mineralization at the Keglovic deposit is potentially synchronously with the Anvil Suite, which contains lead consistent with an upper crustal origin, or the Tay River suite. Therefore, the lead isotopes values observed in the KMD mineralization fit better with mixing between an upper crustal Pb source, which derived from the local country rock or the Anvil suite, and a fluid containing some Pb derived from the lower crustal rocks or the Tay River suite. The similarity between the Pb isotopes observed in the KMD galena and the Tombstone suites would therefore occur as the Tombstone suite forms from lower crustal melting (as proposed in Chapter 2) of the source that provided minor Pb to the galena at the KMD.

The lack of sulphate minerals and presence of pyrrhotite at the KMD suggest that the fluid that was transporting this lead was likely reduced (Barnes 1979) and that the Pb within this fluid is transported as a chlorocomplex (Barrett and Anderson 1988). The source of the other metals cannot be determined from any of the analytical techniques used in this study. However, the other metals present at the KMD (Ag, Cu, Sn, As, Sb and Zn) are all soluble when complexed with chlorine (Seward et al. 2014). Therefore, we suggest that the other metals

present in the Stage 1 and 2 mineralization share a common source with the Pb and are transported predominantly complexed with Cl within the same fluid (Barrett and Anderson 1988).

The concentration of Pb in this metal-bearing, reduced fluid needed to be relatively high (ppb to ppm level) to form the Stage 1 and Stage 2 mineralization; this can only be achieved in a reduced fluid with negligible dissolved HS^- (Barnes 1979, 1997). Therefore, reduced sulphur was added to the metal bearing fluid at the site of mineral precipitation. The sulphur isotope compositions of galena-1 do not indicate a unique sulphur source for Stage 1 mineralization. Galena-1 yielded a range of sulphur isotope values from -1.0 to 0.1 ‰ (Figure 5.9). These sulphide values could derive from a reduced fluid with a contained $\delta^{34}S$ value of 0 ‰ or an oxidized fluid with a $\delta^{34}S$ value of +20 ‰ (Rye 2005, Seal 2006). This range of values could be derived from a magmatic, mantle or sedimentary source (Ohmoto 1972, Rye and Ohmoto 1974, Hoefs 1997). However, whole rock powders from the Anvil, Tay River and Tombstone suites have $\delta^{34}S$ of between 6 to 11.2 ‰ (Rasmussen 2013, Rogers 2017) suggesting that the plutons alone cannot be the source for sulphur in galena-1.

Fluid inclusions from garnet-1 and quartz-1 are primarily aqueous fluids with minor dissolved NaCl, $CaCl_2$ and $MgCl_2$ (salinities range from 3 to 6 wt% $NaCl_{equiv}$). This salinity is lower than would be expected for primary magmatic water, which typically ranges from >10 wt% $NaCl_{equiv}$ to a highly concentrated brine, due to the strong preference of Cl^- to partitions into the aqueous phase during H_2O separating from a crystallizing magma (Kilinc and Burnham 1972, Shinohara et al. 1989, Cline and Bodnar 1991). The fluid inclusions in garnet-1 and quartz-1 have salinities similar to seawater (~3.5 wt% $NaCl_{equiv}$) and within the range of formation and connate waters (0.4 to ~20 wt% $NaCl_{equiv}$; Hitchon and Friedman 1969, Connolly

et al. 1990). The salinity values recorded in Stage 1 inclusions could also derive from meteoric fluids that have been mixed with a more saline fluid or acquired Cl from the local host rock. The tectonic setting of the Tay River district in the core of an orogen suggests that seawater is unlikely to have been present during KMD mineralization. Therefore, the fluid inclusion data is consistent with a fluid that has equilibrated with the surrounding sedimentary rocks (either connate or formation water) or mixing of meteoric water with a more saline fluid.

Homogenization temperatures of 320 to 360°C provide minimum estimates for the temperature of garnet and quartz crystallization and is consistent with typical pluton-distal Pb-Zn skarns (Table 5.10; Meinert et al. 2005).

Silver is contained within the Se-rich galena-1 via a coupled substitution with Bi. The variable presence of pyrrhotite-1 associated with galena-1 indicates reduced conditions within certain stratigraphic horizons. The stratigraphic control of pyrrhotite-1 suggests that organic rich layers in the KCS, potentially representing less altered MT beds or initially more graphitic lithologies, are creating locally reduced conditions rather than a change in source.

Stage 2 mineralization consists of a sulphide-forming event followed by a sulphide-overprinting event. Both events occur in the same stratigraphic horizons as Stage 1 mineralization. Oxygen isotopic values for calcite-1 could indicate either a fluid derived from a magmatic sources (expected $\delta^{18}O_{SMOW}$ values +5.5 to +10.0‰; Sheppard 1986, Taylor and Sheppard 1986) or from mixing of a fluid in equilibrium with the MT limestone, which has relatively high $\delta^{18}O_{SMOW}$ values (+21‰), with regional meteoric water, which has relatively low $\delta^{18}O_{SMOW}$ values in the Cretaceous (<-16‰; Hitchon and Krouse 1972, Ufnar et al. 2001). Calcite-1 has $\delta^{13}C_{PDB}$ values 4-7 ‰ lower than the MT host rock. This can be explained by either: interaction of carbon from the host marine limestones with a fluid rich in reduced or

organic carbon derived from sediments, which would have typical $\delta^{13}C_{PDB}$ values of <-15‰ (Rye and Ohmoto 1974); or carbon derived from a mantle or magmatic source, which would have typical $\delta^{13}C_{PDB}$ values equal to -4±2 ‰ (Rye and Ohmoto 1974, Hoefs 1997). The scatter in $\delta^{13}C_{PDB}$ values of around 4 ‰ observed for calcite-1 is consistent with variable mixing between two carbon bearing sources rather than carbon sourcing from a single deep-large reservoir, which would lead to a far tighter cluster in $\delta^{13}C_{PDB}$ values (Beaudoin et al. 1991). Therefore, the carbon in calcite-1 likely represents mixing between carbon in the host marine limestones and carbon from a reduced or organic sedimentary rock.

Sphalerite-1 has positive $\delta^{34}S_{CDT}$ values, from 0.4 ‰ up to +5.1 ‰. These values within the Stage 2 sulphide could be derived from precipitation from HS^- with a similar $\delta^{34}S$ value to sphalerite-1 or from the reduction of oxidized sedimentary sulfate with $\delta^{34}S$ values from ~20 to 25 ‰. The $\delta^{34}S$ values of sphalerite-1 are too enriched in ^{34}S for mantle derived sulphides (0±3 ‰; Seal 2006) and too enriched in ^{32}S for sulphides derived from the surrounding igneous rocks (6-11 ‰; Rasmussen 2013, Rogers 2017). However, the sphalerite-1 $\delta^{34}S$ values are consistent with sulphide precipitation from the reduction of sedimentary sulphate within typical marine sediments (Seal 2006).

The suggestion that a fluid bearing organic-carbon mixed with the host limestone (as indicated by $\delta^{13}C_{PDB}$ values of calcite-1) suggest that sulfate reduction could be occurring by thermochemical sulphate reduction (TSR; Goldstein and Aizenshtat 1994, Machel 2001), which would lead to the simultaneous reduction of the sulfate in the sediment and oxidation of the carbon species within the fluid.

Fluid inclusions from quartz-2 have similar salinities to Stage 1 inclusions ranging from 4 to 5 wt% $NaCl_{Equiv}$ but have lower T_H values of around 270±20°C suggesting a similar fluid was

involved in Stage 1 and 2 but the fluid had cooled in-between these mineral deposition events. The temperatures obtained from the microthermometry are consistent with the temperature derived from stannite-sphalerite geothermometry. The similarity between the temperatures obtained from fluid inclusion homogenization and an independent geothermometer imply that Stage 2 mineralization occurred under low confining pressures (shallow depths) as there is little to no pressure correction necessary on the fluid inclusion homogenization temperature (Wilkinson 2001).

Stage 2b involves hydrous silicate phases retrograding and overprinting the previously deposited sulphides. During this stage the silver is commonly exsolved from galena-1 leaving a silver-poor galena. This process also leads to the exsolution of bismuth, which was involved in the coupled-substitution of silver into the galena lattice. In some galena grains, the site of deposition of the remobilized silver is not obvious (Figure 5.5K). In other galena grains exsolutions of complex-silver sulfosalts, tellurides and selenides occur within the retrograded galena crystals (Figure 5.5L). The minerals formed – pyrargyrite, stephanite, tetrahedrite and cervelleite – are commonly associated with 250-300°C environments and fluids depleted in sulphur (Lynch 1989).

Overall, the mineralogy, temperatures and low salinity of the fluids associated with Stage 1 and 2 are consistent with the prograde then retrograde metasomatism seen in a distal Pb-Zn skarn or carbonate replacement deposit (Einaudi et al. 1981, Meinert 1987, 1992, Meinert et al. 2005). Analogs to Stage 1 and 2 mineralization exist in the distal regions of the Groundhog Mine in the Central Mining district, New Mexico (Meinert 1987) and within the carbonate hosted deposits of Northern Mexico (Megaw et al. 1988).

Stage 1 and 2 mineralization appears to have formed from two fluids: a metal and organic

carbon bearing fluid and a sulphur bearing fluid. The metal-organic carbonic fluid appears to have sourced metals and carbon predominantly from the upper crust with a minor magmatic or lower crustal metal input. The flow of this mineralizing fluid appears to have been controlled by a single fault at the KMD. The second fluid contains S and C in equilibrium with the KCS host rock (formation water) and appears to have undergone no transport.

Flow of the metal bearing fluid could have been driven by regional geothermal gradients derived in the Jurassic-Cretaceous orogeny and/or due to intrusion of an intrusive body proximal to the KMD. Skarn mineralization occurred before 102-98 Ma, potentially synchronously with the intrusion of the 109-104 Ma Anvil plutonic suite or 100-96 Ma Tay River plutonic suite, which make up the Anvil Batholith (see Chapter 2). The aureole of the Anvil Batholith extends up to 5 km into the surrounding country rock (Pigage 2004) and, therefore, could account for fluid flow at the KMD. However, there is no definitive evidence in the skarn for primary magmatic fluid input, so any proximal intrusive body acted only as a heat source for fluid flow. Stage 1 deposition occurred due to reaction between the carbonate bearing wall rock and the metal-bearing fluid and/ or due to mixing between the fluid concentrated along the fault and formation waters within the carbonate-silicate beds. Neutralization and addition of S to the fluid, due to mixing or reaction with the wall rock, caused the activity of bisulfide (HS^-) to increase leading to a decrease in the solubility of the metals and, therefore, precipitation of the base-metal sulphides (Barnes 1979). Stage 2 followed Stage 1 due to the cooling of the fluid and the potential influx of increased meteoric water.

Stage 3:Ag-Pb-Zn-As-Sb veining

Stage 3 mineralization occurs within planar fractures, which crosscut the surrounding host rock and rarely overprint the previously deposited skarn mineralization. Re-Os dating of

Arsenopyrite-2, from Stage 3b, constrains this mineralization event to between 102 and 98 Ma. Drill core logging suggests that Stage 3 mineralization is not controlled by the same fault that controls Stage 1 and 2 mineralization, but instead Stage 3 mineralization appears to be concentrated at one depth (discussed below). This is best demonstrated by the 3D modeling of the distribution of Sb (Figure 5.13), which is contained within stibnite and the silver sulfosalts within the Stage 3b assemblage, but not present in large concentrations in any of the other paragenetic stages.

Stage 3 mineralization appears to have the same metal, carbon and sulphur sources as the previously deposited skarn. This is demonstrated by: lead isotopes from galena-2, which have a predominantly upper-crustal source identical to Stage 1 and 2; sulphur isotopic compositions of sulphides in Stage 3b and 3c, which are similar to those of the sulphides in Stage 1 and 2, and the carbon and oxygen isotopic composition of calcite-3 which overlaps with the composition of calcite-1. The temperature of Stage 3 mineral deposition (recorded from sphalerite-2 and stannite-2 cation exchange) is also similar to the temperature identified in Stage 2. The skarn and Stage 3 mineralization also have very similar mineral chemistries with galena-2 displaying almost identical chemistry to galena-1. However, galena-2 appears in equilibrium with silver bearing fahlore ores (freibergite) rather than retrograding to epithermal style silver sulfosalts.

The major difference observed between Stage 3 mineralization and the previously deposited skarn is the CO_2 concentrations and high salinities observed in some of the trapped primary fluid inclusions and the abundant evidence for phase separation. Textural evidence for effervescence comes from the acicular needles of calcite-2, which dominate the mineral assemblage of Stage 3a (Figure 5.7A-C). This style of calcite deposition is commonly attributed to fluid boiling (Simmons and Christenson 1994). Isotopic evidence for boiling coeval with

Stage 3 mineralization comes from the carbon and oxygen isotopic composition of calcite-2, which is shifted compared to the earlier calcite-1, and subsequent calcite 3. The change in oxygen and carbon isotopic composition could be due either to mixing with a fluid enriched in ^{13}C and ^{16}O, or due to loss of the ^{12}C and ^{18}O isotopes during kinetically controlled CO_2 separation and the subsequent conversion of water to CO_2 via reaction with the local carbon bearing host rock (Lynch et al. 1990). CO_2 generated during boiling has a strong tendency to incorporate ^{18}O (Bottinga 1968) and therefore CO_2 loss would lower the bulk $\delta^{18}O$ value and increase the $\delta^{13}C$ value of the remaining fluid (Lynch et al. 1990). Evidence for effervescence is also recorded by the primary FIAs in quartz-4, which demonstrate coexistence of vapour rich and liquid rich fluid inclusion assemblages within the same growth zones, variable fluid salinity, and a large range in T_H because of cooling due to loss of high enthalpy steam. The vapour phases in the Stage 3 FIAs consists of CO_2 with variable amount of CH_4, as shown by eutectic depression, clathrate metastability and a very low CO_2 homogenization temperature. The increased CO_2 in this stage could derive from magma, a mantle source or decarbonation reactions within the wallrocks (Lowenstern 2001). As the isotopic studies have shown no definitive evidence for magma or mantle involvement in the Keglovic mineralization we suggest the CO_2 is derived from reactions between the mineralizing fluids with the surrounding wall rock. The CH_4 observed in the Stage 3 fluid inclusions is likely derived from the reduced or organic-rich sedimentary rocks, which carbon isotopic analyses suggested are the carbon source for calcite 1 and 3. The increase in salinity observed in some Stage 3 fluid inclusions is due to the strong partitioning of the salts into the aqueous phase during effervescence (Lynch et al. 1990), with the rarely observed halite saturation indicating fluid inclusions formed in restricted fractures where continuous boiling leading to extensive vapour loss has occurred.

Calcite-1 and calcite-3 have similar carbon and oxygen isotopic values, which are distinctly different from calcite-2. This suggests that the fluid involved in mineralization is similar before and after the boiling event and calcite-2 is interpreted to have been a transient event with conditions returning back to the pre-boiling Stage 1 and 2 environment by Stage 3c and 4.

There are two potential mechanisms for generating a brief, spatially localized period of effervescence; either phase separation of the fluid inclusions due to decreasing confining pressure (Wilkinson 2001) or mixing between two fluids (Wilkinson 1990). Drill hole logging and 3D modeling of the location of Stage 3 veins indicates that the mineralization is spatially confined to a limited depth-horizon which is discordant to bedding and not related to any observed faults or fractures; this supports a pressure-driven mechanism for effervescence, as mixing would have needed to be controlled by a particularly permeable bed or structure and neither has been observed at that depth in the drill core. The ubiquitous effervescence observed in Stage 3 mineralization indicates that this horizon corresponds to where the volatile pressure in the fluid becomes greater than the confining pressure. The fluid volatile content appears to vary in the Stage 3 fluid inclusions, however the phase separation occurs at constant depth indicating a discrete-abrupt pressure decrease rather than a gradual drop. A mechanism for generating an abrupt decrease in confining pressure occurs at the transition from lithostatic to hydrostatic conditions (Meinert and Hedenquist 2003, Tosdal et al. 2009). At this point the total fluid pressure exceeds the confining pressure due to the overlying rock, leading to fracturing of the rock, increasing the volume available to the mineralizing fluid and resulting in a dramatic drop in fluid pressure and the release of the volatile phase in the fluid (Burnham 1985) for fluids with variable volatile contents.

Fluid effervescence promotes the precipitation of minerals due to changes in fluid chemistry (pH and oxidation state) and the drop in temperature associated with fluid boiling (Drummond and Ohmoto 1985, Barnes 1997). 3An increase in pH derived from CO_2 loss leads to calcite-2 precipitation, while quartz-4 precipitates due to the drop in temperature (Barnes 1979). The sulphide precipitation in Stage 3 likely occurs as a sulphur-bearing fluid (equilibrated with the host rock) is drawn into the fractures due to the increase in volume (decrease in pressure). This sulphur bearing fluid mixes with the metal-bearing fluid (which has undergone effervescence) leading to an increase in the activity of HS^- in the fluid and a decrease in the stability of the metal complexes and, therefore, precipitation of the base-metal sulphides.

Overall, Stage 3 appears to represent a Ag-Pb-Zn vein system similar to those found in clastic metasedimentary terranes as defined by Beaudoin and Sangster (1992). Analogs to Stage 3 mineralization include the Keno Hill and Kokanee Range vein systems of western Canada (Lynch et al. 1990, Beaudoin 1992). The metal, sulphur, carbon and fluid sources for Stage 3 mineralization are the same as for Stage 1 and 2 mineralization, although the contained volatile content of the fluid appears to have increased. Stage 3 mineralization was promoted by phase separation within the fluid. Deposition was controlled by pressure and is, therefore, confined to a specific depth horizon.

Stage 4: Meteoric input and collapse of the hydrothermal system

Little data has been collected on Stage 4, which consists predominantly of an assemblage of unmineralized calcite, quartz and zeolites. Calcite-4 has carbon and oxygen isotopic signatures identical to calcite-1 and -3. These are interpreted to indicate that the fluid originated as meteoric water, which has partially equilibrated with the host rocks. However, the presence of euhedral

zeolites in open fractures indicate a change to hydrostatic conditions (Utada 2001). The oxidation of previous sulphides to pyrite, and the iron oxide staining of Stage 1 to 3 silicates and pyrite also indicates oxidized meteoric water input. Quartz-5 is euhedral and fracture filling.

Overall, this stage appears to represent final cooling and infilling of previously generated fractures by late stage minerals.

The Keglovic Deposit, a product of regional geological processes.

The KMD is a zoned Ag-Pb-Zn-Cu-Sn skarn-CRD, which is overprinted by a mid-Cretaceous Ag-Pb-Zn-As-Sb bearing vein system. The mineralization is hosted predominantly within the MT with minor mineralization in the CPMC. The host lithologies have undergone widespread decarbonation, silication and silicification to form interbeds of a carbonate-silicate and calc-silicate (KCS) before the mineralizing events at the KMD. The large volume of silica involved in the metasomatism is likely sourced from the surrounding rocks, as there is no evidence in the KMD mineralization for an input from a magmatic fluid. All four paragenetic stages of mineralization at the KMD appear to have formed from the same fluid. The consistency of the fluid throughout the paragenetic stages indicates that all the mineralization formed from a single long-lived hydrothermal cell.

Fluid flow within this meteoric-hydrothermal system could be driven by either a magmatic heat source, regional geothermal gradient, transcrustal faults connecting deep and shallow fluid reservoirs or a combination of these factors. Chapter 2 demonstrate that there was considerable extrusive and intrusive igneous activity in the Tay River district during the mid-Cretaceous, synchronous with Keglovic deposit formation, including the 110-90 Ma intrusion of the Anvil Batholith. Therefore, numerous potential magmatic heat sources existed to generate large-scale

hydrothermal circulation in the upper crust of the Tay-River district. However, there is no evidence in the KMD mineralization that the igneous activity in the Tay River district provided components to the mineral deposit.

Fluid flow would also be stimulated by the period of rapid regional exhumation synchronous with the Keglovic deposit formation (see Chapter 4). This rapid uplift would have caused shallowing of crustal geotherms promoting fluid flow in the upper crust (Ring et al. 1999, Reiners and Brandon 2006).

Stage 1 and 2 mineralization followed, generating a Ag-Pb-Zn skarn that developed due to fluid flow controlled by an out of sequence upper crustal fault (Figure 5.15A). The skarn is zoned away from the fault, which represents a transition from a fluid dominated system proximal to the central fault to a country-rock dominated system distal to the central fault. During Stage 1 and 2 mineralization the reaction between the local country rock and mineralizing fluid led to the accumulation of CO_2 (released during carbonate replacement) and CH_4 (derived from the organic-rich sedimentary rocks) in the fluid. The volatile content of the fluid can be buffered to very high gas contents due to the nature of the surrounding MT host rock (French 1965, Nokleberg 1973).

The change to Stage 3 vein-hosted mineralization occurred due to phase separation. Keglovic deposit mineralization was coeval with regional exhumation (Chapter 4). This exhumation caused between 1 and 3 $kmMa^{-1}$ shallowing of the hydrothermal system (Chapter 4) equivalent to a decrease in pressure of ~0.3 to 0.8 $KbarMa^{-1}$. These two factors (increasing vapour pressure in the fluid and synchronous decreasing external pressure; Figure 5.15B) eventually led to gas pressure in the fluid exceeding the surrounding confining pressure causing phase separation. Stage 3 mineralization is found at a single depth suggesting that effervescence

occurred as the fluid changed from lithostatic to hydrostatic conditions and the surrounding country rock fractured.

In total, therefore, the mineralization represents the telescoping of a single hydrothermal system due to regional exhumation (Sillitoe 1994). The highest grades at the KMD occur when the vein system intersects the previously developed skarn (Figure 5.15B), which occurs where the fault that controlled skarn mineralization is at the depth where phase separation occurred.

Development of the Keg East Deposit

The same scale of mineralization reported at the KMD has not been found at the Keglovic East deposit, where only minimal development of Stage 3 mineralization occurs (Dumala 2013) and no skarn mineralization has been found. The Keglovic East deposit is to the northeast of the syncline-anticline trace that follows the central fault-2 (Figure 5.2A). This fault controlled the mineralizing fluid flow that led to skarn development (Stage 1 and 2 mineralization); therefore, the ~1 km separation between the hypothesized trace of the fault and the site of Keglovic East likely explains the lack of skarn development. Without skarn development there is no significant accumulation of CO_2 in the fluid at the Keglovic East deposit, although minor CO_2 enriched fluid may be transported from the KMD. The lower CO_2 concentration in the fluid led to more restricted phase separation and, therefore, less developed Stage 3 mineralization. In combination, these effects explain the minimal mineralization found at the Keglovic East deposit.

Similarities to other mineralization styles in the Yukon

While the Keglovic deposit as a whole may be unique within the Yukon, there are analogies within the northern Canadian Cordillera to the individual paragenetic stages

documented here. Firstly, although the Keglovic deposit does occur in proximity to the Anvil Pb-Zn metallogenic province, the mineralogy and textures observed at the Keglovic deposit do not resemble the sediment-hosted massive sulphide (SHMS) Pb-Zn deposits of the northern Cordillera (Lydon 2004, Goodfellow and Lydon 2007). Also, the Keglovic deposit is not the same age, nor does it form in the same stratigraphic horizon as the Anvil (Late Cambrian), Howards Pass (Early Silurian) or Macmillan Pass (Late Devonian) SHMS deposits (Goodfellow 2007, Goodfellow and Lydon 2007). However, the proximity of the two metallogenic anomalies (which is a feature shared by a large number of the Ag-Pb-Zn vein class defined by Beaudoin and Sangster, 1992) suggests that the metals in the Keglovic deposit could be sourced from sedimentary crustal rocks enriched in metals due to the Anvil SHMS or SEDEX event.

Stage 1 and 2 mineralization represents a Pb-Zn skarn; this type of mineral deposit is regularly reported throughout the Yukon (~70 in MINFILE; Yukon Geological Survey 2017). The known economic anomalies tend to be small in size and are all currently considered sub-economic, although in some cases they can attain significant grades (Gordey 2013).

Stage 3 mineralization represents an example of a Ag-Pb-Zn vein system in clastic metasedimentary terranes as defined by Beaudoin and Sangster (1992). Another significant vein system in this class in the Yukon are the Keno Hill deposits, which are also found within the Selwyn Basin. Stage 3 of the Keglovic deposit shares many characteristics with the Keno Hill deposits including: mineralogy; tectonic setting; metal, sulphur and carbon source; and the hypothesized importance of phase separation in mineral deposition (Table 5.11; Boyle et al. 1970, Lynch et al. 1990, Beaudoin and Sangster 1992, Hantelmann 2013). The major difference between Keglovic and Keno Hill mineralization is the presence of the skarn at the Keglovic

deposit. The lack of skarn at Keno Hill potentially derives from the carbonate-poor nature of the Keno Hill host rock (Keno Hill Quartzite; Boyle et al. 1970, Gordey and Anderson 1993).

Seemingly then, the individual mineralization styles that compose the Keglovic deposit are reported elsewhere within the Yukon. What makes the Keglovic deposit appear unique is the telescoped superposition of these individual mineralization events, which is a product of the concurrent regional exhumation occurring in the region surrounding the Keglovic deposit coeval with mineralization.

Conclusions

The Keglovic deposit represents the telescoped superposition of a zoned Ag-Pb-Zn-Cu-Sn skarn-CRD and shallower Ag-Pb-Zn-As-Sb vein mineralization. The skarn mineralization occurs at temperatures between 350-400°C and is controlled by a regional fault that is a first-order control on fluid flow. Deposition of minerals within the skarn occurs due to the replacement of carbonate within limestone horizons of the MT. Metals, carbon and sulphur all appear to be primarily sourced from the upper crust by a fluid derived from meteoric water which has equilibrated with local upper crustal sedimentary rocks. The second stage of mineralization involves the same fluid but with enhanced volatile (CO_2 and CH_4) contents. Decreasing pressure due to the concurrent regional exhumation causes effervescence within this fluid, leading to fracturing and the rapid deposition of the vein system. Veins are concentrated in one depth horizon linked to the pressure at which phase separation occurred. The telescoping of the later vein system and earlier skarn at the Keglovic deposit is caused by the regional exhumation synchronous with deposit formation. The vein mineralization observed at the Keglovic deposit shares a large number of similarities to the Ag mineralization that was mined in

the Keno Hill district. The Keglovic deposit is associated with plutonic suites generally assumed to be barren. While the deposit does not form directly from the magmatic fluids it shows that future exploration cannot be based purely on the occurrence of specific igneous rocks, but needs to consider the entire regional tectonic setting.

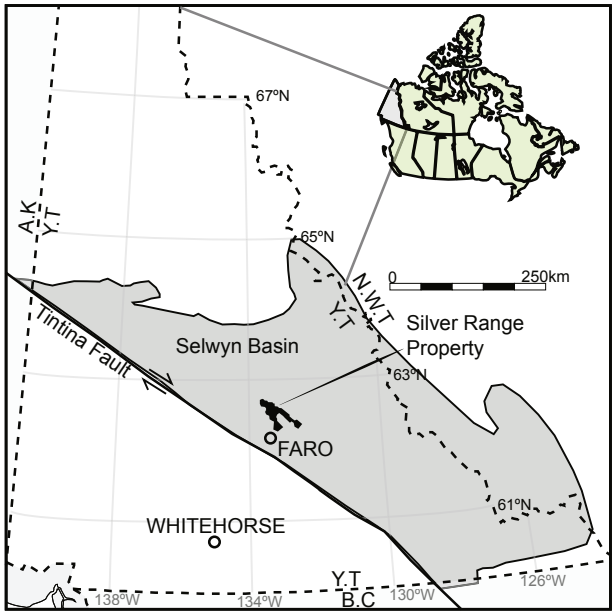

Figure 5.1: Simplified map of Yukon, showing modern extent of the Selwyn Basin assemblage rocks north of the Tintina fault based on Nelson et al. (2013). Black shape shows the extent of the Keg property from Dumala (2013).

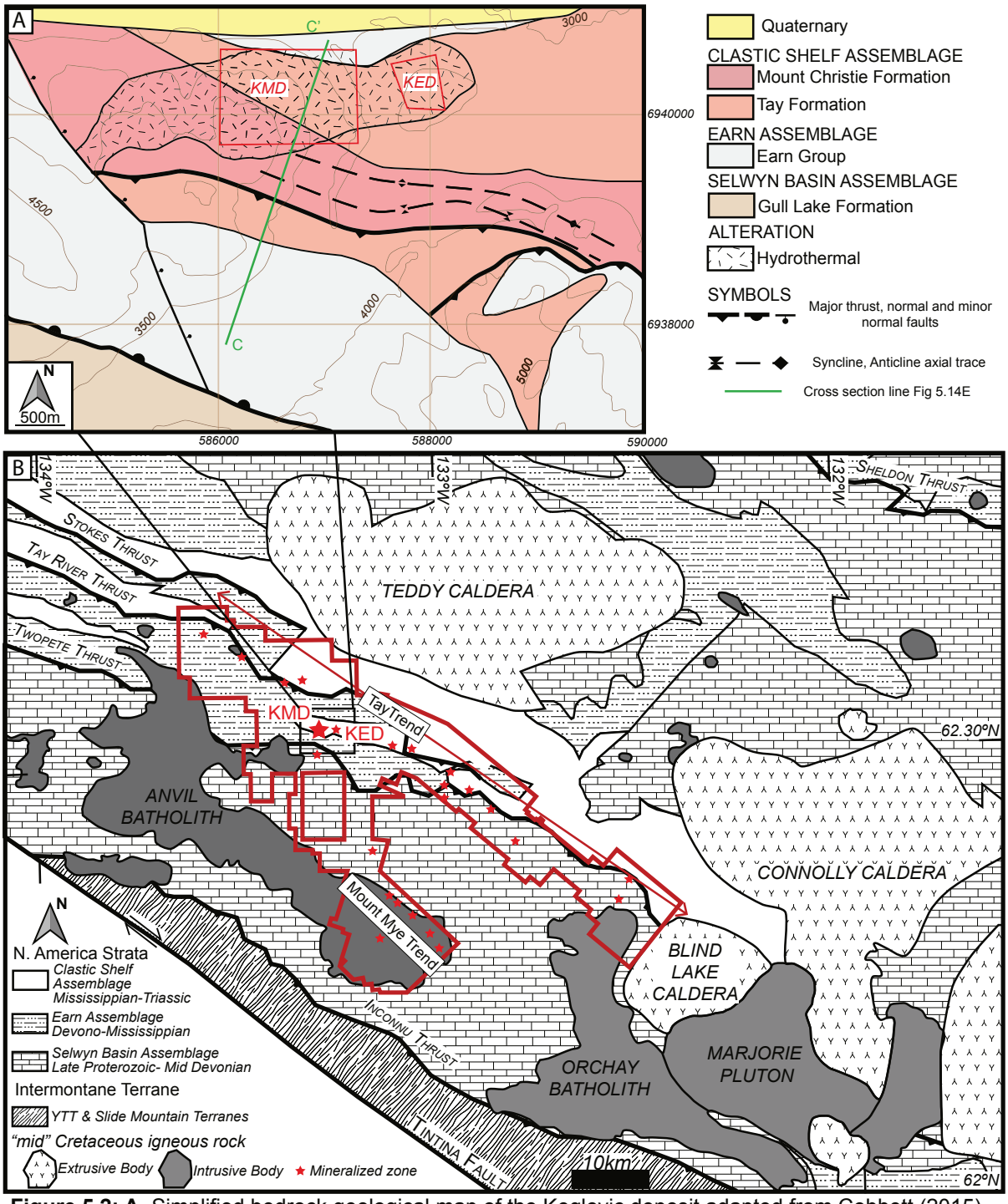

Figure 5.2: A. Simplified bedrock geological map of the Keglovic deposit adapted from Cobbett (2015) and Dumala (2013). UTM Zone 8N. **B**. Simplified bedrock geological map of the Tay River district from Chapter 2. Outline of the Keg property in red. Location of the Keglovic Main Deposit (KMD) and Keglovic East Deposit (KED) from Cobbett (2015). Major thrust faults created during Mesozoic orogeny and major Mid-Cretaceous igneous bodies are labeled after Gordey (2013).

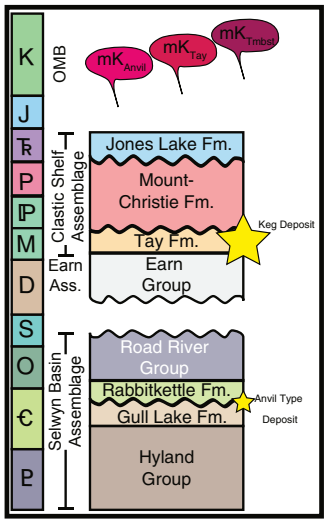

Figure 5.3: Generalized regional stratigraphy surrounding the KMD adapted from Pigage (2004) and Gordey (2013)

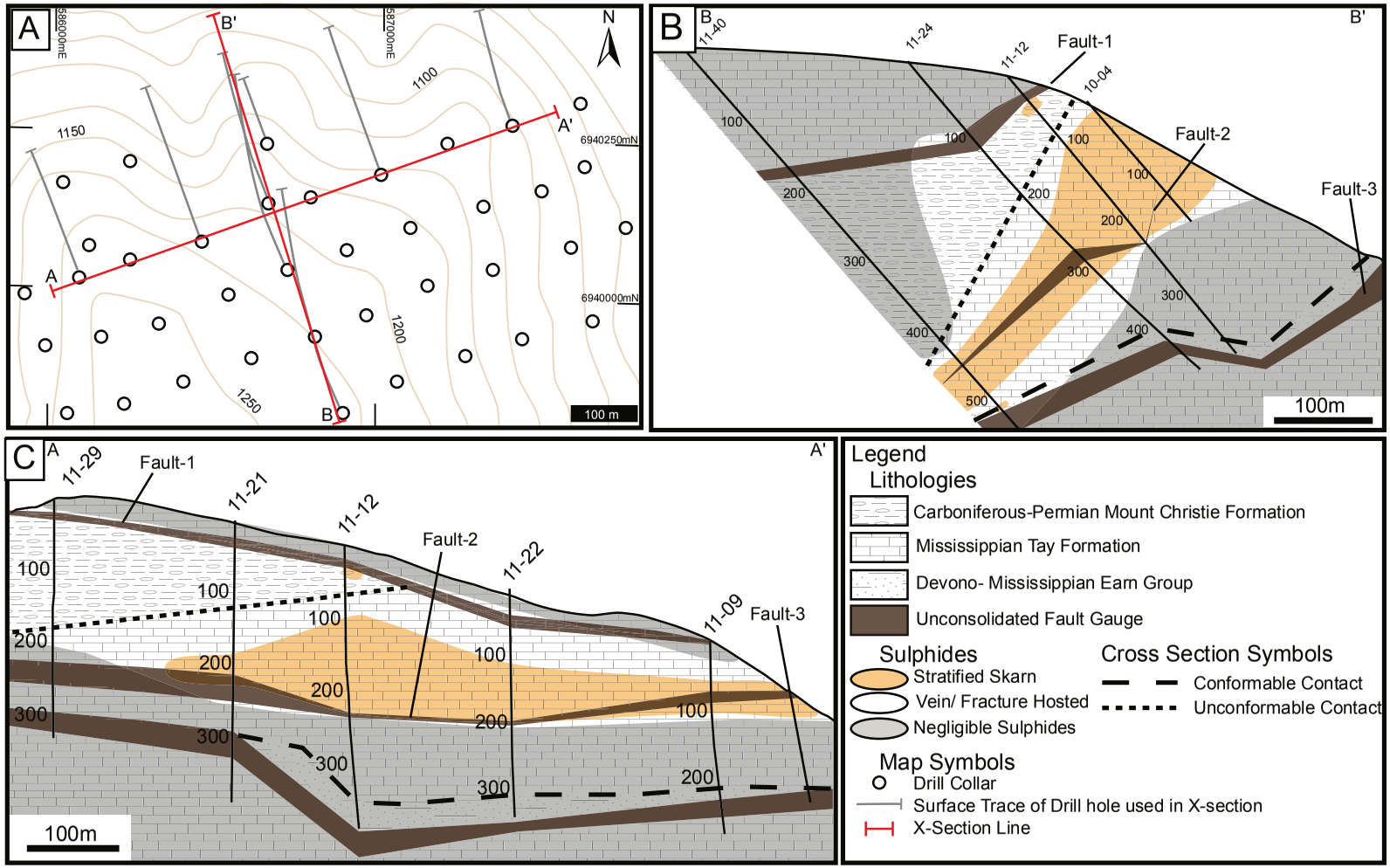

Figure 5.4: A. Map view of the drill hole collars at the KMD from Dumala (2013) showing cross section lines for B and C. Surface drill trace for holes in the cross-section are shown in red. UTM Zone 8. Approximate areal extent of map view is shown on Figure 5.2 A by the red box labelled KMD **B.** Schematic SSE to NNW cross- section through the KMD. **C.** Schematic WSW to ENE cross-section through the KMD. Cross-section B and C were created by relogging of the drill holes in the transects conducted as part of this study. The extent of fault

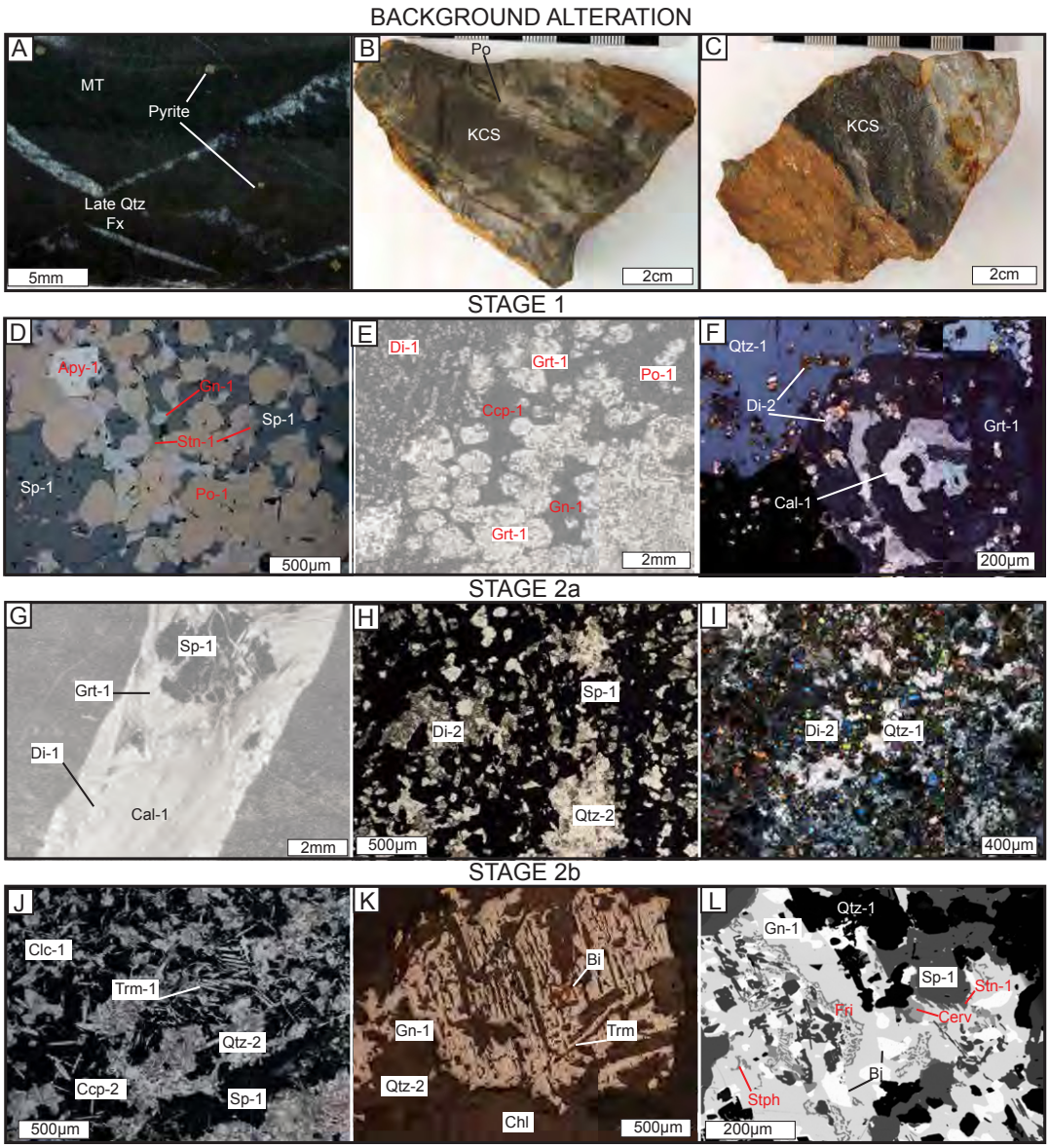

Figure 5.5: Images of KMD host rock, mineralization and paragenetic relationships. A. Visibly unaltered carbonaceous-rich limestone beds in MT drill core, crosscut by late quartz bearing fractures, showing euhedral pyrite cubes. B. KCS handspecimen with minor mineralization. C. Sucrosic texture of a KCS handspecimen. D. Stage 1 and 2 ore minerals in reflected light (RL). E. Typical massive skarn mineralogy in plane-polarized light (PPL). F. Stage 1 and 2 mineral relationships in cross-polarized light (XPL). G. Vein hosted Stage 1 and 2a mineralization (PPL). H. Stage 2a skarn mineralization in PPL. I. Stage 2a skarn mineralization in XPL. J. Tremolite from Stage 2b retrograding sphalerite-1 (PPL). K. Breakdown of galena-1 by Stage 2b minerals to exsolve Bi (RL). L. BSE image showing breakdown of galena-1 by Stage 2 skarn minerals to exsolve a complex array of sulfosalts.

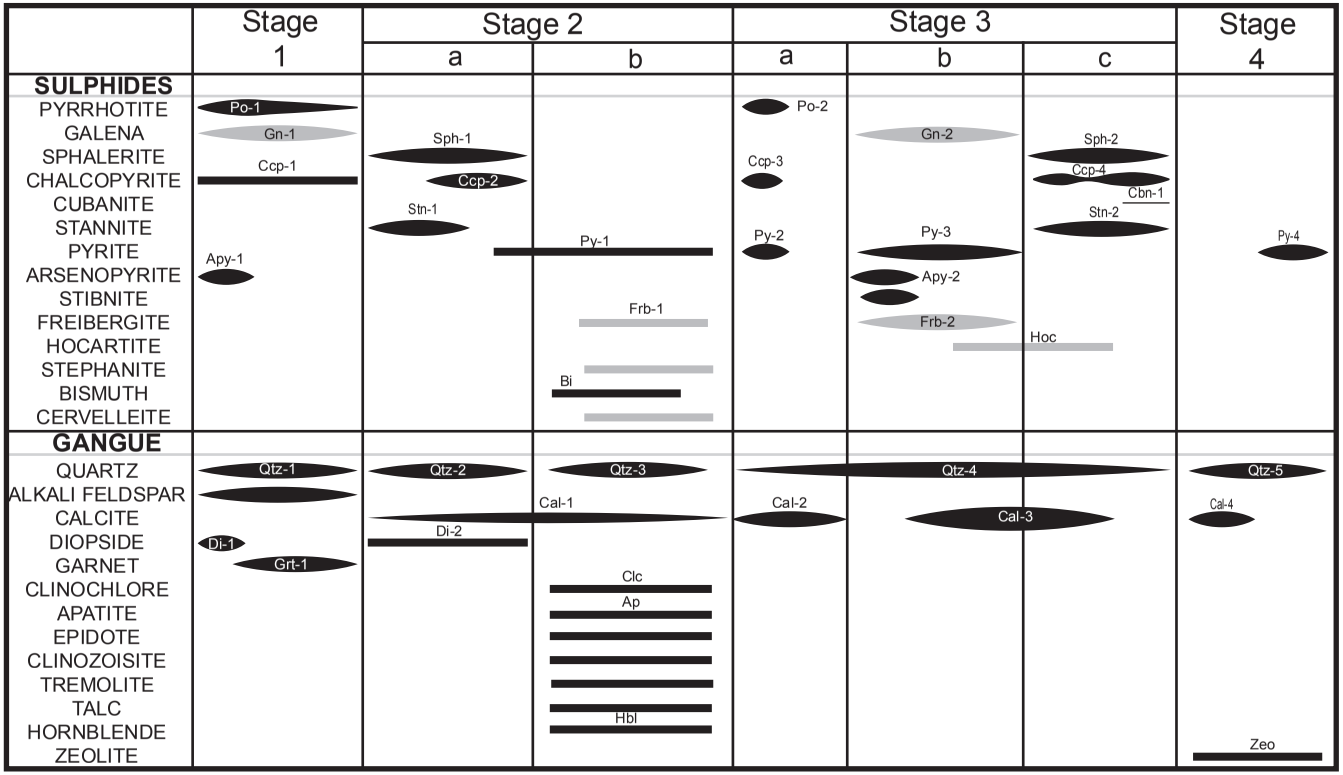

Figure 5.6: Paragenetic sequence for mineralization at the KMD. Line thickness represents approximate relative mineral abundances. Grey blocks shows the location of Ag within each phase.

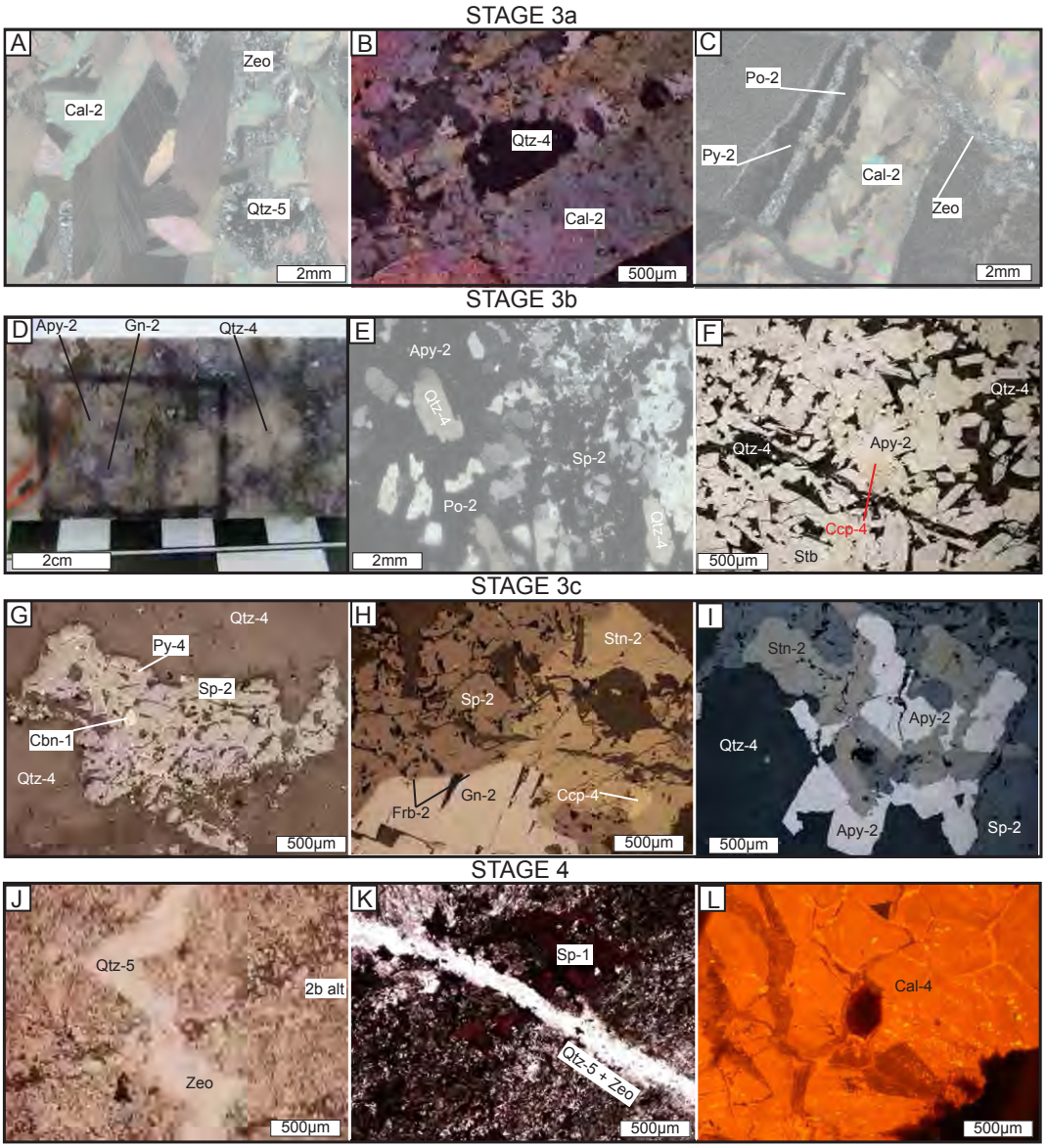

Figure 5.7: Images of KMD host rock, mineralization and paragenetic relationships cont. **A and B.** Acicular void filling calcite-2 with late quartz and zeolite infill (XPL). **C.** Acicular void-filling calcite-2 associated with early pyrite and pyrrhotite and late quartz and zeolite infill (XPL). **D.** Hand specimen texture of quartz-4 and associated ore minerals in Stage 3b. **E.** Euhedral quartz-4 surrounded by Stage 3b and c sulphides (XPL). **F.** Texture of arsenopyrite-2 and stibnite in Stage 3b (RL). **G.** Sphalerite-2 and quartz-4 in Stage 3c (RL). **H.** Stage 3b and 3c sulphides in equilibrium (RL). I. Stage 3c sulphides overprinting Stage 3b sulphides (RL). **J and K.** Late zeolite and quartz fractures (PPL). **L.** CL image of late calcite-4.

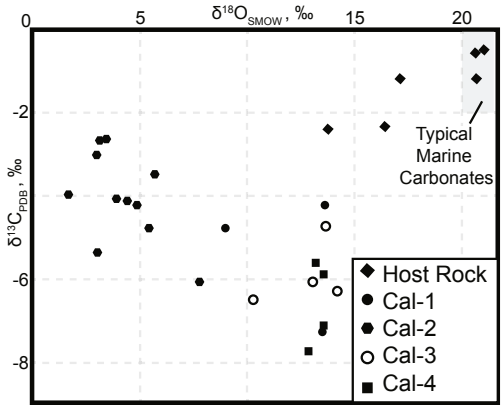

Figure 5.8: Plot of $\delta^{13}C$ vs. $\delta^{18}O$ for host rock and mineralization from the Keglovic deposit. The marine carbonate box is from Veizer et al. (1999). Errors for both $\delta^{13}C$ and $\delta^{18}O$ are 0.2 ‰ (1σ).

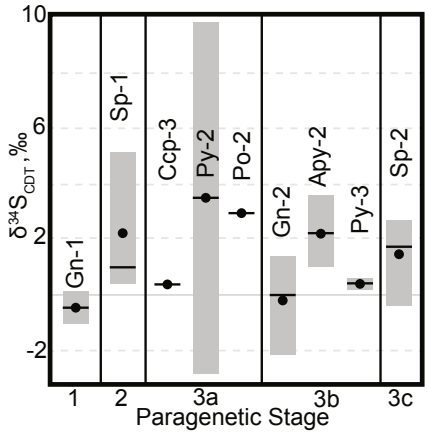

Figure 5.9: Plot showing the range of $\delta^{34}S$ for Keglovic deposit sulphides with respect to mineralogy and paragenetic stage. Black circle indicate a mean value. Black line indicates the median.

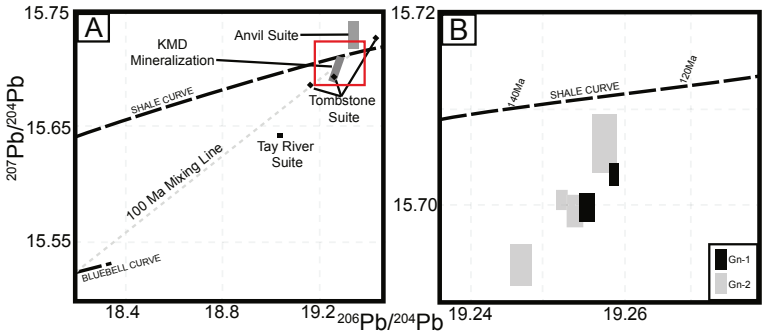

Figure 5.10: A. Plot of $^{207}Pb/^{204}Pb$ vs. $^{206}Pb/^{204}Pb$ for Keglovic deposit mineralization and mid-Cretaceous igneous intrusion of the Tay River district. Upper crustal shale curve is shown for reference from Godwin and Sinclair (1982). Lower crustal bluebell curve is shown for reference from Andrew et al. (1984). A mixing line is drawn by connecting the shale curve and bluebell curve at 100 Ma. Anvil suite lead isotopes are from Chapter 2. Tay River and Tombstone suite lead isotopes are from Rasmussen (2013). Red rectangle shows the area expanded in B. **B.** Plot of $^{207}Pb/^{204}Pb$ vs. $^{206}Pb/^{204}Pb$ for galena at the Keglovic deposit. Upper crustal shale curve is shown for reference from Godwin and Sinclair (1982). Errors (1σ) are shown by the dimensions of the rectangles. Whole rock lead isotope data from the Earn Group, MT and CPMC have typical standard deviations for $^{207}Pb/^{204}Pb$ and $^{206}Pb/^{204}Pb$ of ~0.6 and are therefore not displayed in this figure.

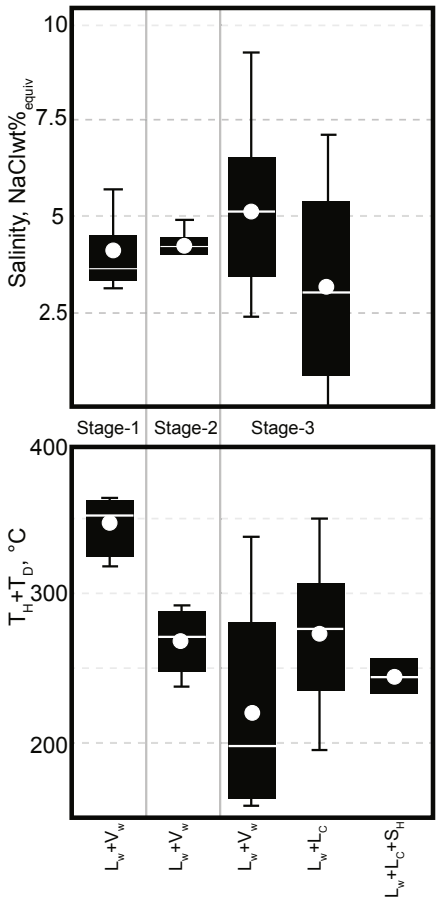

Figure 5.11: Salinity and temperature data from fluid inclusions with respect to paragenetic stage. Salinity for primary aqueous inclusions calculated from T_{ice}. Salinity from carbonic liquid bearing inclusions calculated from Tm_{clath}. Salinity for solid halite bearing inclusions not shown due to axis scale. For carbonic liquid inclusions T_H values include T_D. For both plots, central box represents 50% of values, white circle indicates mean value, white line indicates median value and whiskers indicate the range of data.

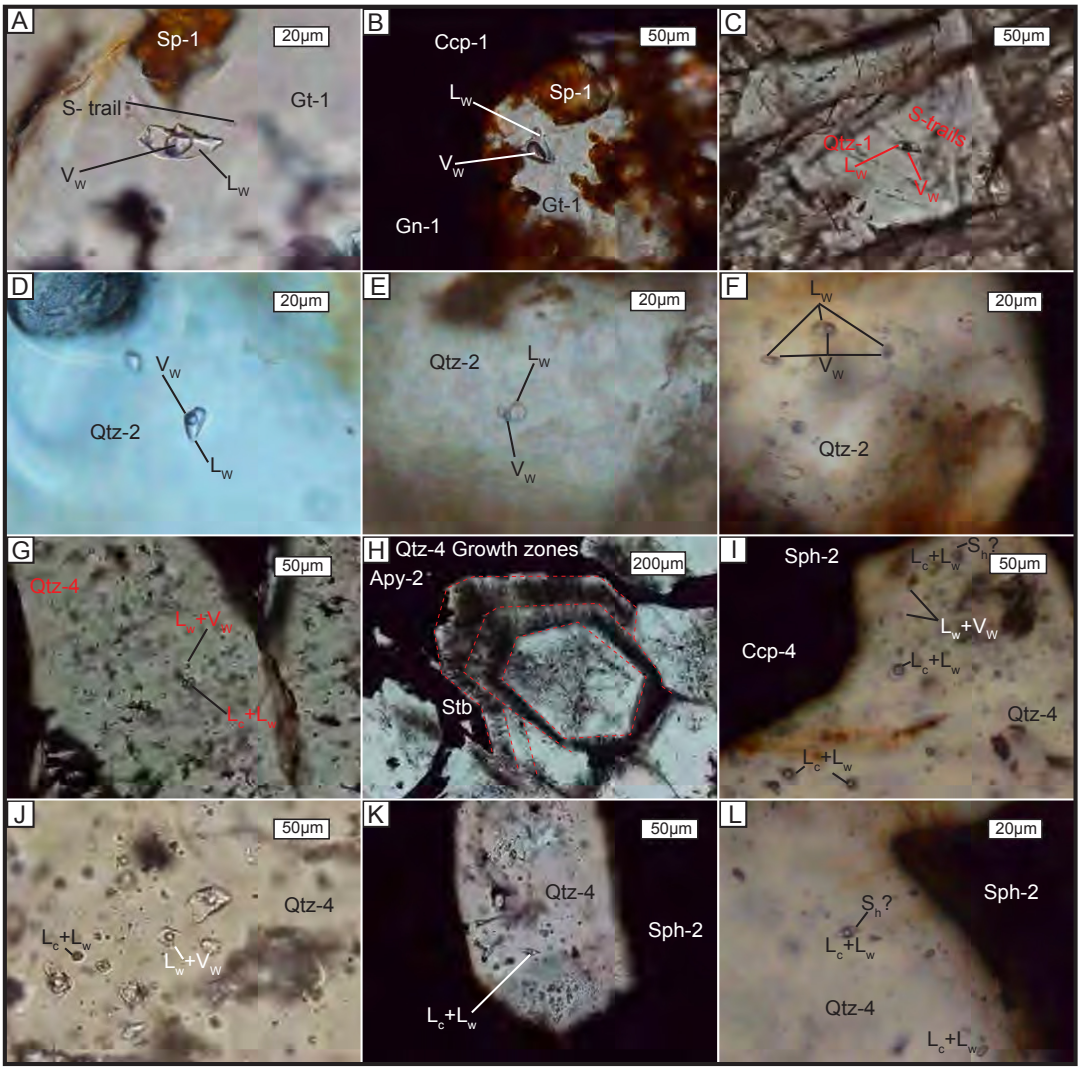

Figure 5.12: Images of typical fluid inclusions from paragenetic Stage 1 (A-C), Stage 2 (D-F) and Stage 3 (G-L).

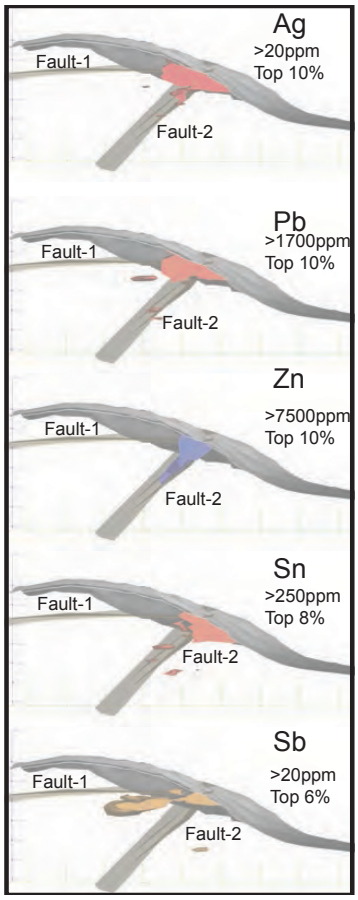

Figure 5.13: Images showing the relationship between interpolants of high assay grade zones and major structures at the KMD. Interpolants and images created in Leapfrog Geo modeling software. Fault numbers refer to Figure 5.4. Each image is labeled with the cut-off metal concentration of the interpolant and the percentage of values (n=7950) included within that cut-off grade.

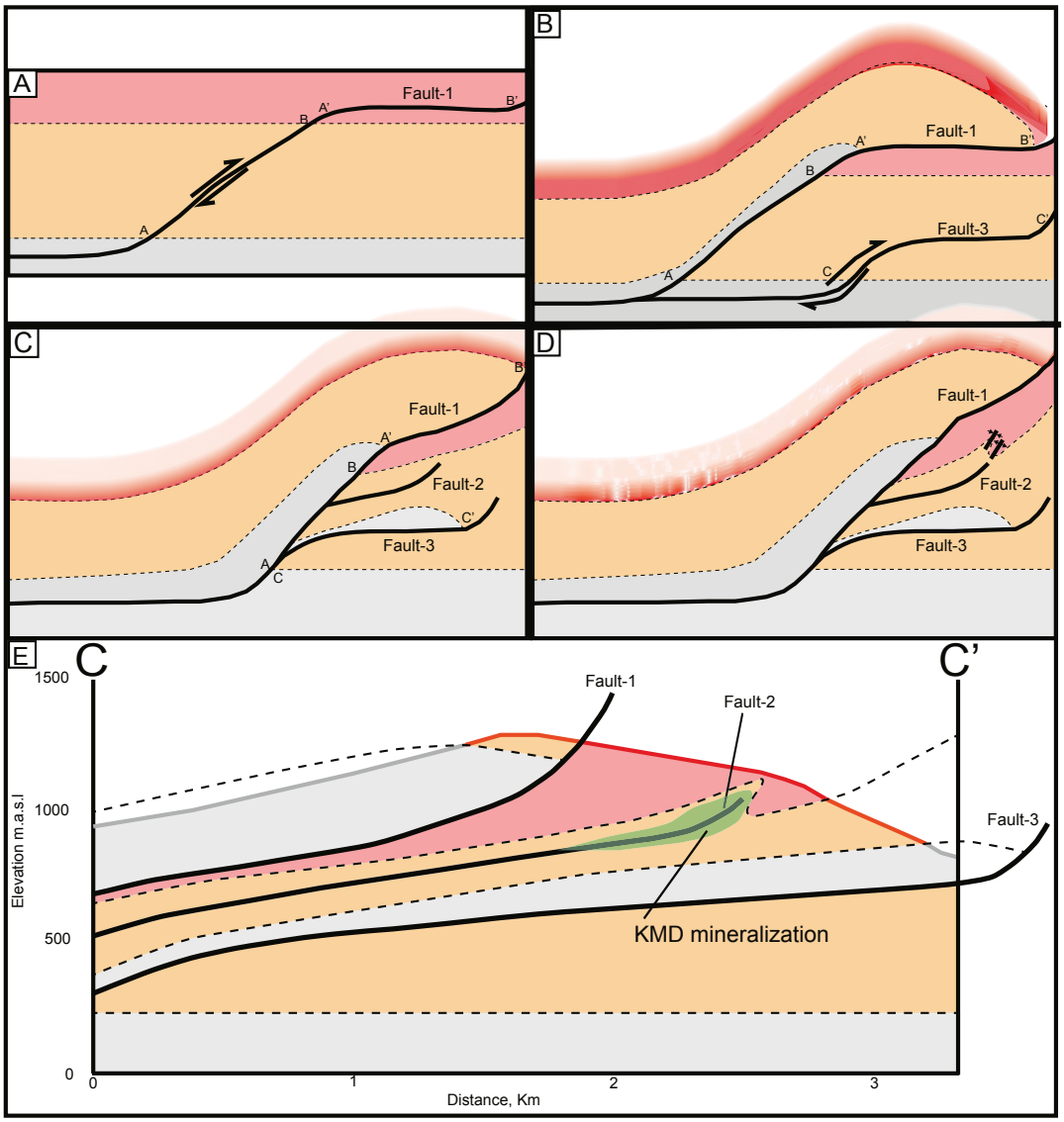

Figure 5.14: Suggested schematic tectonic reconstruction for the present day KMD. Panels A to D represent steps forward in time. Step E shows a modern day cross-section of the KMD from C to C' on Figure 5.2A. Fault numbers refer to Figure 5.4 and Figure 5.13. Schematic position of the skarn mineralization at the KMD is shown in green.

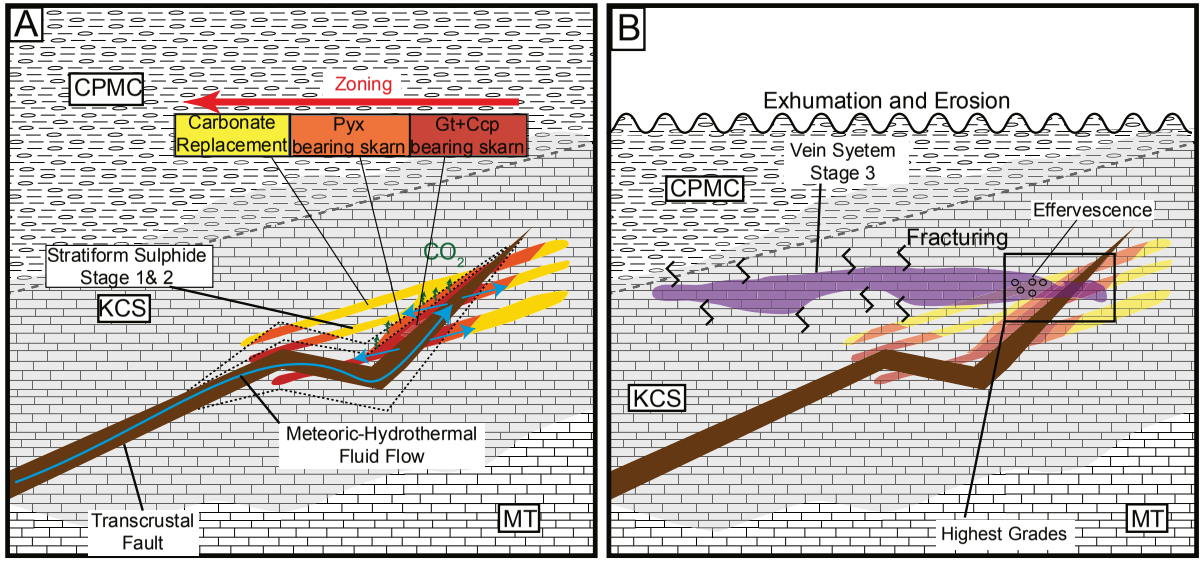

Figure 5.15: Genetic diagram for mineralization at the KMD (not to scale). **A.** Fluid flow focused on a transcrustal fault reacts with carbonate rich horizons in the MT generating skarn mineralization, zoning out to a CRD deposit. **B.** CO2 build up from skarn formation, combined with decreasing pressure due to concurrent regional exhumation leads to phase separation and fracturing of the host rock into which subsequent vein mineral deposition occurs. This potentially occurs as the region moves over the transition from the lithostatic to hydrostatic conditions.

Table 5.1. Galena Chemistry from EPMA

Location	Area	Phase	Stage	# of Points	Fe (wt%)	±1SD (wt%)	Se (wt%)	±1SD (wt%)	Ag (wt%)	±1SD (wt%)	Sb (wt%)	±1SD (wt%)	Bi (wt%)	±1SD (wt%)
10-01 83	KMD	Gn-1	1	31	0.052	0.15	0.87	0.10	1.18	0.26	0.000	0.00	2.92	0.53
10-01 105	KMD	Gn-1	1	52	0.033	0.09	0.89	0.03	0.00	0.01	0.125	0.05	0.01	0.03
10-01 98	KMD	Gn-1	1	23	0.073	0.13	3.20	0.93	1.08	0.53	0.011	0.03	2.32	0.78
11-12 50	KMD	Gn-1	1	9	0.011	0.03	0.96	0.05	1.14	0.09	0.000	0.00	2.81	0.53
11-12 44	KMD	Gn-1	1	11	0.090	0.25	0.99	0.14	1.22	0.15	0.012	0.01	1.81	0.52
11-17 202	KMD	Gn-1	1	8	0.042	0.05	1.36	0.04	0.16	0.05	0.147	0.04	0.00	0.00
11-17 156	KMD	Gn-1	1	15	0.091	0.12	0.77	0.15	0.34	0.32	0.015	0.02	1.10	1.16
11-41 214	KMD	Gn-1	1	15	0.000	0.00	0.85	0.20	0.49	0.05	0.000	0.00	1.41	0.10
11-15 100	KMD	Gn-2	3-b	29	0.093	0.23	1.05	0.05	0.00	0.00	0.055	0.07	0.01	0.03
11-41 144	KMD	Gn-2	3-b	34	0.003	0.02	0.91	0.04	0.01	0.03	0.026	0.04	0.28	0.07
10-01 70	KMD	Gn-2	3-b	62	0.045	0.10	0.85	0.06	1.15	0.18	0.002	0.01	2.68	0.43
HS-G	KMD	Gn-2	3-b	24	0.000	0.00	0.88	0.06	0.98	0.07	0.071	0.26	2.26	0.42
11-14 368	KME	Gn-2	3-b	7	0.029	0.05	1.13	0.05	0.66	0.05	0.000	0.00	2.09	0.07
11-14 359	KME	Gn-2	3-b	21	0.014	0.04	1.25	0.11	0.74	0.08	0.000	0.00	1.97	0.15
11-14 212	KME	Gn-2	3-b	34	0.000	0.00	0.81	0.06	0.09	0.14	0.203	0.14	0.12	0.07
11-14 47	KME	Gn-2	3-b	35	0.123	0.31	0.73	0.36	0.16	0.19	0.366	0.74	0.07	0.07

Table 5.2a. Sphalerite Chemistry From EPMA

Location	Area	Phase	Stage	# of Points	Mn (wt%)	±1SD (wt%)	Fe (wt%)	±1SD (wt%)	Zn (wt%)	±1SD (wt%)	Cd (wt%)	±1SD (wt%)
10-01 60	KMD	Sph-1	2-a	30	0.42	0.12	12.8	1.2	51.4	1.1	0.74	0.06
10-01 105*	KMD	Sph-1	2-a	37	0.52	0.02	10.9	0.7	54.2	0.7	0.87	0.08
10-01 98*	KMD	Sph-1	2-a	24	0.62	0.02	10.8	0.6	52.4	0.6	0.67	0.05
11-41 214	KMD	Sph-1	2-a	32	0.24	0.05	11.5	0.7	52.6	0.8	1.06	0.09
11-12 50*	KMD	Sph-1	2-a	29	0.54	0.05	11.5	0.6	52.9	0.6	0.89	0.07
11-15 100*	KMD	Sph-2	3-c	37	0.34	0.06	10.3	0.6	55.2	0.8	0.53	0.06
11-15 142	KMD	Sph-2	3-c	25	0.48	0.07	11.1	1.1	54.1	1.3	0.71	0.06
HS-G*	KMD	Sph-2	3-c	7	0.44	0.06	6.8	2.1	55.9	2.2	0.75	0.19
11-41 144*	KMD	Sph-2	3-c	30	0.18	0.04	10.4	1.0	53.3	1.2	0.58	0.07
10-01 70*	KMD	Sph-2	3-c	11	0.32	0.04	11.2	0.5	50.9	0.6	0.78	0.06
11-14 212*	KME	Sph-2	3-c	17	0.29	0.04	11.0	1.0	52.6	0.6	0.46	0.07
11-14 368*	KME	Sph-2	3-c	7	0.34	0.09	11.4	1.0	52.3	1.2	0.55	0.04
11-14 47*	KME	Sph-2	3-c	3	0.05	0.02	9.8	0.3	55.6	0.6	1.00	0.30

* Represents also measured for Gn Chemistry

Table 5.2b. Sphalerite Chemistry from LA-ICP-MS

Sample I.D	Area	Phase	Stage	# of Points	Cu (ppm)	±1SD (ppm)	Se (ppm)	±1SD (ppm)	Cd (ppm)	±1SD (ppm)	In (ppm)	±1SD (ppm)
10-01 60	KMD	Sph-1	2-a	25	1766	3176	100	20	8217	967	201	24
11-14 212	KME	Sph-2	3-c	14	380	338	170	19	6072	600	87	8
11-41 144	KMD	Sph-2	3-c	15	2048	1978	167	53	6250	814	56	3

Table 5.3. $\delta^{13}C$ and $\delta_{18}O$ Values for Analyzed Samples

Sample I.D	Phase	Stage	Area	$\delta^{13}C_{PDB}$ (‰)	$\delta^{18}O_{SMOW}$ (‰)
HS-J5	Host Rock	--	KMD	-2.3	16.4
HS-J1	Host Rock	--	KMD	-1.2	20.6
HS-J1	Host Rock	--	KMD	-0.6	20.6
HS-AN2	Host Rock	--	KMD	-1.2	17.1
11-41 69	Host Rock	--	KMD	-2.4	13.8
11-41 246	Host Rock	--	KMD	-0.5	21.0
11-14 220	Cal-1	2	KME	-4.8	9.0
11-41 56	Cal-1	2	KMD	-4.2	13.6
HS-BH2	Cal-1	2	KMD	-7.3	13.5
11-41 214*†	Cal-1	2	KMD	-6.5	10.3
11-15 131	Cal-2	3	KMD	-5.3	3.0
11-14 108	Cal-2	3	KME	-4.2	4.9
11-14 170*	Cal-2	3	KME	-4.0	1.7
11-14 359	Cal-2	3	KME	-2.6	3.4
11-15 163	Cal-2	3	KMD	-4.1	4.4
11-15 165	Cal-2	3	KMD	-2.7	3.1
11-15 291	Cal-2	3	KMD	-3.0	3.0
11-41 102	Cal-2	3	KMD	-4.8	5.4
11-41 172*	Cal-2	3	KMD	-6.1	7.9
11-41 181	Cal-2	3	KMD	-4.0	3.9
HS-BG	Cal-2	3	KMD	-3.5	5.7
11-15 17*	Cal-3	3	KMD	-6.3	14.2
11-15 29*	Cal-3	3	KMD	-6.1	13.1
11-15 98	Cal-3	3	KMD	-4.7	13.6
11-41 149	Cal-4	4	KMD	-7.7	12.9
11-14 111	Cal-4	4	KME	-5.6	13.2
11-14 111	Cal-4	4	KME	-5.9	13.6
11-41 131	Cal-4	4	KMD	-7.1	13.6

All Samples Calcite

* Samples measured for S isotopes

† Samples measured for Pb isotopes

Table 5.4. $\delta^{34}S$ values

Sample I.D	Phase	Stage	Area	$\delta^{34}S_{CDT}$ (‰)
10-01 70†	Gn-1	1	KMD	-1.0
11-41 214*†	Gn-1	1	KMD	0.1
11-41 214*†	Sp-1	2-a	KMD	0.4
10-01 164	Sp-1	2-a	KMD	5.1
10-01 70†	Sp-1	2-a	KMD	1.0
11-14 103	Py-2	3-a	KME	9.8
11-14 170*	Py-2	3-a	KME	-2.8
11-41 172*	Po-2	3-a	KMD	2.9
11-41 172*	Ccp-3	3-a	KMD	0.4
11-14 41	Py-3	3-b	KME	0.2
11-14 47†	Py-3	3-b	KME	0.6
11-14 212†	Gn-2	3-b	KME	-2.1
11-14 47†	Gn-2	3-b	KME	1.4
11-15 17*	Gn-2	3-b	KMD	1.1
HS-G †	Gn-2	3-b	KMD	-1.2
11-15 17*	Apy-2	3-b	KMD	3.5
11-15 25	Apy-2	3-b	KMD	1.0
11-15 17*	Sp-2	3-c	KMD	2.7
11-15 25	Sp-2	3-c	KMD	-0.4
11-15 29*	Sp-2	3-c	KMD	2.4
11-41 144†	Sp-2	3-c	KMD	1.1

Abbreviations from Whitney and Evans (2009).

* Samples measured for C & O isotopes

† Samples measured for Pb isotopes

Table 5.5a. Pb isotopes from Galena Seperates

Sample I.D	Phase	Area	$^{208}Pb/^{204}Pb$	± σ	$^{207}Pb/^{204}Pb$	± σ	$^{206}Pb/^{204}Pb$	± σ	$^{207}Pb/^{206}Pb$	± σ
11-41 214*	Gn-1	KMD	39.196	0.002	15.7028	0.0006	19.2806	0.0007	0.81446	0.00001
10-01 70†	Gn-1	KMD	39.179	0.003	15.6994	0.0007	19.2731	0.0010	0.81458	0.00001
11-14 47†	Gn-2	KME	39.129	0.003	15.6935	0.0010	19.2549	0.0014	0.81505	0.00001
11-14 212†	Gn-2	KME	39.173	0.001	15.7002	0.0005	19.2662	0.0006	0.81491	0.00001
11-41 144†	Gn-2	KMD	39.197	0.004	15.7061	0.0015	19.2780	0.0017	0.81475	0.00001
HS-G†	Gn-2	KMD	39.177	0.002	15.6991	0.0008	19.2696	0.0012	0.81475	0.00001

* C,O and S isotopes measured
† S isotopes also measured

Table 5.5b. Pb isotopes from unaltered host rock

Sample I.D	Lithology	Area	$^{208}Pb/^{204}Pb$	± σ	$^{207}Pb/^{204}Pb$	± σ	$^{206}Pb/^{204}Pb$	± σ	$^{207}Pb/^{206}Pb$	± σ
HS-CL	MT	KMD	38.8	1.4	15.3	0.5	18.3	0.6	--	--
11-24 32	MT	KMD	40.6	1.4	15.9	0.6	20.0	0.7	--	--
HS-CT	CPMC	KMD	41.6	1.5	16.0	0.6	19.6	0.7	--	--
11-40 398	CPMC	KMD	44.2	1.5	17.6	0.6	22.8	0.8	--	--
HS-DA	DME	KMD	38.7	1.4	14.5	0.5	18.5	0.6	--	--
HS-BD	DME	KMD	42.7	1.5	16.4	0.6	20.2	0.7	--	--

Table 5.6. Re-Os dating of Arsenopyrite-2 from Stage 3b

Sample	Re (ppb)	± 2σ	Total Os (ppt)	± 2σ	$^{187}Re/^{188}Os$	± 2σ	$^{187}Os/^{188}Os$	± 2σ	Model Age (Ma) $[Os]_{i=0.12}$	± 2σ	Model Age (Ma) $[Os]_{i=1}$	± 2σ
11-15 25	56.8	0.2	82.9	2.1	12454	297	21.4	0.5	98.2	0.5	102.4	0.5

Table 5.7. Fluid inclusion analyses from Paragenetic Stage 1 and 2

Location	Area	Number of inclusions	FIA	Phase	Type	P,PS,S	T_{MELT} (°C)	T_{ICE} (°C)	T_H (°C)	Salinity* (wt% $NaCl_{EQUIV}$)	Liquid	Vapour
10-01 83	KMD	1	1	Gt-1	Lw+Vw	P	-21.1	-2.0	363	3.4	0.7	0.3
10-01 83	KMD	2	2	Gt-1	Lw+Vw	P	-21.1	-2.2	352	3.6	0.7	0.3
10-01 83	KMD	1	3	Gt-1	Lw+Vw	P	-36	-1.8	341	3.1	0.8	0.2
10-01 83	KMD	1	5	Gt-1	Lw+Vw	P	-36	-2.7	325	4.5	0.7	0.3
10-01 83	KMD	3	6	Gt-1	Lw+Vw	P	-36	-1.9	364	3.2	0.7	0.3
10-01 83	KMD	2	7	Gt-1	Lw+Vw	P	-28	-2.0	357	3.3	0.8	0.3
10-01 83	KMD	1	8	Gt-1	Lw+Vw	P	-41	-2.0	362	3.4	0.6	0.4
10-01 83	KMD	5	9	Gt-1	Lw+Vw	P	-35	-3.1	352	5.1	0.8	0.2
10-01 83	KMD	2	4	Qtz-1	Lw+Vw	P	-36	-2.7	360	4.5	0.9	0.1
10-01 12	KMD	2	12	Qtz-1	Lw+Vw	P	-20.3	-3.5	324	5.7	0.7	0.4
10-01 12	KMD	1	13	Qtz-1	Lw+Vw	P	-21.8	-2.6	318	4.3	0.6	0.4
10-01 12	KMD	1	11	Qtz-1	Lw+Vw	S	-21.2	-2.6	165	4.3	1.0	0.1
10-01 70	KMD	2	14	Qtz-2	Lw+Vw	P	-21	-2.5	292	4.2	0.8	0.2
10-01 70	KMD	3	16	Qtz-2	Lw+Vw	P	-21	-2.5	287	4.2	0.9	0.1
10-01 70	KMD	3	19	Qtz-2	Lw+Vw	P	-23.2	-3.0	266	4.9	0.9	0.1
10-01 60	KMD	1	21	Qtz-2	Lw+Vw	P	-19.9	-2.4	251	4.0	0.7	0.3
10-01 60	KMD	1	23	Qtz-2	Lw+Vw	P	-18.1	-2.4	275	4.0	1.0	0.1
10-01 70	KMD	1	17	Qtz-2	Lw+Vw	PS	-21	-2.6	238	4.3	1.0	0.1
10-01 70	KMD	1	15	Qtz-2	Lw+Vw	S	-21	-1.3	254	2.2	1.0	0.1
10-01 70	KMD	1	18	Qtz-2	Lw+Vw	S	-21	-1.2	256	2.1	0.9	0.1
10-01 60	KMD	3	20	Qtz-2	Lw+Vw	S	-22.5	-2.0	153	3.4	1.0	0.1
10-01 60	KMD	1	22	Qtz-2	Lw+Vw	S	-19.9	-3.2	107	5.3	0.9	0.1

* Calcultaed based on Bodnar (1993).

Table 5.8. Fluid inclusion analyses from quartz-4 from Paragenetic stage 3

Location	Area	Number of inclusion	FIA	Type	P,PS, S	T_{MELT} (°C)	Tm_{Clath} (°C)	Tm_{Car} (°C)	T_{ICE} (°C)	T_H (°C)	T_D (°C)	Salinity† (wt% $NaCl_{EQUIV}$)	Salinity# (wt% $NaCl_{EQUIV}$)	Liquid	Vapour	Solid
11-27 207	KMD	3	28	Lw+Lc	P	-57.8	11.2		-4.5	274*		7.2		0.8	0.2	
11-27 207	KMD	1	29	Lw+Lc	P	-57.4	11.9		-4.2	275		6.7		0.9	0.1	
11-14 212	KME	5	43	Lw+Lc	P	-56.9	9.6	15.4	-2.7		340	4.5	0.8	0.50	0.50	
11-22 109	KMD	2	34	Lw+Lc	P	-56.7	9.6	23.9	-1.8	306*		3.1	0.8	0.70	0.30	
11-22 109	KMD	1	32	Lw+Lc	P	-57.1	10.2	13.7	-1.9	292		3.2	0.0	0.85	0.15	
11-27 207	KMD	1	25	Lw+Lc	P	-56.7	6.2		-1.5	249		2.6	7.1	0.50	0.50	
11-27 207	KMD	1	26	Lw+Lc	P	-56.6	7.2	20.5	-3.9	211		6.3	5.4	0.60	0.40	
11-27 207	KMD	1	27	Lw+Lc	P	-56.6	7.6	19.6	-5.6	242		8.7	4.7	0.70	0.30	
11-14 212	KME	3	44	Lw+Lc	P	-55.4	9.4	13.9	-2.2	195		3.7	1.2	0.60	0.40	
10-01 116	KMD	2	36	Lw+Lc	P	-56.1		13	-1.5	300*		2.6		0.50	0.50	
10-01 116	KMD	2	36	Lw+Lc+Sh	P	-56.7	10.9	13.5	-24.7	233		25.4	0.0	0.75	0.20	0.05
10-01 164	KMD	3	42	Lw+Lc	P	-56.7	7.4	13.5	-6.6		350	10.0	5.1	0.60	0.40	
10-01 116	KMD	1	37	Lw+Lc+Sh	P	-56.8	10		-24.4	255		25.2	0.0	0.90	0.05	0.05
11-22 109	KMD	2	31	Lw+Lc	P	-57.35		18.9	-1.95	258		3.3		0.85	0.15	
10-01 116	KMD	2	39	Lw+Lc	P	-57.4		13.7	-1.5	307		2.6		0.60	0.40	
11-27 207	KMD	1	30	Lw+Lc	P	-57.6		13.7	-4.9	214		7.7		0.60	0.40	
11-27 207	KMD	4	24	Lw+Vw	P	-24.8			-2.5	209		4.2		0.80	0.20	
11-27 207	KMD	3	24	Lw+Vw	P	-21.1			-1.8	247		3.0		0.90	0.10	
11-27 207	KMD	1	25	Lw+Vw	P	-21.1			-4.1	185		6.6		0.95	0.05	
11-27 207	KMD	1	27	Lw+Vw	P	-21.1			-4.4	241		7.0		0.90	0.10	
11-27 207	KMD	1	28	Lw+Vw	P	-22.2			-6.1	162		9.3		0.95	0.05	
11-22 109	KMD	2	35	Lw+Vw	P				-3.7	181		6.0		0.93	0.07	
10-01 116	KMD	5	38	Lw+Vw	P	-21.1			-2.1	305		3.5		0.90	0.10	
10-01 164	KMD	4	41	Lw+Vw	P	-21.1			-2.0	291		3.4		0.90	0.10	
11-14 212	KME	2	43	Lw+Vw	P	-41			-3.2	337		5.3		0.80	0.20	
11-14 212	KME	3	44	Lw+Vw	P	-24			-2.9	162		4.8		0.90	0.10	
11-22 109	KMD	1	33	Lw+Vw	S	-42			-3.6	158		5.9		0.95	0.05	
10-01 164	KMD	2	40	Lw+Vw	S	-21.1			-1.4	161		2.4		0.95	0.05	

* Gas phase homogenizationt, † calcultaed from T_{ICE} (Bodnar 1993), # calculated from Tm_{Clath} (Diamond 1992)

Table 5.9. Whole-Rock Major Element Oxide Data

Sample I.D	Type	SiO_2 (wt%)	Al_2O_3 (wt%)	Fe_2O_3 (wt%)	MgO (wt%)	CaO (wt%)	Na_2O (wt%)	K_2O (wt%)	TiO_2 (wt%)	P_2O_5 (wt%)	MnO (wt%)	Cr_2O_3 (wt%)	LOI (wt%)	Total (wt%)	TOT/C (wt%)	TOT/S (wt%)
11-24 107		51.80	14.16	7.73	1.54	13.07	0.11	0.43	0.69	0.50	0.21	0.02	9.10	99.41	0.40	0.11
11-24 287	**Flt Rck**	66.96	9.57	6.25	1.46	3.58	0.13	1.77	0.69	0.20	0.12	0.01	8.70	99.41	0.81	0.12
11-24 432		62.68	6.17	2.33	1.06	12.68	0.14	1.34	0.30	0.23	0.07	0.01	12.70	99.73	2.66	0.88
HS-CL		10.13	1.31	0.55	0.92	48.26	0.02	0.07	0.07	0.01	0.04	0.00	38.50	99.88	10.48	<0.02
HS-EJ		16.85	4.69	2.23	2.14	40.05	0.23	0.95	0.17	0.02	0.08	0.00	32.40	99.85	8.87	0.03
11-24 32	**Unaltered MT**	27.99	2.65	1.52	2.26	37.58	0.36	0.75	0.14	0.35	0.08	0.01	26.20	99.88	7.62	0.37
11-24 97		54.94	6.77	3.66	3.38	19.42	0.61	2.03	0.37	0.45	0.05	0.01	8.00	99.67	2.49	1.18
11-24 460		38.02	7.43	2.24	6.43	26.71	0.47	2.12	0.43	2.18	0.03	0.04	13.50	99.64	4.65	0.96
HS-AS		84.03	5.21	5.92	1.21	0.26	0.04	1.81	0.27	0.04	0.09	0.01	0.80	99.67	0.06	<0.02
HS-CT	**Unaltered**	59.56	17.62	4.37	3.37	5.30	1.10	5.81	0.71	0.08	0.03	0.01	1.20	99.12	0.05	0.66
11-40 210	**CPMC**	72.87	10.21	3.43	3.40	3.67	0.53	3.85	0.54	0.09	0.03	0.02	1.10	99.78	<0.02	0.89
11-40 398		76.41	9.64	2.96	2.48	3.73	0.56	2.30	0.55	0.31	0.02	0.02	0.60	99.61	0.02	0.88
HS-DA	**Unaltered**	58.18	19.92	5.91	2.87	7.58	1.18	2.49	0.75	0.07	0.05	0.01	0.80	99.78	<0.02	0.12
HS-BD	**DME**	72.06	12.20	2.45	3.41	4.69	0.09	3.48	0.53	0.07	0.03	0.01	0.70	99.72	0.02	0.49
11-12 353		67.51	10.89	3.02	4.60	6.37	0.42	4.12	0.66	0.19	0.03	0.02	1.80	99.64	0.08	1.05
11-12 357		48.22	2.55	1.10	1.96	26.53	0.14	0.90	0.25	0.10	0.03	0.00	18.00	99.79	5.17	0.27
11-12 364		71.54	6.68	2.29	5.14	10.11	0.16	1.97	0.43	0.16	0.04	0.02	1.20	99.76	0.06	0.68
11-12 365		69.28	6.89	2.72	4.88	7.62	0.18	1.70	0.41	0.31	0.04	0.01	5.60	99.67	0.08	0.89
11-12 368	**Transect**	71.14	8.17	2.83	5.17	8.48	0.23	1.62	0.57	0.50	0.04	0.02	1.00	99.73	0.07	0.93
11-12 369a	**One**	48.21	7.23	2.15	3.38	23.98	0.40	1.23	0.43	1.15	0.05	0.03	11.50	99.72	3.55	0.73
11-12 369b		39.75	3.22	2.86	3.35	30.88	0.27	0.19	0.20	0.58	0.10	0.01	18.40	99.78	5.26	0.59
11-12 369c		56.72	3.94	1.17	2.38	20.40	0.24	1.66	0.19	0.49	0.03	0.01	12.50	99.79	3.96	0.31
11-12 372		34.01	2.43	0.81	2.08	32.91	0.78	0.71	0.21	0.39	0.03	0.00	25.40	99.80	7.41	0.25
11-12 387		27.22	3.15	1.12	3.14	36.16	0.08	0.88	0.18	1.88	0.02	0.02	25.80	99.61	8.21	0.50
HS-AI	**Wollastonite**	54.06	4.18	2.03	1.34	34.11	0.10	1.56	0.22	0.06	0.03	0.01	2.10	99.80	0.30	0.02
11-40 534		61.10	7.21	2.56	2.69	19.25	0.15	2.99	0.38	0.24	0.23	0.01	2.50	99.29	0.40	0.03
11-12 164	**KCS**	64.23	11.43	3.82	4.20	8.85	0.68	3.82	0.63	0.74	0.05	0.03	1.20	99.67	0.02	1.24
11-40 119		61.34	8.82	3.36	3.87	14.97	0.42	3.36	0.49	0.33	0.09	0.01	2.50	99.55	0.75	0.52
11-29 51		67.89	11.64	3.52	3.61	4.77	0.91	5.35	0.64	0.36	0.03	0.02	1.00	99.75	0.02	1.02
11-40 535	**Marbles**	49.61	2.53	1.24	1.70	41.61	0.02	0.03	0.18	0.08	0.38	0.00	2.50	99.91	0.61	<0.02
11-12 40	**Stage 3 Min**	64.40	7.30	5.97	5.29	12.83	0.55	0.06	0.51	0.09	0.23	0.01	2.10	99.35	0.05	1.56
10-04 51	**Stage 1- 2 Min**	34.32	1.68	30.18	1.49	6.30	0.01	0.01	0.09	0.03	0.34	<0.002	8.70	83.16	0.17	18.45
11-24 234a		51.77	1.78	26.42	2.26	6.22	0.02	<0.01	0.27	0.25	0.29	0.01	6.00	95.32	0.12	12.27
11-24 234b	**Transect 2**	66.78	2.34	13.54	2.58	6.81	0.07	0.02	0.25	0.40	0.25	0.01	3.50	96.54	0.12	6.18
11-24 234c		64.54	12.14	4.19	3.03	12.22	0.37	0.30	0.69	0.39	0.14	0.02	1.60	99.68	0.07	0.80
11-24 234d		63.67	12.17	3.53	3.61	11.77	0.41	1.92	0.73	0.85	0.11	0.02	0.90	99.68	0.03	0.64

Table 5.10: Idealized skarn to CRD zoning

Feature	Proximal to Fluid source/ Intrusion (<1km)	Central (1-5km)	Distal to fluid source (5-10km)
Skarn: CRD ore	>10	1-10	<1
Garnet:Pyroxene abundance	Pyroxene= garnet	Pyroxene dominated, minor garnet	No garnet
Pyroxene chemistry	Mg rich	Fe rich	Mn rich
Ore sulfides	Ccp>Sp>Gn	Sp>Gn>Ccp	Sp=Gn>Ccp
Peak temperature (^{O}C)	>400	320-400	<320
Fluid inclusion salinity (wt% $NaCl_{equivalent}$)	>15	7.5-15	<7.5
Relative metal concentrations	High Cu and Sn	High Ag	High Zn and Pb
Sphalerite chemistry	Low Fe	In bearing	High Fe
Tetrahedrite chemistry	Cu and Zn rich	--	Ag and Fe rich
Typical structural control	Intrusion related faults	--	Regional tectonic faults
Lithological favorable horizons	Intrusive contacts	Coarse limestones beds	Beneath impermeable horizons

Data from Meinert (1987), Einaudi et al. (1981), Megan et al, (1988), Lynch (1989), Meinert (1992), Sillitoe and Hedenquist (2003), Meinert et al (2005)

Table 5.11. Keg to Keno Comparison Table

	Keno Hill	Stage 3, Keglovic
Mineralogy	Galena, sphalerite, pyrite, pyrrhotite, chalcopyrite, arsenopyrite, jamesonite, tetrahedrite, pyrargyrite, acanthite, stephanite	Galena, sphalerite, pyrite, pyrrhotite, chalocopyrite, arsenipyrite, stephanite, freibergite, hocartite, stannite, cubanite
Depth of Formation	~ 1.6kbar, ~6km	
Tectonic Setting	Transcurrent dextral fault overprinting a regional thrust	Regional thrust
Host Rock	Mississippian Quartzite	Mississippian Limestone/ Siltstone
Metamorphic grade	Greenschist	Greenschist
Fluid Inclusions	Temperature; 205 to 365 (average 300). Salinity; 0 to >20 wt% NaCl Equiv. CO2 and CH4 bearing. Boiling and immiscibility.	Temperature; 162 to 337 (average 300). Salinity; 0 to 25.4 wt% NaCl Equiv. CO2 and CH4 bearing. Boiling and immiscibility.
S, C, Pb sources	Upper crustal	Upper crustal

Keno Hill data from Boyle (1970), Lynch et al. (1990), Beaudoin and Sangster (1992) and Hantelmann (2013).

Chapter 6: Conclusions

The primary aim of this thesis was to link the mineralization at the Keglovic deposit to the tectonic and petrogenetic evolution of the geology in the Tay River district. This thesis first addressed the regional geology of the Tay River district, before focusing on the Keglovic deposit mineralization, including identifying distinct paragenetic stages and placing the mineralized system within a regional context.

Chapter 2 details the results of extensive field mapping, petrography, U-Pb geochronology and whole rock geochemical analyses focused on the study of the voluminous mid-Cretaceous plutons and calderas of the Tay River district; and demonstrates that igneous activity occurred continuously in the district from 110-90 Ma. The igneous activity can be subdivided into three plutonic suites based on time of emplacement: the 109-104 Ma Anvil, the 100-96 Ma Tay River and the 96-90 Ma Tombstone. The younger suites intrude the older suites indicating that the previously hypothesized inboard migration and younging of plutonic suites across the Selwyn Basin (Mortensen et al. 2000, Hart et al. 2004, Rasmussen 2013) does not apply in this region of the northern Cordillera. It was then shown that the temporal classification of suites could be expanded to reclassify mid-Cretaceous plutonism across the northern Cordillera. The reclassified plutonic zones have a concentric pattern around the Yukon-Tanana Terrane and demonstrate an increase in the area affected by mid-Cretaceous igneous activity with time. This new pattern of plutonism cannot be explained by any of the previously published models involving flat slabs, back arc extension or a cryptic western dipping subduction zone (Mortensen et al. 2000, Hart et al. 2004, Mair et al. 2006, Johnston 2008, Rasmussen 2013) and

is best explained by delamination of over thickened lithosphere beneath the Yukon-Tanana terrane at ~115 Ma.

Chapter 3 focused on the development of a method for identifying the sedimentary melt source of an S-type granite, from the Anvil batholith. A novel method involving correcting discordant U-Pb analyses from inherited zircons back onto the concordia was applied to decrypt the age spectrum of discordant zircon cores inherited by the S-type, magma. This method ultimately showed that the Precambrian – Lower Cambrian (Gordey 2013) Hyland Group is the likely melt source for the 109 – 104 Ma S-type granites in the Anvil suite.

Chapter 4 examined the evolution of the Tay River district with the aim of constraining the amount and timing of mid-Cretaceous regional exhumation. U-Pb dating was combined with low temperature thermochronometry from the mid-Cretaceous rocks of the study area. The results of Chapter 4 indicate that intrusion of the Anvil and Tay River suites occurred synchronously with exhumation of the Tay River district. The oldest OMB plutonic rocks, belonging to the Anvil suite, were emplaced at 12–15 km depth at 107±2 Ma. The Anvil suite sample cooled below the ^{40}Ar-^{39}Ar closure temperature in biotite (365–395°C), which corresponds to a depth of 5.5–10.5 km, at ~104±2 Ma. Then subsequently cooled below the U-Th/He closure temperature in zircon (195-215°C), which corresponds to a depth of 2.5-4.7 km, before ~99.2 ± 3 Ma. The magnitude and rate of exhumation is consistent with extensional collapse of previously thickened crust and can be used as support for the delamination hypothesis outlined in Chapter 2. An unexpected conclusion of Chapter 4 was that the zircon U-Th/He data indicated a thermal perturbation in the region in the Late Cretaceous to early Paleogene. Modeling of the thermal perturbation is consistent with derivation from the passage of the northern Cordillera across the Yellowstone hotspot.

Finally, Chapter 5 focused on the study of mineralization at the Keglovic deposit, concluding the Keglovic deposit represents the telescoped superposition of a zoned Ag-Pb-Zn-Cu-Sn skarn, which transitions outwards into a carbonate replacement deposit, and shallower Ag-Pb-Zn-As-Sb vein mineralization. Petrography, isotopic data and a microthermometric study were combined to constrain the fluid chemistry, temperature of formation, mineralogy, and relative age of each of the mineralization events. Dating (via Re-Os on arsenopyrite) of the mineralization at the Keglovic deposit showed that mineral deposition occurred at ~100 Ma concurrent with the igneous activity and regional exhumation outlined in Chapters 2-4. Three main conclusions come out of this study. 1. That meteoric water that had undergone isotopic exchange with the host rock, was involved in all stages of mineralization. 2. That all stages of mineralization at the KMD are created from metals, sulphur and carbon sourced predominantly from the upper crust. 3. That upper crustal fluid circulation was promoted either by igneous intrusion (as shown in Chapter 2), lower crustal heating due to delamination (as shown in Chapter 2), the high geothermal gradient derived from exhumation (as shown in Chapter 4) or a combination of these factors. Chapter 5 also concludes that the principal cause for the change in mineralization from the skarn to vein system is effervescence of the fluid and that the phase separation is promoted by increasing volatile content in the fluid derived from reaction with the local country rock combined with decreasing confining pressure derived from regional exhumation. Therefore, the telescoping of mineralization at the Keglovic deposit is a direct product of the concurrent regional exhumation (constrained in Chapter 4). Overall, Chapter 5 indicates that the individual mineralization events at the Keglovic deposit are comparable with mineralization seen throughout the northern Cordillera. What makes the Keglovic deposit appear unique, and therefore worthy of study, is that these events have been telescoped, which is a direct

consequence of the regional tectonic and igneous events occurring in the Tay River district. Therefore, future exploration for Keglovic type deposits cannot be based purely on the occurrence of specific igneous rocks, but needs to consider the entire regional tectonic setting.

Implications of thesis

The conclusions of this thesis have implications for three broad areas: the regional evolution of the northern Cordillera, mineral exploration within the Cordillera and granite petrology.

Implications for the regional evolution of the northern Cordillera

Chapter 2 concluded that the new pattern of OMB plutonism identified across the northern Cordillera is best explained by delamination of over-thickened lithosphere from beneath the Yukon-Tanana terrane. Lithospheric delamination from specifically below the Yukon-Tanana terrane implies that this allochthonous block was above non-cratonic lithosphere in the mid-Cretaceous. However, seismic imaging of the northern Cordillera (Cook et al. 2004, Cook and Erdmer 2005) indicates that the Yukon-Tanana terrane is presently thrust over the North American craton. The findings outlined in this thesis imply that the transition to thin skinned tectonics in the northern Cordillera did not occur until post the mid-Cretaceous delamination event. Therefore, this constraint must be considered in the development of future models of northern Cordilleran orogeny.

The second broad implication from Chapter 2 comes from the fact that the pattern of OMB plutonism indicates that all terranes covered by the plutonism were accreted to each other prior to the mid-Cretaceous since the suites of plutons span terrane boundaries.

Chapter 4 concluded that the Tay River district underwent significant mid-Cretaceous exhumation likely linked to post-orogenic collapse of a potential mid-Cretaceous plateau. The extent of the exhumation and scale of this plateau has important implications for the nature of Cordilleran development including the propagation of the fold and thrust belt, exposure of deep-crust and development of mineral deposits all of which could be influenced by potential crustal gravity current flow away from the overly thickened lithosphere as inferred in the present day Himalayan system (Copley and McKenzie 2007).

Chapter 4 also suggests that the Tay River district had been thermally affected by the Late Cretaceous passage of the Yellowstone hotspot beneath the northern Cordillera. This represents the most inboard recognition of the Yellowstone hot spot and, therefore, shows that the distribution of hotspot derived thermal/ hydrothermal alteration in the Cordillera is larger than previously recognized. It also raises a question as to why the Carmacks Group Flood basalts are not seen to the north of the Tintina fault, a feature that formed after the basalt extrusion.

Implications for mineral exploration in the northern Cordillera

The new pattern of OMB plutonism defined in this thesis has implications for the distribution of deposit types linked to certain intrusion ages or styles. For example intrusion related gold systems (IRGS) in the Tintina Gold Belt are strongly associated with 92 ± 2 Ma plutons of the Tombstone style (Goldfarb et al., 2000; Hart et al., 2004; Lang and Baker, 2001). The model presented in this thesis suggests that Tombstone style plutonism occurs across the whole OMB not just in the peripheries as was previously believed, therefore there is the potential for IRGS across the Yukon.

This thesis also proposed delamination as the cause of OMB plutonism in the northern Cordillera. Delamination leads to mantle heating from below and coeval regional uplift, which

would generate a high geothermal gradient during OMB magmatism. A high geothermal gradient will promote the development of magmatic-hydrothermal systems and could explain pluton distal deposits and deposits with no genetic link to coeval plutonism (Beaudoin and Sangster, 1992; Robb, 2005). For example, the Keno Hill Ag-Pb-Zn veins are proposed to form from a prolonged hydrothermal cell, but a direct genetic link to a causative pluton has not been found (Lynch, 1989; Hantelmann, 2013). Deposits linked to the flow of metamorphic fluids (i.e. distal base metal veins and orogenic gold deposits) would be expected to occur in areas with the highest geothermal gradient.

Implications for granite petrology

Chapter 3 provided a method to identify the exact melt source of an S-type granite. The ability to identify the protolith of an S-type granite has the potential to solve a number of controversial areas in igneous petrology. Applying the method outlined in this study to identify the sources of other granites could clarify the thermal conditions of the crust at the time of partial melting (Miller et al. 2003, Kemp et al. 2005), the nature of the heat sources causing anatexis (Petford and Gallagher 2001), the processes that control the compositional diversity of granites (Clemens and Stevens 2012), and the kinetics of granitic plumbing systems within sedimentary basins (Petford et al. 2000). Identifying the melt source of an S-type granite could also be used to identify the nature of unexposed crust beneath the igneous body and map the variability of buried sedimentary units across a region.

Future Directions

Although I believe this thesis has improved our understanding of the OMB and the mid-Cretaceous evolution of the northern Cordillera the models developed within these pages need a

substantial amount of support if they are to be accepted by the rest of the northern Cordilleran geological community.

Testing of the model developed in Chapters 2 and 4 requires additional detailed U-Pb, isotopic and petrographic studies of granites from across the OMB gathered within the temporal classification of suites. For example the Yukon wide prevalence of the volumetrically minor 92 Ma plutons can only be confirmed by detailed mapping and dating of plutonic bodies, as the presence of Tombstone suite plutons may be masked by the volumetrically more significant Anvil or Tay River suites.

Thermochronological studies across the Northern Cordillera are needed to define the areal extent of mid-Cretaceous regional exhumation. These studies will also more accurately define the dimensions and properties of the Late Cretaceous to Paleogene thermal pulse and confirm whether it could be linked to the Yellowstone hotspot.

Additionally the method for identifying the melt source of S-type granites developed in Chapter 3 could be used worldwide. Using the method globally will allow the implications for granite petrology to be fully explored.

Overall, the continued exploration within the Yukon relies on the speculation there are still significant mineral deposits to be discovered within the northern Cordillera. The fact these deposits have remained hidden through over 125 years of exploration in the Territory indicates discovery will only occur if exploration is based on a detailed understanding of regional tectonics, geology and igneous petrography. This thesis has hopefully in some small part added to the understanding of the OMB and therefore will help to contribute to the next great mineral discovery in the Yukon. However, confirming, developing and defending the theories outlined within these pages represents a lifetime of work.

References

Adney, T. 1994. The Klondike Stampede. UBC Press, Vancouver.

Aleinikoff, J., Farmer, G.L., Rye, R.O., and Nokleberg, W.J. 2000. Isotopic evidence for the sources of Cretaceous and Tertiary granitic rocks, east-central Alaska: implications for the tectonic evolution of the Yukon-Tanana Terrane. Canadian Journal of Earth Sciences, **37**: 945–956. doi:10.1139/e00-006.

Andrew, A., Godwin, C., and Sinclair, A. 1984. Mixing line isochrons; a new interpretation of galena lead isotope data from southeastern British Columbia. Economic Geology, **79**: 919–932.

Angen, J.J., Van Staal, C.R., Lin, S., Nelson, J.A.L., Mahoney, J.B., Davis, D.W., and McClelland, W.C. 2014. Kinematics and timing of shear zone deformation in the western Coast Belt: Evidence for mid-Cretaceous orogen-parallel extension. Journal of Structural Geology, **68**: 273–299. Elsevier Ltd. doi:10.1016/j.jsg.2014.05.026.

Armstrong, R.L. 1988. Mesozoic and early Cenozoic magmatic evolution of the Canadian Cordillera. *In* Processes in continental lithospheric deformation: Geological Society of America Special Paper 218. pp. 55–91. doi:10.1130/SPE218-p55.

Arndt, N.T., and Goldstein, S.L. 1987. Use and abuse of crust-formation ages. Geology, **15**: 893–895. doi:10.1130/0091-7613(1987)15<893.

Bacon, C.R., Foster, H.L., and Smith, J.G. 1990. Rhyolitic calderas of the Yukon-Tanana terrane, east-central Alaska: volcanic remnants of a mid-Cretaceous magmatic arc. Journal of Geophysical Research, **95**: 21451–21461.

Bakker, R.J. 1997. Clathrates: Computer programs to calculate fluid inclusion V-X properties using clathrate melting temperatures. Computers & Geosciences, **23**: 1–18. doi:10.1016/S0098-3004(96)00073-8.

Baldwin, S.L., and Lister, S. 1998. Thermochronology of the South Cyclades Shear zone, Ios, Greece: Effects of ductile shear in the argon partial retention zone. Journal of Geophysical Research, **103**: 7315–7336.

Bao, X., Eaton, D.W., and Guest, B. 2014. Plateau uplift in western Canada caused by lithospheric delamination along a craton edge. Nature Geoscience, **7**: 830–833. doi:10.1038/ngeo2270.

Bardoux, M., and Mareschal, J.-C. 1994. Extension in south-central British Columbia: mechanical and thermal controls. Tectonophysics, **238**: 451–470. doi:10.1016/0040-1951(94)90068-X.

Barnes, H. 1979. Solubilities of ore minerals. Geochemistry of hydrothermal ore deposits,.

Barnes, H. 1997. Geochemistry of hydrothermal ore deposits. *In* 2nd edition. *Edited by* H.L. Barnes. Wiley- Interscience.

Barrett, T.., and Anderson, G.. 1988. The solubility of sphalerite and galena in 1–5 m NaCl solutions to 300°C. Geochimica et Cosmochimica Acta, **52**: 813–820. doi:10.1016/0016-7037(88)90353-5.

Barton, M.D., and Young, S. 2002. Non-pegmatitic Deposits of Beryllium: Mineralogy, Geology, Phase Equilibria and Origin. Reviews in Mineralogy and Geochemistry,

50: 591–691. doi:10.2138/rmg.2002.50.14.
Batt, G.E., and Brandon, M.T. 2002. Lateral thinking: 2-D interpretation of thermochronology in convergent orogenic settings. Tectonophysics, **349**: 185–201. doi:10.1016/S0040-1951(02)00053-7.
Bea, F. 2012. The sources of energy for crustal melting and the geochemistry of heat-producing elements. Lithos, **153**: 278–291. Elsevier B.V. doi:10.1016/j.lithos.2012.01.017.
Beaudoin, G. 1992. Isotopic evidence for complex Pb sources in the Ag-Pb-Zn-Au veins of the Kokanee Range, southeastern British Columbia. Canadian Journal of Earth Sciences, **29**: 418–431.
Beaudoin, G., and Sangster, D.F. 1992. A descriptive model for silver-lead-zinc veins in clastic metasedimentary terranes. Economic Geology, **87**: 1005–1021. doi:10.2113/gsecongeo.87.4.1005.
Beaudoin, G., Taylor, B.E., and Sangster, D.F. 1991. Silver-lead-zinc veins, metamorphic core complexes, and hydrologic regimes during crustal extension. Geology, **19**: 1217–1220.
Belousova, E.A., Griffin, W.L., O'Reilly, S.Y., and Fisher, N.I. 2002. Igneous zircon: trace element composition as an indicator of source rock type. Contributions to Mineralogy and Petrology, **143**: 602–622. doi:10.1007/s00410-002-0364-7.
Belshaw, N.., Freedman, P.., O'Nions, R.., Frank, M., and Guo, Y. 1998. A new variable dispersion double-focusing plasma mass spectrometer with performance illustrated for Pb isotopes. International Journal of Mass Spectrometry, **181**: 51–58. doi:10.1016/S1387-3806(98)14150-7.
Beranek, L.P., and Mortensen, J.K. 2011. The timing and provenance record of the Late Permian Klondike orogeny in northwestern Canada and arc-continent collision along western North America. Tectonics, **30**: 1–23. doi:10.1029/2010TC002849.
Berman, R.G., Ryan, J.J., Gordey, S.P., and Villeneuve, M. 2007. Permian to Cretaceous polymetamorphic evolution of the Stewart River region, Yukon-Tanana terrane, Yukon, Canada: P-T evolution linked with in situ SHRIMP monazite geochronology. Journal of Metamorphic Geology, **25**: 803–827. doi:10.1111/j.1525-1314.2007.00729.x.
Berry, R.F., Jenner, G.A., Meffre, S., and Tubrett, M.N. 2001. A North American provenance for Neoproterozoic to Cambrian sandstones in Tasmania? Earth and Planetary Science Letters, **192**: 207–222. doi:10.1016/S0012-821X(01)00436-8.
Bineli Betsi, T., Lentz, D., McInnes, B., Evans, N.J., and Hanley, J. 2012. Emplacement ages and exhumation rates for intrusion-hosted Cu–Mo–Sb–Au mineral systems at Freegold Mountain (Yukon, Canada): assessment from U–Pb, Ar–Ar, and (U–Th)/He geochronometers. Canadian Journal of Earth Sciences, **49**: 653–670. doi:10.1139/E2012-009.
Bodnar, R.J. 1993. Revised equation and table for determining the freezing point depression of H2O-Nacl solutions. Geochimica et Cosmochimica Acta, **57**: 683–684. doi:10.1016/0016-7037(93)90378-A.
Boghossian, N.D., Patchett, P.J., Ross, G.M., and Gehrels, G.E. 1996. Nd Isotopes and the Source of Sediments in the Miogeocline of the Canadian Cordillera. The Journal

of Geology, **104**: 259–277.
Borg, L.E., and Clynne, M. a. 1998. The Petrogenesis of Felsic Calc-alkaline Magmas from the Southernmost Cascades, California: Origin by Partial Melting of Basaltic Lower Crust. J. Petrology, **39**: 1197–1222. doi:10.1093/petroj/39.6.1197.
Bortnikov, N.S., Zaozerina, O.N., Genkin, a. D., and Muravitskaya, G.N. 1990. Stannite-Sphalerite intergrowths—Possible Indicators of Conditions of Ore Deposition. International Geology Review, **32**: 1132–1144. doi:10.1080/00206819009465845.
Bottinga, Y. 1968. Calculation of Fractionation Factors for Carbon and Oxygen Isotopic Exchange in the System Calcite-Carbon Dioxide-Water. The Journal of Physical Chemistry, **72**: 800–808. doi:10.1021/j100849a008.
Boyle, R., W, Wanless, R, K., and Stevens, R.D. 1970. Sulfur Isotope Investigation of the Lead-Zinc-Silver-Cadmium Deposits of the Keno Hill- Galena Hill Area, Yukon, Canada. Economic Geology, **65**.
Brand, A. 2011. The Keg Property : Mineralogical Investigation Report.
Brandon, M., Roden-Tice, M., and Garver, J.I. 1998. Late Cenozoic exhumation of the Cascadia accretionary wedge in the Olympic Mountains , northwest Washington State. Geological Society of America Bulletin, **110**: 985–1009.
Brown, P.E., and Lamb, W.M. 1989. P-V-T properties of fluids in the system H 2O±CO 2±NaCl: New graphical presentations and implications for fluid inclusion studies. Geochimica Et Cosmochimica Acta, **53**: 1209–1221.
Burnham, C.W. 1985. Energy release in subvolcanic environments: implications for breccia formation. Economic Geology, **80**: 1515–1522. doi:10.2113/gsecongeo.80.6.1515.
Caine, J.S., Evans, J.P., and Forster, C.B. 1996. Fault zone architechture and permeability structure. Geology, **24**: 1025–1028. doi:10.1130/0091-7613(1996)024<1025.
Campbell, I.H., and Griffihs, R.W. 1990. Implications of mantle plume structure for the evolution of flood basalts. Earth and Planetary Science Letters, **99**: 79–93.
Campbell, R.B. 1967. Campbell, R.B., 1967. Reconnaissance geology of Glenlyon map area, Yukon Territory (105L). al Survey of Canada, Memoir,: 92.
Cathro, R.J. 1967. Preliminary report on 1967 exploration program on the Caribou Lake property; assessment report #019007.
Cecile, M.P., Morrow, D.W., and Williams, G.K. 1997. Early Paleozoic (Cambrian to Early Devonian) tectonic framework, Canadian Cordillera.
Chappell, B.W., and Stephens, W.E. 1988. Origin of infracrustal (I-type) granite magmas. Trans. Royal Soc. Edinburgh: Earth Sciences, **79**: 71–86. doi:10.1017/S0263593300014139.
Chappell, B.W., and White, A.J.R. 1974. Two contrasting granite types. Pacific Geology, **8**: 173–174.
Clemens, J.D. 2003. S-type granitic magmas - petrogenetic issues, models and evidence. Earth-Science Reviews, **61**: 1–18. doi:10.1016/S0012-8252(02)00107-1.
Clemens, J.D., and Mawer, C.K. 1992. Granitic magma transport by fracture propagation. Tectonophysics, **204**: 339–360. doi:10.1016/0040-1951(92)90316-X.

Clemens, J.D., and Stevens, G. 2012. What controls chemical variation in granitic magmas? Lithos, **134–135**: 317–329. Elsevier B.V. doi:10.1016/j.lithos.2012.01.001.

Cline, J., and Bodnar, R.J. 1991. Can Economic Porphry Copper Mineralization be Generated by a Typical Calc-Alkaline Melt? Journal of Geophysical Research, **96**: 8113–8126.

Cobbett, R. 2015. Bedrock Geology of Anvil Lake Area, Central Yukon (1:50000 Scale). Yukon Geological Survey, Open File, **2016**.

Collins, W. 1994. Upper- and middle- crustal response to delamination: An example from the Lachlan fold belt, eastern Australia. Geology, **22**: 143–146.

Colpron, M., Nelson, J.L., and Murphy, D.C. 2007. Northern Cordilleran terranes and their interactions through time. GSA Today, **17**: 4. doi:10.1130/GSAT01704-5A.1.

Colpron, M., Price, R.A., Archibald, D.A., and Carmichael, D.M. 1996. Middle Jurassic exhumation along the western flank of the Selkirk fan structure: Thermobarometric and thermochronometric constraints from the Illecillewaet synclinorium, southeastern British Columbia. Bulletin of the Geological Society of America, **108**: 1372–1392. doi:10.1130/0016-7606(1996)108<1372:MJEATW>2.3.CO;2.

Connolly, C.A., Walter, L.M., and Baadsgarrd, H. 1990. Origin and evolution of formation waters, Alberta Basin, Western Canada Sedimentary Basin. I. Chemistry. Applied Geochemistry, **5**: 375–395.

Cook, F.A., Clowes, R.M., Snyder, D.B., van der Velden, A.J., Hall, K.W., Erdmer, P., and Evenchick, C.A. 2004. Precambrian crust beneath the Mesozoic northern Canadian Cordillera discovered by Lithoprobe seismic reflection profiling. Tectonics, **23**: 28. doi:Tc2010 Artn tc2010.

Cook, F. a, and Erdmer, P. 2005. An 1800 km cross section of the lithosphere through the northwestern North American plate: lessons from 4.0 billion years of Earth's history. Canadian Journal of Earth Sciences, **42**: 1295–1311. doi:10.1139/e04-106.

Cook, N.J., Ciobanu, C.L., Pring, A., Skinner, W., Shimizu, M., Danyushevsky, L., Saini-Eidukat, B., and Melcher, F. 2009. Trace and minor elements in sphalerite: A LA-ICPMS study. Geochimica et Cosmochimica Acta, **73**: 4761–4791. Elsevier Ltd. doi:10.1016/j.gca.2009.05.045.

Copley, A., and McKenzie, D. 2007. Models of crustal flow in the India-Asia collision zone. Geophysical Journal International, **169**: 683–698. doi:10.1111/j.1365-246X.2007.03343.x.

Courtillot, V.E., and Renne, P.R. 2003. On the ages of flood basalt events. Comptes Rendus - Geoscience, **335**: 113–140. doi:10.1016/S1631-0713(03)00006-3.

Crawford, M.L. 1981. Phase equilibria in aqueous fluid inclusions. Mineralogical Association of Canada, **Short Cour**: 75–100.

Creaser, R.A., Erdmer, P., Stevens, R.A., and Grant, S.L. 1997. Tectonic affinity of Nisutlin and Anvil assemblage strata from the Teslin tectonic zone, northern Canadian Cordillera: Constraints from neodymium isotope and geochemical evidence. Tectonics, **16**: 107–121. doi:10.1029/96TC03317.

Creaser, R.A., Gütter, H., Carlson, J., and Crawford, B. 2004. Macrocrystal phlogopite Rb-Sr dates for the Ekati property kimberlites, Slave Province, Canada: Evidence

for multiple intrusive episodes in the Paleocene and Eocene. Lithos, **76**: 399–414. doi:10.1016/j.lithos.2004.03.039.
D'Souza, R.J., Canil, D., and Creaser, R.A. 2016. Assimilation, differentiation, and thickening during formation of arc crust in space and time: The Jurassic Bonanza arc, Vancouver Island, Canada. Bulletin of the Geological Society of America, **128**: 543–557. doi:10.1130/B31289.1.
Dalrymple, G.B., and Lanphere, M.A. 1974. 40Ar/39Ar age spectra of some undisturbed terrestrial samples. Geochimica et Cosmochimica Acta, **38**: 715–738. doi:10.1016/0016-7037(74)90146-X.
Davis, D.W., Lowenstein, T.K., and Spencer, R.J. 1990. Melting behavior of fluid inclusions in laboratory-grown halite crystals in the systems NaCl-H2O, NaCl- KCl-H2O, NaCl-MgCl2-H2O, and NaCl-CaCl2-H2O. Geochimica et Cosmochimica Acta, **54**: 591–601. doi:10.1016/0016-7037(90)90355-O.
Day, W.C., Alenikoff, J.N., Dusel-Bacon, C., Goldfarb, R., Gough, L.P., and O'Neill, J.M. 2002. Complex Mesozoic deformation in the Central part of the Yukon-Tanana Upland, Alaska - Implications for Gold Deposition in the Tintina Gold Province. *In* Geological Society of America Annual Meeting. Denver, Colorado.
DeGraaff-Surpless, K., Mahoney, J.B., Wooden, J.L., and McWilliams, M.O. 2003. Lithofacies control in detrital zircon provenance studies: Insights from the Cretaceous Methow basin, southern Canadian Cordillera. Bulletin of the Geological Society of America, **115**: 899–915. doi:10.1130/B25267.1.
Deklerk, R., and Traynor, S. 2005. Yukon MINFILE- A database of mineral occurrences. Available from http://data.geology.gov.yk.ca/ [accessed 1 January 2017].
Delaney, G.D. 1981. The Mid-Proterozoic Wernecke Supergroup, Wernecke Mountains, Yukon Territory. In: Proterozoic Basins of Canada (eds. Campbell F.H.A). Geological Survey of Canada, **Paper 81-1**: 1–23. Geological Survey of Canada.
Diamond, L.W. 1992. Stability of Co2 Clathrate Hydrate+Co2 Liquid+Co2 Vapour+Aqueous Kcl-Nacl Solutions - Experimental-Determination and Application to Salinity Estimates of Fluid Inclusions. Geochimica et Cosmochimica Acta, **56**: 273–280. doi:10.1016/0016-7037(92)90132-3.
Diamond, L.W. 2001. Review of the systematics of CO2-H2O fluid inclusions. Lithos, **55**: 69–99. doi:10.1016/S0024-4937(00)00039-6.
Dick, L., and Hodgson, C. 1982. The MacTung W-Cu (Zn) Contact Metasomatic and Related Deposits of the Northeastern Canadian Cordillera. Economic geology, **77**: 845–867.
Dilworth, K.M., Mortensen, J.K., Ebert, S., Tosdal, R.M., Smith, M.T., and Roberts, P. 2007. Cretaceous reduced granitoids in the Goodpaster Mining District, east central Alaska. Canadian Journal of Earth Sciences, **44**: 1347–1373. doi:10.1139/E07-014.
Dodson, M.H. 1973. Closure temperature in cooling geochronological and petrological systems. Contributions to Mineralogy and Petrology, **40**: 259–274. doi:10.1007/BF00373790.
Driver, L. 1998. Petrogenesis of the Cretaceous Cassiar Batholith, Yukon-B.C., Canada: Implications for Magmatism in the North Ameircan Corilleran Interior. Masters, Thesis, University of Alberta.

Driver, L.A., Creaser, R.A., Chacko, T., and Erdmer, P. 2000. Petrogenesis of the Cretaceous Cassiar batholith, Yukon–British Columbia, Canada: Implications for magmatism in the North American Cordilleran Interior. Geological Society of America Bulletin, **112**: 1119–1133.

Drummond, S.E., and Ohmoto, H. 1985. Chemical evolution and mineral deposition in boiling hydrothermal systems. Economic Geology, **80**: 126–147. doi:10.2113/gsecongeo.80.1.126.

Ducea, M.N. 2011. Fingerprinting orogenic delamintation. Geology,. doi:10.1016/j.

Dufek, J., and Bergantz, G.W. 2005. Lower crustal magma genesis and preservation: A stochastic framework for the evaluation of basalt-crust interaction. Journal of Petrology, **46**: 2167–2195. doi:10.1093/petrology/egi049.

Dumala, M. 2013. Assessment Report describing Geological Mapping, Prospecting, Geochemical Survery and Diamond Drilling at the Keg Property.

Dusel-Bacon, C., Lanphere, M.A., Sharp, W.D., Layer, P.W., and Hansen, V.L. 2002. Mesozoic thermal history and timing of structural events for the Yukon – Tanana Upland , east-central Alaska : 40 Ar / 39 Ar data from metamorphic and plutonic rocks. Canadian Journal of Earth Sciences, **39**: 1013–1051. doi:10.1139/E02-018.

Eaton, S. 2011. Geological mapping, prospecting, geochemical sampling, geophysical surveying, road building, baseline water surveying and diamond drilling at the Keg property. Whitehorse Mining District, Yukon Territory.

Ehlers, T. a. 2005. Computational Tools for Low-Temperature Thermochronometer Interpretation. Reviews in Mineralogy and Geochemistry, **58**: 589–622. doi:10.2138/rmg.2005.58.22.

Einaudi, M., Meinert, L., and Newberry, R. 1981. Skarn Deposits. Economic Geology, **75th Anniv**: 317–391.

Elston, D.P., Enkin, R.J., Baker, J., and Kisilevsky, D.K. 2002. Tightening the Belt: Paleomagnetic-stratigraphic constraints on deposition, correlation, and deformation of the Middle Proterozoic (ca. 1.4 Ga) Belt-Purcell Supergroup, United States and Canada. Bulletin of the Geological Society of America, **114**: 619–638. doi:10.1130/0016-7606(2002)114<0619:TTBPSC>2.0.CO;2.

England, P.C., and Thompson, A.B. 1986. Some thermal and tectonic models for crustal melting in continental collision zones. *In* Collision Tectonics. *Edited by* M.. Coward and A.C. Ries. pp. 83–94.

Evenchick, C., McMechan, M.E., McNicoll, V.J., and Carr, S.D. 2007. A synthesis of the Jurassic–Cretaceous tectonic evolution of the central and southeastern Canadian Cordillera: Exploring links across the orogen. The Geological Society of America, **Special Pa**: 117–145. doi:10.1130/2007.2433(06).For.

Farley, K.A. 2002. (U-Th)/He Dating: Techniques, Calibrations, and Applications. Reviews in Mineralogy and Geochemistry, **47**: 819–844. doi:10.2138/rmg.2002.47.18.

Farley, K.A., Wolf, R.A., and Silver, L.T. 1996. The effects of long alpha-stopping distances on (U-Th)/He ages. Geochimica et Cosmochimica Acta, **60**: 4223–4229. doi:10.1016/S0016-7037(96)00193-7.

Farmer, G.L., Glazner, A.F., and Manley, C.R. 2002. Did lithospheric delamination

trigger late Cenozoic potassic volcanism in the southern Sierra Nevada, California? Bulletin of the Geological Society of America, **114**: 754–768. doi:10.1130/0016-7606(2002)114<0754:DLDTLC>2.0.CO;2.

Fedo, C.M., Sircombe, K.N., and Rainbird, R.H. 2003. Detrital zircon analysis of the sedimentary record. Reviews in Mineralogy & Geochemistry, **53**: 277–303. doi:10.2113/0530277.

Ferry, J.M., and Watson, E.B. 2007. New thermodynamic models and revised calibrations for the Ti-in-zircon and Zr-in-rutile thermometers. Contributions to Mineralogy and Petrology, **154**: 429–437. doi:10.1007/s00410-007-0201-0.

Flowers, R.M., Ketcham, R.A., Shuster, D.L., and Farley, K.A. 2009. Apatite (U-Th)/He thermochronometry using a radiation damage accumulation and annealing model. Geochimica et Cosmochimica Acta, **73**: 2347–2365. Elsevier Ltd. doi:10.1016/j.gca.2009.01.015.

French, B.M. 1965. Some geological implicatcons of equilibrium between graphite and a C-H-O gas phase at high temperatures and pressures. Reviews in Geophysics, **4**: 223–253.

Fuis, G.S., Moore, T.E., Plafker, G., Brocher, T.M., Fisher, M.A., Mooney, W.D., Nokleberg, W.J., Page, R.A., Beaudoin, B.C., Christensen, N.I., Levander, A.R., Lutter, W.J., Saltus, R.W., and Ruppert, N.A. 2008. Trans-Alaska Crustal Transect and continental evolution involving subduction underplating and synchronous foreland thrusting. Geology, **36**: 267–270. doi:10.1130/G24257A.1.

Furlanetto, F., and Thorkelson, D.J. 2009. Preliminary results of detrital zircon geochronology, Wernecke Supergroup, Yukon. In: Yukon Exploration and Geology 2008, L.H. Weston, L.R. Blackburn and L.L. Lewis (eds.), Yukon Geological Survey,: 125–136.

Gabrielse, H. 1998. Geology of Cry Lake and Dease Lake Map Areas, North-Central British Columbia. Geological Survey of Canada Bulletin, **504**.

Gabrielse, H., Murphy, D.C., and Mortensen, J.K. 2006. Cretaceous and Cenozoic dextral orogen-parallel displacements, magmatism, and paleogeography, north-central Canadian Cordillera. *In* Paleogeography of the North American Cordillera: Evidence for and against Large-Scale displacements, Geological. *Edited by* J.W. Haggart, R.J. Enkin, and J.W.. Monger. Geological Association of Canada. pp. 255–277.

Gallagher, C.C. 1999. Regional-Scale Transposition and Late Large-Scale Folding in the Teslin Zone, Pelly Mountains, Yukon. Carleton University, Ottawa.

Garzione, C.N., Molnar, P., Libarkin, J.C., and MacFadden, B.J. 2006. Rapid late Miocene rise of the Bolivian Altiplano: Evidence for removal of mantle lithosphere. Earth and Planetary Science Letters, **241**: 543–556. doi:10.1016/j.epsl.2005.11.026.

Garzione, C.N., Patchett, P.J., Ross, G.M., and Nelson, J. 1997. Provenance of Paleozoic sedimentary rocks in the Canadian Cordilleran miogeocline: a Nd isotopic study. Canadian Journal of Earth Sciences, **34**: 1603–1618. doi:10.1139/e17-129.

Gehrels, G., Rusmore, M., Woodsworth, G., Crawford, M., Andronicos, C., Hollister, L., Patchett, J., Ducea, M., Butler, R., Klepeis, K., Davidson, C., Friedman, R., Haggart, J., Mahoney, B., Crawford, W., Pearson, D., and Girardi, J. 2009. U-Th-Pb

geochronology of the Coast Mountains batholith in north-coastal British Columbia : Constraints on age and tectonic evolution. Geological Society of America Bulletin, **121**: 1341–1361. doi:10.1130/B26404.1.

Gehrels, G.E., Johnsson, M.J., and Howell, D.G. 1999. Detrital zircon geochronology of the Adams Argillite and Nation River Formation, East-Central Alaska, U.S.A. Journal of Sedimentary Research, **69**: 135–144. doi:10.2110/jsr.69.135.

Ghosh, D.K., and Lambert, R.S.J. 1989. NdSr isotopic study of Proterozoic to Triassic sediments from southeastern British Columbia. Earth and Planetary Science Letters, **94**: 29–44. doi:10.1016/0012-821X(89)90081-2.

Giesemann, A., Jaeger, H.-J., Norman, A.L., Krouse, H.R., and Brand, W.A. 1994. Online Sulfur-Isotope Determination Using an Elemental Analyzer Coupled to a Mass Spectrometer. Analytical Chemistry, **66**: 2816–2819. doi:10.1021/ac00090a005.

Godwin, C., and Sinclair, A. 1982. Average Lead Isotope Growth Curves for Shale-Hosted Zinc-Lead Deposits, Canadian Cordillera. Economic Geology, **77**: 675–690.

Göğüş, O.H., and Pysklywec, R.N. 2008a. Mantle lithosphere delamination driving plateau uplift and synconvergent extension in eastern Anatolia. Geology, **36**: 723. doi:10.1130/G24982A.1.

Göğüş, O.H., and Pysklywec, R.N. 2008b. Near-surface diagnostics of dripping or delaminating lithosphere. Journal of Geophysical Research, **113**: B11404. doi:10.1029/2007JB005123.

Goldfarb, R., Hart, C., Miller, M., Miller, L., Farmer, G.L., and Groves, D. 2000. The Tintina Gold Belt- A Global Perspective. *In* The Tintina Gold Belt: Concepts, …. *Edited by* T.L. Tucker and M.T. Smith. British Columbia and Yukon Chamber of Mines. pp. 5–34.

Goldstein, S.L., O'Nions, R.K., and Hamilton, P.J. 1984. A Sm-Nd isotopic study of atmospheric dusts and particulates from major river systems. Earth and Planetary Science Letters, **70**: 221–236. doi:10.1016/0012-821X(84)90007-4.

Goldstein, T.P., and Aizenshtat, Z. 1994. Thermochemical Sulfate Reduction A Review. Journal of Thermal Analysis, **42**: 241–290.

Goodfellow, W. 2007. Base Metal Metallogeny of the Selwyn Basin, Canada. … deposit-types, district metallogeny, the evolution of …,: 553–579.

Goodfellow, W., and Lydon, J. 2007. Sedimentary Exhalative (SEDEX) Deposits. Mineral deposits of Canada,: 163–183.

Gordey, S.P. 1988. The South Fork Volcanics: mid- Cretaceous caldera fill tuffs in east-central Yukon. *In* Current Research, Part E, Geological Survey of Canada, Paper 88-1E.

Gordey, S.P. 2013. Evolution of the Selwyn Basin region, Sheldon Lake and Tay River map areas, central Yukon. Geological Survey of Canada Bulletin, **599**. doi:10.4095/293034.

Gordey, S.P., and Anderson, R.G. 1993. Evolution of the northern Cordilleran miogeocline, Nahanni map area (105I), Yukon and Northwest Territories. *In* Geological Survey of Canada Memoir.

Gordey, S.P., and Irwin, S.E.B. 1987. Geology of Sheldon Lake and Tay River Map

Areas, Yukon Territory. Geoloigcal Survey of Canada,.
Grant, S.Ll. 1997. Geochemical, radiogenic tracer isotopic, and U-Pb geochronological studies of Yukon Tanana terrane rocks from the Money klippe, southeastern Yukon, Canada.Masters Thesis. University of Alberta.
Grantz, A., and May, S.D. 1983. Rifting history and structural development of the continental margin north of Alaska. *In* Studies in Continental Margin Geology, Memoir 34. *Edited by* J.. Watkins and C.. Drake. American Association of Petroleum Geologists. pp. 77–100.
Grond, H.C., Churchill, S.J., Armstrong, R.L., Harakal, J.E., and Nixon, G.T. 1984. Late Cretaceous age of the Hutshi, Mount Nansen, and Carmacks groups, southwestern Yukon Territory and northwestern British Columbia. Canadian Journal of Earth Sciences, **21**: 554–558.
Grove, M., and Harrison, T.M. 1996. 40Ar* diffusion in Fe-rich biotite. American Mineralogist, **81**: 940–951.
Guenthner, W.R., Reiners, P.W., DeCelles, P.G., and Kendall, J. 2014a. Sevier belt exhumation in central Utah constrained from complex zircon (U-Th)/He data sets: Radiation damage and He inheritance effects on partially reset detrital zircons. Bulletin of the Geological Society of America, **127**: 323–348. doi:10.1130/B31032.1.
Guenthner, W.R., Reiners, P.W., Ketcham, R.A., Nasdala, L., and Giester, G. 2013. Helium diffusion in natural zircon: radiation damage, anisotropy, and the interpretation of zircon (U-TH)/He thermochronology. American Journal of Science, **313**: 145–198. doi:10.2475/03.2013.01.
Guenthner, W.R., Reiners, P.W., and Tian, Y. 2014b. Interpreting date-eU correlations in zircon (U-Th)/He datasets: A case study from the Longmen Shan, China. Earth and Planetary Science Letters, **403**: 328–339. Elsevier B.V. doi:10.1016/j.epsl.2014.06.050.
Guynn, J., and Gehrels, G. 2010. K-S Test. Arizona Laser Chron, Tuscon.
Hadlari, T., Davis, W.J., Dewing, K., Heaman, L.M., Lemieux, Y., Ootes, L., Pratt, B.R., and Pyle, L.J. 2012. Two detrital zircon signatures for the Cambrian passive margin of northern laurentia highlighted by new U-Pb results from Northern Canada. Bulletin of the Geological Society of America, **124**: 1155–1168. doi:10.1130/B30530.1.
Hadlari, T., Lemieux, Y., Tylosky, S.A., Zantvoort, W.G., and Catuneanu, O. 2009. Slope and submarine fan turbidite facies of the Upper Devonian Imperial Formation, northern Mackenzie Mountains, NWT. Bulletin of Canadian Petroleum Geology, **57**: 192–208. doi:10.2113/gscpgbull.57.2.192.
Hansen, V.L., and Dusel-Bacon, C. 1998. Structural and kinematic evolution of the Yukon-Tanana upland tectonites , east-central Alaska : A record of late Paleozoic to Mesozoic crustal assembly. Geological Society of America Bulletin, **110**: 211–230.
Hantelmann, J.J. 2013. The paragenesis & geochemistry of the Bellekeno Ag-Pb-Zn vein, Keno Hill district, Yukon, Canada. Masters Thesis. University of Alberta. doi:10.1017/CBO9781107415324.004.
Hardebol, N.J., Pysklywec, R.N., and Stephenson, R. 2012. Small-scale convection at a

continental back-arc to craton transition: Application to the southern Canadian Cordillera. Journal of Geophysical Research: Solid Earth, **117**: 1–18. doi:10.1029/2011JB008431.

Hart, C. 1995. Magmatic and Tectonic Evolution of the Intermontane Superterrane and Coast Plutonic Complex in Southern Yukon Territory. University of British Columbia.

Hart, C.J.R., Goldfarb, R.J., Lewis, L.L., and Mair, J.L. 2004. The Northern Cordilleran Mid-Cretaceous Plutonic Province : Ilmenite/Magnetite-series granitoids and intrusion-related mineralisation. Resource Geology, **54**: 253–280.

Haschke, M., and Günther, A. 2003. Balancing crustal thickening in arcs by tectonic vs. magmatic means. Geology, **31**: 933–936. doi:10.1130/G19945.1.

Heaman, L.M., LeCheminant, A.N., and Rainbird, R.H. 1992. Nature and timing of Franklin igneous events, Canada: Implications for a Late Proterozoic mantle plume and the break-up of Laurentia. Earth and Planetary Science Letters, **109**: 117–131. doi:10.1016/0012-821X(92)90078-A.

Hedenquist, J.W., and Henley, R.W. 1985. The Importance of CO2 on Freezing Point Measurements of Fluid Inclusions: Evidence from Active Geothermal Systems and Implications for Epithermal Ore Deposition. Economic Geology, **80**: 1379–1406. doi:10.2113/gsecongeo.80.5.1379.

Heffernan, R.S. 2004. Temporal, Geochemical, Isotopic, and Metallogenic Studies of mid-Cretaceous Magmatism in the Tintina Gold Province, southeastern Yukon and southwestern Northwest Territories, Canada. MSc. Thesis, University of British Columbia,.

Hildebrand, R.S. 2009. Did Westward Subduction Cause Cretaceous – Tertiary Orogeny in the North American Cordillera ? Geological Society of America Special Papers, **457**: 1–71. doi:10.1130/2009.2457.

Hildebrand, R.S. 2014. Geology, Mantle Tomography, and Inclination Corrected Paleogeographic Trajectories Support Westard Subduction During Cretaceous Orogensis in the North American Cordillera. Geoscience Canada, **41**: 207–224.

Hildebrand, R.S., Hoffman, P.F., and Bowring, S.A. 1987. Tectono-magmatic evolution of the 1.9-Ga Great Bear magmatic zone, Wopmay orogen, northwestern Canada. Journal of Volcanology and Geothermal Research, **32**: 99–118. doi:10.1016/0377-0273(87)90039-4.

Hitchon, B., and Friedman, I. 1969. Geochemistry and origin of formation waters in the western Canada sedimentary basin-I . Stable isotopes of hydrogen and oxygen. Geochimica et Cosmochimica Acta, **33**.

Hitchon, B., and Krouse, H.R. 1972. Hydrogeochemistry of the surface waters of the Mackenzie River drainage basin, Canada-III. Stable isotopes of oxygen, carbon and sulphur. Geochimica et Cosmochimica Acta, **36**: 1337–1357. doi:10.1016/0016-7037(72)90066-X.

Hodges, K. V. 2003. Geochronology and Thermochronology in Orogenic Systems. *In* Treatise on Geochemistry, 1st edition. *Edited by* R. Rudnick. Elsevier Science. pp. 263–292.

Hoefs, J. 1997. Stable Isotope Geochemistry. *In* 7th edition. Springer.

Hoffman, P.F. 1989. Precambrian geology and tectonic history of North America. In: The geology of North America- an overview. (eds. Bally, A. & Palmer, A.R.). Geological Society of America,: 447–512. Geological Society of America.

Holbek, P.M., and Copeland, D.A. 2000. Structure and stratigraphy of the Marg volcanogenic massive sulphide deposit , north-central Yukon. *In* Yukon Exploration and Geology. *Edited by* D.S. Emond and L.H. Weston. Exploration and Geological Services Division, Indian and Northern Affairs Canada. pp. 319–333.

Hollister, L.S., and Burruss, R.C. 1976. Phase equilibria in fluid inclusions from the Khtada Lake metamorphic complex. Geochimica et Cosmochimica Acta, **40**: 163–175. doi:10.1016/0016-7037(76)90174-5.

Hoskin, P.W.O., and Ireland, T.R. 2000. Rare earth element chemistry of zircon and its use as a provenance indicator. Geology, **28**: 627–630. doi:10.1130/0091-7613(2000)28<627:REECOZ>2.0.CO.

Hoskin, P.W.O., and Schaltegger, U. 2003. The composition of zircon and igneous and metamorphic petrogenesis. Reviews in Mineralogy and Geochemistry, **53**: 27–62. doi:10.2113/0530027.

Hourigan, J.K., Reiners, P.W., and Brandon, M.T. 2005. U-Th zonation-dependent alpha-ejection in (U-Th)/He chronometry. Geochimica et Cosmochimica Acta, **69**: 3349–3365. doi:10.1016/j.gca.2005.01.024.

Houseman, G.A., McKenzie, D.P., and Molnar, P. 1981. Convective instability of a thickened boundary layer and its relevance for the thermal evolution of continental convergent belts. Journal of Geophysical Research: Solid Earth (1978–2012), **86**: 6115–6132. doi:10.1029/JB086iB07p06115.

Hudson, T.L. 1994. Crustal melting events in Alaska. *In* The Geology of Alaska, v. G-1. *Edited by* G. Plafker and H.C. Berg. Geological Society of America, Boulder Colorado. pp. 657–670.

Hults, C.P., Wilson, F.H., Donelick, R. a., and O'Sullivan, P.B. 2013. Two flysch belts having distinctly different provenance suggest no stratigraphic link between the Wrangellia composite terrane and the paleo-Alaskan margin. Lithosphere, **5**: 575–594. doi:10.1130/L310.1.

Jackson, S.E., Pearson, N.J., Griffin, W.L., and Belousova, E.A. 2004. The application of laser ablation-inductively coupled plasma-mass spectrometry to in situ U-Pb zircon geochronology. Chemical Geology, **211**: 47–69. doi:10.1016/j.chemgeo.2004.06.017.

Jacobs, G.K., and Kerrick, D.M. 1981. Methane: An equation of state with application to the ternary system H2O-CO2-CH4. Geochimica et Cosmochimica Acta, **45**: 607–614. doi:10.1016/0016-7037(81)90035-1.

Jellinek, A.M., and DePaolo, D.J. 2003. A model for the origin of large silicic magma chambers: Precursors of caldera-forming eruptions. Bulletin of Volcanology, **65**: 363–381. doi:10.1007/s00445-003-0277-y.

Jennings, D.., and Jilson, G.. 1986. Geology and sulphide deposits of Anvil Range, Yukon Territory. *In* Mineral deposits of the northern Cordillera, Special Vo. *Edited by* J. Morin. Canadian Institute of Mining and Metallogeny. pp. 319–361.

Johnston, S.T. 1999. Large-scale coast-parallel displacements in the Cordillera: A

granitic resolution to a paleomagnetic dilemma. Journal of Structural Geology, **21**: 1103–1108. doi:10.1016/S0191-8141(99)00015-2.

Johnston, S.T. 2008. The Cordilleran Ribbon Continent of North America. Annual Review of Earth and Planetary Sciences, **36**: 495–530. doi:10.1146/annurev.earth.36.031207.124331.

Johnston, S.T., and Borel, G.D. 2007. The odyssey of the Cache Creek terrane, Canadian Cordillera: Implications for accretionary orogens, tectonic setting of Panthalassa, the Pacific superwell, and break-up of Pangea. Earth and Planetary Science Letters, **253**: 415–428. doi:10.1016/j.epsl.2006.11.002.

Johnston, S.T., and Canil, D. 2007. Crustal architecture of SW Yukon, northern Cordillera: Implications for crustal growth in a convergent margin orogen. Tectonics, **26**: 1–18. doi:10.1029/2006TC001950.

Johnston, S.T., Wynne, P.J., Francis, D., Hart, C.J.R., Enkin, R.J., and Engebretson, D.C. 1996. Yellowstone in Yukon: The Late Cretaceous Carmacks Group. Geology, **24**: 997–1000. doi:10.1130/0091-7613(1996)024<0997:YIYTLC>2.3.CO;2.

Joyce, N.L. 2002. Geologic setting, nature, and structural evolution of intrusion-hosted Au- bearing Quartz veins at the Longline occurence, Moosehorn Range area, west-central Yukon Territory. Masters Thesis. The University of British Columbia.

Kay, S.M., and Mpodozis, C. 2001. Central Andean Ore deposits linked to evolving shallow subduction systems and thickening crust. GSA Today, **11**: 4–9. doi:10.1017/CBO9781107415324.004.

Kay, S.M., Mpodozis, C., Ramos, V.A., and Munizaga, F. 1991. Andean Magmatism and Its Tectonic Setting. Geological Society of America Special Papers, **265**: 113–138. doi:10.1130/SPE265.

Keay, S., Steele, D., and Compston, W. 1999. Identifying granite sources by SHRIMP U-Pb zircon geochronology: An application to the Lachlan foldbelt. Contributions to Mineralogy and Petrology, **137**: 323–341. doi:10.1007/s004100050553.

Kemp, A.I.S., Whitehouse, M.J., Hawkesworth, C.J., and Alarcon, M.K. 2005. A zircon U-Pb study of metaluminous (I-type) granites of the Lachlan Fold Belt, southeastern Australia: Implications for the high/low temperature classification and magma differentiation processes. Contributions to Mineralogy and Petrology, **150**: 230–249. doi:10.1007/s00410-005-0019-6.

Kent, D. V., and Irving, E. 2010. Influence of inclination error in sedimentary rocks on the Triassic and Jurassic apparent pole wander path for North America and implications for Cordilleran tectonics. Journal of Geophysical Research: Solid Earth, **115**: 1–25. doi:10.1029/2009JB007205.

Ketcham, R. a. 2005. Forward and Inverse Modeling of Low-Temperature Thermochronometry Data. Reviews in Mineralogy and Geochemistry, **58**: 275–314. doi:10.2138/rmg.2005.58.11.

Kilinc, I.A., and Burnham, C.W. 1972. Partitioning of Chloride Between a Silicate Melt and Coexisting Aqueous Phase from 2 to 8 Kilobars. Economic Geology, **67**: 231–235.

Klepeis, K.A., Crawford, M.L., and Gehrels, G. 1998. Structural history of the crustal-scale Coast shear zone north of Portland Canal, southeast Alaska and British

Columbia. Journal of Structural Geology, **20**: 883–904. doi:10.1016/S0191-8141(98)00020-0.

Knight, E., Schneider, D.A., and Ryan, J. 2013. Thermochronology of the Yukon-Tanana Terrane , West-Central Yukon : Evidence for Jurassic Extension and Exhumation in the Northern Canadian Cordillera. The Journal of Geology, **121**: 371–400. doi:10.1086/670721.

Krystopowicz, N.J., and Currie, C.A. 2013. Crustal eclogitization and lithosphere delamination in orogens. Earth and Planetary Science Letters, **361**: 195–207. Elsevier. doi:10.1016/j.epsl.2012.09.056.

Kumagai, I., Davaille, A., Kurita, K., and Stutzmann, E. 2008. Mantle plumes: Thin, fat, successful, or failing? Constraints to explain hot spot volcanism through time and space. Geophysical Research Letters, **35**: 1–5. doi:10.1029/2008GL035079.

Lane, L.S., and Gehrels, G.E. 2014. Detrital zircon lineages of late Neoproterozoic and Cambrian strata, NW Laurentia. Bulletin of the Geological Society of America, **126**: 398–414. doi:10.1130/B30848.1.

Lang, J.R., and Baker, T. 2001. Intrusion-related gold systems: The present level of understanding. Mineralium Deposita, **36**: 477–489. doi:10.1007/s001260100184.

Lee, J.K.W., Onstott, T.C., Cashman, K. V., Cumbest, R.J., and Johnson, D. 1991. Incremental heating of hornblende in vacuo: implications for 40Ar/39Ar geochronology and the interpretation of thermal histories. Geology, **19**: 872–876. doi:10.1130/0091-7613(1991)019<0872:IHOHIV>2.3.CO.

Lehmann, B. 1994. Petrochemical Factors Governing the Metallogeny of the Bolivian Tin Belt. *In* Tectonics of the Southern Central Andes Structure and Evolution of an Active Continental Margin. *Edited by* K.J. Reutter, E. Scheuber, and Wigger P. Springer-Verlag, Berlin. pp. 317–326.

Leslie, C. 2009. Detrital Zircon Geochronology and Rift-Related Magmatism: Central Mackenzie Mountains, Northwest Territories. Masters Thesis. University of British Columbia.

Lipman, P.W. 1984. The roots of ash flow calderas in western North America: windows into the granitic batholiths. Journal of Geophysical Research, **89**: 8801–8841. doi:10.1029/JB089iB10p08801.

Little, T.A., McWilliams, M.O., and Holcombe, R.J. 1995. 40Ar/39Ar thermochronology of epidote blueschists from the North D'Aguilar block, Queensland, Australia: timing and kinematics of subduction complex unroofing. Geological Society of America Bulletin, **107**: 520–535. doi:10.1130/0016-7606(1995)107<0520:AATOEB>2.3.CO;2.

Long, D.G.F., Lowey G., and Sweet, A.R. 2001. Age and setting of dinosaur trackways, Ross River area, Yukon Territory (105F/15). Yukon Exploration and Geology 2000,: 181–198.

Lovering, T.G. 1962. The origin of jasperoid in limestone. Economic Geology, **57**: 861–889. doi:10.2113/gsecongeo.57.6.861.

Lowenstern, J.B. 2001. Carbon dioxide in magmas and implications for hydrothermal systems. Mineralium Deposita, **36**: 490–502. doi:10.1007/s001260100185.

Lowey, G.W., Sinclair, W.D., and Hills, L. V. 1986. Additional K-Ar isotopic dates for

the Carmacks Group (Upper Cretaceous), west central Yukon. Canadian Journal of Earth Sciences, **23**: 1857–1859.
Luck, J.M., and Allègre, C.J. 1991. Osmium isotopes in ophiolites. Earth and Planetary Science Letters, **107**: 406–415. doi:10.1016/0012-821X(91)90086-W.
Ludwig, K.. 2003. User's manual for Isoplot 3.00. A geochronological Toolkit for Microsoft Excel. Berkeley Geochronology Center, Special Publication, **4a**.
Lund, K. 2008. Geometry of the Neoproterozoic and Paleozoic rift margin of western Laurentia: Implications for mineral deposit settings. Geosphere, **4**: 429. doi:10.1130/GES00121.1.
Lydon, J. 2004. Genetic models for Sullivan and other SEDEX deposits. *In* Sediment - hosted lead zinc sulphide deposits. *Edited by*M. Deb and W. Goodfellow. Narosa.
Lynch, J. 1989. Large-Scale Hydrothermal Zoning Reflected in the Tetrahedrite-Freibergite Solid Solution, Keno Hill Ag-Pb-Zn District, Yukon. Canadian Mineralogist, **27**: 383–400.
Lynch, J.V.G., Longstaffe, F.J., and Nesbitt, B.E. 1990. Stable isotopic and fluid inclusion indications of large-scale hydrothermal paleoflow, boiling, and fluid mixing in the Keno Hill Ag-Pb-Zn district, Yukon Territory, Canada. Geochimica et Cosmochimica Acta, **54**: 1045–1059. doi:10.1016/0016-7037(90)90438-Q.
Machel, H.G. 2001. Bacterial and thermochemical sulfate reduction in diagenetic settings - old and new insights. Sedimentary Geology, **140**: 143–175. doi:10.1016/S0037-0738(00)00176-7.
MacNaughton, R.B., Narbonne, G.M., and Dalrymple, R.W. 2000. Neoproterozoic slope deposits, Mackenzie Mountains, northwestern Canada: implications for passive-margin development and Ediacaran faunal ecology. Canadian Journal of Earth Sciences, **1020**: 997–1020. doi:10.1139/e00-012.
Mair, J.L., Hart, C.J.R., and Stephens, J.R. 2006. Deformation history of the northwestern Selwyn Basin, Yukon, Canada: Implications for orogen evolution and mid-Cretaceous magmatism. Bulletin of the Geological Society of America, **118**: 304–323. doi:10.1130/B25763.1.
Le Maitre, R.. 1989. A classification of igneous rocks & glossary of terms. Blackwell Scientific Publishing, Oxford, UK.
Marillo-Sialer, E., Woodhead, J., Hanchar, J.M., Reddy, S.M., Greig, A., Hergt, J., and Kohn, B. 2016. An investigation of the laser-induced zircon "matrix effect." Chemical Geology, **438**: 11–24. doi:10.1016/j.chemgeo.2016.05.014.
McDonough, W.F., and Sun, S. s. 1995. The composition of the Earth. Chemical Geology, **120**: 223–253. doi:10.1016/0009-2541(94)00140-4.
Megaw, P., Ruiz, J., and Titley, S. 1988. High- Temperature, Carbonate-Hosted Ag-Pb-Zn (Cu) Deposits of Northern Mexico. Economic Geology, **8**: 1856–1885.
Meinert, L. 1987. Skarn Zonation and Fluid Evolution in the Groundhog Mine, Central Mining District, New Mexico. Economic Geology, **82**: 523–545.
Meinert, L. 1992. Skarns and Skarn Deposits. Geoscience Canada, **19**: 145–162.
Meinert, L., Dipple, G., and Nicolescu, S. 2005. World skarn deposits. Economic Geology,: 299–336.
Meinert, L., and Hedenquist, J. 2003. Formation of anhydrous and hydrous skarn in Cu-

Au ore deposits by magmatic fluids. Economic Geology, **98**: 147–156.
Middlemost, E.A.K. 1994. Naming Materials in the Magma Igneous Rock System. Earth-Science Reviews, **37**: 215–224 ST–Naming Materials in the Magma Igneou. doi:10.1016/0012-8252(94)90029-9.
Mihalynuk, M.G., Nelson, J.A., and Diakow, L.J. 1994. Cache Creek terrane entrapment: Oroclinal paradox within the Canadian Cordillera. Tectonics, **13**: 575–595. doi:10.1029/93TC03492.
Miller, C.F. 1986. Comment and Reply on "S-Type Granites and Their Probable Absence in Southwestern North-America." Geology, **14**: 804–806. doi:Doi 10.1130/0091-7613(1986)14<894:Carosg>2.0.Co;2.
Miller, C.F., McDowell, S.M., and Mapes, R.W. 2003. Hot and cold granites: Implications of zircon saturation temperatures and preservation of inheritance. Geology, **31**: 529–532. doi:10.1130/0091-7613(2003)031<0529:HACGIO>2.0.CO;2.
Miller, E.L., and Hudson, T.L. 1991. Mid-Cretaceous extensional fragmentation of a Jurassic-Early Cretaceous Compressional Orogen, Alaska. Tectonics, **10**: 781–796. doi:10.1029/91TC00044.
Monger, J.W.H., Price, R.A., and Tempelman-Kluit, D. 1982. Tectonic accretion and the origin of the two major metamorphic and plutonic welts in the Canadian Cordillera. Geology, **10**: 70–75.
Monger, J.W.H., and Ross, C.A. 1971. Distribution of Fusulinaceans in the Western Canadian Cordillera. Canadian Journal of Earth Sciences, **8**: 259–278. doi:10.1139/e71-026.
Moore, T.E., Wallace, W.K., Bird, K.J., Karl, S.M., Mull, C.G., and Dillon, J.T. 1994. Geology of Northern Alaska. *In* The Geology of North Amera Vol. G-1 The Geology of Alaska. *Edited by* G. Plafker and H.. Berg. Geological Society of America, Boulder Colorado. pp. 49–140.
Morelli, R.M., Bell, C.C., Creaser, R.A., and Simonetti, A. 2010. Constraints on the genesis of gold mineralization at the Homestake Gold Deposit, Black Hills, South Dakota from rhenium-osmium sulfide geochronology. Mineralium Deposita, **45**: 461–480. doi:10.1007/s00126-010-0284-9.
Morris, G. a., and Creaser, R. a. 2008. Correlation of mid-Cretaceous granites with source terranes in the northern Canadian Cordillera Lithoprobe. Canadian Journal of Earth Sciences, **45**: 389–403. doi:10.1139/E08-002.
Morrison, G.W., Godwin, C., and Armstrong, R.L. 1979. Interpretation of isotopic ages and 87Sr/86Sr initial ratios for plutonic rocks in the Whitehorse map area, Yukon. Canadian Journal of Earth Sciences, **16**: 1988–1997.
Mortensen, J., and Ballantyne, S. 1992. Age and Pb isotopic studies of Ag-Sn-base metal epigenetic mineralization in the Mount Mye area, east-central Yukon Territory. *In* Radiogenic age and isotopic studies: Report 6.
Mortensen, J., Hart, C., Murphy, D., and Heffernan, S. 2000. Temporal evolution of Early and mid-Cretaceous magmatism in the Tintina Gold Belt. The Tintina Gold Belt: Concepts, exploration and discovery, **2**.
Mortensen, J.K. 1990. Geology & U-Pb geochronology of the Klondike District, west-

central Yuon Territory. Canadian Journal of Earth Sciences, **27**: 903–914.
Mortensen, J.K. 1992. Pre Mid Mesozoic Tectonic Evolution of the Yukon-Tanana Terrane, Yukon & Alaska. Tectonics, **11**: 836–853.
Murphy, D.C. 1997. Geology of the McQuesten River Region, Northern McQuesten and Mayo Map Areas, Yukon Territory (115P/14,15,16; 105M/13, 14). Exploration and Geological Services Division, Yukon, Indian and Northern Affairs Canada Bulletin, **6**: 122.
Nair, R., and Chacko, T. 2002. Fluid-absent Melting of High-grade Semi-pelites: P-T Constraints on Orthopyroxene Formation and Implications for Granulite Genesis. J. Petrology, **43**: 2121–2142. doi:10.1093/petrology/43.11.2121.
Narbonne, G.M., and Aitken, J.D. 1995. Neoproterozoic of the Mackenzie Mountains, northwestern Canada. Precambrian Research, **73**: 101–121. doi:10.1016/0301-9268(94)00073-Z.
Narbonne, G.M., Kaufman, A.J., and Knoll, A.H. 1994. Integrated chemostratigraphy and biostratigraphy of the Windermere Supergroup, northwestern Canada: implications for Neoproterozoic correlations and the early evolution of animals. Geological Society of America Bulletin, **106**: 1281–1292. doi:10.1130/0016-7606(1994)106<1281:ICABOT>2.3.CO;2.
Nasdala, L. 2003. Spectroscopic methods applied to zircon. Reviews in Mineralogy and Geochemistry, **53**: 427–467. doi:10.2113/0530427.
Nelson, B.K., and DePaolo, D.J. 1984. 1,700-Myr greenstone volcanic successions in southwestern North America and isotopic evolution of Proterozoic mantle. Nature, **312**: 143–146.
Nelson, D.R. 2001. An assessment of the determination of depositional ages for Precambrian clastic sedimentary rocks by U-Pb dating of detrital zircons. Sedimentary Geology, **141**–**142**: 37–60. doi:10.1016/S0037-0738(01)00067-7.
Nelson, J., and Colpron, M. 2007. Tectonics and metallogeny of the British Columbia, Yukon and Alaskan Cordillera, 1.8 Ga to the present. *In* Goodfellow, W.D., ed., Mineral Deposits of Canada: A Synthesis of Major Deposit-Types, District Metallogeny, the Evolution of Geological Provinces, and Exploration Methods. Geological Association of Canada, mineral Deposits Division. pp. 755–791.
Nelson, J., Colpron, M., and Israel, S. 2013. The Cordillera of British Columbia , Yukon , and Alaska : Tectonics and Metallogeny. Society of Economic Geologists Special Publication 17, **Chapter 3**: 53–109.
Nelson, J.L., Colpron, M., Piercey, S.J., Road, R.L., Dusel-bacon, C., Park, M., and Murphy, D.C. 2006. Paleozoic tectonic and metallogenetic evolution of pericratonic terranes in Yukon , northern British Columbia and eastern Alaska 1. GAC Special Paper 45,: 323–360.
Newberry, R.J., and Swanson, S.E. 1986. Scheelite skarn granitoids: An evaluation of the roles of magmatic source and process. Ore Geology Reviews, **1**: 57–81. doi:10.1016/0169-1368(86)90005-3.
Nier, A.O. 1950. A redetermination of the relative abundances of the isotopes of carbon, nitrogen, oxygen, argon, and potassium. Physical Review, **77**: 789–793. doi:10.1103/PhysRev.77.789.

Nokleberg, W.J. 1973. Co2 as a Source of Oxygen in Metasomatism of Carbonates. American Journal of Science, **273**: 498–514.
Ohmoto, H. 1972. Systematics of Sulfur and Carbon Isotopes in Hydrothermal Ore Deposits. Economic Geology, **67**: 551–578.
Orme, D. 2015. Effects of inherited cores and magmatic overgrowths on zircon (U-Th)/He ages and age-eU trends from Greater Himalayan sequence rocks, Mt. Everest region, Tibet. Geochemistry, Geophysics, Geosystems,: 2499–2507. doi:10.1002/2015GC005818.Received.
Patiño Douce, A.E., Humphreys, E.D., and Dana Johnston, A. 1990. Anatexis and metamorphism in tectonically thickened continental crust exemplified by the Sevier hinterland, western North America. Earth and Planetary Science Letters, **97**: 290–315. doi:10.1016/0012-821X(90)90048-3.
Patiño Douce, A.E., and Johnston, A.D. 1991. Phase equilibria and melt productivity in the pelitic system: implications for the origin of peraluminous granitoids and aluminous granulites. Contributions to Mineralogy and Petrology, **107**: 202–218. doi:10.1007/BF00310707.
Patiño Douce, a E., and Beard, J.S. 1994. Dehydrations-melting of Biotite Gneiss ans Quarz Amphibolite from 3 to 15 kbar. Journal of Petrology, **36**: 707–738.
Paton, C., Hellstrom, J., Paul, B., Woodhead, J., and Hergt, J. 2011. Iolite: Freeware for the visualisation and processing of mass spectrometric data. Journal of Analytical Atomic Spectrometry, **26**: 2508. doi:10.1039/c1ja10172b.
Paton, C., Woodhead, J.D., Hellstrom, J.C., Hergt, J.M., Greig, A., and Maas, R. 2010. Improved laser ablation U-Pb zircon geochronology through robust downhole fractionation correction. Geochemistry, Geophysics, Geosystems, **11**. doi:10.1029/2009GC002618.
Patton, W.W.J., and Box, S.E. 1989. Tectonic Setting of the Yukon-Koyukuk Basin and Its Borderlands, Western Alaska. Journal of Geophysical Research, **94**: 807–820.
Pavlis, L., Sisson, B., Foster, H.L., and Nokleberg, W.J. 1993. Mid- Cretaceous Extensional tectonics of the Yukon-Tanana terrane, trans-alaska crustal transect (TACT), East- Central Alaska. Tectonics, **12**: 103–122.
Pavlis, T.L. 1989. Middle Cretaceous orogenesis in the northern Cordillera: a Mediterranean analog of collision-related extensional tectonics. Geology, **17**: 947–950. doi:10.1130/0091-7613(1989)017<0947:MCOITN>2.3.CO;2.
Pearce, J.A.A. 1982. Trace element characteristics of lavas from destructive plate boundaries. Andesites,: 525–548.
Petford, N., Cruden, A.R., McCaffrey, K.J., and Vigneresse, J.-L. 2000. Granite magma formation, transport and emplacement in the Earth's crust. Nature, **408**: 669–673. doi:10.1038/35047000.
Petford, N., and Gallagher, K. 2001. Partial melting of mafic (ambphibolitic) lower crust by periodic influx of basaltic magma. Earth and Planetary Science Letters, **193**: 483–499. doi:10.1016/S0012-821X(01)00481-2.
Petford, N., Lister, J.R., and Kerr, R.C. 1994. The ascent of felsic magmas in dykes. Lithos, **32**: 161–168. doi:10.1016/0024-4937(94)90028-0.
Pigage, L. 2004. Bedrock geology compilation of the Anvil District (parts of NTS

105K/2,3,4,6,7 and 11), Central Yukon. Yukon Geological Survey, Bulletin 15,.
Pigage, L.C., and Anderson, R.G. 1985. The Anvil plutonic suite, Faro, Yukon Territory. Canadian Journal of Earth Sciences, **22**: 1204–1216. doi:10.1139/e85-122.
Powell, J., Schneider, D., Stockli, D., and Fallas, K. 2016. Zircon (U-Th)/He thermochronology of Neoproterozoic strata from the Mackenzie Mountains, Canada: Implications for the Phanerozoic exhumation and deformation history of the northern Canadian Cordillera. Tectonics, **35**: 663–689. doi:10.1002/2015TC003989.Received.
Rainbird, R.H., Heaman, L.M., and Young, G. 1992. Sampling Laurentia: detrital zircon geochronology offers evidence for an extensive Neoproterozoic river system originating from the Grenville orogen. Geology, **20**: 351–354. doi:10.1130/0091-7613(1992)020<0351:SLDZGO>2.3.CO;2.
Rainbird, R.H., Jefferson, C.W., and Young, G.M. 1996. The early Neoproterozoic sedimentary Succession B of northwestern Laurentia: Correlations and paleogeographic significance. Bulletin of the Geological Society of America, **108**: 454–470. doi:10.1130/0016-7606(1996)108<0454:TENSSB>2.3.CO;2.
Rainbird, R.H., McNicoll, V.J., Thériault, R.J., Heaman, L.M., Abbott, J.G., Long, D.G.F., and Thorkelson, D.J. 1997. Pan-Continental River System Draining Grenville Orogen Recorded by U-Pb and Sm-Nd Geochronology of Neoproterozoic Quartzarenites and Mudrocks, Northwestern Canada. The Journal of Geology, **105**: 1–17. doi:10.1086/606144.
Rampino, M.R., and Stothers, R.B. 1988. Flood basalt volcanism during the past 250 million years. Science (New York, N.Y.), **241**: 663–8. doi:10.1126/science.241.4866.663.
Ranalli, G., Brown, R.L., and Bosdachin, R. 1986. A geodynamic model for extension in the Shuswap core complex, southeastern Canadian Cordillera. Canadian Journal of Earth Sciences, **26**: 1647–1653.
Rasmussen, K. 2013. The timing, composition, and petrogenesis of syn- to post-accretionary magmatism in the Northern Cordilleran miogeocline, Eastern Yukon and Southwestern Northwest Territories. PhD Thesis. University of British Columbia.
Reimink, J.R., Davies, J.H.F.L., Waldron, J.W.F., and Rojas, X. 2016. Dealing with discordance: a novel approach for analysing U–Pb detrital zircon datasets. Journal of the Geological Society,: 2015–114. doi:10.1144/jgs2015-114.
Reiners, P.W. 2005. Zircon (U-Th)/He Thermochronometry. Reviews in Mineralogy and Geochemistry, **58**: 151–179. doi:10.2138/rmg.2005.58.6.
Reiners, P.W. 2007. Overview of Analytical Methods in the ARHDL. Available from http://www.geo.arizona.edu/~reiners/arhdl/procs.htm [accessed 25 January 2017].
Reiners, P.W., and Brandon, M.T. 2006. Using Thermochronology To Understand Orogenic Erosion. Annual Review of Earth and Planetary Sciences, **34**: 419–466. doi:10.1146/annurev.earth.34.031405.125202.
Reiners, P.W., Farley, K.A., and Hickes, H.J. 2002. He diffusion and (U-Th)/He thermochronometry of zircon: Initial results from Fish Canyon Tuff and Gold Butte. Tectonophysics, **349**: 297–308. doi:10.1016/S0040-1951(02)00058-6.

Reiners, P.W., and Nicolescu, S. 2006. Measurement of parent nuclides for (U-Th)/He chronometry by solution sector ICP-Ms. ARDHL Report 1,: 1–33.
Reiners, P.W., Spell, T.L., Nicolescu, S., and Zanetti, K.A. 2004. Zircon (U-Th)/He thermochronometry: He diffusion and comparisons with 40Ar/39Ar dating. Geochimica et Cosmochimica Acta, **68**: 1857–1887. doi:10.1016/j.gca.2003.10.021.
Richards, D.R., Butler, R.F., and Harms, T. a. 1993. Paleomagnetism of the late Paleozoic Slide Mountain terrane, northern and central British Columbia. Canadian Journal of Earth Sciences, **30**: 1898–1913. doi:10.1139/e93-168.
Rickwood, P.C. 1989. Boundary lines within petrologic diagrams which use oxides of major and minor elements. Lithos, **22**: 247–263. doi:10.1016/0024-4937(89)90028-5.
Ring, U., Brandon, M.T., Willett, S.D., and Lister, G.S. 1999. Exhumation processes. Geological Society, London, Special Publications, **154**: 1–27. doi:10.1144/GSL.SP.1999.154.01.01.
Robb, L. 2005. Introduction to Ore-Forming Processes. *In* 1st edition. Blackwell Publishing.
Roedder, E. 1984. Fluid Inclusions. Reviews in Mineralogy, **12**: 646.
Rogers, M.A. 2017. Genesis and controls on mineralization at the Hammer Zone Ag showing , Mount Mye Trend , South-Central Yukon. Masters Thesis. University of Alberta.
Rosen, O., Desmons, J., and Fettes, D. 2007. A systematic nomenclature for metamorphic rocks: 7. Metacarbonate and related rocks. Provisional recommendations by the IUGS Subcommission on the systematics of metamorphic rocks. Brtish Geological Survey.
Ross, G.., Friedman, R., and Mortensen, J.. 2005a. Detrital zircon and monazite from the Hyland Group northern Canadian Cordillera and Alaska: Evidence for intracordilleran “Grenville” basement. *In* Geoloigal Society of America, Abstracts with Programmes. Vol 37. No 4. p. 56.
Ross, G.M. 1991a. Precambrian basement in the Canadian Cordillera: an introduction. Canadian Journal of Earth Sciences, **28**: 1133–1139. doi:10.1139/e91-103.
Ross, G.M. 1991b. Geology Tectonic setting of the Windermere Supergroup revisited Tectonic setting of the Windermere Supergroup revisited. Geology,: 1125–1128. doi:10.1130/0091-7613(1991)019<1125.
Ross, G.M., Patchett, P.J., Hamilton, M., Heaman, L., DeCelles, P.G., Rosenberg, E., and Giovanni, M.K. 2005b. Evolution of the Cordilleran orogen (southwestern Alberta, Canada) inferred from detrital mineral geochronology, geochemistry, and Nd isotopes in the foreland basin. Bulletin of the Geological Society of America, **117**: 747–763. doi:10.1130/B25564.1.
Ross, G.M., and Villeneuve, M. 2003. Provenance of the Mesoproterozoic (1.45 Ga) Belt basin (western North America): Another piece in the pre-Rodinia paleogeographic puzzle. Bulletin of the Geological Society of America, **115**: 1191–1217. doi:10.1130/B25209.1.
Rye, R.O. 2005. A review of the stable-isotope geochemistry of sulfate minerals in selected igneous environments and related hydrothermal systems. Chemical

Geology, **215**: 5–36. doi:10.1016/j.chemgeo.2004.06.034.
Rye, R.O., and Ohmoto, H. 1974. Sulfur and carbon isotopes and ore genesis: A review. Economic Geology, **69**: 826–842. doi:10.2113/gsecongeo.69.6.826.
Scott, S., and Barnes, H. 1971. Sphalerite geothermometry and geobarometry. Economic Geology, **66**: 653–669.
Seal, R.R. 2006. Sulfur Isotope Geochemistry of Sulfide Minerals. Reviews in Mineralogy and Geochemistry, **61**: 633–677. doi:10.2138/rmg.2006.61.12.
Searle, M.P., Cottle, J.M., Streule, M.J., and Waters, D.J. 2009. Crustal melt granites and migmatites along the Himalaya: melt source, segregation, transport and granite emplacement mechanisms. Earth and Environmental Science Transactions of the Royal Society of Edinburgh, **100**: 219–233. doi:10.1017/S175569100901617X.
Selby, D., Creaser, R. a, and Nesbitt, B.E. 1999. Major and trace element compositions and Sr-Nd-Pb systematics of crystalline rocks from the Dawson Range, Yukon, Canada. Canadian Journal of Earth Sciences, **36**: 1463–1481. doi:10.1139/e99-058.
Seward, T.M., Williams-Jones, A.E., and Migdisov, A.A. 2014. The Chemistry of Metal Transport and Deposition by Ore-Forming Hydrothermal Fluids. *In* Treatise on Geochemistry, 2nd edition. Elsevier Ltd. doi:10.1016/B978-0-08-095975-7.01102-5.
Shanks, W., and Woodruff, L. 1987. Sulfur and lead isotope studies of stratiform Zn-Pb-Ag deposits, Anvil Range, Yukon; basinal brine exhalation and anoxic bottom-water mixing. Economic Geology, **82**: 600–634.
Sheldon, H.A., and Micklethwaite, S. 2007. Damage and permeability around faults: Implications for mineralization. Geology, **35**: 903–906. doi:10.1130/G23860A.1.
Sheppard, S.M.F. 1986. Characterization and isotopic variations in natural waters. Reviews in Mineralogy & Geochemistry, **16**: 165–183.
Shimizu, M., and Shikazono, N. 1985. Iron and zinc partitioning between coexisiting stannite and sphalerite: a possible indicator of temperature and sulfur fugacity. Mineralium Deposita, **320**: 314–320.
Shinohara, H., Iiyama, J.T., and Matsuo, S. 1989. Partition of chlorine compounds between silicate melt and hydrothermal solutions : I . Partition of NaCl-KCl. Geochimica et Cosmochimica Acta, **53**: 2617–2630.
Sigloch, K. 2012. Mantle provinces under North America from multifrequency P wave tomography. Geochemistry, Geophysics, Geosystems, **12**: 1–27. doi:10.1029/2010GC003421.
Sigloch, K., and Mihalynuk, M.G. 2013. Intra-oceanic subduction shaped the assembly of Cordilleran North America. Nature, **496**: 50–56. doi:10.1038/nature12019.
Sigmundsson, F. 1991. Post-glacial rebound and asthenosphere viscosity in Iceland. Geophysical Research Letters, **18**: 1131–1134. doi:10.1029/91GL01342.
Sillitoe, R.H. 1994. Erosion and collapse of volcanoes: Causes of telescoping in intrusion-centered ore deposits. Geology, **22**: 945–948.
Sillitoe, R.H., and Thompson, J.F.H. 1998. Intrusion-Related Vein Gold Deposits: Types, Tectono-Magmatic Settings and Difficulties of Distinction from Orogenic Gold Deposits. Resource Geology, **48**: 237–250. doi:10.1111/j.1751-3928.1998.tb00021.x.

Simmons, S., and Christenson, B. 1994. Origins of Calcite in a boiling geothermal system. American Journal of Science,.

Simonetti, A., Heaman, L.M., Hartlaub, R.P., Creaser, R. a., MacHattie, T.G., and Böhm, C. 2005. U–Pb zircon dating by laser ablation-MC-ICP-MS using a new multiple ion counting Faraday collector array. Journal of Analytical Atomic Spectrometry, **20**: 677. doi:10.1039/b504465k.

Smith, J. 1989. P, T, and relative timing of metamorphism in the aureole around the Anvil batholith, south central Yukon. Masters Thesis. University of Alberta.

Smith, J., and Erdmer, P. 1990. The Anvil aureole, an atypical mid-Cretaceous culmination in the northern Canadian Cordillera. Canadian Journal of Earth Sciences, **27**: 344–356.

Solie, D.N., Sullivan, P.O., Werdon, M.B., Freeman, L.K., Newberry, R.J., Szumigala, D.J., and Hubbard, T.D. 2014. Zircon U-Pb Age Data , Alaska Highway Corridor , Tanacross and Nabesna quadrangles , Alaska. *In* Division of Geological and Geophysical Surveys.

Spear, F.S., and Cheney, J.T. 1989. A petrogenetic grid for pelitic schists in the system SiO2-Al2O3-FeO-MgO-K2O-H2O. Contributions to Mineralogy and Petrology, **101**: 149–164. doi:10.1007/BF00375302.

Spell, T.L., and McDougall, I. 2003. Characterization and calibration of 40Ar/39Ar dating standards. Chemical Geology, **198**: 189–211. doi:10.1016/S0009-2541(03)00005-6.

Staples, R.D., Gibson, H.D., Berman, R.G., Ryan, J.J., and Colpron, M. 2013. A window into the Early to mid-Cretaceous infrastructure of the Yukon-Tanana terrane recorded in multi-stage garnet of west-central Yukon, Canada. Journal of Metamorphic Geology,: n/a-n/a. doi:10.1111/jmg.12042.

Staples, R.D., Gibson, H.D., Colpron, M., and Ryan, J.J. 2016. An orogenic wedge model for diachronous deformation, metamorphism, and exhumation in the hinterland of the northern Canadian Cordillera. Lithosphere,: L472.1-20. doi:10.1130/L472.1.

Staples, R.D., Murphy, D.C., Gibson, H.D., Colpron, M., Berman, R.G., and Ryan, J.J. 2014. Middle Jurassic to earliest Cretaceous mid-crustal tectono-metamorphism in the northern Canadian Cordillera: Recording foreland-directed migration of an orogenic front. Geological Society of America Bulletin,: 1511–1530. doi:10.1130/B31037.1.

Staudacher, T., Jessberger, E.K., Dorflinger, D., and Kiko, J. 1978. A refined ultrahigh-vacuum furnace for rare gas analysis. Journal of Physics E: Scientific Instruments, **11**: 781. doi:10.1088/0022-3735/12/3/513.

Strauss, J. V., Macdonald, F. a., Taylor, J.F., Repetski, J.E., and McClelland, W.C. 2013. Laurentian origin for the North Slope of Alaska: Implications for the tectonic evolution of the Arctic. Lithosphere,: L284.1. doi:10.1130/L284.1.

Sylvester, P.J. 1998. Post-collisional strongly peraluminous granites. Lithos, **45**: 29–44. doi:10.1016/S0024-4937(98)00024-3.

Taylor, H.P., and Sheppard, S.M.F. 1986. Igneous rocks:I, Processes of isotopic fractionation and isotope systematics. Reviews in Mineralogy & Geochemistry, **16**:

227–271.
Tempelman-Kluit, D. 1972. Geology and origin of the Faro, Vangorda, and Swim concordant zinc-lead deposits, central Yukon Territory. Information Canada.
Theriault, R.J., and Ross, G.M. 1990. Nd isotopic evidence for crustal recycling in the ca. 2.0 Ga subsurface of western Canada. Canadian Journal of Earth Sciences, **28**: 1140–1147.
Thiessen, E.J., Gleeson, S.A., Bennett, V., and Creaser, R.A. 2016. The tiger deposit: A carbonate-hosted, magmatic-hydrothermal gold deposit, Central Yukon, Canada. Economic Geology, **111**: 421–446. doi:10.2113/econgeo.111.2.421.
Thompson, A.B., and Connolly, J.A.D. 1995. Melting of the continental crust: Some thermal and petrological constraints on anatexis in continental collision zones and other tectonic settings. Journal of Geophysical Research, **100**: 15565. doi:10.1029/95JB00191.
Thorkelson, D.J., Mortensen, J.K., Creaser, R.A., Davidson, G.J., and Abbott, G.J. 2001. Early Proterozoic magmatism in Yukon, Canada: constraints on the evolution of northwestern Laurentia. Canadian Journal of Earth Sciences, **38**: 1479–1494. doi:10.1139/cjes-38-10-1479.
Todt, W., Cliff, R., Hanser, A., and Hofmann, A. 1996. Evaluation of a 202Pb–205Pb double spike for high - precision lead isotope analysis. Geophysical Monograph Series, **95**: 429–437. doi:10.1029/GM095p0429.
Tosdal, R.M., Dilles, J.H., and Cooke, D.R. 2009. From Source to Sinks in Auriferous Magmatic-Hydrothermal Porphyry and Epithermal Deposits. Elements, **5**: 289–295. doi:10.2113/gselements.5.5.289.
Ufnar, D.F., González, L.A., Ludvigson, G.A., Brenner, R.L., and Witzke, B.J. 2001. Stratigraphic Implications of Meteoric Sphaerosiderite δ18O Values in Paleosols of the Cretaceous (Albian) Boulder Creek Formation, NE British Columbia Foothills, Canada. Journal of Sedimentary Research, **71**: 1017–1028. doi:10.1306/042601711017.
Underschultz, J.R., and Erdmer, P. 1991. Tectonic loading in the Canadian Cordillera as recorded by mass accumulation in the Foreland Basin. Tectonics, **10**: 367–380. doi:10.1029/90TC02442.
USGS. 2015. Radiometric ages of rocks from Alaska. Available from http://mrdata.usgs.gov/catalog/cite-view.php?cite=18.
Utada, M. 2001. Zeolites in Hydrothermally Altered Rocks. Reviews in Mineralogy and Geochemistry, **45**: 305–322. doi:10.2138/rmg.2001.45.10.
Veizer, J., Ala, D., Azmy, K., Bruckschen, P., Buhl, D., Bruhn, F., Carden, G.A.F., Diener, A., Ebneth, S., Godderis, Y., Jasper, T., Korte, C., Pawellek, F., Podlaha, O.G., and Strauss, H. 1999. 87Sr/86Sr, δ13C and δ18O evolution of Phanerozoic seawater. Chemical Geology, **161**: 59–88. Elsevier Science B.V. doi:10.1016/S0009-2541(99)00081-9.
Vermeesch, P. 2013. On the visualisation of detrital age distributions. Chemical Geology, **341**: 140–146. Elsevier B.V. doi:10.1016/j.chemgeo.2013.01.010.
Vielzeuf, D., and Montel, J.M. 1994. Partial Melting of Metagreywackes .1. Fluid-Absent Experiments and Phase-Relationships. Contributions to Mineralogy and

Petrology, **117**: 375–393.
Villeneuve, M.E., Ross, G.M., Thériault, R.J., Miles, W., Parrish, R.R., and Broome, J. 1993. Tectonic subdivision and U-Pb geochronology of the crystalline basement of the Alberta Basin, Western Canada. Geological Survey of Canada, Bulletin 447,: 1–93.
Villeneuve, M.E., Thériault, R.J., and Ross, G.M. 1991. U–Pb ages and Sm–Nd signature of two subsurface granites from the Fort Simpson magnetic high, northwest Canada. Canadian Journal of Earth Sciences, **28**: 1003–1008. doi:10.1139/e91-091.
Wang, H. 2015. Intracontinental Deformation caused by Gravitational Lithosphere Removal. PhD Thesis. University of Alberta. doi:10.1017/CBO9781107415324.004.
Wang, H., and Currie, C. 2015. Magmatic expressions of continental lithosphere removal. Journal of Geophysical Research: Solid Earth,: 5535–5548. doi:10.1002/2014JB011859.Received.
Wheeler, J.O., and Gabrielse, H. 1972. The Cordilleran structural province. Variations in tectonic styles in Canada: Geological Association of Canada Special Paper 11, **1**–**81**.
White, R., and McKenzie, D. 1989. Magmatism at rift zones: The generation of volcanic continental margins and flood basalts. Journal of Geophysical Research, **94**: 7685. doi:10.1029/JB094iB06p07685.
Wiedenbeck, M., Alle, P., Corfu, F., Griffin, W.L., Meier, M., Oberli, F., Quadt, A. VON, Roddick, J.C., and Spiegl, W. 1995. Three Natural Zircon Standards for U-Th-Pb, Lu-Hf, Trace Element and REE Analyses. Geostandards Newsletter, **19**: 1–23. doi:10.1111/j.1751-908X.1995.tb00147.x.
Wilkinson, J.. 2001. Fluid inclusions in hydrothermal ore deposits. Lithos, **55**: 229–272. doi:10.1016/S0024-4937(00)00047-5.
Wilkinson, J.J. 1990. The role of metamorphic fluids in the development of the Cornubian orefield: fluid inclusion evidence from south Cornwall. Mineralogical Magazine, **54**: 219–230. doi:10.1180/minmag.1990.054.375.08.
Wolf, R.A., Farley, K.A., and Kass, D.M. 1998. Modeling of the temperature sensitivity of the apatite (U-Th)/He thermochronometer. Chemical Geology, **148**: 105–114. doi:10.1016/S0009-2541(98)00024-2.
Woodhead, J., and Hergt, J.M. 2001. Strontium, Neodymium and Lead Isotope Analyses of NIST Glass Certified Reference Materials: SRM 610, 612, 614. Geostandards Newsletter, **25**: 261–266. doi:http://dx.doi.org/10.1111/j.1751-908X.2001.tb00601.x.
Woodsworth, G.J., Anderson, R.G., and Armstrong, R.L. 1991. Plutonic regimes. *In* Geology of the Cordilleran Orogen in Canada.Edited by H. Gabrielse and CJ Yorath. Geological Survey of Canada, Geology of Canada. pp. 491–531.
Wynne, P.J., Enkin, R.J., Baker, J., Johnston, S.T., and Hart, C.J. 1998. The big flush: paleomagnetic signature of a 70 Ma regional hydrothermal event in displaced rocks of the northern Canadian Cordillera. Canadian Journal of Earth Sciences, **35**: 657–671. doi:10.1139/e98-014.

Young, G., Jefferson, C., Delaney, G., and Yeo, G. 1979. Middle and late Proterozoic evolution of the northern Canadian Cordillera and Shield. Geology, **7**: 125–128.
Young, G.M. 1984. Proterozoic plate tectonics in Canada with emphasis on evidence for a Late Proterozoic rifting event. Precambrian Research, **25**: 233–256. doi:10.1016/0301-9268(84)90035-4.
Yukon Geological Survey. 2014. Geochronology (Rock Ages) for the Yukon. Available from http://www.geology.gov.yk.ca/databases_gis.html.
Yukon Geological Survey. 2017. Yukon Digital Bedrock Geology. Available from http://www.geology.gov.yk.ca/update_yukon_bedrock_geology_map.html [accessed 20 April 2017].
Yukon Government. 2014. Mining and Geology Facts. Available from http://www.emr.gov.yk.ca/mining/mining_geology_facts.html.

Appendix

Chapter 2 Supplemental Information

TABLE A1. GRANITE SAMPLE LOCATIONS

Sample #	UTM E	UTM N	UTM Zone	Igneous Body	Suite	Sample #	UTM E	UTM N	UTM Zone	Igneous Body	Suite
G1	593582	6909787	8	Anvil Batholith	Anvil	**G18**	595522	6918027	8	Anvil Batholith	Tay River
G2	592680	6908833	8	Anvil Batholith	Anvil	**G19**	353406	6897304	9	NC Road Pluton	Tay River
G3	587557	6918824	8	Anvil Batholith	Anvil	**G20**	349370	6897387	9	Connolly Caldera	South Fork
G4	586071	6916583	8	Anvil Batholith	Tay River	**G21**	349894	6897506	9	Connolly Caldera	South Fork
G5	596975	6905848	8	Anvil Batholith	Anvil	**G22**	348143	6890689	9	Marjorie Pluton	Tay River
G6	598538	6907922	8	Anvil Batholith	Anvil	**G23**	348222	6889353	9	Marjorie Pluton	Tay River
G7	590582	6908448	8	Anvil Batholith	Anvil	**G24**	345494	6886194	9	NC Road Caldera	South Fork
G8	590282	6907815	8	Anvil Batholith	Anvil	**G25**	344927	6885933	9	NC Road Caldera	South Fork
G9	599724	6912611	8	Anvil Batholith	Anvil	**G26**	344638	6885143	9	NC Road Caldera	South Fork
G10	584712	6934088	8	Anvil Batholith	TTB	**G27**	646969	6881669	8	Orchay Batholith	Tay River
G11	576538	6948979	8	Minor Plug	Tay River	**G28**	573038	6933245	8	Anvil Batholith	Anvil
G12	565363	6951516	8	Minor Plug	TTB	**G29**	558848	6933152	8	Anvil Batholith	Anvil
G13	595532	6918142	8	Anvil Batholith	Tay River	**G30**	562589	6936244	8	Anvil Batholith	TTB
G14	595532	6918142	8	Anvil Batholith	Anvil	**G31**	566662	6934014	8	Anvil Batholith	TTB
G15	595506	6918128	8	Anvil Batholith	Anvil	**G32**	554195	6954948	8	Minor Plug	Tay River
G16	595506	6918128	8	Anvil Batholith	Anvil	**G33**	549637	6932775	8	Minor Plug	TTB
G17	595506	6918128	8	Anvil Batholith	Tay River	**G34**	548710	6936657	8	Minor Plug	Anvil

TABLE A2. RAW U-Pb DATA

Grain #	^{206}Pb (cps)	^{204}Pb (cps)	Isotopic Ratios						Apparent ages (Ma)						Disc (%)
			$\frac{^{207}Pb}{^{206}Pb}$	± (2σ)	$\frac{^{207}Pb}{^{235}U}$	± (2σ)	$\frac{^{206}Pb}{^{238}U}$	± (2σ)	$\frac{^{207}Pb^*}{^{206}Pb^*}$	± (2σ)	$\frac{^{207}Pb^*}{^{235}U}$	± (2σ)	$\frac{^{206}Pb^*}{^{238}U}$	± (2σ)	
Sample G1 (UTM Zone 8N, N6909787, E593582)															
1	461652	295	0.05265	0.00125	0.12730	0.00754	0.01754	0.00095	314	53	122	7	112	6	64.8
2	419447	169	0.05360	0.00059	0.12331	0.00580	0.01669	0.00076	354	25	118	5	107	5	70.4
3	312307	64	0.04978	0.00055	0.11619	0.00686	0.01693	0.00098	185	26	112	6	108	6	41.7
4	393902	107	0.05193	0.00058	0.12500	0.00690	0.01746	0.00094	282	25	120	6	112	6	61.0
5	404301	46	0.04893	0.00053	0.11337	0.00534	0.01680	0.00077	144	25	109	5	107	5	25.8
6	415353	28	0.04874	0.00052	0.11375	0.00522	0.01693	0.00076	135	25	109	5	108	5	20.1
7	421301	44	0.04859	0.00054	0.11459	0.00571	0.01710	0.00083	128	26	110	5	109	5	14.9
8	362080	36	0.04949	0.00058	0.11743	0.00730	0.01721	0.00105	171	27	113	7	110	7	36.1
9	337793	96	0.05232	0.00090	0.11987	0.00670	0.01662	0.00088	300	39	115	6	106	6	65.1
10	404859	98	0.05167	0.00068	0.11762	0.00632	0.01651	0.00086	271	30	113	6	106	5	61.5
11	299913	59	0.05082	0.00061	0.12099	0.00705	0.01727	0.00098	233	28	116	6	110	6	53.0
12	294393	101	0.05391	0.00074	0.12618	0.00592	0.01697	0.00076	367	31	121	5	109	5	71.1
13	236644	111	0.05185	0.00064	0.11894	0.00625	0.01664	0.00085	279	28	114	6	106	5	62.4
14	227384	85	0.04917	0.00061	0.12115	0.00559	0.01787	0.00079	156	29	116	5	114	5	27.0
15	153057	79	0.04981	0.00069	0.12288	0.00727	0.01789	0.00103	186	32	118	7	114	7	38.9
16	159009	82	0.04844	0.00060	0.11581	0.00610	0.01734	0.00089	121	29	111	6	111	6	8.4
17	148828	37	0.04830	0.00060	0.11413	0.00597	0.01714	0.00087	114	29	110	5	110	6	3.9
18	211266	21	0.04825	0.00055	0.11214	0.00601	0.01686	0.00088	112	27	108	5	108	6	3.5
19	331520	30	0.04850	0.00051	0.10784	0.00600	0.01613	0.00088	124	25	104	5	103	6	16.6
20	350226	82	0.05047	0.00060	0.11427	0.00568	0.01642	0.00079	217	27	110	5	105	5	52.0
21	223537	36	0.04853	0.00054	0.11715	0.00556	0.01751	0.00081	125	26	112	5	112	5	10.7
22	246001	60	0.04970	0.00055	0.11596	0.00721	0.01692	0.00104	181	25	111	7	108	7	40.5
23	296151	42	0.04853	0.00053	0.11702	0.00526	0.01749	0.00076	125	25	112	5	112	5	10.9
24	353458	55	0.04928	0.00055	0.11634	0.00595	0.01712	0.00085	161	26	112	5	109	5	32.3
25	400301	49	0.04877	0.00053	0.11145	0.00561	0.01657	0.00081	137	25	107	5	106	5	22.8
26	378840	509	0.05691	0.00092	0.13498	0.00672	0.01720	0.00081	488	35	129	6	110	5	78.1
27	440152	68	0.04992	0.00054	0.11321	0.00607	0.01645	0.00086	191	25	109	6	105	5	45.4
28	334852	117	0.05294	0.00059	0.11968	0.00579	0.01640	0.00077	326	25	115	5	105	5	68.4
29	42686	30	0.05008	0.00088	0.11106	0.00522	0.01609	0.00070	199	40	107	5	103	4	48.6
30	372946	41	0.04961	0.00055	0.11433	0.00567	0.01671	0.00081	177	26	110	5	107	5	39.9

TABLE A2 Cont. RAW U-Pb DATA

Grain #	^{206}Pb (cps)	^{204}Pb (cps)	Isotopic Ratios						Apparent ages (Ma)						Disc (%)
			$^{207}Pb/^{206}Pb$	± (2σ)	$^{207}Pb/^{235}U$	± (2σ)	$^{206}Pb/^{238}U$	± (2σ)	$^{207}Pb^*/^{206}Pb^*$	± (2σ)	$^{207}Pb^*/^{235}U$	± (2σ)	$^{206}Pb^*/^{238}U$	± (2σ)	
Sample G3 (UTM Zone 8N, N6918824, E587557)															
1	94437	74	0.07620	0.00057	1.79683	0.10961	0.17102	0.01035	1100	15	1044	39	1018	57	8.1
2	289935	118	0.07918	0.00042	2.03141	0.14467	0.18608	0.01321	1177	10	1126	47	1100	71	7.0
3	247829	110	0.07485	0.00053	1.74025	0.08676	0.16862	0.00832	1064	14	1024	32	1005	46	6.0
4	120709	118	0.09651	0.00129	0.81500	0.03987	0.06125	0.00288	1558	25	605	22	383	17	306.5
5	163547	119	0.08478	0.00066	1.32216	0.07555	0.11311	0.00640	1310	15	855	33	691	37	89.7
6	73442	131	0.11625	0.00088	5.15822	0.24282	0.32180	0.01495	1899	14	1846	39	1799	73	5.6
7	31113	132	0.10922	0.00224	4.20871	0.26156	0.27948	0.01640	1786	37	1676	50	1589	82	12.4
8	41926	90	0.05250	0.00084	0.13097	0.00629	0.01809	0.00082	307	36	125	6	116	5	165.6
9	328474	97	0.11840	0.00066	2.92591	0.15594	0.17923	0.00950	1932	10	1389	40	1063	52	81.8
10	125251	64	0.04879	0.00033	0.11799	0.00595	0.01754	0.00088	138	16	113	5	112	6	22.9
11	234732	100	0.22556	0.00105	17.49760	0.90938	0.56262	0.02912	3021	7	2963	49	2877	119	5.0
12	114649	50	0.07260	0.00273	0.25715	0.02476	0.02569	0.00228	1003	74	232	20	164	14	513.2
13	301911	102	0.07676	0.00036	1.18301	0.06566	0.11177	0.00618	1115	9	793	30	683	36	63.2
14	143176	43	0.06448	0.00068	0.26531	0.01505	0.02984	0.00166	757	22	239	12	190	10	299.6
15	76675	85	0.10319	0.00247	0.37783	0.02450	0.02656	0.00160	1682	44	325	18	169	10	895.6
16	311431	38	0.06722	0.00070	0.33862	0.02280	0.03653	0.00243	845	21	296	17	231	15	265.2
17	415309	47	0.09630	0.00293	0.34351	0.02637	0.02587	0.00182	1554	56	300	20	165	11	843.6
18	594569	302	0.05642	0.00125	0.12734	0.00765	0.01637	0.00091	469	48	122	7	105	6	347.9
19	380876	66	0.05101	0.00050	0.12994	0.00633	0.01847	0.00088	241	22	124	6	118	6	104.6
20	372489	71	0.07340	0.00242	0.25786	0.02274	0.02548	0.00208	1025	65	233	18	162	13	531.9
21	322279	203	0.07492	0.00316	0.25210	0.02538	0.02441	0.00223	1066	83	228	20	155	14	585.9
22	474637	145	0.04961	0.00063	0.11305	0.00613	0.01653	0.00087	177	29	109	6	106	6	67.3
23	313323	59	0.05868	0.00234	0.16143	0.01447	0.01995	0.00160	555	85	152	13	127	10	336.1
24	274997	47	0.06443	0.00131	0.21259	0.01285	0.02393	0.00136	756	42	196	11	152	9	395.8
25	189723	72	0.05170	0.00034	0.14666	0.00819	0.02057	0.00114	272	15	139	7	131	7	107.3
26	294094	43	0.05025	0.00039	0.11836	0.00573	0.01708	0.00082	207	18	114	5	109	5	89.2
27	374135	265	0.05748	0.00150	0.12777	0.00788	0.01612	0.00090	510	56	122	7	103	6	394.8
28	247633	36	0.04944	0.00032	0.11847	0.00610	0.01738	0.00089	169	15	114	6	111	6	51.7
29	136202	111	0.06309	0.00080	0.19992	0.01345	0.02298	0.00152	711	27	185	11	146	10	385.6
30	88172	55	0.10178	0.00076	1.27077	0.07289	0.09055	0.00515	1657	14	833	32	559	30	196.5

TABLE A2 Cont. RAW U-Pb DATA

Grain #	^{206}Pb (cps)	^{204}Pb (cps)	Isotopic Ratios						Apparent ages (Ma)						Disc (%)
			$\frac{^{207}Pb}{^{206}Pb}$	± (2σ)	$\frac{^{207}Pb}{^{235}U}$	± (2σ)	$\frac{^{206}Pb}{^{238}U}$	± (2σ)	$\frac{^{207}Pb^*}{^{206}Pb^*}$	± (2σ)	$\frac{^{207}Pb^*}{^{235}U}$	± (2σ)	$\frac{^{206}Pb^*}{^{238}U}$	± (2σ)	
Sample G4 (UTM Zone 8N, N6916583, E586071)															
1	39275	4	0.04842	0.00068	0.10433	0.00608	0.01563	0.00088	120	33	101	6	100	6	16.7
2	19028	10	0.05391	0.00124	0.11226	0.00716	0.01510	0.00090	367	51	108	7	97	6	74.2
3	20925	12	0.04920	0.00091	0.10413	0.00601	0.01535	0.00084	157	43	101	6	98	5	37.8
4	22793	29	0.04987	0.00139	0.10599	0.00803	0.01541	0.00109	189	64	102	7	99	7	48.2
5	15200	85	0.04952	0.00151	0.10679	0.00746	0.01564	0.00098	172	70	103	7	100	6	42.3
6	19022	39	0.04962	0.00132	0.10277	0.00622	0.01502	0.00082	177	61	99	6	96	5	46.1
7	11087	24	0.04989	0.00187	0.11189	0.00760	0.01627	0.00092	190	85	108	7	104	6	45.6
8	10910	0	0.05077	0.00103	0.10615	0.00633	0.01517	0.00085	307	36	125	6	116	5	165.6
9	19140	87	0.04963	0.00211	0.10311	0.00807	0.01507	0.00099	1932	10	1389	40	1063	52	81.8
10	16005	3	0.04935	0.00078	0.10512	0.00564	0.01545	0.00079	138	16	113	5	112	6	22.9
11	18088	16	0.04840	0.00089	0.09968	0.00593	0.01494	0.00085	3021	7	2963	49	2877	119	5.0
12	8416	3	0.05032	0.00127	0.11510	0.00707	0.01659	0.00093	1003	74	232	20	164	14	513.2
13	11530	10	0.04880	0.00118	0.10571	0.00807	0.01571	0.00114	1115	9	793	30	683	36	63.2
14	15089	3	0.05027	0.00086	0.10119	0.00633	0.01460	0.00088	757	22	239	12	190	10	299.6
15	9829	2	0.04934	0.00147	0.11205	0.00698	0.01647	0.00090	1682	44	325	18	169	10	895.6
16	8611	14	0.05161	0.00136	0.11518	0.00738	0.01619	0.00094	845	21	296	17	231	15	265.2
17	15546	1	0.04937	0.00084	0.10354	0.00598	0.01521	0.00084	1554	56	300	20	165	11	843.6
18	12827	3	0.05151	0.00190	0.11370	0.00725	0.01601	0.00083	469	48	122	7	105	6	347.9
19	13913	5	0.04906	0.00114	0.10582	0.00679	0.01564	0.00094	241	22	124	6	118	6	104.6
20	21061	19	0.05016	0.00106	0.11313	0.00658	0.01636	0.00089	1025	65	233	18	162	13	531.9
21	28734	3	0.04814	0.00100	0.10334	0.00585	0.01557	0.00082	1066	83	228	20	155	14	585.9
22	18440	3	0.04831	0.00114	0.10712	0.00706	0.01608	0.00099	177	29	109	6	106	6	67.3
23	21997	3	0.04891	0.00092	0.10411	0.00631	0.01544	0.00089	555	85	152	13	127	10	336.1
24	14135	10	0.05266	0.00170	0.11023	0.00767	0.01518	0.00094	756	42	196	11	152	9	395.8
25	11253	0	0.05114	0.00143	0.11014	0.00667	0.01562	0.00084	272	15	139	7	131	7	107.3
26	19518	3	0.04843	0.00075	0.10177	0.00605	0.01524	0.00087	207	18	114	5	109	5	89.2
27	32177	1	0.04903	0.00078	0.10364	0.00579	0.01533	0.00082	510	56	122	7	103	6	394.8
28	30408	3	0.04885	0.00092	0.10269	0.00579	0.01525	0.00081	169	15	114	6	111	6	51.7
29	20452	3	0.04857	0.00090	0.10450	0.00602	0.01561	0.00085	711	27	185	11	146	10	385.6
30	26339	60	0.04785	0.00079	0.10555	0.00774	0.01600	0.00114	1657	14	833	32	559	30	196.5

TABLE A2 Cont. RAW U-Pb DATA

Grain #	^{206}Pb (cps)	^{204}Pb (cps)	Isotopic Ratios						Apparent ages (Ma)						Disc (%)
			$^{207}Pb/^{206}Pb$	± (2σ)	$^{207}Pb/^{235}U$	± (2σ)	$^{206}Pb/^{238}U$	± (2σ)	$^{207}Pb^*/^{206}Pb^*$	± (2σ)	$^{207}Pb^*/^{235}U$	± (2σ)	$^{206}Pb^*/^{238}U$	± (2σ)	
Sample G10 (UTM Zone 8N, N6934088, E584712)															
1	277069	78	0.05017	0.00072	0.10024	0.00311	0.01449	0.00040	203	33	97	3	93	3	118.5
2	419974	28	0.04839	0.00038	0.09608	0.00369	0.01440	0.00054	118	18	93	3	92	3	28.4
3	188820	20	0.04874	0.00042	0.09521	0.00269	0.01417	0.00038	135	20	92	2	91	2	49.2
4	479585	104	0.05112	0.00075	0.10015	0.00301	0.01421	0.00037	246	33	97	3	91	2	170.7
5	104027	68	0.04847	0.00066	0.09730	0.00307	0.01456	0.00041	122	32	94	3	93	3	31.0
6	81082	65	0.04845	0.00050	0.09295	0.00278	0.01392	0.00039	121	24	90	3	89	2	35.9
7	34892	79	0.05223	0.00102	0.10169	0.00388	0.01412	0.00046	296	44	98	4	90	3	227.1
8	239985	98	0.05021	0.00044	0.09843	0.00363	0.01422	0.00051	205	20	95	3	91	3	125.0
9	252242	122	0.05055	0.00072	0.10173	0.00349	0.01460	0.00046	220	33	98	3	93	3	135.8
10	60245	74	0.04918	0.00067	0.10091	0.00323	0.01488	0.00043	157	32	98	3	95	3	64.4
14	231089	108	0.04920	0.00044	0.09517	0.00399	0.01403	0.00057	158	21	92	4	90	4	75.4
15	456625	133	0.04944	0.00048	0.10493	0.00620	0.01539	0.00090	169	23	101	6	98	6	71.5
16	523445	169	0.04991	0.00037	0.09757	0.00340	0.01418	0.00048	191	17	95	3	91	3	110.0
17	265795	118	0.04785	0.00038	0.09523	0.00329	0.01443	0.00048	92	19	92	3	92	3	-0.8
18	486257	135	0.04904	0.00037	0.09596	0.00303	0.01419	0.00044	150	17	93	3	91	3	64.6
19	271410	250	0.05643	0.00049	0.11267	0.00379	0.01448	0.00047	469	19	108	3	93	3	406.4
20	253096	117	0.04777	0.00041	0.09301	0.00331	0.01412	0.00049	88	20	90	3	90	3	-2.6
21	1307621	286	0.05070	0.00037	0.09744	0.00772	0.01394	0.00110	227	17	94	7	89	7	154.4
22	433124	101	0.04789	0.00037	0.09500	0.00244	0.01439	0.00035	94	18	92	2	92	2	1.9
23	100621	164	0.05228	0.00089	0.11460	0.00420	0.01590	0.00052	298	38	110	4	102	3	192.6
24	212071	108	0.04870	0.00048	0.09604	0.00341	0.01430	0.00049	133	23	93	3	92	3	45.7
25	222027	117	0.04946	0.00042	0.09809	0.00282	0.01438	0.00040	170	20	95	3	92	3	84.2
26	151934	109	0.04856	0.00049	0.09726	0.00414	0.01453	0.00060	127	23	94	4	93	4	36.4
27	126455	120	0.04902	0.00054	0.09603	0.00362	0.01421	0.00051	149	26	93	3	91	3	63.5
28	184050	130	0.04879	0.00048	0.09625	0.00337	0.01431	0.00048	138	23	93	3	92	3	50.7
29	240059	86	0.04889	0.00038	0.09885	0.00423	0.01466	0.00062	143	18	96	4	94	4	52.1
30	20275	67	0.05017	0.00089	0.09946	0.00395	0.01438	0.00051	203	41	96	4	92	3	120.3

TABLE A2 Cont. RAW U-Pb DATA

Grain #	^{206}Pb (cps)	^{204}Pb (cps)	Isotopic Ratios						Apparent ages (Ma)						Disc (%)
			$^{207}Pb/^{206}Pb$	± (2σ)	$^{207}Pb/^{235}U$	± (2σ)	$^{206}Pb/^{238}U$	± (2σ)	$^{207}Pb^*/^{206}Pb^*$	± (2σ)	$^{207}Pb^*/^{235}U$	± (2σ)	$^{206}Pb^*/^{238}U$	± (2σ)	
Sample G11 (UTM Zone 8N, N6948979, E576538)															
1	97461	36	0.04988	0.00076	0.10533	0.00339	0.01531	0.00043	190	35	102	3	98	3	93.5
2	83694	30	0.04878	0.00059	0.10350	0.00320	0.01539	0.00044	137	28	100	3	98	3	39.7
3	164334	27	0.04858	0.00033	0.10495	0.00292	0.01567	0.00042	128	16	101	3	100	3	27.5
4	65629	25	0.04903	0.00075	0.10430	0.00424	0.01543	0.00058	149	36	101	4	99	4	51.0
5	125007	26	0.04921	0.00057	0.10989	0.00437	0.01620	0.00062	158	27	106	4	104	4	52.4
6	98949	24	0.04789	0.00037	0.09802	0.00389	0.01485	0.00058	94	18	95	4	95	4	-1.2
7	87596	17	0.04780	0.00042	0.09957	0.00343	0.01511	0.00050	89	21	96	3	97	3	-7.7
8	110895	49	0.05044	0.00107	0.10936	0.00472	0.01573	0.00059	215	48	105	4	101	4	113.9
9	109963	40	0.04828	0.00043	0.10194	0.00349	0.01531	0.00051	113	21	99	3	98	3	15.5
10	107218	26	0.04827	0.00053	0.10287	0.00284	0.01546	0.00039	112	26	99	3	99	2	13.7
11	112692	7	0.04798	0.00037	0.10065	0.00337	0.01522	0.00050	98	18	97	3	97	3	0.8
12	74306	4	0.04893	0.00050	0.10372	0.00368	0.01537	0.00052	144	24	100	3	98	3	46.8
13	92234	2	0.04775	0.00044	0.09976	0.00449	0.01515	0.00067	87	22	97	4	97	4	-10.6
14	82845	2	0.04825	0.00035	0.10161	0.00409	0.01527	0.00061	111	17	98	4	98	4	14.0
15	95964	12	0.04979	0.00046	0.10576	0.00373	0.01541	0.00052	185	21	102	3	99	3	87.9
16	20486	17	0.04922	0.00103	0.10632	0.00471	0.01567	0.00061	158	48	103	4	100	4	57.8
17	92348	112	0.06878	0.00266	0.15222	0.00857	0.01605	0.00066	892	78	144	8	103	4	769.0
18	49389	40	0.06597	0.00320	0.14740	0.00887	0.01620	0.00058	806	98	140	8	104	4	677.4
19	47979	4	0.04872	0.00063	0.10175	0.00403	0.01515	0.00057	134	30	98	4	97	4	38.5
20	69611	4	0.04923	0.00057	0.10326	0.00363	0.01521	0.00050	159	27	100	3	97	3	63.2
21	93133	15	0.04854	0.00044	0.10481	0.00448	0.01566	0.00065	126	21	101	4	100	4	25.6
22	60581	16	0.04918	0.00192	0.10343	0.00552	0.01525	0.00055	156	89	100	5	98	4	60.2
23	93601	23	0.04875	0.00082	0.10337	0.00477	0.01538	0.00066	136	39	100	4	98	4	38.1
24	89440	33	0.04943	0.00142	0.10575	0.00530	0.01552	0.00064	168	66	102	5	99	4	69.5
25	16018	12	0.05582	0.00252	0.11795	0.00808	0.01533	0.00079	445	97	113	7	98	5	354.1
26	82548	6	0.04771	0.00049	0.10109	0.00509	0.01537	0.00076	85	24	98	5	98	5	-13.7
27	35355	14	0.04936	0.00132	0.10344	0.00517	0.01520	0.00064	165	61	100	5	97	4	69.4
28	97820	19	0.05017	0.00183	0.10556	0.00547	0.01526	0.00056	203	83	102	5	98	4	107.8
29	96346	1	0.04822	0.00054	0.10262	0.00457	0.01544	0.00067	110	26	99	4	99	4	11.3
30	104251	12	0.05103	0.00052	0.10824	0.00487	0.01538	0.00067	242	23	104	4	98	4	146.1

TABLE A2 Cont. RAW U-Pb DATA

Grain #	^{206}Pb (cps)	^{204}Pb (cps)	Isotopic Ratios						Apparent ages (Ma)						Disc (%)
			$^{207}Pb/^{206}Pb$	± (2σ)	$^{207}Pb/^{235}U$	± (2σ)	$^{206}Pb/^{238}U$	± (2σ)	$^{207}Pb^*/^{206}Pb^*$	± (2σ)	$^{207}Pb^*/^{235}U$	± (2σ)	$^{206}Pb^*/^{238}U$	± (2σ)	
Sample G12 (UTM Zone 8N, N6951516, E565363)															
1	31437	40	0.04850	0.00055	0.09885	0.00441	0.01478	0.00064	124	27	96	4	95	4	31.0
2	35049	24	0.05138	0.00057	0.10641	0.00450	0.01502	0.00061	258	25	103	4	96	4	168.2
3	23039	30	0.05231	0.00156	0.10870	0.00513	0.01507	0.00055	299	67	105	5	96	4	209.9
4	32658	49	0.05096	0.00097	0.10398	0.00470	0.01480	0.00061	239	43	100	4	95	4	152.6
5	36972	47	0.05012	0.00063	0.10514	0.00447	0.01521	0.00062	201	29	102	4	97	4	106.2
6	23146	34	0.04831	0.00105	0.10087	0.00533	0.01514	0.00073	114	50	98	5	97	5	18.0
7	56045	22	0.04890	0.00056	0.09845	0.00458	0.01460	0.00066	143	27	95	4	93	4	53.1
8	60469	33	0.04849	0.00043	0.09993	0.00372	0.01495	0.00054	123	21	97	3	96	3	29.1
9	19101	8	0.04913	0.00070	0.10219	0.00533	0.01509	0.00076	154	33	99	5	97	5	59.7
10	57393	116	0.05854	0.00308	0.11996	0.00819	0.01486	0.00065	550	111	115	7	95	4	478.2
11	11768	12	0.04936	0.00079	0.09974	0.00457	0.01466	0.00063	165	37	97	4	94	4	75.7
12	28990	28	0.04931	0.00098	0.10232	0.00453	0.01505	0.00060	162	46	99	4	96	4	68.7
13	22044	30	0.05083	0.00086	0.10349	0.00507	0.01477	0.00068	233	39	100	5	95	4	146.6
14	23050	27	0.05090	0.00113	0.10387	0.00538	0.01480	0.00069	236	50	100	5	95	4	149.5
15	59439	15	0.04851	0.00048	0.09980	0.00435	0.01492	0.00063	124	23	97	4	95	4	30.1
16	69142	15	0.04841	0.00042	0.09659	0.00418	0.01447	0.00061	119	20	94	4	93	4	28.9
17	62616	18	0.05041	0.00048	0.10328	0.00448	0.01486	0.00063	214	22	100	4	95	4	124.9
18	20341	15	0.05039	0.00181	0.10231	0.00530	0.01473	0.00055	213	81	99	5	94	3	125.9
19	75515	30	0.05062	0.00090	0.10182	0.00490	0.01459	0.00065	224	41	98	5	93	4	139.5
20	25725	23	0.04918	0.00106	0.09848	0.00454	0.01452	0.00059	156	49	95	4	93	4	68.1
21	41376	121	0.04993	0.00049	0.10587	0.00499	0.01538	0.00071	192	23	102	5	98	4	94.8
22	168492	132	0.04825	0.00050	0.09944	0.00397	0.01495	0.00058	112	24	96	4	96	4	16.6
23	14774	83	0.05482	0.00320	0.11421	0.00854	0.01511	0.00071	405	126	110	8	97	4	319.0
24	24089	58	0.04953	0.00091	0.10081	0.00445	0.01476	0.00059	173	42	98	4	94	4	83.3
25	55361	81	0.05595	0.00215	0.11208	0.00622	0.01453	0.00058	450	83	108	6	93	4	384.2
26	61805	64	0.04881	0.00065	0.10104	0.00502	0.01502	0.00072	139	31	98	5	96	5	44.2
27	77445	49	0.05040	0.00099	0.10376	0.00484	0.01493	0.00063	213	45	100	4	96	4	123.3
28	19912	14	0.04919	0.00124	0.09996	0.00469	0.01474	0.00058	157	58	97	4	94	4	66.5
29	20336	16	0.05106	0.00176	0.10371	0.00621	0.01473	0.00072	243	78	100	6	94	5	158.3
30	38206	28	0.05136	0.00080	0.10587	0.00497	0.01495	0.00066	257	35	102	5	96	4	168.9

TABLE A2 Cont. RAW U-Pb DATA

Grain #	^{206}Pb (cps)	^{204}Pb (cps)	Isotopic Ratios						Apparent ages (Ma)						Disc (%)
			$^{207}Pb/^{206}Pb$	± (2σ)	$^{207}Pb/^{235}U$	± (2σ)	$^{206}Pb/^{238}U$	± (2σ)	$^{207}Pb^*/^{206}Pb^*$	± (2σ)	$^{207}Pb^*/^{235}U$	± (2σ)	$^{206}Pb^*/^{238}U$	± (2σ)	
Sample G18 (UTM Zone 8N, N6918027, E595522)															
1	37398	0	0.04856	0.00070	0.10271	0.00405	0.01534	0.00056	127	33	99	4	98	4	22.7
2	30980	0	0.04808	0.00074	0.10196	0.00364	0.01538	0.00049	103	36	99	3	98	3	4.7
3	34689	2	0.04793	0.00077	0.10175	0.00434	0.01540	0.00061	96	37	98	4	99	4	-2.9
4	20512	4	0.04787	0.00072	0.09956	0.00351	0.01508	0.00048	93	35	96	3	97	3	-3.7
5	38843	0	0.04834	0.00073	0.10266	0.00444	0.01540	0.00062	116	35	99	4	99	4	15.0
6	27976	3	0.04918	0.00092	0.10376	0.00370	0.01530	0.00046	156	43	100	3	98	3	37.7
7	29299	76	0.04833	0.00080	0.10196	0.00339	0.01530	0.00044	115	38	99	3	98	3	15.4
8	30076	1	0.04819	0.00070	0.10059	0.00323	0.01514	0.00043	109	34	97	3	97	3	11.1
9	15284	2	0.04831	0.00100	0.10136	0.00368	0.01522	0.00045	115	48	98	3	97	3	15.2
10	28939	2	0.04779	0.00083	0.10045	0.00359	0.01524	0.00048	89	41	97	3	98	3	-10.0
11	48418	2	0.04809	0.00077	0.10274	0.00375	0.01550	0.00051	104	37	99	3	99	3	4.3
12	25869	0	0.04824	0.00100	0.10363	0.00477	0.01558	0.00064	111	48	100	4	100	4	10.3
13	21933	1	0.04840	0.00109	0.10171	0.00462	0.01524	0.00060	119	52	98	4	98	4	18.0
14	9797	0	0.04870	0.00133	0.10294	0.00509	0.01533	0.00063	133	63	99	5	98	4	26.7
15	145947	77	0.09834	0.00108	3.37777	0.14855	0.24911	0.01061	1593	20	1499	34	1434	55	11.1
16	37254	4	0.04859	0.00091	0.10437	0.00387	0.01558	0.00050	128	44	101	4	100	3	22.5
17	11264	26	0.05018	0.00129	0.10652	0.00631	0.01540	0.00082	203	59	103	6	98	5	52.0
18	26192	3	0.04841	0.00090	0.10259	0.00382	0.01537	0.00050	119	43	99	4	98	3	17.7
19	43099	0	0.04896	0.00081	0.10256	0.00365	0.01519	0.00048	146	38	99	3	97	3	33.5
20	53608	1	0.04787	0.00070	0.10068	0.00477	0.01525	0.00069	93	34	97	4	98	4	-5.0
21	31817	1	0.04817	0.00076	0.09898	0.00470	0.01490	0.00067	108	37	96	4	95	4	11.7
22	47147	0	0.04837	0.00061	0.10254	0.00323	0.01538	0.00044	117	29	99	3	98	3	16.3
23	32366	0	0.04945	0.00064	0.10553	0.00368	0.01548	0.00050	169	30	102	3	99	3	41.9
24	70374	0	0.04813	0.00065	0.09670	0.00378	0.01457	0.00053	105	32	94	3	93	3	11.7
25	34825	0	0.04851	0.00075	0.10122	0.00420	0.01513	0.00058	124	36	98	4	97	4	22.2
26	99645	1	0.04805	0.00058	0.10218	0.00321	0.01542	0.00045	102	28	99	3	99	3	3.1
27	37257	2	0.04822	0.00074	0.10292	0.00364	0.01548	0.00049	110	36	99	3	99	3	10.1
28	21404	0	0.04757	0.00087	0.10330	0.00410	0.01575	0.00056	78	43	100	4	101	4	-29.1
29	21248	76	0.04794	0.00106	0.10189	0.00447	0.01542	0.00058	96	52	99	4	99	4	-2.7
30	29181	0	0.04779	0.00110	0.10278	0.00520	0.01560	0.00070	89	54	99	5	100	4	-12.2

TABLE A2 Cont. RAW U-Pb DATA

Grain #	^{206}Pb (cps)	^{204}Pb (cps)	Isotopic Ratios						Apparent ages (Ma)						Disc (%)
			$^{207}Pb/^{206}Pb$	± (2σ)	$^{207}Pb/^{235}U$	± (2σ)	$^{206}Pb/^{238}U$	± (2σ)	$^{207}Pb^*/^{206}Pb^*$	± (2σ)	$^{207}Pb^*/^{235}U$	± (2σ)	$^{206}Pb^*/^{238}U$	± (2σ)	
Sample G20 (UTM Zone 9N, N6897387, E349370)															
1	25513	28	0.04874	0.00075	0.10141	0.00469	0.01509	0.00066	135	36	98	4	97	4	29.0
2	30298	35	0.05155	0.00085	0.10932	0.00632	0.01538	0.00085	266	38	105	6	98	5	63.5
3	37915	54	0.04868	0.00086	0.10134	0.00525	0.01510	0.00073	133	41	98	5	97	5	27.4
4	28588	50	0.04870	0.00079	0.10440	0.00567	0.01555	0.00081	134	38	101	5	99	5	25.7
5	15116	33	0.04994	0.00146	0.11240	0.00661	0.01632	0.00083	192	67	108	6	104	5	46.1
6	15769	34	0.05074	0.00122	0.10902	0.00634	0.01558	0.00083	229	55	105	6	100	5	56.9
7	17603	3	0.05308	0.00166	0.10844	0.00597	0.01482	0.00067	332	69	105	5	95	4	72.0
8	20498	26	0.04862	0.00100	0.10133	0.00492	0.01512	0.00066	129	48	98	5	97	4	25.5
9	21990	12	0.04911	0.00107	0.10428	0.00556	0.01540	0.00075	153	50	101	5	99	5	35.8
10	31071	16	0.04901	0.00076	0.10323	0.00527	0.01528	0.00074	148	36	100	5	98	5	34.4
11	17843	6	0.04808	0.00093	0.10219	0.00531	0.01542	0.00074	103	45	99	5	99	5	4.4
12	19904	2	0.04854	0.00124	0.10598	0.00528	0.01584	0.00068	125	59	102	5	101	4	19.4
13	23183	3	0.04744	0.00073	0.10360	0.00477	0.01584	0.00069	72	36	100	4	101	4	-41.8
14	14205	7	0.04867	0.00118	0.10654	0.00596	0.01588	0.00080	132	56	103	5	102	5	23.2
15	15808	1	0.04872	0.00137	0.10549	0.00518	0.01570	0.00063	134	65	102	5	100	4	25.4
16	14093	1	0.04973	0.00165	0.10634	0.00704	0.01551	0.00089	182	76	103	6	99	6	45.9
17	19825	12	0.04866	0.00119	0.10536	0.00609	0.01571	0.00082	131	56	102	6	100	5	23.6
18	22938	0	0.04799	0.00079	0.10596	0.00532	0.01601	0.00076	99	38	102	5	102	5	-3.6
19	17817	1	0.05261	0.00126	0.11040	0.00713	0.01522	0.00091	312	54	106	7	97	6	69.3
20	32527	1	0.04836	0.00074	0.10322	0.00466	0.01548	0.00066	117	36	100	4	99	4	15.3
21	26839	0	0.04885	0.00081	0.10225	0.00462	0.01518	0.00064	141	38	99	4	97	4	31.3
22	26125	0	0.04850	0.00080	0.10290	0.00492	0.01539	0.00069	124	38	99	5	98	4	20.5
23	33953	1	0.04871	0.00079	0.10573	0.00509	0.01574	0.00071	134	38	102	5	101	5	25.0
24	41074	0	0.04760	0.00061	0.10149	0.00430	0.01546	0.00062	79	30	98	4	99	4	-24.6
25	15672	0	0.04975	0.00197	0.10154	0.00634	0.01480	0.00071	183	90	98	6	95	5	48.6
26	28474	0	0.04769	0.00074	0.10089	0.00486	0.01534	0.00070	84	36	98	4	98	4	-16.8
27	31399	0	0.04791	0.00067	0.09909	0.00484	0.01500	0.00070	95	33	96	4	96	4	-1.4
28	18121	0	0.04814	0.00081	0.10143	0.00460	0.01528	0.00064	106	39	98	4	98	4	7.9
29	17581	0	0.04893	0.00112	0.10966	0.00612	0.01626	0.00083	144	53	106	6	104	5	28.2
30	38394	0	0.04820	0.00059	0.10133	0.00445	0.01525	0.00064	109	28	98	4	98	4	10.5

TABLE A2 Cont. RAW U-Pb DATA

Grain #	^{206}Pb (cps)	^{204}Pb (cps)	Isotopic Ratios						Apparent ages (Ma)						Disc (%)
			$^{207}Pb/^{206}Pb$	± (2σ)	$^{207}Pb/^{235}U$	± (2σ)	$^{206}Pb/^{238}U$	± (2σ)	$^{207}Pb^*/^{206}Pb^*$	± (2σ)	$^{207}Pb^*/^{235}U$	± (2σ)	$^{206}Pb^*/^{238}U$	± (2σ)	
Sample G22 (UTM Zone 9N, N6890689, E348143)															
1	73621	33	0.04857	0.00056	0.10354	0.00488	0.01546	0.00071	127	27	100	4	99	4	-12.2
2	31985	38	0.04949	0.00086	0.10548	0.00477	0.01546	0.00064	171	40	102	4	99	4	29.0
3	46602	38	0.04812	0.00069	0.10234	0.00415	0.01543	0.00058	105	34	99	4	99	4	63.5
4	32785	33	0.04786	0.00073	0.10208	0.00451	0.01547	0.00064	92	36	99	4	99	4	27.4
5	50206	42	0.04839	0.00079	0.10290	0.00473	0.01542	0.00066	119	38	99	4	99	4	25.7
6	46043	38	0.04855	0.00069	0.10238	0.00470	0.01529	0.00067	126	33	99	4	98	4	46.1
7	22853	87	0.04835	0.00091	0.10668	0.00549	0.01600	0.00077	117	44	103	5	102	5	56.9
8	28497	36	0.04818	0.00082	0.10241	0.00612	0.01542	0.00088	108	40	99	6	99	6	72.0
9	84591	32	0.04864	0.00068	0.10329	0.00512	0.01540	0.00073	131	32	100	5	99	5	25.5
10	10927	37	0.04718	0.00120	0.09657	0.00478	0.01485	0.00063	58	60	94	4	95	4	35.8
11	25636	31	0.04903	0.00084	0.10326	0.00417	0.01528	0.00056	149	40	100	4	98	4	34.4
12	13150	42	0.04921	0.00113	0.10438	0.00498	0.01538	0.00064	158	53	101	5	98	4	4.4
13	60591	39	0.04839	0.00062	0.10129	0.00393	0.01518	0.00055	118	30	98	4	97	4	19.4
14	112864	21	0.04843	0.00053	0.09980	0.00374	0.01495	0.00054	120	26	97	3	96	3	-41.8
15	58395	23	0.04837	0.00081	0.10275	0.00474	0.01541	0.00066	117	39	99	4	99	4	23.2
16	33297	57	0.04849	0.00078	0.10271	0.00444	0.01536	0.00062	123	38	99	4	98	4	25.4
17	26349	12	0.04828	0.00091	0.10329	0.00530	0.01552	0.00074	113	44	100	5	99	5	45.9
18	21023	26	0.04753	0.00109	0.10220	0.00519	0.01560	0.00071	76	53	99	5	100	4	23.6
19	24826	51	0.04862	0.00093	0.09811	0.00513	0.01464	0.00071	129	45	95	5	94	5	-3.6
20	48470	30	0.04839	0.00064	0.10214	0.00530	0.01531	0.00077	118	31	99	5	98	5	69.3
21	18572	14	0.04883	0.00105	0.10523	0.00453	0.01563	0.00058	140	50	102	4	100	4	15.3
22	31667	24	0.04861	0.00098	0.09869	0.00435	0.01472	0.00058	129	47	96	4	94	4	31.3
23	32757	30	0.04875	0.00073	0.10272	0.00421	0.01528	0.00058	136	35	99	4	98	4	20.5
24	16409	35	0.04973	0.00126	0.10153	0.00602	0.01481	0.00079	182	58	98	6	95	5	25.0
25	54127	29	0.04884	0.00075	0.10822	0.00465	0.01607	0.00064	140	36	104	4	103	4	-24.6
26	34370	93	0.04902	0.00084	0.10247	0.00521	0.01516	0.00073	149	40	99	5	97	5	48.6
27	31301	33	0.04830	0.00084	0.09973	0.00453	0.01498	0.00063	114	40	97	4	96	4	-16.8
28	13273	41	0.04947	0.00177	0.10475	0.00599	0.01536	0.00069	170	81	101	5	98	4	-1.4
29	95559	67	0.04856	0.00068	0.10662	0.00461	0.01593	0.00065	127	33	103	4	102	4	7.9
30	24566	27	0.07362	0.00122	1.68355	0.08563	0.16585	0.00798	1031	33	1002	32	989	44	28.2

TABLE A2 Cont. RAW U-Pb DATA

Grain #	^{206}Pb (cps)	^{204}Pb (cps)	Isotopic Ratios						Apparent ages (Ma)						Disc (%)
			$\frac{^{207}Pb}{^{206}Pb}$	± (2σ)	$\frac{^{207}Pb}{^{235}U}$	± (2σ)	$\frac{^{206}Pb}{^{238}U}$	± (2σ)	$\frac{^{207}Pb^*}{^{206}Pb^*}$	± (2σ)	$\frac{^{207}Pb^*}{^{235}U}$	± (2σ)	$\frac{^{206}Pb^*}{^{238}U}$	± (2σ)	
Sample G27 (UTM Zone 9N, N6881669, E64696)															
1	240923	71	0.04982	0.00040	0.11155	0.00439	0.01624	0.00063	187	18	107	4	104	4	79.9
2	283952	60	0.04893	0.00043	0.10571	0.00451	0.01567	0.00065	144	21	102	4	100	4	43.9
3	204291	87	0.04901	0.00051	0.10775	0.00608	0.01595	0.00089	148	24	104	6	102	6	45.4
4	185986	129	0.05264	0.00097	0.11571	0.00480	0.01594	0.00059	313	42	111	4	102	4	207.2
5	210574	87	0.05014	0.00041	0.10706	0.00480	0.01549	0.00068	201	19	103	4	99	4	103.1
6	147242	34	0.05381	0.00050	0.40082	0.01672	0.05402	0.00220	363	21	342	12	339	13	7.1
7	516479	123	0.05072	0.00062	0.11290	0.00453	0.01614	0.00062	228	28	109	4	103	4	121.1
8	105060	61	0.04803	0.00052	0.10065	0.00415	0.01520	0.00060	101	26	97	4	97	4	3.5
9	59413	11	0.04810	0.00058	0.10402	0.00358	0.01568	0.00051	104	28	100	3	100	3	4.1
10	108298	52	0.05155	0.00105	0.11058	0.00484	0.01556	0.00060	265	46	106	4	100	4	166.8
11	171881	245	0.06800	0.00400	0.14430	0.01608	0.01539	0.00146	869	117	137	14	98	9	782.2
12	120456	50	0.04973	0.00075	0.10979	0.00441	0.01601	0.00060	183	35	106	4	102	4	78.2
13	236548	39	0.04932	0.00044	0.10006	0.00345	0.01471	0.00049	163	21	97	3	94	3	73.4
14	297887	134	0.05447	0.00097	0.11595	0.00542	0.01544	0.00067	390	39	111	5	99	4	295.3
15	73760	32	0.04868	0.00076	0.10150	0.00435	0.01512	0.00060	133	36	98	4	97	4	37.0
16	248000	50	0.04997	0.00042	0.10612	0.00477	0.01540	0.00068	194	19	102	4	99	4	96.6
17	41099	26	0.04812	0.00075	0.10453	0.00422	0.01576	0.00059	105	37	101	4	101	4	4.1
18	31070	122	0.07884	0.00271	0.17273	0.00880	0.01589	0.00060	1168	67	162	8	102	4	1049.3
19	268688	47	0.04934	0.00042	0.10551	0.00412	0.01551	0.00059	164	20	102	4	99	4	65.4
20	423955	254	0.05026	0.00053	0.11117	0.00491	0.01604	0.00069	207	24	107	4	103	4	101.6
21	19358	60	0.05632	0.00093	0.11906	0.00555	0.01533	0.00067	465	36	114	5	98	4	374.3
22	49343	72	0.04941	0.00066	0.10413	0.00459	0.01529	0.00064	167	31	101	4	98	4	71.0
23	58277	277	0.05577	0.00124	0.11840	0.00700	0.01540	0.00084	443	49	114	6	98	5	350.2
24	18486	113	0.05645	0.00481	0.12373	0.01207	0.01590	0.00075	470	178	118	11	102	5	362.4
25	109757	110	0.04972	0.00069	0.10992	0.00420	0.01603	0.00057	182	32	106	4	103	4	77.5
26	79759	120	0.04989	0.00110	0.10423	0.00530	0.01515	0.00069	190	51	101	5	97	4	96.0
27	20521	47	0.05064	0.00100	0.10669	0.00504	0.01528	0.00066	224	45	103	5	98	4	129.6
28	39241	40	0.04883	0.00058	0.10249	0.00486	0.01522	0.00070	140	27	99	4	97	4	43.4
29	251681	74	0.04948	0.00049	0.10397	0.00517	0.01524	0.00074	171	23	100	5	97	5	74.9
30	15781	116	0.04854	0.00121	0.10343	0.00528	0.01546	0.00069	126	58	100	5	99	4	27.0

TABLE A3. BULK ROCK MAJOR AND MINOR ELEMENT CHEMISTRY OF GRANITES

Sample #	Suite	UTM E	UTM N	SiO_2 (wt%)	Al_2O_3 (wt%)	TiO_2 (wt%)	Fe_2O_3 (wt%)	MnO (wt%)	MgO (wt%)	CaO (wt%)	Na_2O (wt%)	K_2O (wt%)	P_2O_5 (wt%)	LOI (wt%)	Total (wt%)
G1	Anvil	593582	6909787	72.53	14.98	0.19	1.39	0.02	0.39	1.47	3.20	4.96	0.05	0.70	99.88
G3	Anvil	587557	6918824	71.59	14.82	0.41	2.93	0.04	0.90	1.50	2.70	4.12	0.13	0.70	99.85
G4	Tay River	586071	6916583	64.68	16.23	0.58	5.46	0.10	1.59	4.47	2.76	2.62	0.15	1.20	99.79
G10	Tombstone	584712	6934088	70.35	14.88	0.28	2.71	0.05	0.59	1.69	2.95	4.91	0.09	1.30	99.83
G11	Tay River	576538	6948979	68.08	14.74	0.50	4.34	0.08	1.29	3.70	2.38	3.75	0.09	0.90	99.80
G12	Tombstone	565363	6951516	64.42	16.39	0.64	5.72	0.09	1.49	3.97	2.11	3.59	0.14	1.20	99.73
G18	Tay River	595522	6918027	61.43	16.10	0.67	6.29	0.12	1.93	4.56	2.98	2.28	0.15	3.30	99.76
G18*	Tay River	595522	6918027	61.97	15.97	0.65	5.96	0.11	1.75	4.46	2.99	2.42	0.15	3.40	99.78
G20	South Fork	349370	6897387	63.94	15.95	0.62	5.00	0.09	1.87	4.31	2.33	2.77	0.10	2.80	99.80
G21	South Fork	349894	6897506	61.94	16.51	0.62	4.80	0.06	2.41	4.81	2.83	3.68	0.16	1.90	99.71
G22	Tay River	348143	6890689	66.33	15.58	0.56	4.54	0.07	1.25	3.70	2.75	3.09	0.11	1.80	99.74
G27	Tay River	646969	6881669	72.04	14.18	0.29	2.69	0.05	0.59	1.90	3.14	4.42	0.09	0.50	99.86

TABLE A3 CONT. BULK ROCK TRACE AND REE CHEMISTRY OF GRANITES

#	Rb (ppm)	Cu (ppm)	Cs (ppm)	Ba (ppm)	Sr (ppm)	Ga (ppm)	Ta (ppm)	Nb (ppm)	Hf (ppm)	Zr (ppm)	Y (ppm)	Th (ppm)	U (ppm)	Au (ppm)	In (ppm)	Tl (ppm)	Be (ppm)	Cd (ppm)	Cr (ppm)	Ni (ppm)	Co (ppm)	Sc (ppm)	V (ppm)
G1	198.6	5.1	4.2	571.0	216.1	20.5	0.7	5.1	3.2	95.5	6.7	14.4	3.0	0.0028	<0.02	0.30	2.0	0.02	11.6	5.3	2.0	2.0	12
G3	185.7	9.6	4.6	558.0	178.6	21.3	1.1	11.3	5.2	173.7	14.5	23.5	4.6	--*	0.03	0.32	4.0	0.09	16.7	7.7	5.2	6.0	35
G4	142.5	6.8	10.5	805.0	374.9	17.4	0.7	9.2	3.7	123.0	22.6	11.7	2.1	--	<0.02	0.51	1.0	0.03	4.5	1.6	7.9	13.0	80
G10	239.7	3.1	9.5	949.0	192.4	16.5	1.9	11.4	3.8	111.2	21.8	14.7	3.4	0.0003	0.02	0.29	3.0	0.02	6.2	2.6	3.3	6.0	22
G11	132.9	8.1	4.2	915.0	231.3	15.7	1.1	9.9	4.7	148.7	22.0	17.5	3.3	--	0.02	0.36	0.5	0.16	11.8	2.3	6.1	12.0	54
G12	140.6	11.7	6.2	1311.0	187.7	19.5	0.9	13.8	5.6	197.0	26.0	18.4	2.6	0.0004	0.08	0.52	4.0	0.18	8.2	2.3	7.2	15.0	39
G18	90.5	4.4	5.0	883.0	384.3	17.7	0.7	8.4	4.0	138.0	25.3	11.3	2.1	0.0002	<0.02	0.02	3.0	0.04	3.1	1.4	9.4	18.0	104
G18*	84.1	6.6	5.7	849.0	359.5	17.5	0.6	8.2	3.8	133.2	22.8	10.7	2.4	--	<0.02	0.03	3.0	0.08	5.2	2.6	9.2	16.0	99
G20	100.9	7.3	1.7	708.0	292.3	17.2	0.7	8.5	4.4	153.7	20.8	13.8	2.6	--	0.03	<0.02	0.4	0.13	15.1	2.6	8.4	15.0	90
G21	137.4	20.5	2.1	1070.0	476.4	15.9	1.2	10.8	5.6	189.3	17.0	23.2	5.5	--	<0.02	<0.02	4.0	0.06	23.7	27.0	11.3	14.0	101
G22	106.7	3.6	3.8	1293.0	305.3	17.8	0.8	11.6	4.9	182.5	20.8	15.9	1.8	--	0.05	0.06	3.0	0.04	13.3	3.7	7.3	12.0	55
G27	195.1	8.1	5.5	637.0	219.7	15.1	1.7	13.5	4.8	136.4	26.2	21.2	4.9	--	0.03	0.44	4.0	0.02	2.2	0.8	3.0	5.0	26

#	Pb (ppm)	Zn (ppm)	As (ppm)	Ag (ppm)	Bi (ppm)	Mo (ppm)	La (ppm)	Ce (ppm)	Pr (ppm)	Nd (ppm)	Sm (ppm)	Eu (ppm)	Gd (ppm)	Tb (ppm)	Dy (ppm)	Ho (ppm)	Er (ppm)	Tm (ppm)	Yb (ppm)	Lu (ppm)	Sb (ppm)	Sn (ppm)	W (ppm)
G1	15.7	35.9	<0.1	0.022	1.67	1.73	29.9	61.6	6.9	25.3	4.3	0.88	2.72	0.31	1.3	0.24	0.75	0.11	0.74	0.11	0.03	10.0	0.60
G3	6.2	51.4	1.2	0.019	0.43	0.83	46.5	93.7	11.1	38.9	6.5	0.92	4.57	0.63	3.0	0.51	1.56	0.22	1.37	0.21	0.03	17.0	0.90
G4	11.3	69.2	<0.1	0.059	0.17	1.13	33.0	67.1	8.0	29.9	5.7	1.13	4.92	0.76	4.1	0.83	2.50	0.37	2.42	0.37	<0.02	2.0	1.60
G10	7.8	34.6	3.9	0.029	0.05	0.86	22.5	43.0	5.1	18.9	3.9	0.73	3.72	0.64	3.8	0.73	2.20	0.37	2.56	0.39	0.07	6.0	0.60
G11	8.0	59.8	1.4	0.035	0.07	1.44	36.4	71.3	8.2	29.3	5.7	1.07	4.88	0.73	4.2	0.85	2.51	0.37	2.30	0.38	0.07	2.0	0.60
G12	9.7	94.1	1.7	0.054	0.14	0.89	56.7	116.6	13.5	51.1	9.2	1.57	7.73	1.12	5.8	0.99	2.58	0.35	2.19	0.33	0.09	3.0	1.40
G18	10.4	83.3	0.1	0.040	0.04	0.59	31.1	65.7	7.8	30.5	5.7	1.26	5.53	0.84	4.7	0.90	2.48	0.37	2.54	0.39	0.08	2.0	0.60
G18*	11.4	82.5	0.2	0.047	0.05	1.37	30.2	60.4	7.5	29.2	5.4	1.29	5.14	0.80	4.4	0.86	2.45	0.36	2.54	0.36	0.04	2.0	1.00
G20	14.0	58.7	0.7	0.044	<0.02	0.57	31.0	61.8	7.2	26.0	4.8	1.10	4.59	0.71	3.8	0.76	2.33	0.34	2.25	0.35	0.04	2.0	0.80
G21	10.3	47.2	0.4	0.038	<0.02	0.52	47.3	90.5	10.3	34.8	5.4	1.13	4.42	0.61	3.4	0.63	1.79	0.27	1.77	0.29	0.03	2.0	1.10
G22	10.9	70.0	0.4	0.027	0.02	0.89	50.9	95.7	10.8	38.6	6.2	1.26	5.26	0.80	4.2	0.77	2.28	0.32	2.09	0.30	0.02	2.0	0.50
G27	6.8	34.5	<0.1	0.008	0.06	3.28	28.7	54.8	5.9	20.7	4.4	0.71	4.02	0.72	4.3	0.90	2.74	0.43	3.06	0.50	0.02	2.0	0.10

* Value below limit of detection

TABLE A4. ZIRCON LA-ICP-MS DATA

Sample #	La (ppm)	±2σ	Ce (ppm)	±2σ	Pr (ppm)	±2σ	Nd (ppm)	±2σ	Sm (ppm)	±2σ	Eu (ppm)	±2σ	Gd (ppm)	±2σ	Tb (ppm)	±2σ	Dy (ppm)	±2σ
Int Std	Nist 612	Nist 612	Nist 612	Nist 612	Nist 612	Nist 612	Nist 610	Nist 610	Nist 610	Nist 610	Nist 610	Nist 610	Nist 610	Nist 610	Nist 612	Nist 612	Nist 610	Nist 610
G1																		
1	0.13	0.03	1.69	0.21	0.19	0.03	1.21	0.20	1.49	0.16	0.18	0.03	9.26	0.39	4.25	0.12	69.00	1.40
2	1.04	0.09	4.06	0.24	0.66	0.06	3.43	0.24	2.68	0.18	0.40	0.04	10.52	0.47	4.44	0.12	69.50	1.10
3	95.00	36.00	218.00	78.00	23.30	8.20	84.00	29.00	20.70	5.30	1.53	0.22	25.20	3.20	6.87	0.37	92.00	2.80
4	2.91	0.22	6.68	0.79	1.98	0.22	10.10	1.10	6.34	0.72	0.96	0.13	17.62	0.96	6.86	0.22	101.60	2.30
5	2.66	0.86	17.70	6.10	3.60	1.40	23.30	9.70	17.60	7.00	1.94	0.80	32.20	9.40	9.30	1.90	123.00	12.00
6	1.81	0.17	11.10	1.40	2.56	0.34	16.60	2.40	14.70	2.70	1.58	0.27	28.30	4.80	8.40	1.20	111.00	13.00
7	0.31	0.03	1.89	0.17	0.25	0.03	1.47	0.16	1.74	0.14	0.19	0.03	9.28	0.34	4.67	0.13	81.80	1.40
8	0.02	0.01	0.36	0.06	0.01	0.01	0.12	0.06	0.77	0.19	0.07	0.02	7.61	0.64	3.86	0.17	64.80	1.70
9	0.46	0.07	1.16	0.13	0.19	0.03	0.96	0.15	0.97	0.11	0.12	0.02	6.87	0.27	3.29	0.08	55.83	0.68
10	0.12	0.03	0.96	0.09	0.05	0.01	0.35	0.09	0.91	0.14	0.12	0.03	7.89	0.43	3.95	0.20	71.70	3.00
G4																		
1	0.02	0.01	9.44	0.41	0.05	0.01	1.02	0.09	2.49	0.18	0.51	0.03	16.72	0.61	5.74	0.19	80.90	2.50
2	1.46	0.57	12.50	1.60	0.59	0.23	3.70	1.30	2.91	0.33	0.50	0.03	15.23	0.53	5.18	0.13	72.30	1.70
3	4.30	1.60	24.10	4.40	1.67	0.61	9.60	3.20	5.44	0.66	0.95	0.06	26.05	0.86	8.81	0.18	124.50	2.20
4	0.07	0.04	10.05	0.36	0.07	0.01	1.38	0.18	3.14	0.36	0.74	0.08	21.60	1.50	7.29	0.46	103.80	6.30
5	0.02	0.01	31.09	0.50	0.13	0.01	2.37	0.16	4.38	0.21	0.95	0.05	20.90	0.47	6.17	0.11	77.10	1.10
6	0.80	0.43	10.70	0.93	0.33	0.12	3.41	0.86	5.04	0.43	0.77	0.06	30.40	2.00	10.47	0.65	144.20	8.30
7	23.50	3.80	73.90	9.70	9.20	1.30	48.10	6.30	13.50	1.40	1.37	0.14	32.60	1.90	8.95	0.30	119.20	2.80
8	0.03	0.02	9.61	0.65	0.05	0.01	0.97	0.11	2.68	0.24	0.60	0.06	18.50	1.30	6.34	0.38	91.20	4.80
9	1.47	0.48	15.90	1.50	0.59	0.17	4.09	0.87	4.76	0.31	0.70	0.05	31.13	0.93	10.80	0.26	150.60	2.40
10	0.57	0.35	22.00	1.70	0.41	0.17	3.60	0.84	6.21	0.55	1.10	0.12	37.50	3.50	12.00	1.00	162.00	12.00
11	6.70	1.90	30.20	5.50	2.98	0.84	15.80	4.00	7.90	1.10	1.16	0.09	31.50	1.70	9.93	0.45	131.80	5.30
12	0.15	0.05	8.64	0.32	0.10	0.02	1.66	0.19	4.07	0.40	0.63	0.05	25.70	1.90	8.79	0.65	115.90	7.90
13	0.03	0.01	8.82	0.46	0.05	0.01	0.98	0.09	2.94	0.22	0.54	0.05	19.49	0.98	6.74	0.31	94.60	4.10
14	3.20	2.70	17.50	7.80	1.30	1.10	7.90	5.50	4.64	0.95	0.81	0.12	27.60	3.00	8.16	0.66	107.60	7.90
15	0.10	0.04	14.76	0.22	0.08	0.01	1.56	0.13	4.00	0.24	0.80	0.05	26.47	0.75	9.25	0.19	130.70	2.20

TABLE A4 Cont. ZIRCON LA-ICP-MS DATA

Sample #	Ho (ppm)	±2σ	Er (ppm)	±2σ	Tm (ppm)	±2σ	Yb (ppm)	±2σ	Lu (ppm)	±2σ	Ti (ppm)	±2σ	Pb (ppm)	±2σ	Th (ppm)	±2σ	U (ppm)	±2σ
Int Std	Nist 612	Nist 612	Nist 610	Nist 610	Nist 612	Nist 612	Nist 610	Nist 610	Nist 612	Nist 612	Nist 612	Nist 612	Nist 612	Nist 612	Nist 612	Nist 612	Nist 612	Nist 612
G1																		
1	30.67	0.58	190.90	3.80	54.80	1.50	631.00	19.00	117.30	3.90	1.1	0.3	0.57	0.08	24	1	3710	120
2	28.39	0.34	156.30	1.80	36.96	0.46	374.00	4.00	67.52	0.84	2.2	0.4	1.31	0.23	32	1	2842	29
3	37.30	1.30	217.30	9.80	56.70	3.10	653.00	37.00	127.20	8.10	3.3	0.5	2.31	0.25	110	15	3350	55
4	40.04	0.64	221.10	3.30	53.03	0.76	562.70	7.50	103.30	1.70	3.5	0.5	2.98	0.19	60	2	5194	96
5	47.10	3.00	258.60	8.30	65.00	2.50	736.00	30.00	124.00	3.20	5.2	1.8	1.75	0.52	34	2	3920	250
6	43.40	3.80	245.00	17.00	63.10	3.50	706.00	38.00	132.50	7.50	4.1	0.9	2.53	0.37	31	1	4327	65
7	36.77	0.64	227.90	3.80	64.00	1.20	777.00	18.00	153.60	2.90	1.1	0.3	3.57	0.46	48	2	3689	48
8	26.69	0.49	151.40	3.40	39.80	0.98	448.40	7.20	74.60	3.60	1.3	0.6	0.31	0.05	24	1	3690	130
9	24.70	0.35	149.00	3.00	40.47	0.94	473.00	11.00	92.10	3.40	1.4	0.3	0.68	0.07	21	1	3020	110
10	31.90	1.70	198.00	13.00	52.60	3.40	634.00	37.00	122.30	9.90	1.3	1.0	0.33	0.05	25	2	3183	65
G4																		
1	31.77	0.87	168.00	4.30	36.07	0.94	369.00	10.00	70.90	1.70	5.5	0.5	1.36	0.10	130	8	220	13
2	28.11	0.60	148.40	3.20	31.91	0.73	326.50	6.70	62.50	1.50	9.5	1.4	1.91	0.17	135	7	224	7
3	48.91	0.70	259.00	4.20	55.66	0.93	569.00	10.00	108.50	1.60	6.2	0.5	1.43	0.07	173	8	289	9
4	41.10	2.10	218.00	11.00	47.50	2.20	497.00	24.00	97.00	4.30	5.1	0.5	1.13	0.08	108	5	206	8
5	27.71	0.32	135.30	1.30	28.19	0.34	274.50	3.40	48.38	0.45	16.8	0.8	19.73	0.52	131	2	109	2
6	54.80	3.00	276.00	13.00	58.30	2.50	573.00	23.00	105.50	3.40	4.7	0.8	1.39	0.13	154	14	298	23
7	45.80	1.00	240.50	5.10	52.10	1.00	530.40	9.50	101.90	1.90	5.0	0.9	1.43	0.10	148	6	275	7
8	36.50	1.90	199.00	10.00	44.20	2.30	462.00	22.00	91.00	4.00	4.9	0.6	1.05	0.11	118	17	222	22
9	56.80	0.90	288.70	4.00	58.92	0.78	566.90	7.00	105.50	1.50	16700	1200	3.17	0.18	391	21	517	13
10	60.90	4.40	309.00	21.00	65.00	4.00	657.00	37.00	123.10	7.40	8.2	1.7	3.73	0.36	537	50	606	37
11	50.40	1.90	260.10	9.00	55.10	1.80	554.00	17.00	106.10	3.50	11.6	2.4	2.18	0.12	178	6	271	9
12	43.90	2.60	223.00	12.00	45.80	2.30	448.00	22.00	84.10	3.60	5.3	1.1	1.22	0.14	133	11	225	19
13	37.20	1.50	195.40	6.90	41.70	1.20	417.50	9.70	80.90	2.00	13.1	4.5	1.50	0.17	130	16	219	16
14	40.30	2.50	207.00	12.00	44.00	2.60	436.00	25.00	83.30	4.50	3.5	0.6	1.38	0.19	125	16	221	19
15	51.67	0.89	273.30	4.30	58.97	0.99	601.00	11.00	117.70	2.20	4.5	0.5	2.24	0.16	274	15	480	23

TABLE A4 Cont. ZIRCON LA-ICP-MS DATA

Sample #	La (ppm)	±2σ	Ce (ppm)	±2σ	Pr (ppm)	±2σ	Nd (ppm)	±2σ	Sm (ppm)	±2σ	Eu (ppm)	±2σ	Gd (ppm)	±2σ	Tb (ppm)	±2σ	Dy (ppm)	±2σ
Int Std	*Nist 612*	*Nist 612*	*Nist 612*	*Nist 612*	*Nist 612*	*Nist 612*	*Nist 610*	*Nist 610*	*Nist 610*	*Nist 610*	*Nist 610*	*Nist 610*	*Nist 610*	*Nist 610*	*Nist 612*	*Nist 612*	*Nist 610*	*Nist 610*
G10																		
1	1.48	0.25	7.60	0.91	0.64	0.11	3.98	0.68	3.80	0.43	0.59	0.09	22.90	1.70	7.77	0.53	107.90	7.50
2	21.70	4.70	76.00	13.00	9.90	2.00	58.00	11.00	27.50	3.00	2.63	0.14	92.00	4.10	27.40	1.30	341.00	17.00
3	9.30	1.70	29.80	4.70	4.20	0.75	23.00	4.10	8.60	1.40	0.45	0.06	21.60	1.50	6.51	0.26	87.20	1.70
4	9.60	2.40	24.10	3.80	3.62	0.71	20.70	3.90	14.20	2.40	2.27	0.33	51.10	7.50	15.10	2.00	181.00	21.00
5	0.95	0.10	6.30	0.31	0.55	0.06	4.26	0.30	6.27	0.48	0.89	0.07	34.80	1.70	11.52	0.47	153.40	5.60
6	0.26	0.10	5.34	0.85	0.17	0.06	1.70	0.48	1.74	0.33	0.53	0.16	10.70	1.70	3.76	0.44	55.00	5.70
7	2.99	0.37	16.40	1.10	1.53	0.14	11.28	0.94	13.00	1.10	2.14	0.22	60.40	5.00	18.70	1.30	230.00	14.00
8	0.95	0.15	12.28	0.97	0.60	0.06	5.93	0.61	9.10	1.20	1.30	0.19	44.70	5.30	13.70	1.40	169.00	15.00
9	7.80	3.60	32.00	12.00	4.80	2.20	30.00	12.00	20.70	5.60	0.95	0.14	66.60	8.90	18.10	1.60	205.00	13.00
10	0.10	0.02	2.35	0.14	0.14	0.02	2.45	0.22	6.27	0.41	0.34	0.03	38.00	1.90	12.48	0.57	163.10	6.80
11	2.13	0.43	12.70	1.50	1.06	0.21	6.70	1.20	5.56	0.61	0.46	0.05	29.80	1.30	10.75	0.43	147.60	4.00
12	1.83	0.38	11.70	1.30	1.06	0.20	6.60	1.10	6.46	0.61	0.64	0.08	35.90	1.90	12.84	0.59	173.40	6.70
13	0.58	0.15	24.60	1.10	0.49	0.13	4.35	0.92	7.30	1.30	4.30	1.20	35.00	5.40	12.50	2.40	160.00	28.00
14	0.04	0.01	9.20	1.30	0.29	0.06	5.50	1.00	11.50	1.90	1.45	0.26	58.90	8.10	17.70	2.20	212.00	24.00
15	14.70	4.70	51.00	15.00	6.90	2.20	39.00	12.00	16.90	4.40	0.73	0.15	51.90	7.90	15.60	1.90	201.00	21.00
G18																		
1	1.16	0.90	13.40	2.50	0.60	0.43	3.80	1.80	4.84	0.57	0.79	0.07	26.70	1.30	8.98	0.36	122.60	4.60
2	16.50	2.70	58.60	7.00	6.60	1.10	33.90	5.50	10.20	1.20	0.98	0.08	26.75	0.94	7.89	0.14	103.50	1.30
3	20.40	7.00	64.00	19.00	8.00	2.70	40.00	13.00	12.00	2.80	1.27	0.20	29.30	2.30	8.18	0.39	101.60	5.10
4	0.67	0.33	8.85	0.80	0.39	0.14	3.21	0.60	4.76	0.43	0.78	0.08	22.80	1.40	7.72	0.47	101.80	6.10
5	6.70	2.40	29.40	6.50	2.89	0.99	16.30	5.10	7.70	1.20	1.14	0.10	32.30	1.60	10.00	0.30	133.60	2.90
6	21.60	5.50	68.00	15.00	8.40	2.10	42.00	10.00	11.30	2.20	1.03	0.14	26.60	1.90	7.66	0.32	101.50	4.40
7	1.03	0.31	10.29	0.45	0.25	0.07	1.62	0.23	2.49	0.21	0.46	0.05	16.70	1.60	6.12	0.56	87.20	7.90
8	0.11	0.04	13.40	1.50	0.12	0.02	1.99	0.21	5.28	0.50	0.96	0.11	35.20	3.30	12.40	1.10	170.00	16.00
9	3.20	1.00	18.60	2.90	1.33	0.42	8.10	2.10	5.96	0.63	0.88	0.07	30.90	1.30	10.39	0.34	139.20	3.80
10	141.00	33.00	415.00	97.00	52.00	12.00	250.00	57.00	52.00	11.00	4.30	0.84	65.50	8.80	12.61	0.83	132.70	6.50
11	20.60	5.20	67.00	14.00	8.10	2.00	41.20	9.90	13.30	2.10	1.33	0.15	39.90	1.90	12.42	0.34	162.10	3.40
12	13.60	2.60	46.80	7.20	5.50	1.00	29.50	5.10	12.90	1.40	1.79	0.18	48.20	3.20	13.92	0.77	173.40	8.30
13	0.86	0.28	11.77	0.78	0.41	0.11	3.23	0.63	5.00	0.36	0.71	0.06	27.40	1.10	9.18	0.33	122.90	3.40
14	7.60	2.10	31.10	5.50	2.95	0.77	16.20	4.00	5.93	0.92	0.72	0.07	22.30	1.00	7.18	0.20	97.30	2.50
15	9.50	4.70	37.00	13.00	3.80	1.80	17.80	8.30	8.20	1.90	1.11	0.14	30.80	1.70	9.66	0.25	127.90	2.40

TABLE A4 Cont. ZIRCON LA-ICP-MS DATA

Sample #	Ho (ppm)	±2σ	Er (ppm)	±2σ	Tm (ppm)	±2σ	Yb (ppm)	±2σ	Lu (ppm)	±2σ	Ti (ppm)	±2σ	Pb (ppm)	±2σ	Th (ppm)	±2σ	U (ppm)	±2σ
Int Std	*Nist 612*	*Nist 612*	*Nist 610*	*Nist 610*	*Nist 612*	*Nist 612*	*Nist 610*	*Nist 610*	*Nist 612*	*Nist 612*	*Nist 612*	*Nist 612*	*Nist 612*	*Nist 612*	*Nist 612*	*Nist 612*	*Nist 612*	*Nist 612*
G10																		
1	41.40	2.50	218.00	14.00	47.20	3.00	477.00	30.00	89.10	4.70	2.7	0.5	2.60	0.22	299	29	1280	130
2	121.10	6.20	571.00	28.00	107.00	4.90	989.00	46.00	168.40	7.10	3.4	0.4	5.67	0.26	764	47	1920	130
3	33.75	0.55	178.50	2.30	39.39	0.60	407.60	5.70	77.70	1.10	1.3	0.4	2.70	0.10	305	4	1884	26
4	64.00	6.40	316.00	29.00	67.30	5.80	694.00	61.00	130.00	11.00	29.0	13.0	12.40	2.10	685	66	2130	210
5	57.30	1.80	279.40	7.60	55.10	1.50	522.00	14.00	94.40	2.10	4.0	0.6	2.11	0.14	286	15	684	25
6	23.30	2.30	127.00	11.00	30.60	2.50	336.00	28.00	68.80	6.30	1.8	0.4	1.93	0.34	207	43	963	58
7	80.90	4.30	379.00	18.00	73.60	3.00	702.00	25.00	123.90	4.00	10.5	1.6	3.94	0.24	492	25	1317	76
8	59.90	4.60	290.00	20.00	57.60	3.40	563.00	32.00	100.90	5.20	5.5	1.1	3.57	0.25	376	33	1030	100
9	68.40	3.30	310.00	13.00	59.50	2.10	549.00	17.00	96.20	2.90	3.1	0.4	3.86	0.58	317	19	1126	54
10	60.50	2.30	292.00	11.00	57.90	2.00	560.00	20.00	100.70	2.80	*660*	240	1.19	0.08	115	9	510	20
11	57.50	1.50	297.40	6.70	63.70	1.50	633.00	13.00	118.00	2.20	4.6	1.1	3.59	0.19	485	24	2654	36
12	65.80	2.50	330.00	11.00	70.40	2.20	704.00	21.00	127.20	3.70	4.6	1.0	4.56	0.32	439	17	2139	71
13	55.50	8.00	264.00	32.00	55.20	5.30	542.00	44.00	97.40	6.20	84.0	30.0	9.60	0.83	210	9	826	90
14	74.30	7.50	343.00	32.00	66.50	5.40	615.00	45.00	108.80	7.10	3.9	0.5	3.09	0.39	415	58	972	55
15	74.00	6.70	355.00	28.00	70.80	4.90	671.00	43.00	120.60	6.30	2.2	0.4	4.32	0.54	546	74	1720	100
G18																		
1	47.70	1.50	247.10	7.60	52.30	1.50	523.00	15.00	100.60	2.60	5.5	0.8	1.71	0.14	165	7	294	13
2	39.41	0.52	204.20	2.40	43.84	0.57	443.30	5.80	86.28	0.98	3.1	0.4	4.06	0.35	306	19	491	11
3	38.00	2.00	191.70	9.90	40.10	2.00	396.00	19.00	76.50	3.70	4.3	0.6	1.31	0.17	103	8	164	10
4	36.70	2.20	184.00	11.00	37.80	2.40	365.00	24.00	67.00	4.30	6.8	0.8	4.38	0.22	85	3	658	77
5	51.50	1.10	266.10	4.70	55.60	1.00	562.00	9.60	107.30	1.50	4.0	0.6	1.72	0.09	193	6	315	9
6	39.40	1.70	203.50	8.90	43.00	1.90	430.00	19.00	82.60	3.30	4.0	0.5	2.29	0.52	117	3	259	10
7	35.50	3.30	192.00	18.00	42.30	3.90	434.00	40.00	85.20	7.30	20.7	5.0	1.81	0.21	114	11	249	24
8	65.30	6.20	333.00	32.00	68.60	6.40	671.00	62.00	127.00	12.00	6.1	1.0	2.47	0.26	284	35	466	46
9	52.50	1.20	265.80	5.00	53.60	1.00	521.50	9.00	97.90	1.40	4.6	0.7	1.68	0.10	196	6	340	6
10	45.70	2.70	223.00	14.00	45.30	3.00	455.00	31.00	87.20	5.00	2.8	0.6	8.30	1.30	162	8	377	24
11	61.90	1.10	311.90	5.20	63.50	1.10	619.00	10.00	116.70	2.20	150	130	5.18	0.62	200	10	344	15
12	61.40	2.90	290.00	12.00	56.40	2.30	529.00	20.00	97.40	3.40	7.0	1.0	6.94	0.87	182	8	227	7
13	47.20	1.30	237.00	5.70	49.30	1.00	499.80	9.90	96.10	1.90	2110	450	1.72	0.12	192	8	387	16
14	37.26	0.95	193.20	4.70	39.92	0.99	397.90	9.40	77.40	1.70	10.1	2.5	2.32	0.22	224	11	362	11
15	48.72	0.75	250.10	3.90	51.96	0.70	524.70	8.30	102.00	1.40	4.8	0.5	1.80	0.25	163	6	260	7

TABLE A4 Cont. ZIRCON LA-ICP-MS DATA

Sample #	La (ppm)	±2σ	Ce (ppm)	±2σ	Pr (ppm)	±2σ	Nd (ppm)	±2σ	Sm (ppm)	±2σ	Eu (ppm)	±2σ	Gd (ppm)	±2σ	Tb (ppm)	±2σ	Dy (ppm)	±2σ
Int Std	Nist 612	Nist 612	Nist 612	Nist 612	Nist 612	Nist 612	Nist 610	Nist 610	Nist 610	Nist 610	Nist 610	Nist 610	Nist 610	Nist 610	Nist 612	Nist 612	Nist 610	Nist 610
G20																		
1	10.70	3.20	40.00	10.00	4.70	1.40	27.10	7.40	14.80	2.80	0.71	0.12	50.30	6.20	13.70	1.50	160.00	16.00
2	--	--	7.58	0.13	0.03	0.01	0.75	0.09	1.71	0.14	0.37	0.03	10.64	0.58	3.60	0.17	48.20	1.70
3	0.71	0.22	8.83	0.80	0.30	0.08	2.55	0.45	4.06	0.22	0.26	0.02	28.64	0.75	10.17	0.26	140.70	3.50
4	40.00	12.00	100.00	28.00	10.90	3.30	48.00	14.00	10.60	2.40	0.82	0.16	23.60	2.00	6.55	0.23	82.50	1.30
5	0.20	0.07	10.38	0.21	0.09	0.01	0.99	0.12	2.10	0.13	0.48	0.04	12.08	0.40	4.27	0.10	59.30	1.10
6	17.00	5.70	58.00	18.00	6.80	2.30	35.00	12.00	10.40	2.70	0.71	0.18	27.50	2.50	8.30	0.35	108.90	3.00
7	10.50	2.00	32.80	4.60	3.23	0.59	15.40	2.50	7.82	0.57	0.78	0.06	33.60	1.30	10.53	0.40	136.60	5.00
8	4.10	2.50	17.10	4.60	0.97	0.57	5.90	3.30	3.24	0.68	0.39	0.05	14.58	0.88	4.76	0.25	61.10	3.00
9	3.49	0.67	16.10	1.50	0.95	0.19	4.72	0.76	2.62	0.24	0.53	0.04	12.04	0.72	3.97	0.17	53.60	1.80
10	1.13	0.38	13.00	1.20	0.39	0.12	2.18	0.50	2.08	0.15	0.46	0.04	10.75	0.43	3.59	0.10	50.30	1.30
11	1.36	0.46	7.60	1.00	0.20	0.06	1.21	0.25	1.96	0.40	0.39	0.08	11.70	2.40	4.14	0.79	57.00	11.00
12	9.00	3.30	29.10	7.20	2.50	0.90	11.30	3.90	3.40	0.68	0.48	0.06	10.89	0.55	3.32	0.11	43.70	1.00
13	37.10	9.50	94.00	22.00	9.60	2.50	40.00	10.00	8.20	1.70	0.90	0.15	15.10	1.40	3.98	0.19	51.30	1.50
14	2.90	1.30	15.00	2.30	0.93	0.40	5.50	1.70	4.57	0.71	0.55	0.06	20.50	2.00	6.26	0.56	78.70	5.90
15	1.73	0.57	8.88	0.44	0.37	0.16	1.31	0.20	1.25	0.14	0.23	0.03	6.90	0.62	2.37	0.21	34.80	3.00

TABLE A4 Cont. ZIRCON LA-ICP-MS DATA

Sample #	Ho (ppm)	±2σ	Er (ppm)	±2σ	Tm (ppm)	±2σ	Yb (ppm)	±2σ	Lu (ppm)	±2σ	Ti (ppm)	±2σ	Pb (ppm)	±2σ	Th (ppm)	±2σ	U (ppm)	±2σ
Int Std	Nist 612	Nist 612	Nist 610	Nist 610	Nist 612	Nist 612	Nist 610	Nist 610	Nist 612	Nist 612	Nist 612	Nist 612	Nist 612	Nist 612	Nist 612	Nist 612	Nist 612	Nist 612
G20																		
1	54.20	5.00	249.00	22.00	48.70	3.90	447.00	33.00	77.40	5.70	6.2	1.1	4.13	0.52	481	59	940	43
2	19.28	0.54	104.50	2.50	23.93	0.46	258.60	3.60	52.85	0.67	160	100	1.02	0.05	108	2	237	3
3	54.40	1.50	275.90	7.60	59.00	1.50	585.00	15.00	107.40	2.80	2.4	0.3	4.47	0.33	489	37	1410	73
4	31.20	0.39	158.90	1.90	34.89	0.49	350.70	5.50	67.30	1.10	3.4	0.4	2.89	0.15	332	15	704	22
5	24.36	0.41	133.10	2.00	30.78	0.52	331.90	6.30	67.78	0.94	6.5	0.8	1.59	0.08	156	5	339	9
6	40.99	0.93	205.30	5.00	43.60	1.20	419.00	12.00	77.30	1.80	3.9	0.5	4.53	0.33	380	11	1299	19
7	50.70	1.70	249.90	7.90	51.50	1.40	496.00	13.00	92.30	1.80	14400	1500	2.82	0.11	254	11	564	11
8	23.60	1.10	123.00	5.30	27.00	1.10	278.00	12.00	55.70	2.20	7.3	1.4	2.13	0.12	184	5	404	7
9	21.42	0.73	117.00	3.60	27.25	0.78	292.10	7.60	60.50	1.80	127	85.0	2.39	0.39	144	8	284	7
10	20.72	0.47	116.30	2.30	28.17	0.61	311.90	8.00	64.60	1.20	78.0	36.0	1.55	0.10	181	8	414	16
11	21.90	3.90	122.00	21.00	27.30	4.20	281.00	40.00	57.00	7.70	15.5	4.2	2.46	0.43	124	25	326	32
12	17.36	0.47	94.00	2.50	21.47	0.60	229.10	6.80	46.30	1.30	7.7	1.2	1.56	0.08	155	4	321	9
13	20.19	0.58	110.10	2.90	25.31	0.77	271.60	9.10	54.50	1.50	16.8	3.1	2.00	0.22	160	10	324	13
14	29.60	2.10	146.10	8.20	31.10	1.50	308.00	13.00	57.90	1.70	3.8	0.4	1.92	0.21	205	25	350	28
15	14.10	1.20	76.50	6.30	17.70	1.40	189.00	15.00	37.80	2.70	21.1	4.1	2.11	0.21	95	8	208	16

TABLE A5. RAW K-FELDSPAR Pb-Pb DATA

Sample I.D	$^{208}Pb/^{204}Pb$	±2σ	$^{207}Pb/^{204}Pb$	±2σ	$^{206}Pb/^{204}Pb$	±2σ	$^{207}Pb/^{206}Pb$	±2σ
C64-D2	39.347	0.013	15.732	0.008	19.341	0.005	0.8133	0.0003
C64-D	39.324	0.020	15.726	0.011	19.339	0.006	0.8131	0.0005
C55-D2	39.335	0.012	15.728	0.008	19.334	0.004	0.8135	0.0003
C55-D	39.325	0.014	15.722	0.006	19.343	0.008	0.8127	0.0003
C55-C2	39.320	0.019	15.721	0.011	19.331	0.006	0.8131	0.0003
C55-C	39.315	0.018	15.722	0.011	19.333	0.006	0.8131	0.0005
C55-B2	39.350	0.020	15.729	0.011	19.350	0.009	0.8129	0.0004
C55-B	39.356	0.022	15.732	0.015	19.348	0.007	0.8130	0.0006
C50-D2	39.330	0.019	15.730	0.008	19.336	0.006	0.8136	0.0003
C50-D	39.309	0.021	15.720	0.009	19.330	0.008	0.8132	0.0003
C50-C2	39.330	0.020	15.731	0.012	19.332	0.006	0.8136	0.0005
C50-C	39.307	0.024	15.722	0.012	19.328	0.010	0.8134	0.0005
C50-B2	39.339	0.021	15.724	0.010	19.334	0.007	0.8134	0.0003
C50-B	39.323	0.016	15.722	0.010	19.332	0.006	0.8134	0.0003
C50-A	39.352	0.025	15.741	0.016	19.345	0.008	0.8135	0.0005
Reference Curves at 100Ma								
Shale Curve*	39.586	--	15.714	--	19.336	--	--	--
Bluebell Curve†	38.884	--	15.525	--	18.199	--	--	--

* from Godwin and Sinclair (1982)
† from Andrew et al. (1984)

TABLE A6. Ti THERMOMETRY

Point #	Ti (ppm)	±2σ	T (°C)	±2σ
SAMPLE G1				
1	*1.1*	*0.3*	*575*	*17*
2	*2.2*	*0.4*	*621*	*11*
3	*3.3*	*0.5*	*652*	*10*
4	*3.5*	*0.5*	*655*	*11*
5	*5.2*	*1.8*	*688*	*25*
6	*4.1*	*0.9*	*669*	*16*
7	*1.1*	*0.3*	*574*	*17*
8	*1.3*	*0.6*	*583*	*25*
9	*1.4*	*0.3*	*591*	*15*
10	*1.3*	*1.0*	*584*	*39*
SAMPLE G4				
1	*5.5*	*0.5*	*692.5*	*8.0*
2	*9.5*	*1.4*	*741.1*	*13.0*
3	*6.2*	*0.5*	*702.7*	*6.3*
4	*5.1*	*0.5*	*686.0*	*8.2*
5	*16.8*	*0.8*	*796.9*	*4.9*
6	*4.7*	*0.8*	*679.8*	*12.6*
7	*5.0*	*0.9*	*685.0*	*13.6*
8	*4.9*	*0.6*	*682.3*	*8.9*
9	*16700*	*1200*	*2952.2*	*66.7*
10	*8.2*	*1.7*	*727.6*	*17.4*
11	*11.6*	*2.4*	*760.0*	*18.5*
12	*5.3*	*1.1*	*689.6*	*16.1*
13	*13.1*	*4.5*	*771.9*	*30.0*
14	*3.5*	*0.6*	*656.9*	*12.0*
15	*4.5*	*0.5*	*675.1*	*9.4*
SAMPLE G10				
1	*2.7*	*0.5*	*635*	*14*
2	*3.4*	*0.4*	*654*	*9*
3	*1.3*	*0.4*	*585*	*19*
4	*29.0*	*13.0*	*857*	*44*
5	*4.0*	*0.6*	*667*	*12*
6	*1.8*	*0.4*	*606*	*15*
7	*10.5*	*1.6*	*750*	*14*
8	*5.5*	*1.1*	*693*	*16*
9	*3.1*	*0.4*	*647*	*10*
10	*660*	*240*	*1387*	*81*

Point #	Ti (ppm)	±2σ	T (°C)	±2σ
SAMPLE G10 CONT.				
11	*4.6*	*1.1*	*678*	*18*
12	*4.6*	*1.0*	*677*	*16*
13	*84*	*30*	*995*	*46*
14	*3.9*	*0.5*	*665*	*10*
15	*2.2*	*0.4*	*622*	*12*
SAMPLE G18				
1	*5.5*	*0.8*	*692*	*12*
2	*3.1*	*0.4*	*646*	*10*
3	*4.3*	*0.6*	*671*	*11*
4	*6.8*	*0.8*	*711*	*10*
5	*4.0*	*0.6*	*667*	*10*
6	*4.0*	*0.5*	*666*	*9*
7	*20.7*	*5.0*	*819*	*24*
8	*6.1*	*1.0*	*701*	*13*
9	*4.6*	*0.7*	*677*	*11*
10	*2.8*	*0.6*	*638*	*15*
11	*150*	*130*	*1085*	*113*
12	*7.0*	*1.0*	*713*	*12*
13	*2110*	*450*	*1738*	*73*
14	*10.1*	*2.5*	*747*	*21*
15	*4.8*	*0.5*	*681*	*9*
SAMPLE G20				
1	*6.2*	*1.1*	*703*	*14*
2	*160*	*100*	*1096*	*88*
3	*2.4*	*0.3*	*627*	*10*
4	*3.4*	*0.4*	*653*	*9*
5	*6.5*	*0.8*	*706*	*10*
6	*3.9*	*0.5*	*665*	*10*
7	*14400*	*1500*	*2819*	*88*
8	*7.3*	*1.4*	*717*	*16*
9	*127*	*85*	*1058*	*87*
10	*78*	*36*	*984*	*57*
11	*15.5*	*4.2*	*789*	*25*
12	*7.7*	*1.2*	*722*	*13*
13	*16.8*	*3.1*	*797*	*18*
14	*3.8*	*0.4*	*663*	*9*
15	*21.1*	*4.1*	*821*	*20*

Note: Shaded rows represent ablated Rutile inclusion

Chapter 3 Supplemental Information

Supplemental Methods

U-Pb Analysis

Zircons were separated from two samples of the APS granite (G1 and G3) using standard gravimetric and magnetic techniques. From the heavy mineral separate, we randomly selected ~150 zircons for further processing. These zircons were subsequently annealed for 48 hours at 1000°C. The annealed zircons, along with two reference grains (Zircon 94-35), were mounted in epoxy using 25mm round plastic molds. The mounted zircons were imaged using secondary electron, cathodoluminescence and backscatter electron signals with a Zeiss Evo-MA-15 scanning electron microscope (SEM). Representative zircons are shown in Figure A1. U-Pb dating was carried out by LA-ICPMS spot analysis on 108 inherited zircon components. Laser ablation sites were selected from the SEM images to minimize mixing with the magmatic rims and to pick parts of the inherited cores with favorable uranium concentrations. U-Pb analyses were performed using a New Wave UP-213 laser coupled to a NuPlasma Multi-Collector ICP Mass Spectrometer using procedures modified from Simonetti et al (2005). The laser was operated at a 4 Hz pulse rate, with a beam spot size of 30 μm and a fluence of ~3 J/cm^2. Analyses were taken in groups of ten, bracketed by analysis of zircon reference materials GJ-1 (Jackson et al., 2004), 94-35 (Klepeis et al., 1998) and, a 30s on-peak gas + acid blank. Reproducibility of the primary reference GJ1 is estimated to be ~1% 2 SD for $^{207}Pb/^{206}Pb$ and ~3% 2 SD for $^{206}Pb/^{238}U$. The secondary reference, 94-35, yields a weighted regression intercept of 55.96±0.54 Ma (MSWD 0.18, n =17) for Mount 1 and 55.54±0.48 Ma (MSWD 0.87, n=20) for Mount 2 in Tera Wasserburg space (94-35 accepted value is 55.5±1.5 Ma (Klepeis et al., 1998)).

The errors reported in Table A7, are a quadratic combination of the within run standard error and the external reproducibility of the primary reference in terms of standard deviation. All data points were plotted on a concordia plot (Figure 3.2A) using the Isoplot software of Ludwig (2003)

Whole Rock Sm-Nd Isotope Methodology

Samarium- Neodymium isotopes were measured via whole rock digestion of un-weathered samples of G1 and G3 that had been ground to a fine powder in an agate mill. The digestion, chemical separation, and isotopic analysis methodology followed that outlined by D'Souza et al. (2016) and references therein. Age corrections, based on the U-Pb age of the granites, were applied to calculate the εNd_T of each sample, representing the isotopic ratios at the time of granite crystallization. Data presented in Table A8.

Correcting Discordant Points Methodology

The R modeling procedure of Reimink et al. (2016) was used to assess the relative likelihood of each potential lower intercept age. The code was run with a node spacing of 4 Myr. U-Pb data from the 108 zircon cores was analyzed. The lower intercept age with the highest likelihood was ~110 Ma, which is consistent with the intrusion age derived from U-Pb dating of 107 ± 3 Ma (Pigage, 2004; Gordey, 2013; Rasmussen, 2013). The output figures from the modeling procedure, performed on the APS U-Pb data, are shown in Figure A2.

Anchoring the lower intercept at 110 Ma allowed upper intercept probabilities to be extracted from the modeling procedure (Reimink et al., 2016). Essentially, this entails calculating the upper intercept ages of all zircon ages anchored at a lower intercept of 110 Ma. In practice,

this ‘anchored upper intercept’ age spectrum is created by calculating the total probability along a discrete line in U-Pb Concordia space that has a lower intercept of 110 Ma and an upper intercept of *t*. This *t* value in changed in 4 Myr intervals, creating ca. 1,110 distinct lines between 110 Ma and 4500 Ma. Lines that cross one or more discordant data points (including full uncertainties) accrue more probability, and end up with higher total probability, or ‘likelihood’ in our terminology. A spectrum is then created from the upper intercept likelihoods of these lines, which we interpret to be the age spectrum of the inherited zircon population from the APS granites. This interpretation is valid if discordance in the U-Pb zircon analyses is created by either Pb-loss from inherited grains during intrusion of the granite or by mixing of multiple U-Pb age domains (inherited core and magmatic rim) during sampling by the laser beam. We consider these two explanations for U-Pb discordance in the APS grains to be by far the most likely; therefore the upper intercept age spectrum represents the age spectrum of the zircon component inherited during APS granite emplacement. In order to estimate uncertainties in the inherited fractions of the APS zircon age spectrum, the anchored lower intercept was varied by ±2 Myr (anchored at 108 and 112 Ma) and ±4 Myr (anchored at 106 and 114 Ma) to produce Figure 3.3. This is demonstrated on Figure A4. For Figure 3.3 the conservative error envelope is taken from 110 ± 4 Ma.

Discrete data inputs (zircon ages in this case) are required in order to perform statistical tests on the corrected APS zircon spectrum; these are not produced by the modeling procedure outlined above. To extract discrete data the discordant U-Pb analyses are corrected back onto the concordia, producing discrete corrected concordia ages. This is done by fixing the lower intercept at 110 Ma (which corresponds to a $^{206}Pb/^{238}U$ ratio of 0.017 and a $^{207}Pb/^{235}U$ ratio of 0.112) and solving the equations between the polynomial concordia and a discordia line (defined

by the lower intercept and the data point) simultaneously (Figure A5). An iterative solution is required, which was solved with the "What if Goal Seeker Function" in Excel. While errors on the discrete corrected concordia ages are not required for the K-S test (see below), they are calculated for completeness. Errors on the corrected points were calculated by repeating the calculation (above) for each data point +/- the 1σ error in $^{206}Pb/^{238}U$. The $^{206}Pb/^{238}U$ error has a greater affect on the gradient of the discordia than the $^{207}Pb/^{235}U$, so will therefore create a larger inaccuracy. Results and errors for each stage of the calculation are shown in Table A9.

Data points around the fixed lower-intercept point ($^{206}Pb/^{238}U < 0.05$ and $^{207}Pb/^{235}U < 0.5$; grey shading on Table A9) were removed. These filtered results were not corrected as these analyses are dominated by lead loss or magmatic rim overprinting, and therefore, would require large extrapolations (introducing large errors) to calculate the upper intercept. In some cases, an upper intercept could not be calculated for these points (i.e. Grain # 19 and 26 from Sample G1; Table A9). Seventy-one out of the 108 analyses were corrected back onto the concordia (Table A10). Figure A6 shows the enhanced clarity in the upper intercept output figure from the modeling procedure when only the filtered data is run.

Kolmogorov-Smirnov testing between the zircons from individual stratigraphic units and the APS zircons

The Kolmogorov- Smirnov (or K-S) two-sample test is a statistical test that can be used to provide validation of the visual comparison of strata age probability diagrams with the APS zircon age pattern. The K-S test evaluates the null hypothesis that "two distributions are the same or came from the same parent population". The output of the K-S test is a value P; in this study if P is less than 0.05 (i.e >95% level of confidence), then we conclude that the zircons from a

sedimentary unit cannot produce the pattern seen in the APS zircons. If P is greater than 0.05, then the null hypothesis cannot be rejected and the sedimentary unit cannot be discarded as the source of the APS zircons. The K-S test cannot determine if the sedimentary unit is the source, the test can only eliminate strata that do not contain zircons from the same population as the APS. A more detailed explanation of the K-S test can be found in Berry et al. (2001) and DeGraaff-Surpless et al. (2003). Values for the sedimentary units equivalent to those proposed to be present in the Anvil region (Table A12) are from Lane and Gehrels (2014), Gehrels et al. (1999) and Leslie (2009) the raw data for the Hyland Group from Ross et al. (2005) could not be located.

To run the K-S test the data for each unit and the APS were plotted as Cumulative Distribution Functions (CDF; Figure A7). The K-S test values are calculated, using the CDF, for the zircons from each stratigraphic unit and the APS zircons using the program developed by Guynn and Gehrels (2010) (Table A11). The green cells in Table A11 shows that the Keele Formation (Windermere Supergroup) and Gull Lake Formation equivalent strata have P>0.05 and therefore cannot be rejected as being the source of the APS. The P value for the Keele Formation compared to the APS, of 0.9994 shows the very high similarity between the zircons in these two samples. The P value is very sensitive to the number of analyses included for each sample (Table A12), generally as n goes up P goes down. For most of the samples the number of analyses is similar except for the Gull Lake Formation equivalent sample, which has nearly twice as many analyses as the other samples, meaning that P is comparatively lower for this sample than it would be for a sample with fewer analyses. However, even with the higher number of analyses the Gull Lake Formation equivalent sample shows a P value greater than 0.05 meaning,

while the P value may have decreased, the K-S test result is not changed by the larger sample size.

Therefore, the K-S test confirms the visual interpretation that the Windermere Supergroup could share a zircon source with the APS. However, the statistical testing also shows that the Gull Lake Formation, into which the APS is emplaced, cannot be ruled out as a source for the Anvil zircons.

How to deal with mixing and assimilation

The zircons of the APS may not be derived from a single source; instead the population seen in the crystallized granite could represent zircons derived from the melting of multiple sources, or from one source plus assimilation from other units. We can use two methods to constrain to what extent melting and assimilation have affected the zircon population in the APS: the K-S test and Nd isotope mixing.

K-S test on zircons from multiple sources

To test whether mixed sedimentary units can produce the populations of zircons recorded in the APS three simplifying assumptions are made:

1. That the abundance of zircons in each unit is identical; this means that if you assimilate a volume of unit 1 you will inherit the same number of zircons as you would assimilating the same volume of unit 2.
2. That the units mix in equal quantities and provide an equal number of zircons to the final mixture. This assumption follows from assumption one, but indicates that if two units

mix each unit provides 50% of the total number of zircons and if 5 units mix each units provides 20% of the total number of zircons e.t.c.

3. That you will only melt sequential sedimentary units in contact with each other. This means that the melt will not pass through a middle unit without melting it if melt is generated in the sedimentary sequences above and below that unit.

These three assumptions allow us to more simply model mixing between combinations of units. Populations of 250 zircon ages were chosen randomly from each sedimentary sample, creating a representative sample of the zircons ages in each unit and removing the bias due to the number of analyses in each sample. This was done five times leading to five runs. For each run the representative samples were mixed in combinations of two sequential units, three sequential units and all five potential melt sources. Then, 200 grains were randomly selected from each theoretical mixed zircon population to create a sample that could be compared to the zircon age pattern recorded in the APS via the K-S test (Table A13). The K-S test was run using the same method and limits as for the individual strata.

The K-S test shows that most mixed populations of zircons are not statistically capable of being the source for the APS zircons (i.e. $P<0.05$). The only mixed zircon populations that consistently gave P values greater than 0.05 were the mixtures of Windermere Supergroup and Gull Lake Formation equivalent strata, which are interpreted as the source rock and host rock for the APS respectively.

Combinations of the Windermere Supergroup samples and Gull Lake Formation equivalent samples with either the Little Dal Group (MMSG) or Rabbitkettle Formation equivalent strata returned P values greater than 0.05 in particular runs.

Overall, these results indicate that while assimilation of the host rock (Gull Lake Formation) and contribution of low volumes of zircons from either the Little Dal Group or Rabbitkettle formation, cannot be ruled out; the K-S test does supports the conclusion that the Windermere Supergroup is the source for the APS.

Mixing from Nd isotopes

Following on from the K-S tests above, we can assume that the zircons in the APS are derived only from a mixture of the Windermere Supergroup and the current host rock for the APS (Cambrian Gull Lake Formation and overlying Ordovician to Silurian Rabbitkettle Formation equivalent strata). Therefore, binary mixing of Nd isotopes can provide constraints on the amount of assimilation/ mixing that has occurred between the two units (Figure A8). This calculation gives the fraction of Nd provided from each end member, there is no evidence to suggest Nd mixing and zircon mixing should correlate. Therefore, a 50% addition of Nd from mixing/assimilation may not mean a 50% zircon addition from mixing/assimilation; however, this method can provide a good, rough, approximation of the degree of importance of assimilation/mixing in the generation of the APS. For the average Hyland Group sediments no mixing is necessary to explain the Nd isotopes and concentration of the APS. Individual samples of the Hyland group can mix with up to ~40±5% Silurian-Ordovician Rabbitkettle equivalent sediments and up to ~65±15% Gull Lake equivalent strata to generate the Nd values seen in the APS. It is unlikely that only the isotopically extreme samples produce the melt so the degree of assimilation is likely to be lower than calculated above.

Neodymium isotopes show that while assimilation/mixing is not necessary to generate the APS from the Hyland Group (Windermere Supergroup; Figure A9) the assimilation/mixing

of the host rock into the melt cannot be ruled out. Regionally the amphibolite facies Gull Lake Formation has not achieved the temperature required to melt, therefore, we assume assimilation due to intrusion of the APS, rather than magma mixing, was the dominant process. Assimilation of the Gull Lake formation into melt derived from the Hyland group would change both the Nd concentration and zircon age spectra of the final crystallized batholith. However, the Nd isotopes (like the K-S test) cannot be explained by only melting of the Gull Lake Formation implying a role for Windermere Supergroup (Hyland group) sediments in the generation of the APS.

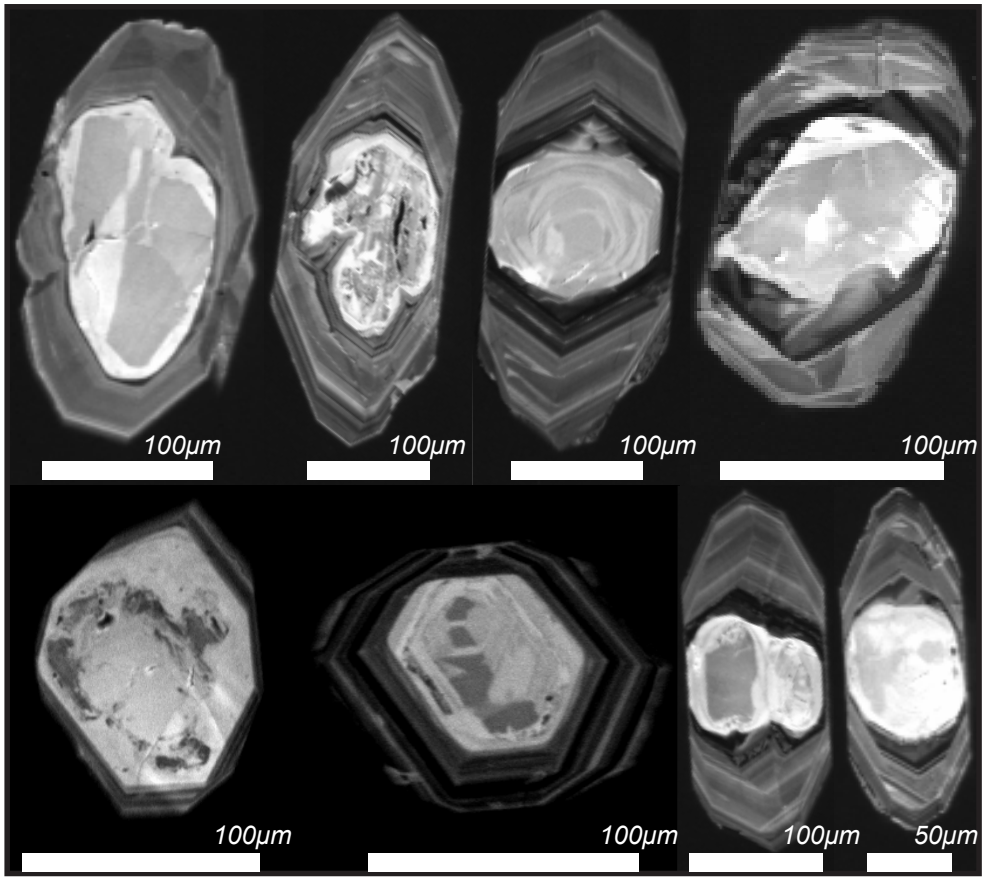

Figure A1: Typical zircons from Sample G1 and G3 imaged in cathodoluminescent light on the Zeiss Evo-MA-15 scanning electron microscope (SEM).

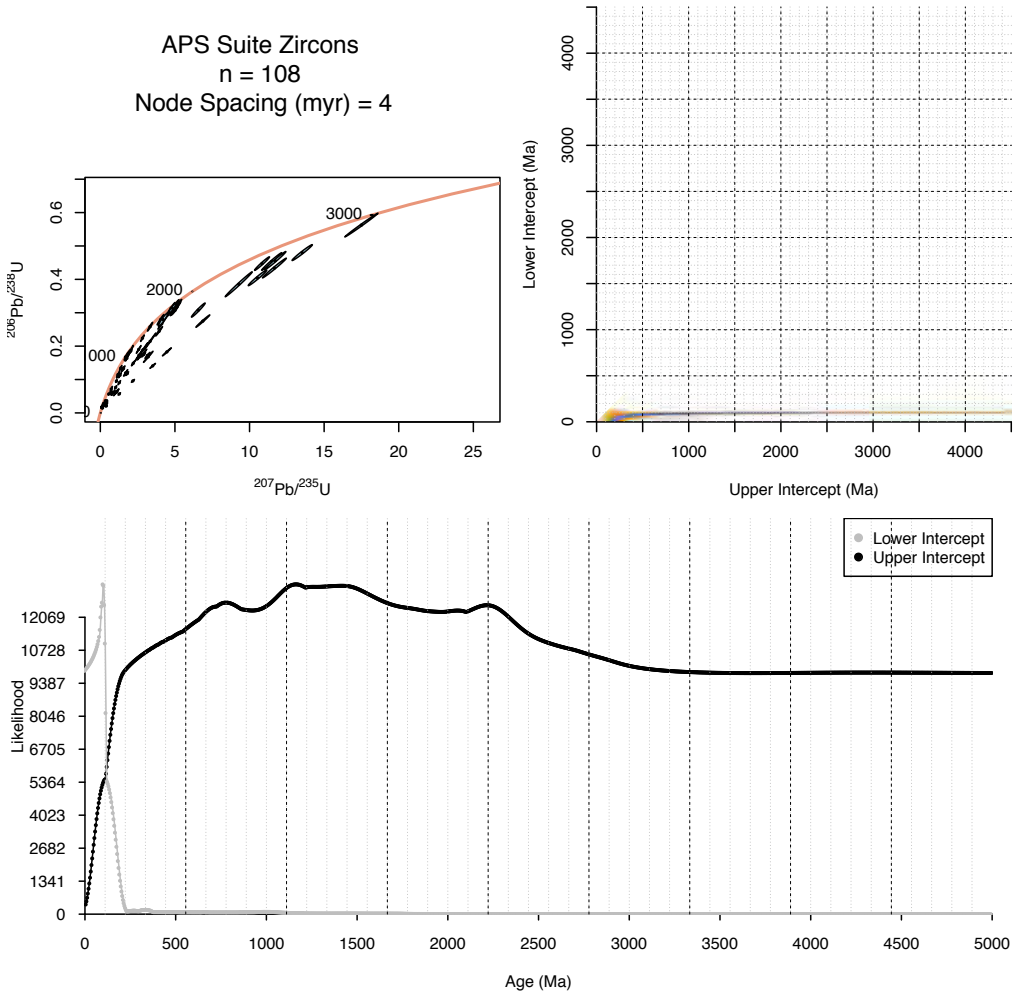

Figure A2: Output compilation figure from Reimink et al. (2016) showing the dataset from the 108 core analyses.

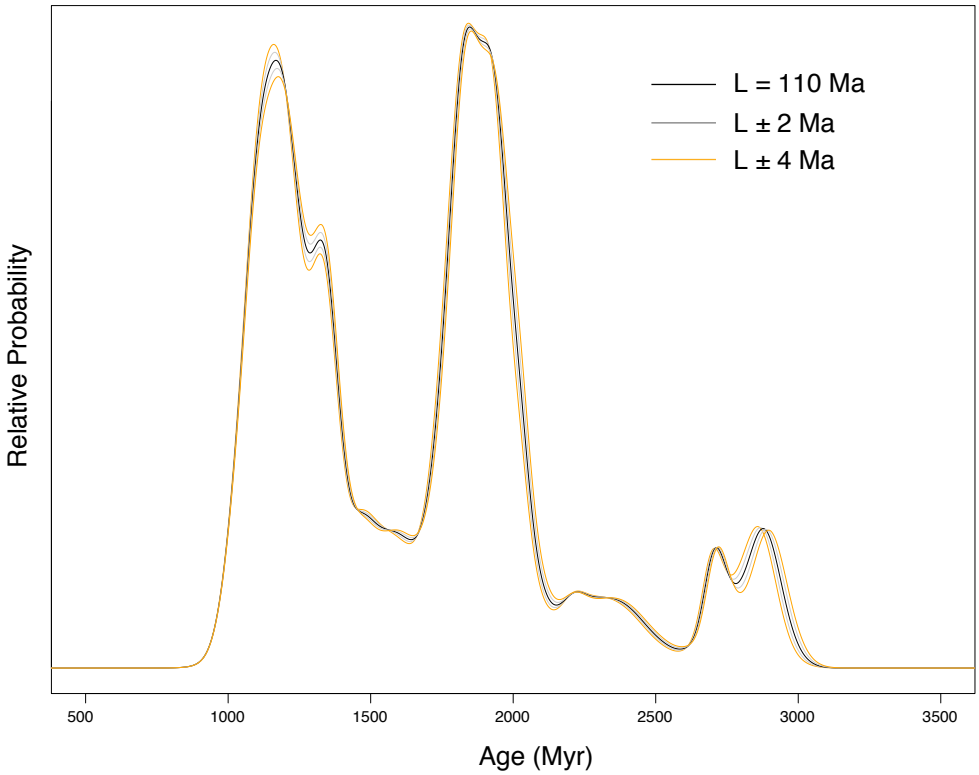

Figure A3: Age probability spectra for the zircons from the APS showing the affect of varying the lower intercept by 2 Myr and 4 Myr increments. Output from modeling procedure of Reimink et al. (2016).

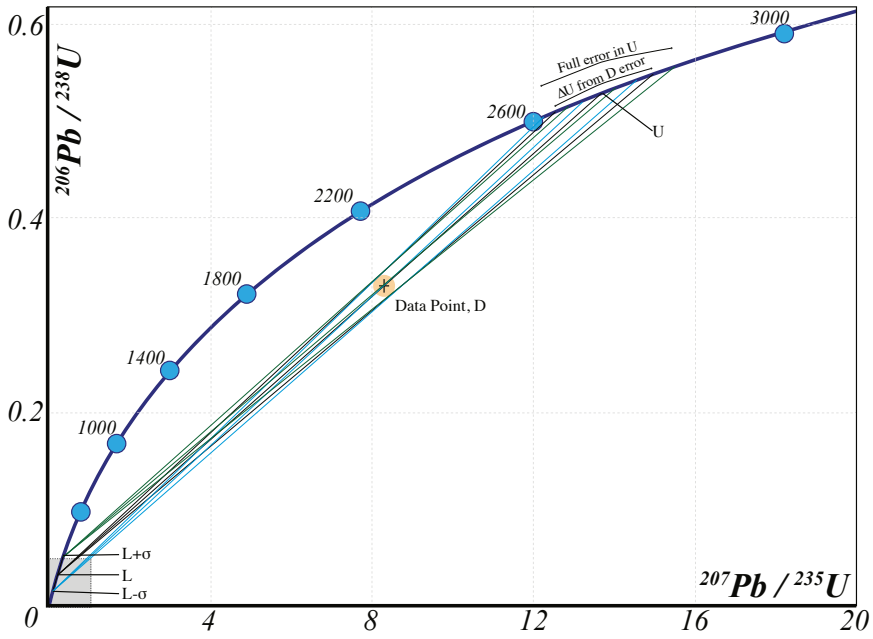

Figure A4: Schematic illustration of the errors in the upper intercept U derived from considering errors in both the data point (D, shown by the orange ellipse of 2 σ probability) and by varying the fixed lower intercept L±σ.

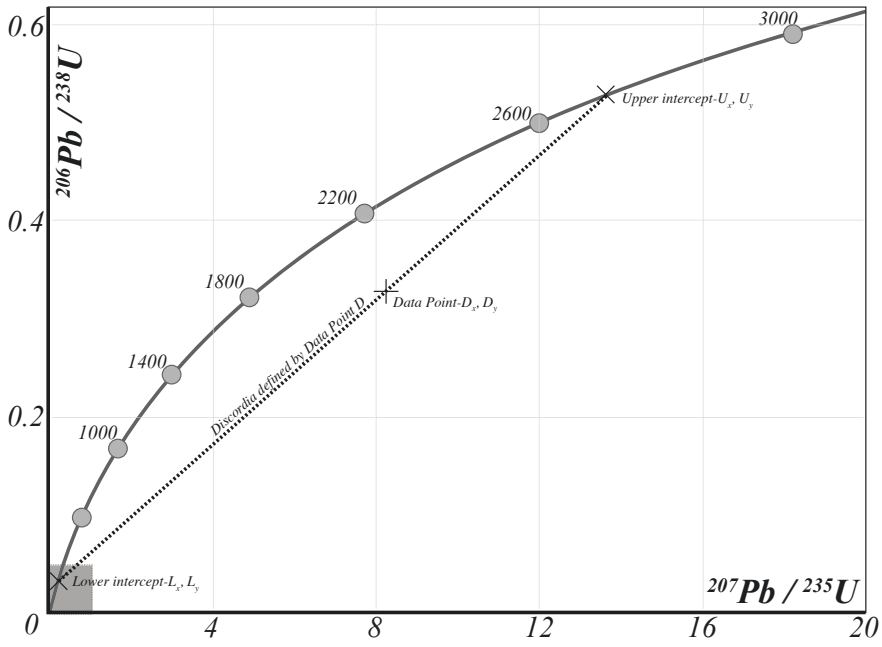

Figure A5: Schematic concordia and discordant zircon core analysis showing graphically the calculation that is performed to calculate the upper intercept by fixing the lower intercept.

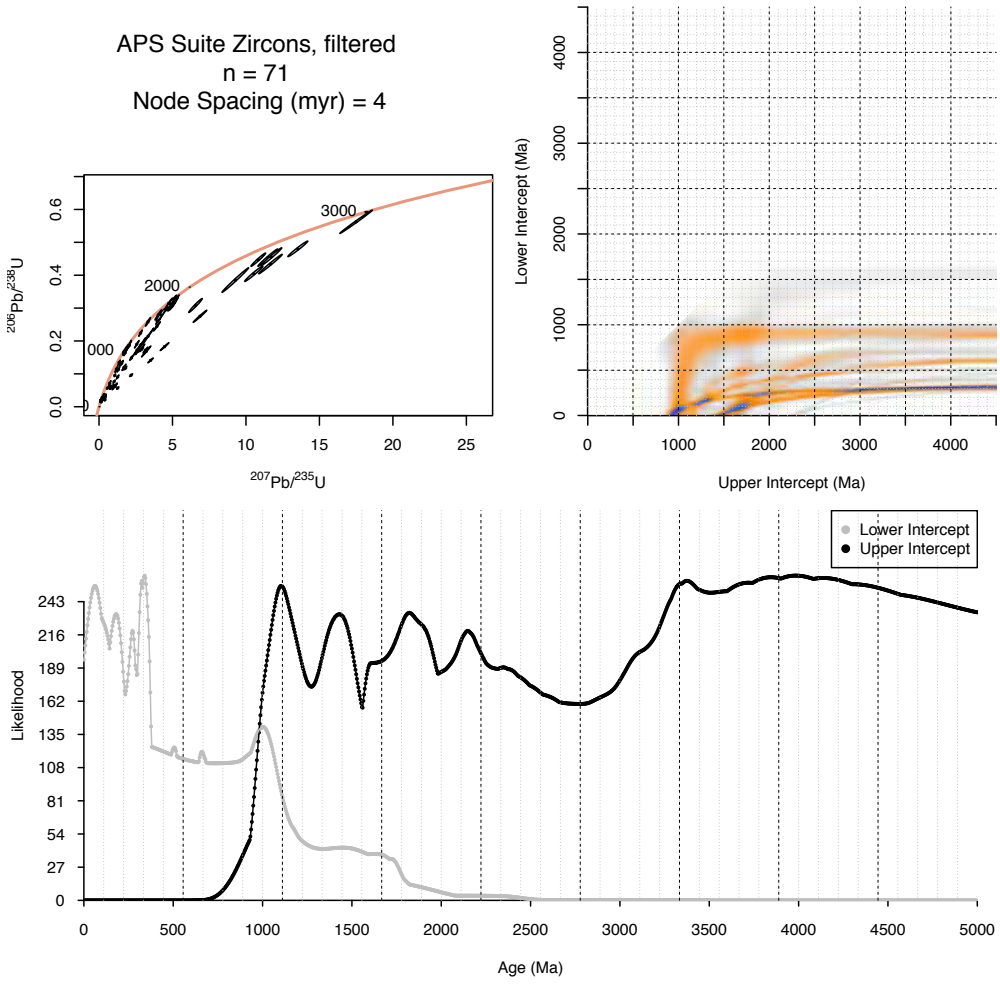

Figure A6: Output compilation figure from Reimink et al. (2016) showing the dataset from the 71 filtered analyses.

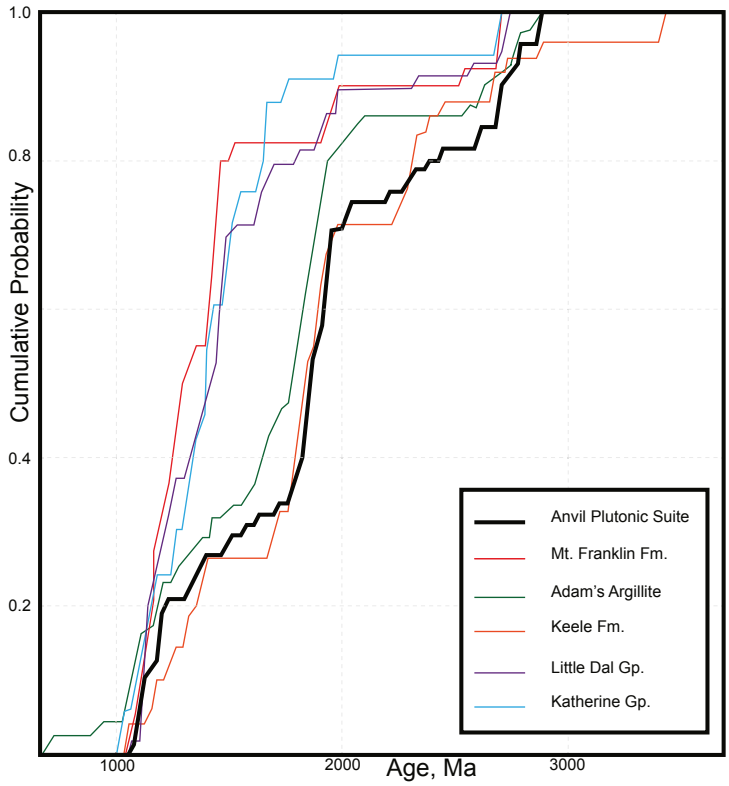

Figure A7: Cumulative Distribution Functions for the zircon ages of potential sedimentary melt sources of the APS and the corrected zircon ages from the APS.

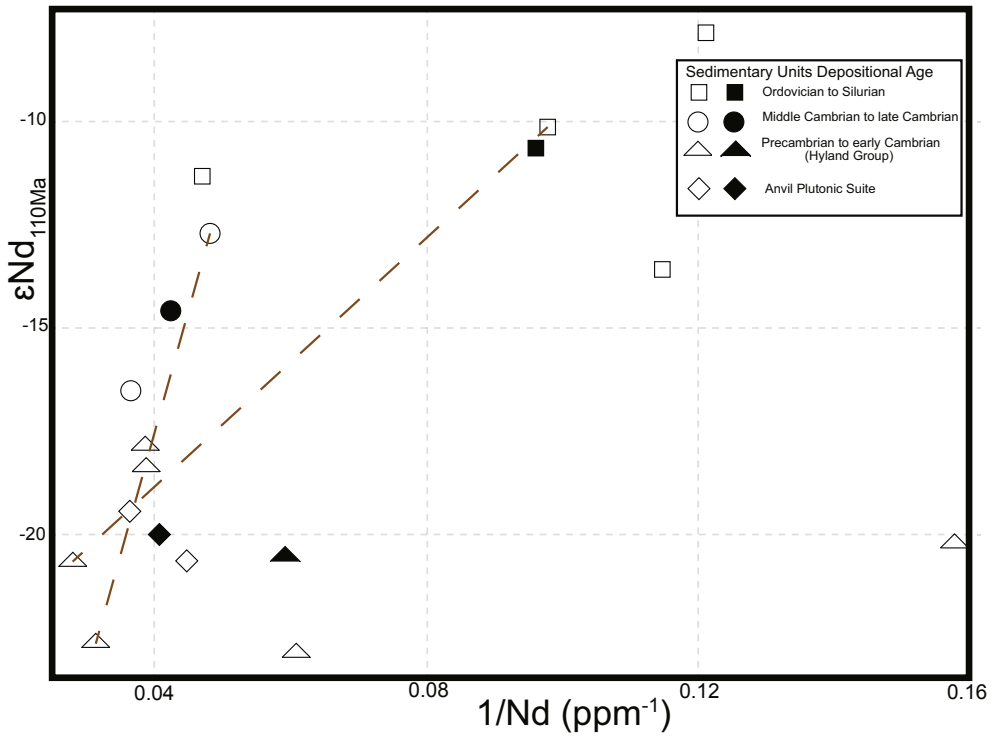

Figure A8: Isotopic ratios of Nd at 110 Ma versus 1/Nd ppm for Precambrian to Silurian sedimentary units in Yukon (Garzione et al., 1997) and the APS. Shaded shapes show average values for each unit. Brown lines represent possible mixing paths behind Hyland Group and younger samples that could explain the isotopic signature measured in the APS.

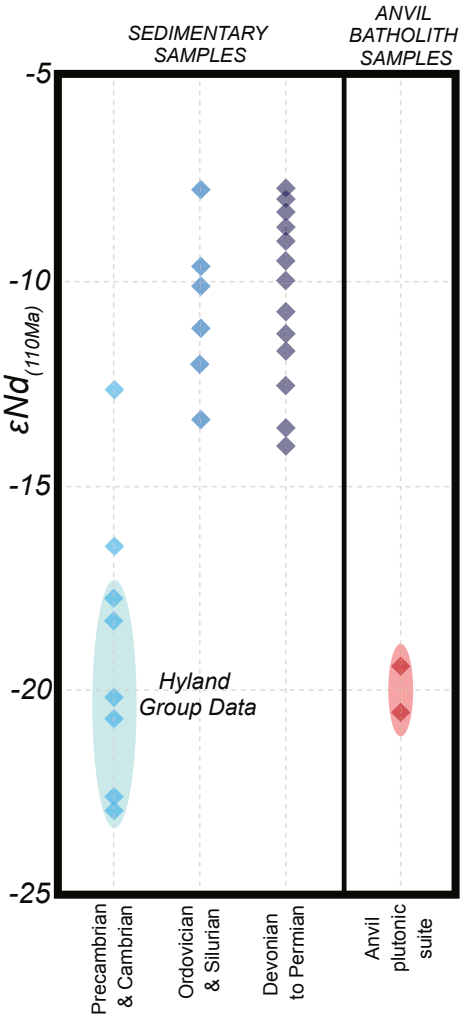

Figure A9: Comparison of Anvil plutonic suite εNdT at the time of crystallization (110Ma) with sedimentary sample values corrected to 110 Ma. Sedimentary sample values taken from Garzione et al. (1997).

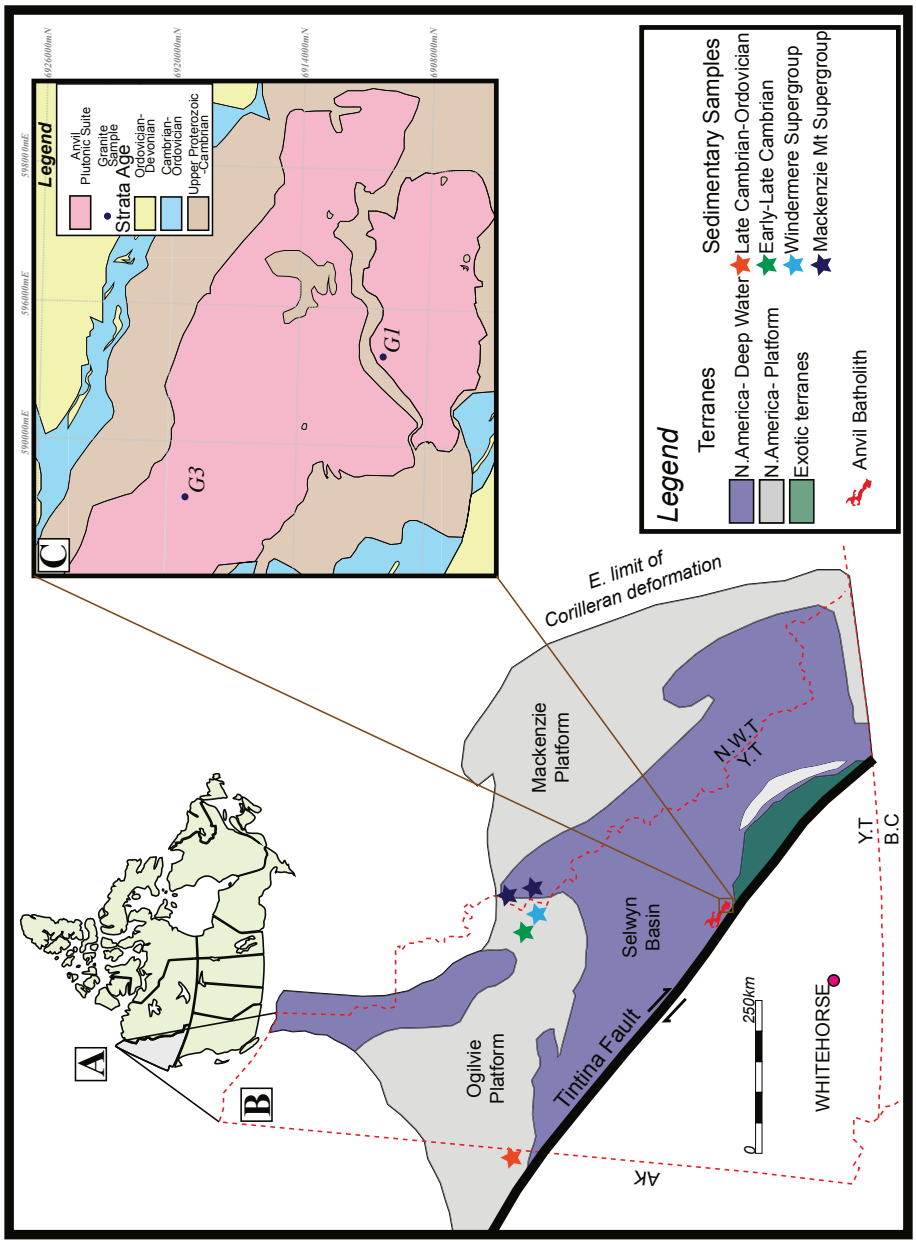

Figure A10: A) Map of Canada showing the location of the Yukon Territory in grey. **B)** Map of Yukon showing geological terranes to the northeast of the Tintina Fault including location of the Anvil batholith and sedimentary rock samples cited in this study. Adapted from Nelson et al. (2013). **C)** Detailed geological map of the Anvil plutonic suite with sample locations. Adapted from Pigage (2004).

Table A7. Raw U-Pb Data

Grain #	^{206}Pb (cps)	^{204}Pb (cps)	Isotopic Ratios						Apparent ages (Ma)						Disc (%)
			$^{207}Pb/^{206}Pb$	± (2σ)	$^{207}Pb/^{235}U$	± (2σ)	$^{206}Pb/^{238}U$	± (2σ)	$^{207}Pb^*/^{206}Pb^*$	± (2σ)	$^{207}Pb^*/^{235}U$	± (2σ)	$^{206}Pb^*/^{238}U$	± (2σ)	
Sample G1 (UTM Zone 8N, N6909787, E593582)															
1	114542	214	0.1116	0.0009	4.5245	0.2066	0.2942	0.0132	1825	15	1735	37	1662	65	10
2	248881	465	0.1950	0.0015	11.6678	0.6556	0.4340	0.0242	2785	12	2578	51	2324	108	20
3	116913	297	0.1387	0.0013	3.2131	0.2617	0.1681	0.0136	2211	16	1460	61	1001	75	121
4	118232	331	0.0827	0.0008	1.4932	0.0722	0.1309	0.0062	1263	19	928	29	793	35	59
5	105077	191	0.1049	0.0010	4.0381	0.1880	0.2792	0.0127	1713	18	1642	37	1587	64	8
6	111911	133	0.0668	0.0010	0.2553	0.0112	0.0277	0.0011	832	31	231	9	176	7	372
7	263339	109	0.2044	0.0015	13.5307	0.5577	0.4802	0.0195	2861	12	2717	38	2528	84	13
8	141209	105	0.1097	0.0009	4.7484	0.2105	0.3138	0.0137	1795	14	1776	37	1760	67	2
9	248009	95	0.1118	0.0009	4.1189	0.2112	0.2672	0.0135	1829	14	1658	41	1527	69	20
10	71517	128	0.0502	0.0011	0.1258	0.0065	0.0182	0.0008	205	52	120	6	116	5	77
11	164325	279	0.1806	0.0014	3.5089	0.1528	0.1409	0.0060	2658	13	1529	34	850	34	213
12	320820	472	0.0879	0.0034	0.4302	0.0357	0.0355	0.0026	1380	73	363	25	225	16	513
13	56599	129	0.1889	0.0018	10.5345	0.5089	0.4045	0.0192	2732	15	2483	44	2190	87	25
14	43988	180	0.0618	0.0015	0.2286	0.0100	0.0268	0.0010	669	52	209	8	171	6	292
15	128360	107	0.0740	0.0006	1.3703	0.0649	0.1344	0.0063	1041	18	876	27	813	35	28
16	89446	98	0.1135	0.0010	2.6293	0.1225	0.1680	0.0077	1856	17	1309	34	1001	42	85
17	72383	86	0.0540	0.0007	0.1390	0.0077	0.0187	0.0010	373	29	132	7	119	6	213
18	190151	79	0.0974	0.0014	1.0254	0.0593	0.0763	0.0043	1576	27	717	29	474	26	232
19	14937	21	0.0487	0.0010	0.1072	0.0063	0.0160	0.0009	134	50	103	6	102	6	31
20	23516	27	0.0564	0.0010	0.2131	0.0085	0.0274	0.0010	469	40	196	7	174	6	169
21	152000	259	0.1623	0.0016	1.2734	0.0656	0.0569	0.0029	2480	16	834	29	357	18	595
22	126238	91	0.0756	0.0006	1.7157	0.0732	0.1647	0.0069	1084	17	1014	27	983	38	10
23	340174	284	0.1401	0.0017	0.4030	0.0451	0.0209	0.0023	2229	20	344	32	133	15	1575
24	165368	85	0.1770	0.0014	4.4623	0.2447	0.1829	0.0099	2625	13	1724	44	1083	54	142
25	140531	148	0.0720	0.0025	0.2219	0.0103	0.0223	0.0007	986	69	203	9	142	4	592
26	25002	104	0.0710	0.0021	0.1439	0.0066	0.0147	0.0005	958	60	137	6	94	3	919
27	149948	151	0.0818	0.0011	1.0775	0.0412	0.0955	0.0034	1241	25	742	20	588	20	111
28	178609	122	0.1000	0.0011	0.7724	0.0363	0.0560	0.0026	1624	20	581	21	351	16	362
29	299734	172	0.1063	0.0015	0.9117	0.0669	0.0622	0.0045	1737	25	658	35	389	27	346
30	270061	86	0.1063	0.0011	1.7199	0.0735	0.1174	0.0049	1736	20	1016	27	715	28	143
31	311428	147	0.1127	0.0012	4.9564	0.2625	0.3190	0.0166	1843	19	1812	44	1785	80	4
32	108264	98	0.1263	0.0020	1.0678	0.1410	0.0613	0.0080	2047	28	738	67	384	49	84
33	82980	83	0.1033	0.0018	0.4266	0.0260	0.0300	0.0017	1684	33	361	18	190	11	90
34	38356	22	0.0518	0.0009	0.1307	0.0085	0.0183	0.0011	276	38	125	8	117	7	58
35	152669	48	0.1547	0.0018	6.5670	0.3767	0.3080	0.0173	2398	20	2055	49	1731	85	32
36	50874	150	0.0658	0.0014	0.1856	0.0107	0.0205	0.0011	799	44	173	9	131	7	84
37	83567	25	0.0487	0.0006	0.1137	0.0058	0.0169	0.0008	133	29	109	5	108	5	19
38	198438	34	0.0506	0.0007	0.1174	0.0064	0.0168	0.0009	222	30	113	6	108	6	52

Table A7 Cont. Raw U-Pb Data

Grain #	^{206}Pb (cps)	^{204}Pb (cps)	Isotopic Ratios						Apparent ages (Ma)						Disc (%)
			$^{207}Pb/^{206}Pb$	± (2σ)	$^{207}Pb/^{235}U$	± (2σ)	$^{206}Pb/^{238}U$	± (2σ)	$^{207}Pb^*/^{206}Pb^*$	± (2σ)	$^{207}Pb^*/^{235}U$	± (2σ)	$^{206}Pb^*/^{238}U$	± (2σ)	
Sample G3 (UTM Zone 8N, N6918824, E587557)															
1	88070	164	0.0762	0.0009	1.8818	0.0691	0.1791	0.0062	1101	23	1075	24	1062	34	4
2	260595	219	0.1652	0.0018	2.1851	0.0836	0.0959	0.0035	2510	18	1176	26	590	21	325
3	62133	156	0.0744	0.0013	0.2407	0.0140	0.0235	0.0013	1051	35	219	11	150	8	603
4	85166	143	0.0766	0.0011	1.8678	0.0759	0.1769	0.0067	1111	29	1070	27	1050	36	6
5	50110	124	0.1076	0.0014	2.2051	0.0949	0.1486	0.0061	1760	24	1183	30	893	34	97
6	232462	127	0.1207	0.0010	2.9123	0.0976	0.1750	0.0057	1967	15	1385	25	1039	31	89
7	201428	186	0.1332	0.0013	3.1653	0.1403	0.1723	0.0075	2141	16	1449	34	1025	41	109
8	196422	156	0.1251	0.0030	1.1133	0.1055	0.0646	0.0059	2030	42	760	49	403	36	403
9	86011	60	0.1028	0.0012	1.6987	0.1139	0.1199	0.0079	1675	22	1008	42	730	45	130
10	245138	41	0.1169	0.0009	3.9377	0.1891	0.2444	0.0116	1909	15	1621	38	1409	60	35
11	355868	111	0.1113	0.0010	1.8093	0.0698	0.1179	0.0044	1821	16	1049	25	718	25	154
12	262407	58	0.1129	0.0009	3.3368	0.3235	0.2143	0.0207	1847	15	1490	73	1252	109	48
13	47193	47	0.0734	0.0009	1.6905	0.0765	0.1671	0.0073	1025	25	1005	28	996	40	3
14	70590	23	0.0751	0.0009	1.1900	0.0852	0.1150	0.0081	1070	23	796	39	702	47	52
15	73317	33	0.0789	0.0008	1.7795	0.0761	0.1637	0.0068	1168	21	1038	27	977	37	20
16	246421	51	0.0742	0.0007	0.7339	0.0665	0.0717	0.0065	1047	19	559	38	447	39	135
17	281717	45	0.1758	0.0013	10.8387	0.4112	0.4472	0.0166	2613	12	2509	35	2383	74	10
18	202322	34	0.1837	0.0014	11.4865	0.5540	0.4535	0.0216	2687	12	2563	44	2411	95	11
19	379259	41	0.0794	0.0006	2.0179	0.1036	0.1844	0.0093	1181	16	1122	34	1091	51	8
20	267115	34	0.0794	0.0006	2.0440	0.0938	0.1868	0.0084	1181	16	1130	31	1104	46	7
21	286595	44	0.1098	0.0009	2.8614	0.2671	0.1891	0.0176	1795	14	1372	68	1116	95	61
22	248982	343	0.1865	0.0014	11.7252	0.5830	0.4560	0.0224	2711	13	2583	45	2422	98	12
23	117171	183	0.0848	0.0011	1.5544	0.0793	0.1329	0.0066	1312	25	952	31	804	37	63
24	382983	66	0.1812	0.0014	6.8729	0.3816	0.2751	0.0151	2664	13	2095	48	1567	76	70
25	277584	195	0.1746	0.0016	9.2770	0.7413	0.3853	0.0306	2603	15	2366	71	2101	141	24
26	212474	56	0.0855	0.0008	0.7186	0.0511	0.0610	0.0043	1326	19	550	30	382	26	248
27	153223	66	0.0915	0.0008	2.8234	0.1031	0.2237	0.0079	1457	17	1362	27	1302	42	12
28	170789	47	0.1182	0.0010	5.0039	0.1859	0.3071	0.0111	1929	15	1820	31	1726	54	12
29	56401	189	0.1149	0.0015	4.8910	0.1608	0.3088	0.0094	1878	23	1801	27	1735	46	8
30	201761	113	0.1173	0.0010	5.1289	0.2155	0.3171	0.0130	1916	16	1841	35	1775	63	8
31	210246	67	0.1087	0.0009	2.5892	0.2236	0.1728	0.0149	1778	14	1298	61	1027	81	73
32	171293	110	0.1169	0.0009	4.9168	0.1852	0.3051	0.0112	1909	14	1805	31	1717	55	11
33	197605	225	0.1164	0.0014	5.0238	0.2822	0.3131	0.0172	1901	21	1823	46	1756	84	8
34	165815	140	0.1119	0.0011	4.7515	0.1669	0.3080	0.0104	1830	17	1776	29	1731	51	6
35	131669	184	0.0937	0.0009	3.3335	0.1418	0.2581	0.0107	1502	18	1489	33	1480	55	1
36	44561	101	0.0727	0.0011	0.5684	0.0304	0.0567	0.0029	1006	30	457	19	355	18	183
37	45958	121	0.0585	0.0033	0.1662	0.0194	0.0206	0.0021	550	118	156	17	131	13	319
38	32709	146	0.0514	0.0013	0.1199	0.0048	0.0169	0.0005	261	58	115	4	108	3	141

Table A7 Cont. Raw U-Pb Data

Grain #	^{206}Pb (cps)	^{204}Pb (cps)	Isotopic Ratios						Apparent ages (Ma)						Disc (%)
			^{207}Pb/^{206}Pb	± (2σ)	^{207}Pb/^{235}U	± (2σ)	^{206}Pb/^{238}U	± (2σ)	^{207}Pb*/^{206}Pb*	± (2σ)	^{207}Pb*/^{235}U	± (2σ)	^{206}Pb*/^{238}U	± (2σ)	
39	107622	124	0.0981	0.0008	2.5719	0.1307	0.1900	0.0095	1589	16	1293	36	1122	51	42
40	12940	178	0.1118	0.0018	4.8318	0.1981	0.3135	0.0118	1828	29	1790	34	1758	58	4
41	94437	74	0.0762	0.0006	1.7968	0.1096	0.1710	0.0104	1100	15	1044	39	1018	57	8
42	289935	118	0.0792	0.0004	2.0314	0.1447	0.1861	0.0132	1177	10	1126	47	1100	71	7
43	247829	110	0.0749	0.0005	1.7402	0.0868	0.1686	0.0083	1064	14	1024	32	1005	46	6
44	120709	118	0.0965	0.0013	0.8150	0.0399	0.0612	0.0029	1558	25	605	22	383	17	306
45	163547	119	0.0848	0.0007	1.3222	0.0756	0.1131	0.0064	1310	15	855	33	691	37	90
46	73442	131	0.1163	0.0009	5.1582	0.2428	0.3218	0.0150	1899	14	1846	39	1799	73	6
47	31113	132	0.1092	0.0022	4.2087	0.2616	0.2795	0.0164	1786	37	1676	50	1589	82	12
48	41926	90	0.0525	0.0008	0.1310	0.0063	0.0181	0.0008	307	36	125	6	116	5	166
49	328474	97	0.1184	0.0007	2.9259	0.1559	0.1792	0.0095	1932	10	1389	40	1063	52	82
50	125251	64	0.0488	0.0003	0.1180	0.0059	0.0175	0.0009	138	16	113	5	112	6	23
51	234732	100	0.2256	0.0010	17.4976	0.9094	0.5626	0.0291	3021	7	2963	49	2877	119	5
52	114649	50	0.0726	0.0027	0.2571	0.0248	0.0257	0.0023	1003	74	232	20	164	14	513
53	301911	102	0.0768	0.0004	1.1830	0.0657	0.1118	0.0062	1115	9	793	30	683	36	63
54	143176	43	0.0645	0.0007	0.2653	0.0150	0.0298	0.0017	757	22	239	12	190	10	300
55	76675	85	0.1032	0.0025	0.3778	0.0245	0.0266	0.0016	1682	44	325	18	169	10	896
56	311431	38	0.0672	0.0007	0.3386	0.0228	0.0365	0.0024	845	21	296	17	231	15	265
57	415309	47	0.0963	0.0029	0.3435	0.0264	0.0259	0.0018	1554	56	300	20	165	11	844
58	594569	302	0.0564	0.0013	0.1273	0.0076	0.0164	0.0009	469	48	122	7	105	6	348
59	380876	66	0.0510	0.0005	0.1299	0.0063	0.0185	0.0009	241	22	124	6	118	6	105
60	372489	71	0.0734	0.0024	0.2579	0.0227	0.0255	0.0021	1025	65	233	18	162	13	532
61	322279	203	0.0749	0.0032	0.2521	0.0254	0.0244	0.0022	1066	83	228	20	155	14	586
62	474637	145	0.0496	0.0006	0.1130	0.0061	0.0165	0.0009	177	29	109	6	106	6	67
63	313323	59	0.0587	0.0023	0.1614	0.0145	0.0200	0.0016	555	85	152	13	127	10	336
64	274997	47	0.0644	0.0013	0.2126	0.0129	0.0239	0.0014	756	42	196	11	152	9	396
65	189723	72	0.0517	0.0003	0.1467	0.0082	0.0206	0.0011	272	15	139	7	131	7	107
66	294094	43	0.0503	0.0004	0.1184	0.0057	0.0171	0.0008	207	18	114	5	109	5	89
67	374135	265	0.0575	0.0015	0.1278	0.0079	0.0161	0.0009	510	56	122	7	103	6	395
68	247633	36	0.0494	0.0003	0.1185	0.0061	0.0174	0.0009	169	15	114	6	111	6	52
69	136202	111	0.0631	0.0008	0.1999	0.0135	0.0230	0.0015	711	27	185	11	146	10	386
70	88172	55	0.1018	0.0008	1.2708	0.0729	0.0905	0.0052	1657	14	833	32	559	30	197

Table A8. Whole Rock Nd Data

Sample #	Age (Ma)	Sm (ppm)	Nd (ppm)	$^{147}Sm/^{144}Nd$	$^{143}Nd/^{144}Nd_{0}$	± (2σ)	εNd_{0}	$^{143}Nd/^{144}Nd_{(100Ma)}$	$\varepsilon Nd_{(100Ma)}$	T_{DM} (Ga)
G1	110	4.74	28.14	0.1018	0.511574	0.000008	-20.8	0.511501	-19.4	2.16
G3	110	3.85	22.77	0.1023	0.511517	0.000015	-21.9	0.511443	-20.6	2.24

Table A9. Error Correction for discrete data set

Grain #	Δx (Dx-Lx)	Δy (Dy-Ly)	(Δy) ±σ	m= Δy/Δx	(m) ±σ	c	(c) ±σ	Ux	(Ux) ±σ	Uy	(Uy) ±σ	Concordant age (Ma)	Error in age (Ma)
Sample G1 (UTM Zone 8N, N6909787, E593582)													
1	4.41	0.277	0.007	0.063	0.001	0.010	0.0002	5.1	0.3	0.33	0.32	1835	47
2	11.56	0.417	0.012	0.036	0.001	0.013	0.0001	14.7	0.7	0.54	0.53	2794	47
3	3.10	0.151	0.007	0.049	0.002	0.011	0.0002	8.5	0.7	0.42	0.41	2284	75
4	1.38	0.114	0.003	0.083	0.002	0.008	0.0003	2.7	0.2	0.23	0.22	1316	56
5	3.93	0.262	0.006	0.067	0.002	0.009	0.0002	4.4	0.2	0.30	0.30	1717	44
6	0.14	0.011	0.001	0.076	0.004	0.008	0.0004	3.3	0.4	0.26	0.24	1483	101
7	13.42	0.463	0.010	0.035	0.001	0.013	0.0001	15.8	0.6	0.56	0.55	2867	34
8	4.64	0.297	0.007	0.064	0.001	0.010	0.0002	4.9	0.2	0.32	0.31	1795	42
9	4.01	0.250	0.007	0.062	0.002	0.010	0.0002	5.1	0.3	0.33	0.32	1841	48
10	0.01	0.001	0.000	0.095	0.031	0.006	0.0035	1.8	1.2	0.17	0.07	1035	591
11	3.40	0.124	0.003	0.037	0.001	0.013	0.0001	14.4	0.6	0.54	0.53	2775	41
12	0.32	0.019	0.001	0.059	0.004	0.010	0.0005	5.9	0.8	0.35	0.33	1958	122
13	10.42	0.388	0.010	0.037	0.001	0.013	0.0001	13.9	0.6	0.53	0.52	2745	42
14	0.12	0.010	0.000	0.085	0.004	0.007	0.0005	2.4	0.3	0.21	0.20	1256	104
15	1.26	0.117	0.003	0.093	0.002	0.006	0.0003	1.9	0.1	0.18	0.17	1066	53
16	2.52	0.151	0.004	0.060	0.002	0.010	0.0002	5.6	0.3	0.35	0.34	1913	45
17	0.03	0.002	0.001	0.066	0.019	0.009	0.0021	4.5	2.1	0.31	0.22	1735	477
18	0.91	0.059	0.002	0.065	0.002	0.010	0.0003	4.7	0.4	0.31	0.30	1766	65
19	-0.01	-0.001	0.000	0.183	-0.087	-0.004	-0.0097	0.1	0.0	0.02	0.02	123	0
20	0.10	0.011	0.000	0.104	0.005	0.005	0.0005	1.3	0.2	0.14	0.12	844	100
21	1.16	0.040	0.001	0.034	0.001	0.013	0.0001	15.9	1.0	0.56	0.55	2871	59
22	1.60	0.148	0.003	0.092	0.002	0.007	0.0002	1.9	0.1	0.18	0.18	1093	47
23	0.29	0.004	0.001	0.014	0.004	0.015	0.0004	68.2	21.7	0.95	0.84	4302	382
24	4.35	0.166	0.005	0.038	0.001	0.013	0.0001	13.3	0.7	0.52	0.51	2701	49
25	0.11	0.005	0.000	0.050	0.003	0.011	0.0004	8.2	1.0	0.42	0.39	2248	111
26	0.03	-0.002	0.000	-0.069	0.008	0.025	0.0009	0.1	0.0	0.02	0.02	108	0
27	0.97	0.079	0.002	0.081	0.002	0.008	0.0002	2.7	0.2	0.23	0.22	1338	42
28	0.66	0.039	0.001	0.059	0.002	0.010	0.0002	5.7	0.4	0.35	0.34	1937	58
29	0.80	0.045	0.002	0.057	0.003	0.011	0.0003	6.3	0.6	0.37	0.35	2017	84
30	1.61	0.101	0.002	0.063	0.002	0.010	0.0002	5.1	0.3	0.33	0.32	1841	44
31	4.84	0.302	0.008	0.062	0.002	0.010	0.0002	5.2	0.3	0.33	0.32	1845	50
32	0.96	0.044	0.004	0.046	0.004	0.012	0.0005	9.3	1.4	0.44	0.41	2368	151
33	0.31	0.013	0.001	0.042	0.003	0.012	0.0003	11.4	1.2	0.49	0.46	2557	107
34	0.02	0.001	0.001	0.077	0.031	0.008	0.0035	3.2	2.1	0.25	0.13	1459	689
35	6.45	0.291	0.009	0.045	0.001	0.012	0.0002	9.8	0.5	0.46	0.44	2421	52
36	0.07	0.004	0.001	0.049	0.007	0.011	0.0008	8.4	2.1	0.42	0.37	2278	251
37	0.00	0.000	0.000	0.041	0.276	0.012	0.0309	11.6	11.5	0.49	0.02	2575	2467
38	0.01	0.000	0.000	-0.011	0.086	0.018	0.0097	0.1	0.0	0.02	0.02	109	0

Table A9 Cont. Error Correction for discrete data set

Grain #	Δx (Dx-Lx)	Δy (Dy-Ly)	(Δy) ±σ	m= Δy/Δx	(m) ±σ	c	(c) ±σ	Ux	(Ux) ±σ	Uy	(Uy) ±σ	Concordant age (Ma)	Error in age (Ma)
Sample G3 (UTM Zone 8N, N6918824, E587557)													
1	1.77	0.162	0.003	0.092	0.002	0.007	0.0002	2.0	0.1	0.19	0.18	1102	38
2	2.07	0.079	0.002	0.038	0.001	0.013	0.0001	13.3	0.5	0.52	0.51	2703	37
3	0.13	0.007	0.001	0.051	0.005	0.011	0.0006	7.7	1.3	0.41	0.37	2196	165
4	1.76	0.160	0.003	0.091	0.002	0.007	0.0002	2.0	0.1	0.19	0.18	1115	42
5	2.09	0.132	0.003	0.063	0.001	0.010	0.0002	5.0	0.2	0.33	0.32	1824	38
6	2.80	0.158	0.003	0.056	0.001	0.011	0.0001	6.3	0.2	0.37	0.36	2023	30
7	3.05	0.155	0.004	0.051	0.001	0.011	0.0001	7.8	0.3	0.41	0.40	2207	40
8	1.00	0.048	0.003	0.048	0.003	0.012	0.0003	8.9	0.9	0.43	0.41	2323	101
9	1.59	0.103	0.004	0.065	0.002	0.010	0.0003	4.7	0.4	0.32	0.30	1774	71
10	3.83	0.227	0.006	0.059	0.002	0.010	0.0002	5.7	0.3	0.35	0.34	1933	47
11	1.70	0.101	0.002	0.060	0.001	0.010	0.0001	5.7	0.3	0.35	0.34	1930	39
12	3.22	0.197	0.010	0.061	0.003	0.010	0.0004	5.4	0.6	0.34	0.32	1881	93
13	1.58	0.150	0.004	0.095	0.002	0.006	0.0003	1.8	0.1	0.17	0.16	1032	53
14	1.08	0.098	0.004	0.091	0.004	0.007	0.0004	2.0	0.2	0.19	0.18	1121	78
15	1.67	0.147	0.003	0.088	0.002	0.007	0.0002	2.2	0.1	0.20	0.19	1187	48
16	0.62	0.055	0.003	0.088	0.005	0.007	0.0006	2.2	0.4	0.20	0.18	1185	118
17	10.73	0.430	0.008	0.040	0.001	0.012	0.0001	12.2	0.4	0.50	0.49	2617	32
18	11.37	0.437	0.011	0.038	0.001	0.013	0.0001	13.2	0.6	0.52	0.51	2691	41
19	1.91	0.168	0.005	0.088	0.002	0.007	0.0003	2.2	0.2	0.20	0.19	1187	54
20	1.93	0.170	0.004	0.088	0.002	0.007	0.0002	2.2	0.1	0.20	0.19	1186	48
21	2.75	0.172	0.009	0.063	0.003	0.010	0.0004	5.1	0.5	0.33	0.31	1841	93
22	11.61	0.439	0.011	0.038	0.001	0.013	0.0001	13.5	0.6	0.52	0.51	2718	44
23	1.44	0.116	0.003	0.080	0.002	0.008	0.0003	2.9	0.2	0.24	0.23	1370	60
24	6.76	0.258	0.008	0.038	0.001	0.013	0.0001	13.3	0.7	0.52	0.51	2700	48
25	9.16	0.368	0.015	0.040	0.002	0.012	0.0002	12.2	0.9	0.50	0.48	2616	70
26	0.61	0.044	0.002	0.073	0.004	0.009	0.0004	3.7	0.4	0.27	0.26	1561	90
27	2.71	0.207	0.004	0.076	0.001	0.008	0.0002	3.3	0.2	0.26	0.25	1473	43
28	4.89	0.290	0.006	0.059	0.001	0.010	0.0001	5.7	0.2	0.35	0.34	1935	34
29	4.78	0.292	0.005	0.061	0.001	0.010	0.0001	5.4	0.2	0.34	0.33	1882	29
30	5.02	0.300	0.007	0.060	0.001	0.010	0.0001	5.6	0.2	0.35	0.34	1920	39
31	2.48	0.156	0.007	0.063	0.003	0.010	0.0003	5.1	0.5	0.33	0.31	1829	84
32	4.80	0.288	0.006	0.060	0.001	0.010	0.0001	5.6	0.2	0.35	0.34	1915	36
33	4.91	0.296	0.009	0.060	0.002	0.010	0.0002	5.5	0.3	0.34	0.33	1906	52
34	4.64	0.291	0.005	0.063	0.001	0.010	0.0001	5.1	0.2	0.33	0.32	1835	34
35	3.22	0.241	0.005	0.075	0.002	0.008	0.0002	3.4	0.2	0.26	0.25	1502	42
36	0.46	0.040	0.001	0.087	0.003	0.007	0.0004	2.3	0.2	0.21	0.19	1206	73
37	0.05	0.004	0.001	0.069	0.020	0.009	0.0022	4.2	1.9	0.29	0.20	1666	480
38	0.01	0.000	0.000	0.003	0.034	0.017	0.0038	550.1	536.0	1.70	0.53	6409	3658

Table A9 Cont. Error Correction for discrete data set

Grain #	Δx (Dx-Lx)	Δy (Dy-Ly)	(Δy) ±σ	m= Δy/Δx	(m) ±σ	c	(c) ±σ	Ux	(Ux) ±σ	Uy	(Uy) ±σ	Concordant age (Ma)	Error in age (Ma)
Sample G3 Cont. (UTM Zone 8N, N6918824, E587557)													
39	2.46	0.173	0.005	0.070	0.002	0.009	0.0002	3.9	0.2	0.29	0.28	1619	51
40	4.72	0.297	0.006	0.063	0.001	0.010	0.0001	5.1	0.2	0.33	0.32	1834	40
41	1.68	0.154	0.005	0.091	0.003	0.007	0.0003	2.0	0.2	0.19	0.18	1108	66
42	1.92	0.169	0.007	0.088	0.003	0.007	0.0004	2.2	0.2	0.20	0.19	1182	75
43	1.63	0.152	0.004	0.093	0.003	0.006	0.0003	1.9	0.2	0.18	0.17	1071	56
44	0.70	0.044	0.001	0.063	0.002	0.010	0.0002	5.0	0.3	0.33	0.31	1823	59
45	1.21	0.096	0.003	0.080	0.003	0.008	0.0003	2.9	0.2	0.24	0.23	1385	62
46	5.05	0.305	0.007	0.060	0.001	0.010	0.0002	5.5	0.3	0.34	0.33	1903	45
47	4.10	0.263	0.008	0.064	0.002	0.010	0.0002	4.9	0.3	0.32	0.31	1795	58
48	0.02	0.001	0.000	0.065	0.022	0.010	0.0025	4.8	2.4	0.32	0.21	1778	551
49	2.81	0.162	0.005	0.058	0.002	0.010	0.0002	6.1	0.4	0.36	0.35	1986	52
50	0.01	0.001	0.000	0.114	0.076	0.004	0.0085	0.9	0.8	0.10	0.02	643	531
51	17.39	0.546	0.015	0.031	0.001	0.013	0.0001	18.6	0.8	0.60	0.59	3022	42
52	0.14	0.009	0.001	0.061	0.008	0.010	0.0009	5.4	1.3	0.34	0.29	1892	225
53	1.07	0.095	0.003	0.089	0.003	0.007	0.0003	2.2	0.2	0.20	0.19	1172	64
54	0.15	0.013	0.001	0.085	0.005	0.007	0.0006	2.5	0.4	0.22	0.19	1263	122
55	0.27	0.010	0.001	0.036	0.003	0.013	0.0003	14.4	1.9	0.54	0.51	2779	132
56	0.23	0.020	0.001	0.087	0.005	0.007	0.0006	2.3	0.4	0.21	0.18	1214	119
57	0.23	0.009	0.001	0.039	0.004	0.013	0.0004	12.9	2.0	0.51	0.48	2672	162
58	0.02	-0.001	0.000	-0.034	0.030	0.021	0.0034	0.1	0.0	0.02	0.02	105	0
59	0.02	0.002	0.000	0.090	0.025	0.007	0.0028	2.1	1.2	0.19	0.10	1144	513
60	0.15	0.009	0.001	0.059	0.007	0.010	0.0008	5.8	1.3	0.35	0.31	1945	211
61	0.14	0.008	0.001	0.054	0.008	0.011	0.0009	7.0	1.7	0.39	0.33	2111	249
62	0.00	0.000	0.000	-0.430	0.528	0.065	0.0593	0.1	0.0	0.02	0.02	107	0
63	0.05	0.003	0.001	0.062	0.016	0.010	0.0018	5.2	2.2	0.33	0.24	1846	438
64	0.10	0.007	0.001	0.070	0.007	0.009	0.0008	4.0	0.8	0.29	0.25	1629	182
65	0.03	0.004	0.001	0.107	0.017	0.005	0.0019	1.2	0.6	0.13	0.08	793	321
66	0.01	0.000	0.000	0.033	0.066	0.013	0.0075	17.2	15.7	0.58	0.16	2946	2005
67	0.02	-0.001	0.000	-0.049	0.029	0.022	0.0033	0.1	0.0	0.02	0.02	109	0
68	0.01	0.000	0.000	0.080	0.071	0.008	0.0080	2.9	2.7	0.24	0.02	1375	1232
69	0.09	0.006	0.001	0.070	0.009	0.009	0.0010	4.1	1.0	0.29	0.25	1647	229
70	1.16	0.074	0.003	0.064	0.002	0.010	0.0002	5.0	0.4	0.32	0.31	1811	65

Grey cells represent filtered values ($^{206}Pb/^{238}U$ <0.05 and $^{207}Pb/^{235}U$ < 0.5)

Table A10. Corrected Ages From APS Inherited Zircon Cores

Grain #	Corrected Age (Ma)	Error in age (Ma)
Sample G1		
1	1835	47
2	2794	47
3	2284	75
4	1316	56
5	1717	44
7	2867	34
8	1795	42
9	1841	48
11	2775	41
13	2745	42
15	1066	53
16	1913	45
18	1766	65
21	2871	59
22	1093	47
24	2701	49
27	1338	42
28	1937	58
29	2017	84
30	1841	44
31	1845	50
32	2368	151
35	2421	52

Grain #	Corrected Age (Ma)	Error in age (Ma)
Sample G3		
1	1102	38
2	2703	37
4	1115	42
5	1824	38
6	2023	30
7	2207	40
8	2323	101
9	1774	71
10	1933	47
11	1930	39
12	1881	93
13	1032	53
14	1121	78
15	1187	48
16	1185	118
17	2617	32
18	2691	41
19	1187	54
20	1186	48
21	1841	93
22	2718	44
23	1370	60
24	2700	48
25	2616	70
26	1561	90
27	1473	43
28	1935	34
29	1882	29
30	1920	39
31	1829	84
32	1915	36
33	1906	52
34	1835	34
35	1502	42
36	1206	73
39	1619	51
40	1834	40
41	1108	66
42	1182	75
43	1071	56
44	1823	59
45	1385	62
46	1903	45
47	1795	58
49	1986	52
51	3022	42
53	1172	64
70	1811	65

Table A11. K-S test results

	Unit				
	Rabbitkettle Fm.	**Gull Lake Fm.**	**Windermere SGp**	**Little Dal Gp.**	**Katherine Gp.**
Anvil plutonic Suite	0.000	0.139	0.999	0.000	0.000

Green squares show P values >0.05

Table A12. Strat Correlation Table

Strata name in original source	Equivalent strata in the Anvil region	Number of analyses
Mt. Franklin Fm.	Rabbitkettle Fm.	40
Adam's Argillite	Gull Lake Fm.	116
Keele Fm.	Hyland Gp. (Windermere SGp)	49
Hyland Gp.	Hyland Gp. (Windermere SGp)	90
Little Dal Gp.	MMSG	59
Katherine Gp.	MMSG	33
Anvil plutonic suite	Anvil plutonic suite	71

Table A13. K-S test Results from Mixed Samples

	2 Unit Mixing				3 Unit Mixing			5 Unit
	Katherine Gp. & Little Dal Gp.	Little Dal Gp. & Windermere SGp.	Windermere SGp. & Gull Lake Fm.	Gull Lake Fm. & Rabbitkettle Fm.	Katherine Gp., Little Dal Gp. & Windermere SGp.	Little Dal Gp., Windermere SGp. & Gull Lake Fm.	Windermere SGp, Gull Lake Fm. & Rabbitkettle Fm.	All
Run 1	0.000	0.033	**0.563**	0.000	0.000	0.020	**0.060**	0.000
Run 2	0.000	0.044	**0.108**	0.000	0.003	**0.107**	0.001	0.000
Run 3	0.000	0.011	**0.751**	0.000	0.000	**0.074**	0.013	0.000
Run 4	0.000	0.009	**0.146**	0.000	0.000	0.040	0.018	0.001
Run 5	0.000	0.015	**0.119**	0.000	0.000	0.011	0.001	0.000
Average	**0.000**	**0.023**	**0.337**	**0.000**	**0.001**	**0.050**	**0.018**	**0.000**
±σ	**0.000**	**0.015**	**0.300**	**0.000**	**0.001**	**0.040**	**0.024**	**0.000**

Green squares show P values >0.05

Chapter 4 Supplemental Information

Supplemental Methods

Modeling the effect of exhumation on thermochronometer T_c and Z_c

The effective closure depth (Z_c)- the depth at which the effective closure temperature (T_c) occurs for each mineral system- can be modeled in an exhuming upper crust via a two step methods outlined in Reiners and Brandon (2006) and below.

The first step involves modeling the geothermal profile of eroding crust in the region based on a one dimensional thermal field of infinite thickness, L, with fixed, constant, temperatures at the surface and base, T_S and T_L respectively, and a uniform internal heat production H_T (Reiners and Brandon 2006). We assume that horizontal velocities do not significantly affect the model (Batt and Brandon 2002). Material moves through this one-dimensional layer at a constant speed, equal to the rate of exhumation, $\dot{\varepsilon}$. The layer remains at a constant thickness as erosion rate matches the exhumation rate.

In this model temperature can be calculated as a function of depth, T(z) within the one dimensional layer for two end member conditions:

1. When erosion approaches zero

$$T(z) = T_s + \frac{(T_L - T_S)z}{L} + \frac{H_T z(L - z)}{2\kappa} \qquad (1)$$

Where κ is the average thermal diffusivity of the layer

2.When erosion rates are high such that heat transport due to erosion is important

$$T(z) = T_S + \left(T_L - T_S + \frac{H_T L}{\dot{\varepsilon}}\right)\frac{1 - \exp\left(\frac{-\dot{\varepsilon}z}{\kappa}\right)}{1 - \exp\left(\frac{-\dot{\varepsilon}L}{\kappa}\right)} - \frac{H_T z}{\dot{\varepsilon}} \qquad (2)$$

Parameters for the model were based on typical convergent orogens, as reported by Reiners and Brandon (2006): $\kappa = 27.4$ km^2 Myr^{-1}, $H_T = 4.5^{\circ}$C Myr^{-1} and $T_S = 14^{\circ}$C. In areas without erosion, the surface thermal gradient is ~20°Ckm^{-1}. The thickness of the layer (L) was set to 40 km based on the current crustal thickness identified in the Lithoprobe SNORCLE Line 3 (Cook et al. 2004). Therefore T_L is ~800°C. Geotherms were calculated for constant exhumation rates of 0, 0.5, 1, 2, 3 and 10 kmMyr^{-1}.

The second step is to calculate the T_c and Z_c for each thermochronometer based on the modeled geotherms. T_c is a function of cooling rate (Figure 4.3), which can be evaluated for a mineral exhuming through the 1D model. Cooling rate is calculated by differentiation of equation 1 and 2 to find geothermal gradients within each system $\left(\frac{\partial T}{\partial z}\right)$, which can then be converted to a cooling rate, $\dot{T}(z)$ via equation 3:

$$\dot{T}(z) = \dot{\varepsilon}\frac{\delta T}{\delta z} \qquad (3)$$

The closure temperature is then extracted via an iterative solution of equation 3 and the Dobson equation (Dodson 1973) for which the effect of pressure is taken to be negligible (equation 4).

$$\dot{T} = \frac{\Omega R T_c^2}{E_a} \exp^{\left(\frac{-E_a}{RT_c}\right)} \quad (4)$$

For U-Th/ He in Zircon E_a =169 kJmol^{-1} and Ω=7.03 x 10^5 s^{-1} (Reiners et al. 2004, Reiners and Brandon 2006). For Ar-Ar in biotite E_a=197 kJmol^{-1} and Ω=733 s^{-1} (Grove and Harrison 1996, Reiners and Brandon 2006). R is the Regnault or gas constant.

Finally, Z_c is estimated by inserting the calculated T_c into equation 1 or 2 and solving for z. This process can be repeated for multiple exhumation rates to give the effective closure paths shown on (Figure 4.6).

G1

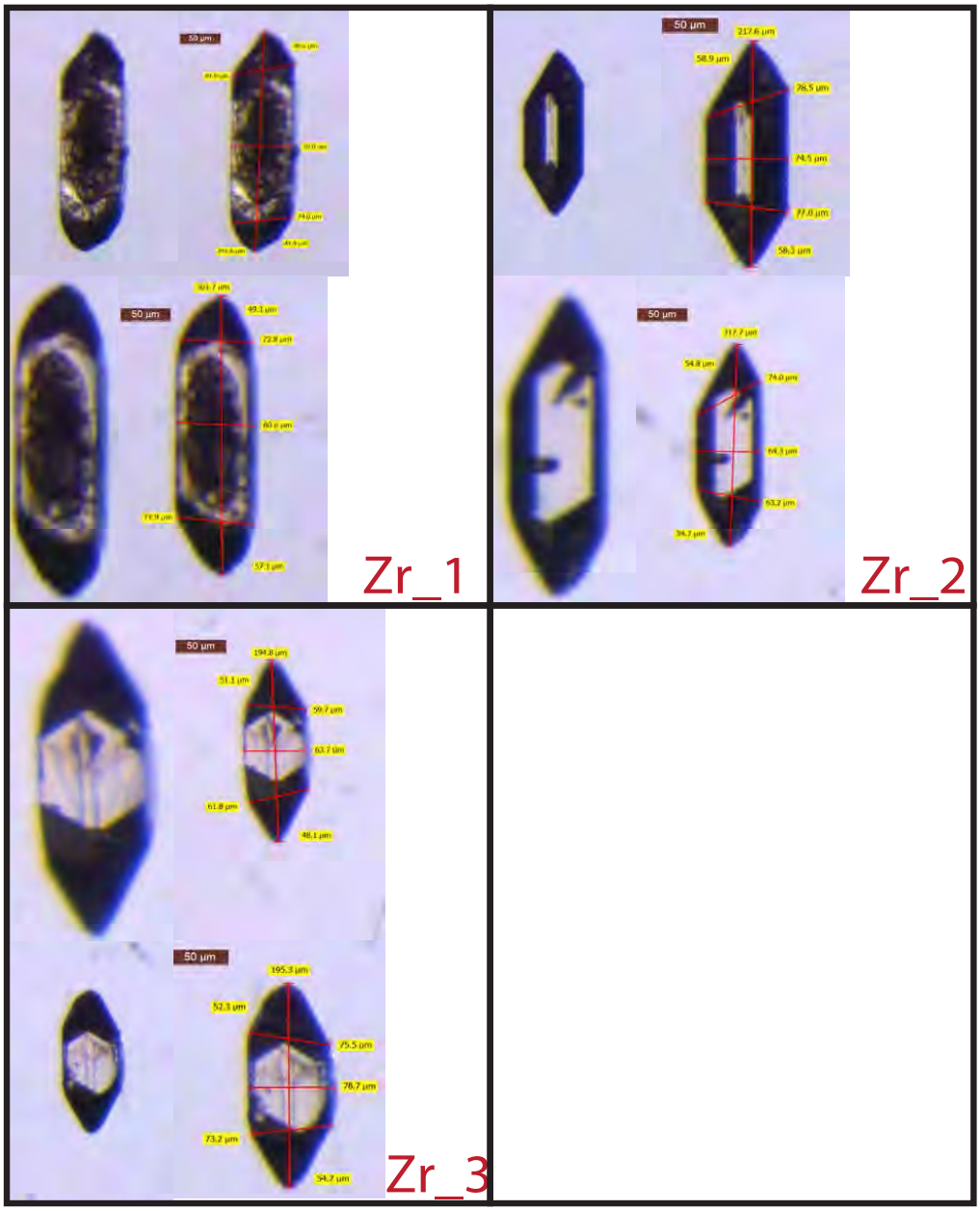

G3

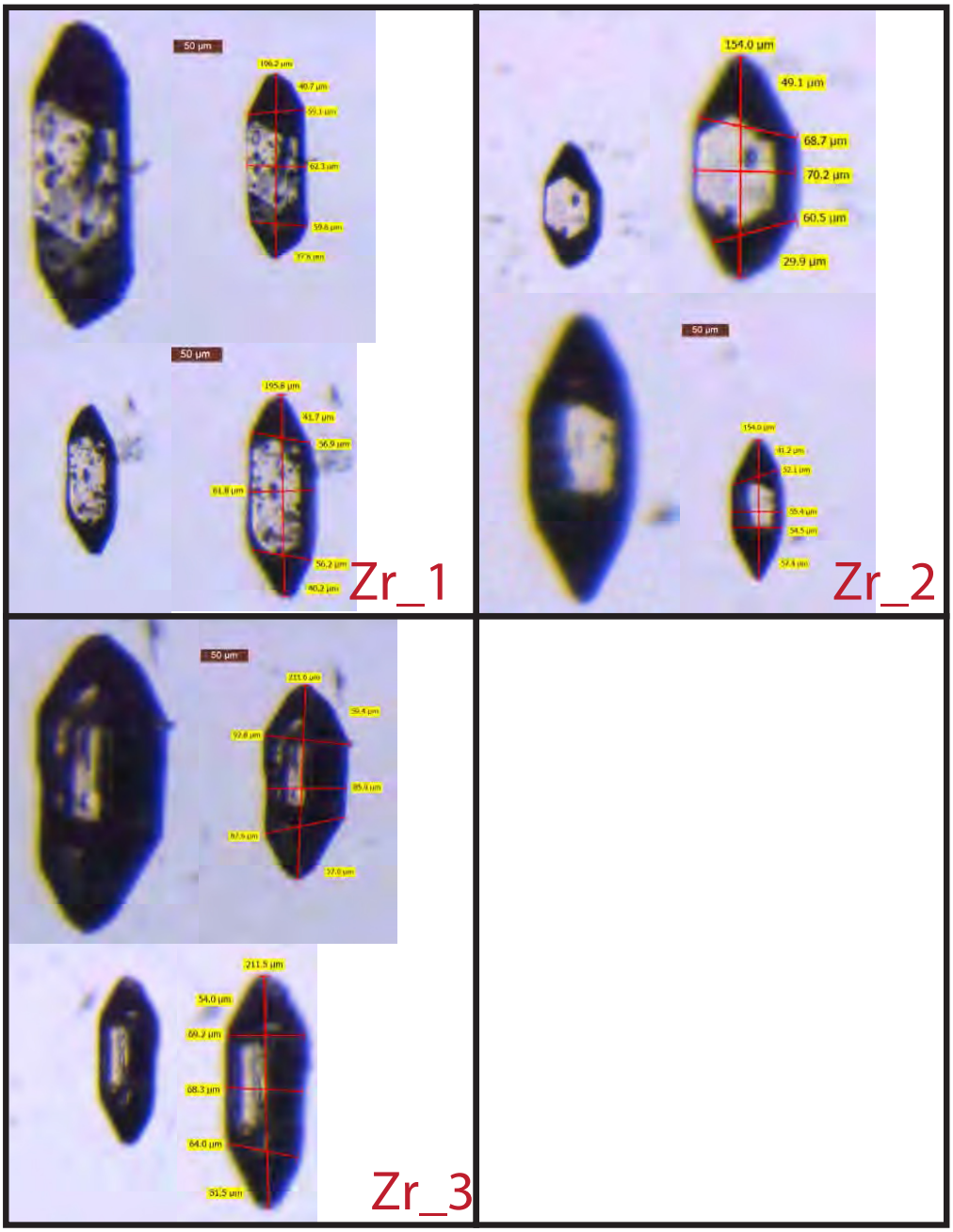

G4

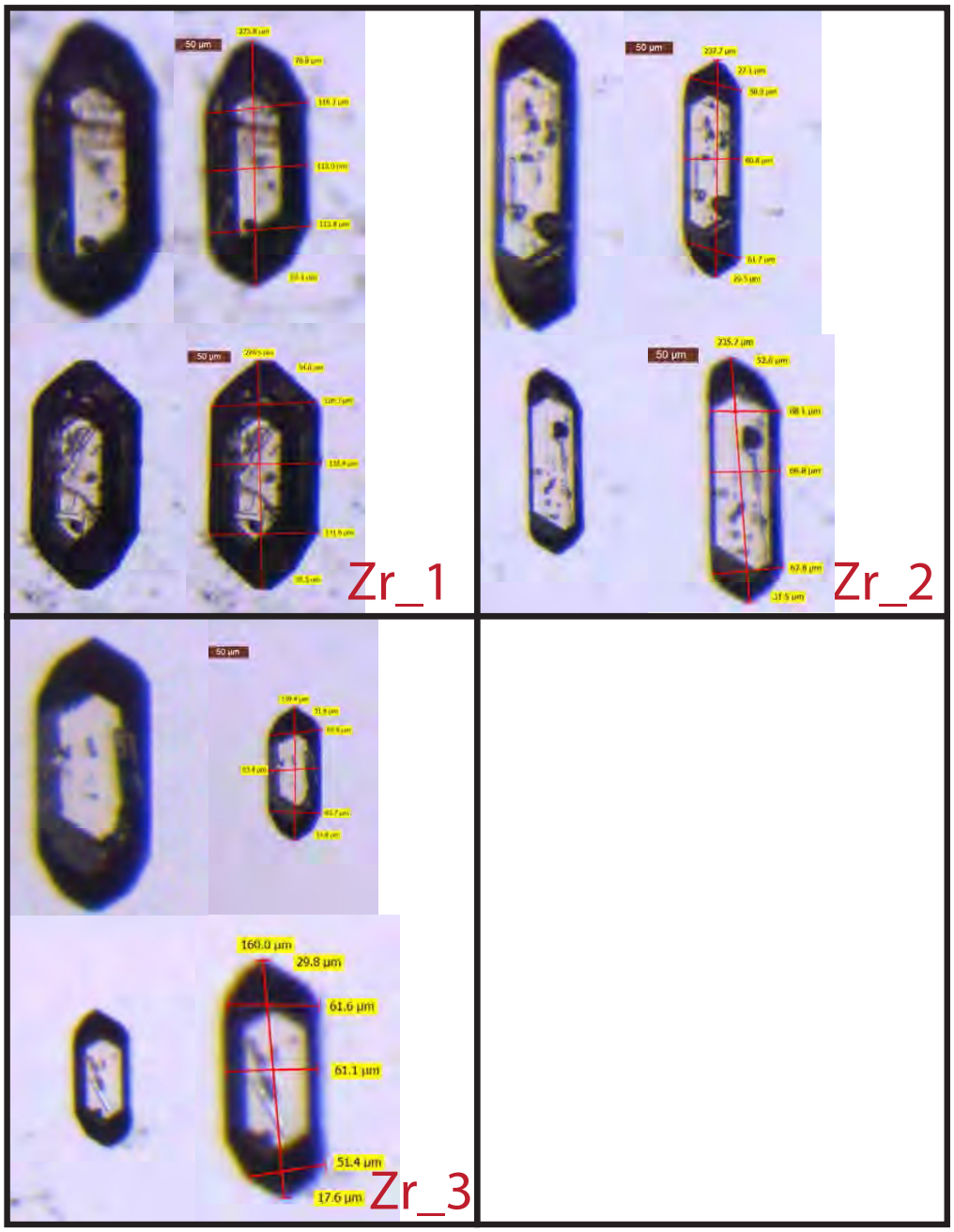

G10

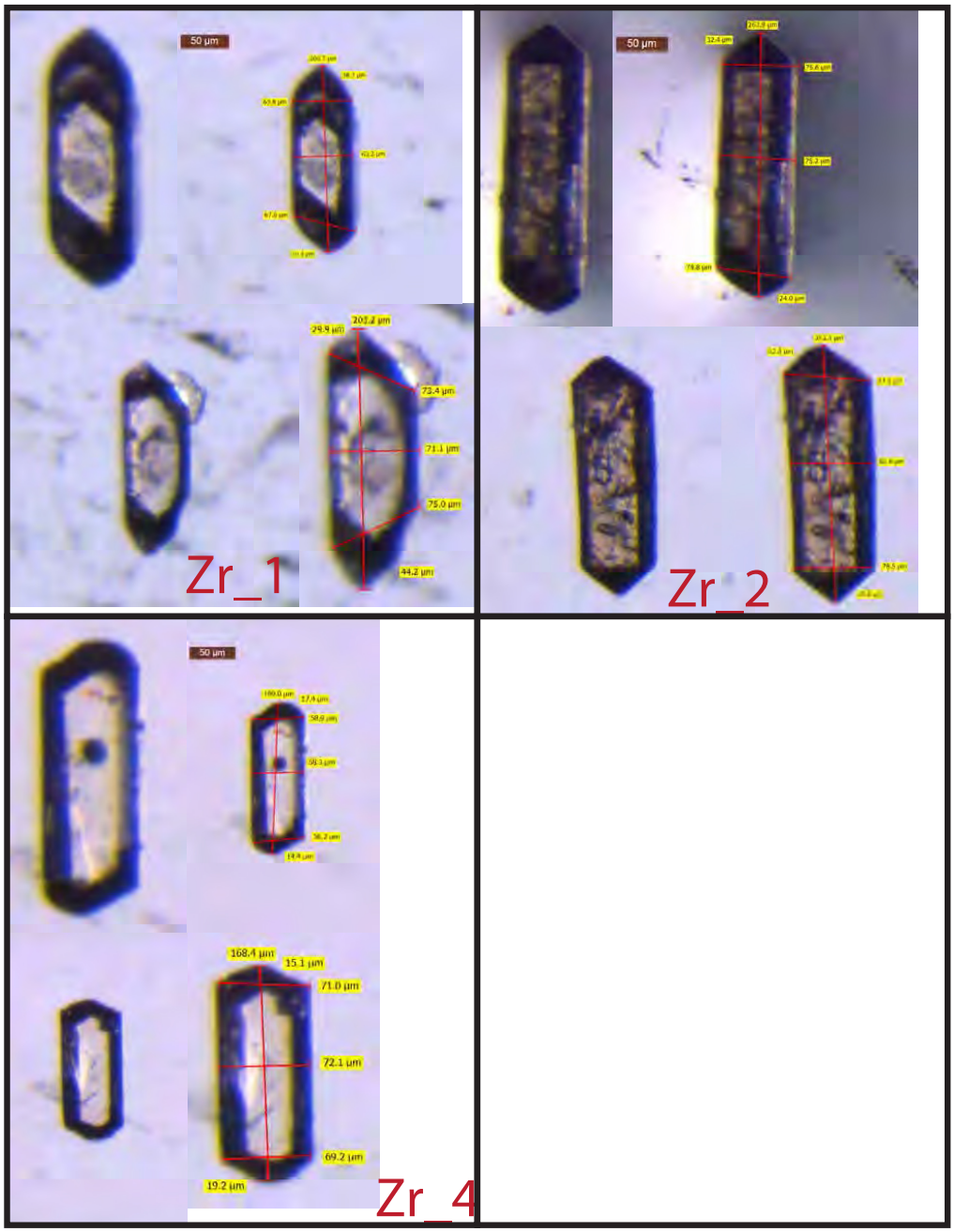

G11

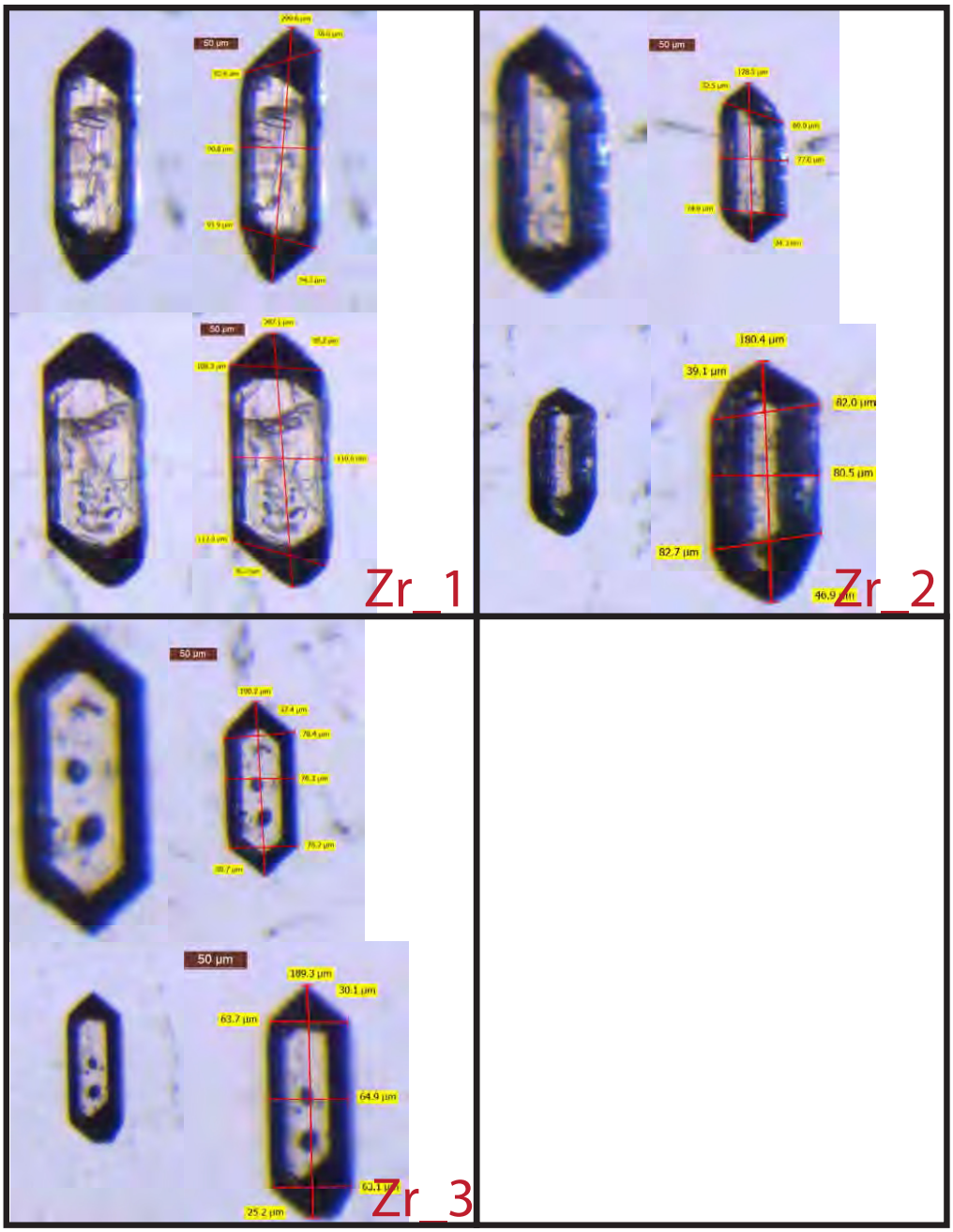
50 µm
Zr_1
50 µm
180.4 µm
39.1 µm
82.0 µm
80.5 µm
82.7 µm
Zr_2
50 µm
50 µm
189.3 µm
30.1 µm
63.7 µm
64.9 µm
25.2 µm
Zr_3

G12

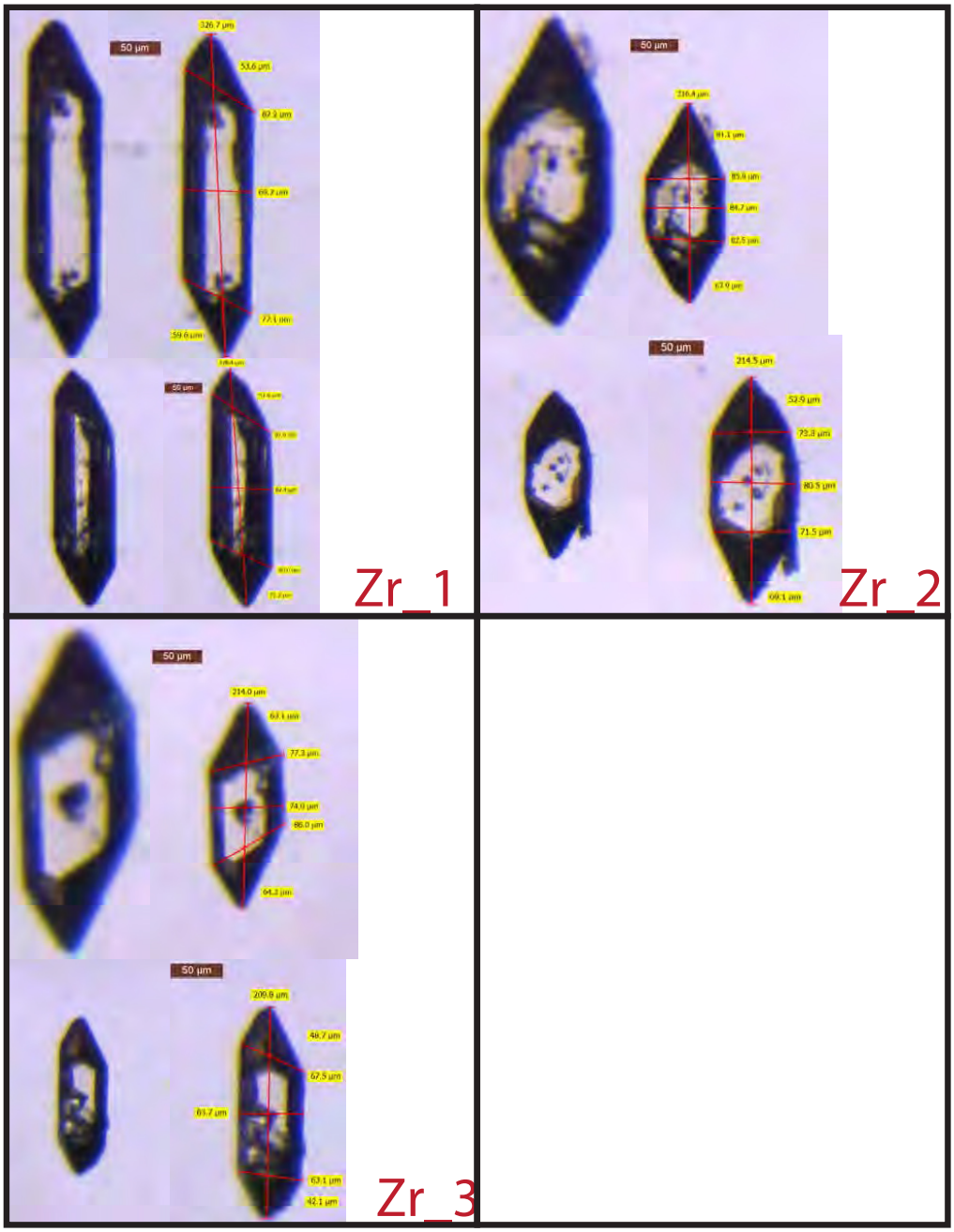

G18

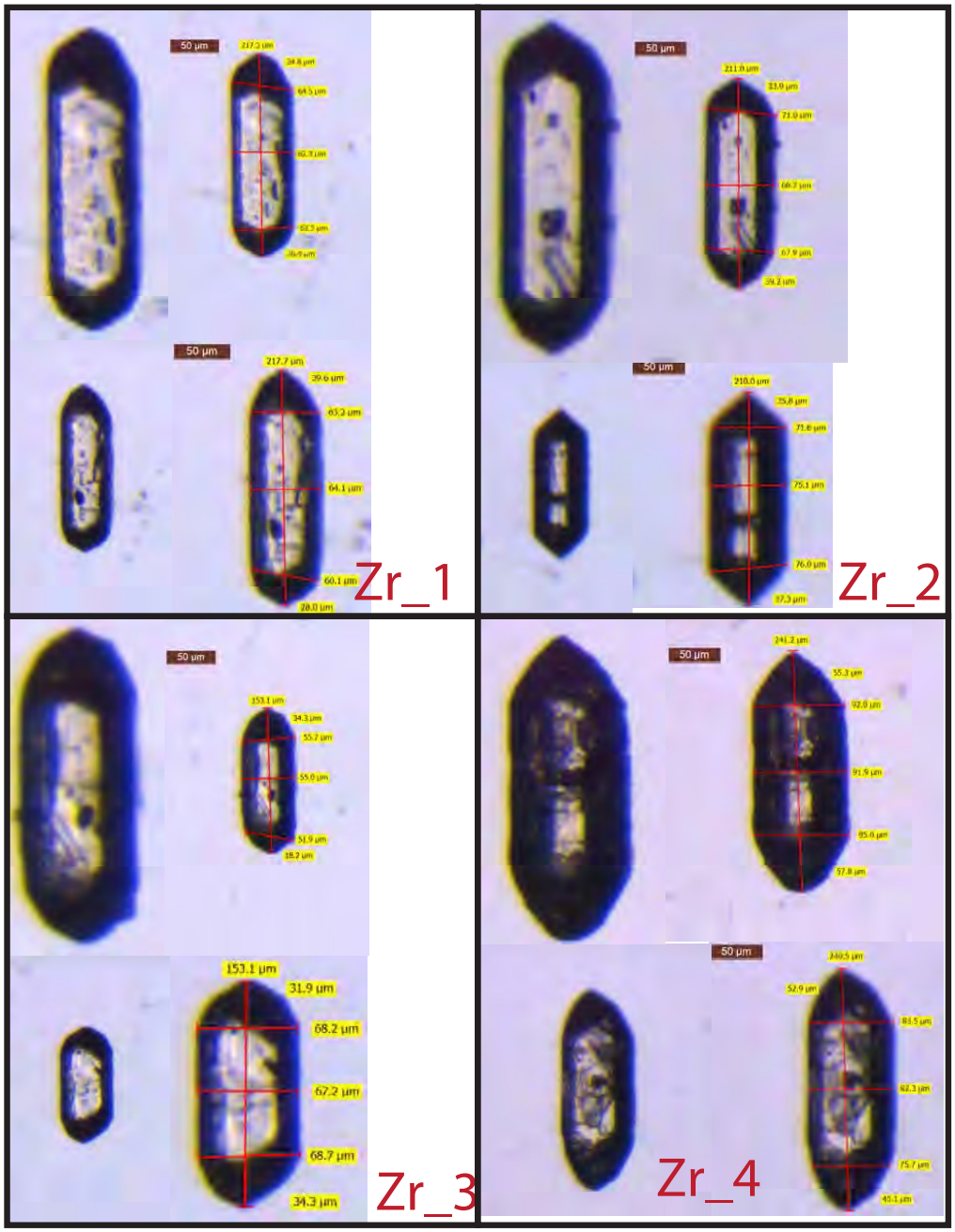

G22

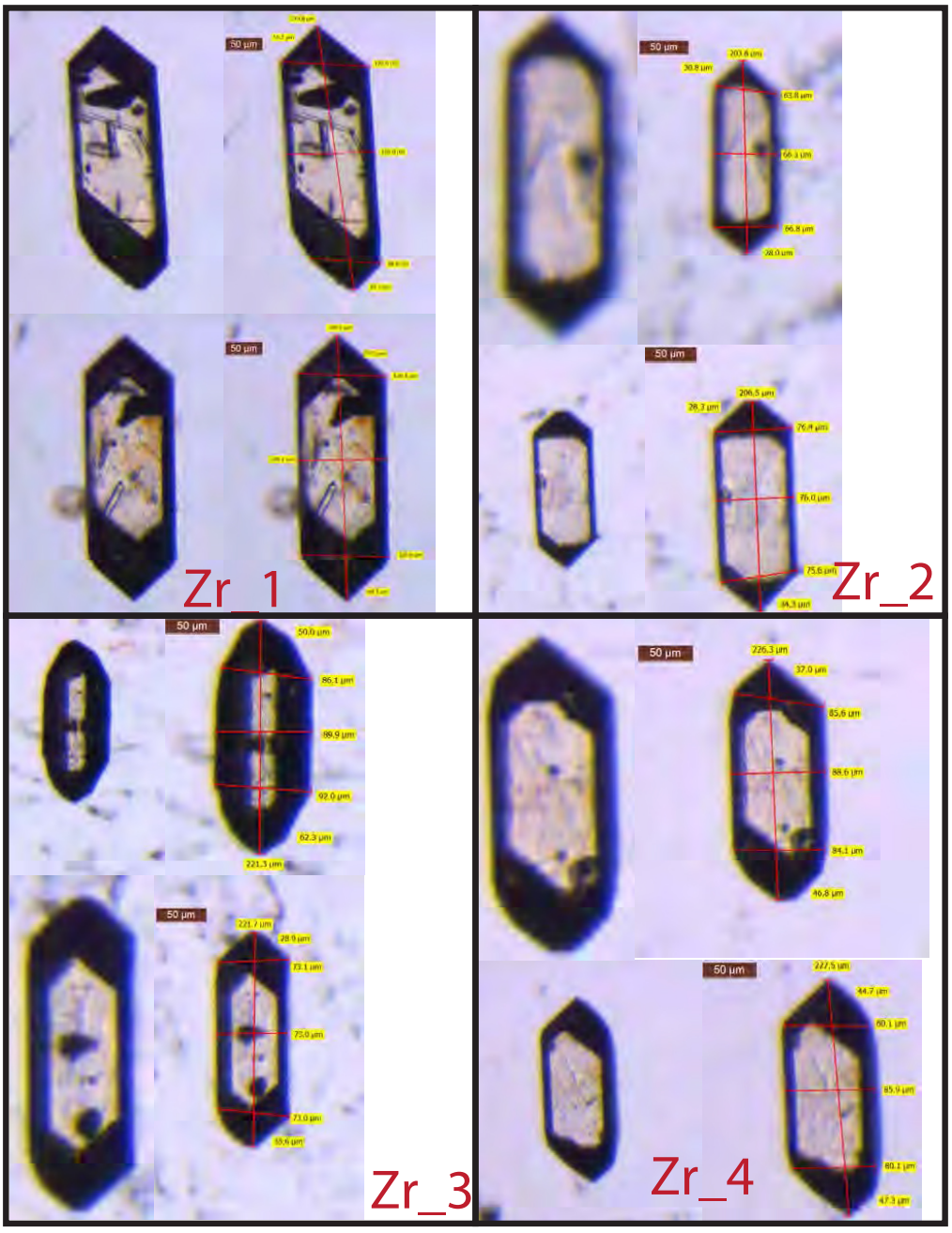

G27

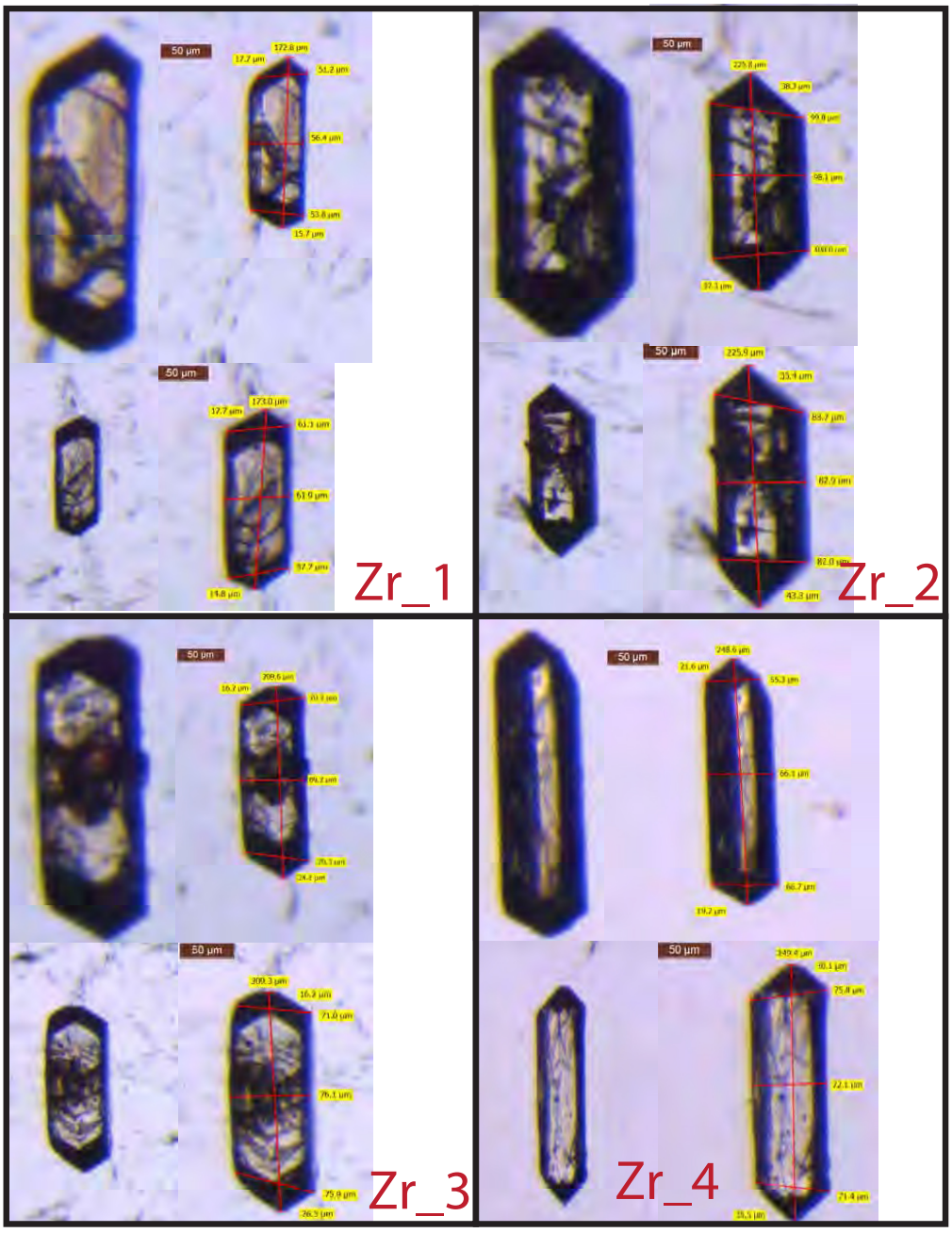

Table A14. Raw Ar-Ar Data

Step #	T (°C)	t (min)	Measured Beam Intensity (mV) ^{36}Ar	^{37}Ar	^{38}Ar	^{39}Ar	^{40}Ar	% $^{40}Ar^*$	% ^{39}Ar released	Ca/K	$^{40}Ar^*/^{39}ArK$	Age (Ma)	±σ (Ma)
G1, Biotite, 9.26 mg, J = 0.00619 ± 0.55%													
1	600	12	0.435	0.174	0.374	17.212	221.77	44.5	0.5	0.078	5.34	58.7	0.7
2	650	12	0.389	0.118	0.591	35.853	445.91	76.5	1.1	0.025	9.15	99.4	0.6
3	700	12	0.514	0.169	2.548	168.827	1763.83	92.0	5.4	0.008	9.45	102.6	0.6
4	740	12	0.229	0.177	5.418	367.102	3603.95	98.5	11.7	0.004	9.54	103.6	0.6
5	770	12	0.116	0.177	5.321	367.853	3576.30	99.4	11.7	0.004	9.54	103.5	0.6
6	810	12	0.099	0.237	5.047	351.606	3420.05	99.6	11.2	0.005	9.56	103.7	0.6
7	860	12	0.086	0.329	3.068	208.559	2032.74	99.5	6.6	0.012	9.55	103.6	0.6
8	910	12	0.080	0.431	1.798	124.043	1213.15	99.3	4.0	0.027	9.52	103.3	0.6
9	950	12	0.089	0.354	1.996	136.973	1350.52	99.2	4.4	0.020	9.60	104.1	0.6
10	990	12	0.097	0.294	2.766	188.689	1859.89	99.3	6.0	0.012	9.63	104.4	0.6
11	1030	12	0.110	0.256	3.456	235.172	2281.77	99.2	7.5	0.008	9.48	102.9	0.6
12	1070	12	0.112	0.221	3.716	258.083	2508.59	99.3	8.2	0.007	9.51	103.2	0.6
13	1120	12	0.119	0.342	4.231	288.162	2809.60	99.3	9.2	0.009	9.54	103.6	0.6
14	1180	12	0.124	1.010	4.319	293.902	2866.19	99.2	9.4	0.027	9.54	103.6	0.6
15	1400	12	0.137	4.746	1.369	96.155	962.04	98.3	3.1	0.381	9.54	103.5	0.6
										Total Gas Age		**103.2**	**0.1**

Step #	T (°C)	t (min)	Measured Beam Intensity (mV) ^{36}Ar	^{37}Ar	^{38}Ar	^{39}Ar	^{40}Ar	% $^{40}Ar^*$	% ^{39}Ar released	Ca/K	$^{40}Ar^*/^{39}ArK$	Age (Ma)	±σ (Ma)
G3, Biotite, 10.67 mg, J = 0.00613 ± 0.45%													
1	600	12	0.607	0.829	0.641	36.318	349.02	49.9	1.1	0.179	4.57	49.8	0.3
2	650	12	0.391	0.320	0.687	46.463	543.15	80.7	1.4	0.054	9.12	98.1	0.5
3	700	12	0.498	0.467	2.023	151.746	1645.60	91.7	4.7	0.024	9.77	105.0	0.5
4	740	12	0.212	0.582	3.402	264.914	2646.31	98.1	8.1	0.017	9.67	103.8	0.5
5	770	12	0.120	0.542	3.206	253.436	2486.53	99.2	7.8	0.017	9.59	103.0	0.5
6	810	12	0.108	0.781	3.947	310.002	3051.08	99.4	9.5	0.020	9.65	103.7	0.5
7	860	12	0.105	1.117	3.373	267.612	2652.99	99.4	8.2	0.033	9.71	104.4	0.5
8	910	12	0.100	1.446	2.554	199.045	1970.66	99.3	6.1	0.057	9.67	103.9	0.5
9	950	12	0.083	1.398	2.104	168.104	1682.33	99.5	5.2	0.065	9.79	105.1	0.5
10	990	12	0.097	1.372	2.855	225.259	2257.49	99.4	6.9	0.048	9.81	105.4	0.5
11	1030	12	0.102	1.419	3.415	270.790	2709.99	99.4	8.3	0.041	9.81	105.4	0.5
12	1070	12	0.101	1.635	3.402	272.279	2705.74	99.4	8.4	0.047	9.74	104.7	0.5
13	1120	12	0.104	1.838	2.408	189.946	1881.93	99.2	5.8	0.076	9.67	103.9	0.5
14	1180	12	0.107	3.488	5.235	411.926	4054.22	99.6	12.7	0.067	9.68	104.0	0.5
15	1400	12	0.192	16.554	2.427	187.028	1877.31	98.3	5.7	0.696	9.67	103.9	0.5
										Total Gas Age		**103.6**	**0.1**

Table A14 Cont. Raw Ar-Ar Data

Step #	T (°C)	t (min)	Measured Beam Intensity (mV)					% $^{40}Ar^*$	% ^{39}Ar released	Ca/K	$\frac{^{40}Ar^*}{^{39}ArK}$	Age (Ma)	±σ (Ma)
			^{36}Ar	^{37}Ar	^{38}Ar	^{39}Ar	^{40}Ar						
G4, Biotite, 14.57 mg, J = 0.00605 ± 0.44%													
1	650	12	0.794	6.477	0.981	34.237	438.25	47.3	0.8	1.516	5.82	62.5	0.5
2	700	12	0.455	3.907	1.586	52.563	612.38	79.8	1.3	0.595	9.02	95.8	0.5
3	740	12	0.310	2.807	4.084	143.689	1403.59	94.4	3.5	0.156	9.06	96.2	0.4
4	770	12	0.185	2.107	6.434	230.096	2175.91	98.1	5.5	0.073	9.14	97.1	0.4
5	810	12	0.163	2.443	10.470	380.974	3549.50	99.0	9.2	0.051	9.11	96.8	0.5
6	860	12	0.107	2.807	10.458	382.896	3619.04	99.5	9.2	0.059	9.29	98.7	0.4
7	910	12	0.107	3.517	7.254	265.378	2522.91	99.3	6.4	0.106	9.31	98.9	0.4
8	950	12	0.105	3.657	6.346	227.351	2173.05	99.3	5.5	0.129	9.35	99.3	0.4
9	990	12	0.108	3.332	8.021	290.253	2778.77	99.4	7.0	0.092	9.39	99.7	0.4
10	1030	12	0.099	3.276	8.968	327.094	3090.67	99.5	7.9	0.080	9.28	98.6	0.4
11	1070	12	0.112	3.875	9.977	365.228	3447.89	99.5	8.8	0.085	9.27	98.5	0.4
12	1120	12	0.136	6.252	12.965	473.704	4446.96	99.4	11.4	0.106	9.24	98.1	0.4
13	1180	12	0.142	20.131	17.459	618.822	5831.01	99.6	14.9	0.261	9.28	98.5	0.4
14	1400	12	0.224	18.904	10.441	371.233	3544.30	98.8	8.9	0.408	9.30	98.7	0.4
										Total Gas Age		**98.0**	**0.1**

Step #	T (°C)	t (min)	Measured Beam Intensity (mV)					% $^{40}Ar^*$	% ^{39}Ar released	Ca/K	$\frac{^{40}Ar^*}{^{39}ArK}$	Age (Ma)	±σ (Ma)
			^{36}Ar	^{37}Ar	^{38}Ar	^{39}Ar	^{40}Ar						
G10, Biotite, 10.55 mg, J = 0.00601 ± 0.47%													
1	650	12	1.522	2.712	2.526	95.249	802.39	43.3	3.5	0.229	3.55	38.1	0.3
2	700	12	0.512	0.425	2.306	91.058	975.21	85.5	3.4	0.038	8.95	94.6	0.5
3	740	12	0.298	0.437	5.935	242.603	2257.33	96.6	8.9	0.015	8.86	93.6	0.4
4	770	12	0.164	0.420	8.405	343.211	3114.55	98.9	12.6	0.010	8.86	93.6	0.4
5	810	12	0.144	0.482	9.237	374.856	3441.13	99.1	13.8	0.010	8.99	94.9	0.5
6	860	12	0.146	0.570	5.378	216.048	2025.01	98.6	8.0	0.021	9.10	96.1	0.5
7	910	12	0.187	0.892	3.468	139.636	1388.46	97.1	5.1	0.051	9.47	99.9	0.5
8	950	12	0.174	1.312	3.399	137.741	1419.28	97.4	5.1	0.077	9.86	103.8	0.5
9	990	12	0.131	1.783	4.149	173.268	1709.07	98.6	6.4	0.083	9.57	100.9	0.5
10	1030	12	0.102	2.425	5.339	225.244	2140.91	99.3	8.3	0.087	9.30	98.1	0.5
11	1070	12	0.090	3.231	4.219	176.724	1651.62	99.4	6.5	0.147	9.13	96.4	0.5
12	1120	12	0.095	10.015	3.054	127.949	1183.79	99.1	4.7	0.631	8.99	94.9	0.5
13	1180	12	0.117	29.358	5.868	239.604	2196.85	99.5	8.8	0.987	8.98	94.9	0.5
14	1400	12	0.178	17.673	3.221	131.682	1247.39	97.9	4.9	1.082	9.04	95.5	0.5
										Total Gas Age		**94.2**	**0.1**

Table A14 Cont. Raw Ar-Ar Data

Step #	T (°C)	t (min)	Measured Beam Intensity (mV) ^{36}Ar	^{37}Ar	^{38}Ar	^{39}Ar	^{40}Ar	% ^{40}Ar*	% ^{39}Ar released	Ca/K	$^{40}Ar^*/^{39}ArK$	Age (Ma)	±σ (Ma)
G11, Biotite, 9.78 mg, J = 0.00594 ± 0.48%													
1	650	12	0.902	1.588	0.803	20.074	404.22	34.0	0.6	0.646	6.57	69.1	0.5
2	700	12	0.418	0.919	1.641	45.721	543.36	79.2	1.5	0.164	9.10	95.0	0.8
3	740	12	0.243	0.809	4.397	129.150	1251.72	95.4	4.1	0.051	9.07	94.6	0.5
4	770	12	0.153	0.830	7.616	222.406	2081.41	98.5	7.1	0.030	9.08	94.8	0.5
5	810	12	0.113	1.127	12.497	367.365	3412.88	99.4	11.7	0.025	9.12	95.2	0.5
6	860	12	0.085	1.328	12.148	356.467	3271.64	99.7	11.4	0.030	9.03	94.3	0.5
7	910	12	0.084	1.169	8.022	238.817	2221.40	99.6	7.6	0.040	9.13	95.3	0.5
8	950	12	0.095	0.931	5.559	166.456	1542.30	99.2	5.3	0.046	9.03	94.3	0.5
9	990	12	0.072	0.833	5.090	153.454	1437.06	99.6	4.9	0.044	9.16	95.6	0.5
10	1030	12	0.089	0.992	5.233	156.563	1447.16	99.3	5.0	0.052	9.01	94.1	0.5
11	1070	12	0.082	1.500	7.073	210.132	1948.42	99.5	6.7	0.058	9.09	94.9	0.5
12	1120	12	0.123	2.960	12.620	370.698	3431.27	99.4	11.8	0.065	9.08	94.8	0.5
13	1180	12	0.143	12.418	17.259	512.208	4734.25	99.5	16.3	0.198	9.09	94.9	0.5
14	1400	12	0.212	10.270	6.396	188.164	1791.15	97.8	6.0	0.446	9.13	95.3	0.5
										Total Gas Age		**94.7**	**0.1**

Step #	T (°C)	t (min)	Measured Beam Intensity (mV) ^{36}Ar	^{37}Ar	^{38}Ar	^{39}Ar	^{40}Ar	% ^{40}Ar*	% ^{39}Ar released	Ca/K	$^{40}Ar^*/^{39}ArK$	Age (Ma)	±σ (Ma)
G12, Biotite, 8.61 mg, J = 0.00591 ± 0.47%													
1	650	12	2.119	1.751	1.768	51.773	1073.05	40.6	2.0	0.278	8.23	85.7	0.4
2	700	12	0.694	1.870	5.568	209.423	2090.67	90.6	7.9	0.073	8.90	92.5	0.5
3	740	12	0.260	2.009	11.250	426.201	3950.33	98.4	16.1	0.039	9.00	93.5	0.4
4	770	12	0.130	1.382	11.450	436.575	3985.32	99.4	16.5	0.026	8.95	93.0	0.4
5	810	12	0.096	1.381	9.012	343.022	3151.57	99.6	13.0	0.033	9.02	93.7	0.4
6	860	12	0.087	1.555	4.143	156.254	1432.98	99.3	5.9	0.082	8.94	92.8	0.5
7	910	12	0.095	2.011	2.830	107.492	1000.58	98.8	4.1	0.154	8.99	93.4	0.4
8	950	12	0.095	2.018	2.977	113.735	1055.52	98.8	4.3	0.146	8.97	93.2	0.4
9	990	12	0.080	1.285	3.770	142.968	1326.18	99.4	5.4	0.074	9.04	93.9	0.4
10	1030	12	0.088	1.230	4.220	160.950	1484.66	99.3	6.1	0.063	8.99	93.4	0.5
11	1070	12	0.083	1.720	4.488	173.543	1596.62	99.4	6.6	0.081	8.98	93.3	0.4
12	1120	12	0.089	4.008	2.491	95.492	885.13	98.9	3.6	0.345	8.94	92.9	0.4
13	1180	12	0.082	10.863	3.706	140.395	1304.49	99.6	5.3	0.636	9.07	94.2	0.4
14	1400	12	0.136	11.330	2.035	82.489	790.91	98.1	3.1	1.129	9.07	94.2	0.5
										Total Gas Age		**93.2**	**0.1**

Table A14 Cont. Raw Ar-Ar Data

Step #	T (°C)	t (min)	Measured Beam Intensity (mV) ^{36}Ar	^{37}Ar	^{38}Ar	^{39}Ar	^{40}Ar	% $^{40}Ar^*$	% ^{39}Ar released	Ca/K	$\frac{^{40}Ar^*}{^{39}ArK}$	Age (Ma)	±σ (Ma)
G22, Biotite, 9.19 mg, J = 0.00581 ± 0.52%													
1	650	12	2.865	18.998	2.750	69.412	1024.99	15.6	4.7	2.282	2.26	23.6	0.3
2	700	12	0.653	2.340	1.307	35.585	466.56	59.9	2.4	0.548	7.56	77.6	0.5
3	740	12	0.293	1.871	1.693	44.641	481.25	84.6	3.0	0.349	8.79	89.9	0.5
4	770	12	0.205	2.990	2.443	63.626	665.74	93.1	4.3	0.392	9.47	96.6	0.5
5	810	12	0.210	7.764	4.541	115.790	1227.81	96.2	7.8	0.559	10.01	102.0	0.5
6	860	12	0.200	8.733	6.655	169.984	1777.55	97.6	11.4	0.428	10.04	102.3	0.5
7	910	12	0.185	3.782	6.542	168.342	1758.91	97.7	11.3	0.187	10.05	102.4	0.5
8	950	12	0.267	8.272	3.999	95.361	1097.97	94.2	6.4	0.723	10.63	108.1	0.6
9	990	12	0.294	11.770	3.546	79.768	957.22	94.0	5.4	1.230	11.04	112.1	0.7
10	1030	12	0.160	13.588	3.671	89.145	995.84	97.1	6.0	1.271	10.61	107.9	0.6
11	1070	12	0.121	13.618	4.244	103.459	1090.05	98.4	6.9	1.097	10.16	103.4	0.6
12	1120	12	0.150	17.809	4.205	101.711	1047.91	97.6	6.8	1.460	9.85	100.4	0.5
13	1180	12	0.157	31.129	7.717	183.689	1843.93	98.7	12.3	1.413	9.75	99.4	0.5
14	1400	12	0.260	20.208	6.671	168.829	1724.24	97.0	11.3	0.998	9.70	99.0	0.5
										Total Gas Age		**97.8**	**0.1**

Step #	T (°C)	t (min)	Measured Beam Intensity (mV) ^{36}Ar	^{37}Ar	^{38}Ar	^{39}Ar	^{40}Ar	% $^{40}Ar^*$	% ^{39}Ar released	Ca/K	$\frac{^{40}Ar^*}{^{39}ArK}$	Age (Ma)	±σ (Ma)
G27, Biotite, 8.62 mg, J = 0.00578 ± 0.62%													
1	650	12	0.997	0.916	1.178	34.251	547.37	46.2	1.4	0.224	7.14	73.0	1.0
2	700	12	0.390	0.414	2.463	78.418	899.82	88.5	3.1	0.044	9.91	100.5	0.6
3	740	12	0.186	0.446	5.637	181.833	1912.08	97.9	7.2	0.021	10.12	102.6	0.6
4	770	12	0.114	0.406	7.676	245.888	2534.84	99.2	9.7	0.014	10.08	102.2	0.7
5	810	12	0.084	0.445	10.267	326.932	3383.74	99.7	13.0	0.011	10.18	103.2	0.6
6	860	12	0.077	0.499	9.258	296.978	3088.42	99.7	11.8	0.014	10.23	103.7	0.6
7	910	12	0.092	0.652	5.434	174.358	1821.37	99.3	6.9	0.031	10.21	103.4	0.6
8	950	12	0.101	0.867	3.637	115.472	1224.00	98.8	4.6	0.063	10.27	104.0	0.6
9	990	12	0.088	1.042	4.203	134.752	1407.76	99.3	5.3	0.065	10.18	103.1	0.6
10	1030	12	0.088	1.293	5.619	181.663	1885.38	99.5	7.2	0.060	10.15	102.9	0.6
11	1070	12	0.089	1.791	7.757	249.803	2592.84	99.6	9.9	0.060	10.19	103.2	0.6
12	1120	12	0.090	4.397	6.531	211.221	2199.34	99..5	8.4	0.175	10.21	103.4	0.6
13	1180	12	0.130	20.782	6.816	219.281	2286.39	99.2	8.7	0.795	10.19	103.2	0.6
14	1400	12	0.168	6.370	1.565	72.311	793.70	96.7	2.9	0.739	10.24	103.7	0.7
										Total Gas Age		**102.7**	**0.1**

Table A14 Cont. Raw Ar-Ar Data

Step #	T (°C)	t (min)	Measured Beam Intensity (mV)					% $^{40}Ar^*$	% ^{39}Ar released	Ca/K	$\frac{^{40}Ar^*}{^{39}ArK}$	Age (Ma)	±σ (Ma)
			^{36}Ar	^{37}Ar	^{38}Ar	^{39}Ar	^{40}Ar						
G18, Amphibole, 20.19 mg, J = 0.00585 ± 0.47%													
1	550	12	1.316	0.809	0.268	0.852	392.49	3.5	0.6	10.100	16.39	165.2	13.2
2	590	12	0.298	2.233	0.083	1.336	97.32	16.0	1.0	17.815	10.47	107.2	2.8
3	630	12	0.510	7.198	0.159	2.674	183.91	23.5	2.0	28.777	15.41	155.7	4.8
4	660	12	0.447	11.782	0.129	2.429	161.20	25.1	1.8	52.183	15.80	159.5	2.1
5	680	12	0.330	13.350	0.113	2.140	125.86	29.5	1.6	67.387	16.18	163.1	3.0
6	700	12	0.491	19.761	0.149	2.652	170.39	22.9	2.0	80.779	14.15	143.5	6.6
7	720	12	0.528	26.146	0.140	2.879	183.13	23.6	2.1	98.929	14.53	147.2	6.0
8	750	12	0.719	38.329	0.214	4.352	263.82	26.9	3.2	95.862	16.08	162.2	4.1
9	780	12	0.469	42.233	0.156	4.033	192.38	38.9	3.0	114.546	18.03	180.9	4.7
10	810	12	0.423	43.192	0.143	4.114	159.12	34.3	3.0	114.850	12.69	129.2	2.2
11	850	12	0.399	19.530	0.153	5.316	155.02	32.0	3.9	39.387	8.72	89.7	1.2
12	900	12	0.323	2.911	0.164	7.637	170.96	49.5	5.7	4.048	10.32	105.7	1.5
13	950	12	0.181	3.683	0.222	13.467	175.15	75.7	10.0	2.903	9.05	93.1	0.6
14	990	12	0.185	10.758	0.301	20.197	243.37	83.4	14.9	5.659	9.48	97.4	0.6
15	1050	12	0.288	17.089	0.422	29.575	350.06	80.4	21.9	6.139	9.16	94.1	0.5
16	1130	12	0.486	16.453	0.375	12.792	258.70	49.4	9.5	13.694	9.50	97.5	0.8
17	1210	12	1.251	105.337	1.799	11.851	526.82	38.5	8.8	96.769	17.03	171.3	2.6
18	1400	12	1.044	37.647	0.990	6.844	408.89	30.2	5.1	59.291	17.16	172.6	1.2
											Total Gas Age	**118.1**	**0.3**

For all samples:

4 amu discrimination = 0.9680 ± 0.08%, 40/39K = 0.0071 ± 9.38%, 36/37Ca = 0.000231 ± 0.29%, 39/37Ca = 0.000627 ± 0.08%

Error in age includes J error,

^{36}Ar through ^{40}Ar are measured beam intensities, corrected for decay for the age calculations

Table A15. U-Th/He Core Correction Worksheet

Zircon #	c axis (µm)	a axis (µm)	Tip 1 Index	Tip height 1 (µm)	Tip 2 Index	Tip height 2 (µm)	Core length (µm)	Core Width (µm)	ECR zircon (µm)	ECR Core (µm)	Rim thickness (µm)
1	259	76	1	69	3	73	124	63	63	39	24
2	279	79	2	77	2	67	121	52	69	34	34
3	308	113	2	109	2	110	127	96	86	53	34
4	326	125	3	121	2	101	153	90	97	54	43
5	233	79	3	76	3	76	40	66	65	28	37
6	344	124	2	107	2	113	153	115	97	63	33
7	324	179	3	127	3	122	116	150	122	69	53
8	321	99	2	101	3	81	119	84	83	47	36
9	305	107	2	96	2	100	130	88	85	50	35
10	343	119	2	116	2	118	134	99	94	55	39
11	284	116	3	68	2	80	195	107	88	66	23
12	338	120	2	91	1	118	173	93	93	57	36
13	341	127	2	108	2	101	157	58	97	40	57
14	282	102	1	86	3	94	154	98	79	57	22
15	254	139	3	110	3	110	170	94	95	57	38
16	334	105	2	104	2	87	186	85	88	55	33
17	232	73	1	72	2	72	110	57	59	36	24
18	217	75	1	75	2	66	72	54	58	30	28
19	304	96	2	97	2	93	160	80	79	50	29
20	242	99	1	84	1	86	141	82	71	49	22
21	184	63	2	61	2	63	94	56	50	33	17
22	288	110	2	93	2	109	74	74	85	37	48
23	183	109	3	92	3	92	69	107	74	46	28
24	304	84	1	83	2	84	143	65	73	42	31
25	272	79	1	78	2	78	138	69	67	44	24
26	242	71	3	60	2	73	157	69	62	45	17
27	254	81	3	78	1	78	123	78	66	46	21
28	365	137	2	143	2	125	175	111	106	65	41

Table A15 Cont. U-Th/He Core Correction Worksheet

Zircon #	c axis (µm)	a axis (µm)	Tip 1 Index	Tip height 1 (µm)	Tip 2 Index	Tip height 2 (µm)	Core length (µm)	Core Width (µm)	ECR zircon (µm)	ECR Core (µm)	Rim thickness (µm)
29	337	102	2	104	1	107	179	96	86	59	27
30	351	147	3	149	2	141	149	134	112	70	42
31	291	83	1	83	3	84	177	70	72	48	24
32	234	113	3	93	2	97	104	67	79	39	40
33	173	56	2	54	3	54	52	51	47	26	21
34	275	107	2	107	1	93	75	102	82	46	36
35	183	63	2	52	1	61	101	54	51	33	17
36	219	78	2	79	3	78	88	72	62	38	24
37	302	94	1	93	3	99	101	80	78	43	35
38	232	72	2	63	2	57	94	63	60	36	24
39	274	110	2	110	3	116	204	106	83	66	17
40	287	116	2	117	2	116	122	103	86	55	31
41	426	150	3	149	2	149	212	130	121	76	45
42	345	107	3	111	2	96	184	100	91	61	29
43	283	80	2	77	3	78	177	78	71	51	20
44	214	74	2	73	1	75	48	69	56	31	26
45	172	60	3	60	1	57	94	56	49	33	16
46	205	90	3	71	3	84	74	67	65	35	31
47	206	77	2	61	1	66	141	69	61	44	17
48	313	107	2	109	2	110	116	85	86	47	39
49	245	72	1	66	3	69	146	37	62	29	33
50	305	69	3	69	1	55	175	59	65	42	22
51	313	128	3	95	3	127	130	107	97	57	40
52	231	51	1	43	1	38	145	38	47	30	18
53	163	51	3	54	3	59	102	48	45	31	14
54	316	111	2	104	3	116	219	109	91	69	22
55	251	53	1	54	1	52	87	46	50	29	21
56	217	85	3	64	2	86	114	47	66	32	34
57	166	65	3	53	2	49	121	57	50	37	13

Table A16. Raw U-Th/He Data

Sample #	Grain I.D	Raw Date (Ma)	±σ (Ma)	U (ppm)	Th (ppm)	^{4}He (nmol/g)	Mass zircon (µg)	ESR (µm)	Corrected date (Ma)	±σ (Ma)
G1	*1*	60.4	0.9	3160	131	1044	6.5	52	**78.8**	**1.2**
	2	59.0	0.9	830	144	276	2.4	43	**81.8**	**1.3**
	3	67.5	1.0	3060	39	1123	2.5	43	**93.2**	**1.4**
G3	*1*	49.2	0.8	893	49	241	2.2	40	**70.1**	**1.1**
	2	43.2	0.7	938	62	223	1.3	37	**63.5**	**1.0**
	3	51.5	0.8	962	72	273	3.2	47	**69.3**	**1.1**
G4	*1*	77.8	1.0	235	124	112	10.7	74	**93.8**	**1.3**
	2	62.7	0.8	332	195	129	3.3	42	**87.8**	**1.1**
	3	60.4	0.8	379	233	142	2.0	39	**87.0**	**1.2**
G10	*1*	52.1	0.7	553	140	165	2.8	43	**72.2**	**1.0**
	2	52.7	0.7	2404	436	714	5.0	52	**68.7**	**1.0**
	4	35.0	0.6	1940	272	379	3.2	41	**49.2**	**0.8**
G11	*1*	62.0	1.0	611	255	225	11.5	65	**76.6**	**1.2**
	2	55.3	0.9	737	243	238	2.7	48	**74.0**	**1.2**
	3	59.0	0.9	496	247	177	3.5	45	**80.9**	**1.3**
G12	*1*	55.9	0.9	339	199	117	5.7	50	**74.0**	**1.2**
	2	40.5	0.7	542	88	123	3.7	49	**53.9**	**0.9**
	3	44.1	0.7	405	86	101	3.4	43	**61.3**	**1.0**
G18	*1*	47.8	0.7	501	304	148	2.9	42	**67.4**	**1.0**
	2	47.0	0.7	284	141	81	2.9	46	**64.1**	**0.9**
	3	48.1	0.7	444	228	130	1.7	38	**70.3**	**1.0**
	4	53.8	0.8	346	200	114	6.9	55	**69.5**	**1.0**
G22	*1*	44.7	0.6	456	452	136	22.7	82	**53.0**	**0.7**
	2	60.8	0.9	502	278	187	3.8	46	**82.8**	**1.2**
	3	59.3	0.8	456	302	169	4.1	51	**78.2**	**1.1**
	4	50.5	0.7	438	384	145	7.2	55	**65.4**	**0.9**
G27	*1*	59.0	0.8	2004	842	703	1.9	38	**85.5**	**1.1**
	2	55.3	0.7	961	367	314	5.2	57	**70.7**	**1.0**
	3	62.8	0.8	2379	1216	908	3.9	47	**84.7**	**1.1**
	4	48.9	0.7	1339	478	384	3.7	46	**66.3**	**1.0**

Table A17. Raw Zircon LA-ICP-MS Data

Zircon Region	*Grain #*	*U (ppm)*	*±2σ (ppm)*	*Th (ppm)*	*±2σ (ppm)*
Rims	*1*	3710	120	24	1
	2	2842	29	32	1
	3	3350	55	110	15
	4	5194	96	60	2
	5	3920	250	34	2
	6	4327	65	31	1
	7	3689	48	48	2
	8	3690	130	24	1
	9	3020	110	21	1
	10	3183	65	25	2
Cores	*1*	2186	68	90	8
	2	177	25	47	1
	3	925	16	162	6
	4	1588	68	137	8
	5	2750	250	320	38
	6	759	23	114	8
	7	583	50	172	6
	8	1790	130	110	4
	9	1750	86	165	2

Chapter 5 Supplemental Information

Table A18. Drill Core Sample Locations

I.D	Drill Hole	Depth (m)	Area	UTM E Collar*	UTM N Collar*	I.D	Drill Hole	Depth (m)	Area	UTM E Collar*	UTM N Collar*
10-01 12	10-01	12.18	KMD	586396	6940142	11-14 170	11-14	169.86	KME	587744	6940265
10-01 34	10-01	34.07	KMD	586396	6940142	11-14 182	11-14	182.19	KME	587744	6940265
10-01 51	10-01	50.82	KMD	586396	6940142	11-14 195	11-14	195.00	KME	587744	6940265
10-01 60	10-01	60.00	KMD	586396	6940142	11-14 199	11-14	199.00	KME	587744	6940265
10-01 69	10-01	69.75	KMD	586396	6940142	11-14 212	11-14	212.06	KME	587744	6940265
10-01 70	10-01	69.83	KMD	586396	6940142	11-14 245	11-14	244.50	KME	587744	6940265
10-01 83	10-01	83.20	KMD	586396	6940142	11-14 306	11-14	306.08	KME	587744	6940265
10-01 98	10-01	98.44	KMD	586396	6940142	11-14 308	11-14	307.98	KME	587744	6940265
10-01 99	10-01	99.09	KMD	586396	6940142	11-14 327	11-14	327.09	KME	587744	6940265
10-01 105	10-01	104.57	KMD	586396	6940142	11-14 330	11-14	330.51	KME	587744	6940265
10-01 116	10-01	116.20	KMD	586396	6940142	11-14 331	11-14	331.10	KME	587744	6940265
10-01 142	10-01	141.79	KMD	586396	6940142	11-14 335	11-14	335.15	KME	587744	6940265
10-01 164	10-01	163.94	KMD	586396	6940142	11-14 341	11-14	340.69	KME	587744	6940265
11-05 42	11-05	41.69	KMD	586661	6940139	11-14 346	11-14	345.65	KME	587744	6940265
11-05 63	11-05	63.34	KMD	586661	6940139	11-14 354	11-14	353.65	KME	587744	6940265
11-05 73	11-05	72.85	KMD	586661	6940139	11-14 359	11-14	359.00	KME	587744	6940265
11-05 95	11-05	94.82	KMD	586661	6940139	11-14 367	11-14	367.38	KME	587744	6940265
11-05 129	11-05	128.80	KMD	586661	6940139	11-14 369	11-14	369.40	KME	587744	6940265
11-05 133	11-05	133.02	KMD	586661	6940139	11-15 14	11-15	14.10	KMD	586816	6940203
11-05 135	11-05	135.13	KMD	586661	6940139	11-15 18	11-15	17.80	KMD	586816	6940203
11-05 136	11-05	135.75	KMD	586661	6940139	11-15 25a	11-15	25.36	KMD	586816	6940203
11-05 241	11-05	241.43	KMD	586661	6940139	11-15 25b	11-15	25.40	KMD	586816	6940203
11-05 253	11-05	253.11	KMD	586661	6940139	11-15 26	11-15	26.24	KMD	586816	6940203
11-07 224	11-07	224.00	KMD	586661	6940139	11-15 29	11-15	29.09	KMD	586816	6940203
11-12 28	11-12	27.86	KMD	586331	6940135	11-15 52	11-15	52.45	KMD	586816	6940203
11-12 30	11-12	30.28	KMD	586331	6940135	11-15 61	11-15	61.12	KMD	586816	6940203
11-12 40	11-12	40.38	KMD	586331	6940135	11-15 80	11-15	80.15	KMD	586816	6940203
11-12 42	11-12	41.65	KMD	586331	6940135	11-15 98	11-15	98.09	KMD	586816	6940203
11-12 44	11-12	44.00	KMD	586331	6940135	11-15 100	11-15	100.07	KMD	586816	6940203
11-12 50	11-12	49.89	KMD	586331	6940135	11-15 116	11-15	115.84	KMD	586816	6940203
11-12 212	11-12	212.40	KMD	586331	6940135	11-15 117	11-15	116.79	KMD	586816	6940203
11-12 240	11-12	240.18	KMD	586331	6940135	11-15 129	11-15	128.95	KMD	586816	6940203
11-12 266	11-12	266.23	KMD	586331	6940135	11-15 131	11-15	130.55	KMD	586816	6940203
11-12 347	11-12	347.40	KMD	586331	6940135	11-15 142	11-15	142.34	KMD	586816	6940203
11-12 351	11-12	351.19	KMD	586331	6940135	11-15 165	11-15	164.79	KMD	586816	6940203
11-12 376	11-12	376.18	KMD	586331	6940135	11-15 182	11-15	182.23	KMD	586816	6940203
11-14 30	11-14	30.08	KME	587744	6940265	11-15 201	11-15	200.60	KMD	586816	6940203
11-14 40	11-14	40.55	KME	587744	6940265	11-15 291	11-15	291.16	KMD	586816	6940203
11-14 41	11-14	41.16	KME	587744	6940265	11-15 385	11-15	385.00	KMD	586816	6940203
11-14 46	11-14	46.10	KME	587744	6940265	11-16 224	11-16	224.00	KMD	586323	6940128
11-14 47	11-14	46.70	KME	587744	6940265	11-17 156	11-17	156.00	KMD	586455	6940065
11-14 103	11-14	103.11	KME	587744	6940265	11-17 160	11-17	160.00	KMD	586455	6940065
11-14 108	11-14	107.72	KME	587744	6940265	11-17 201	11-17	201.00	KMD	586455	6940065
11-14 121	11-14	121.03	KME	587744	6940265	11-17 202	11-17	202.00	KMD	586455	6940065
11-14 139	11-14	138.60	KME	587744	6940265	11-18 136	11-18	136.00	KMD	586323	6940128
11-14 141	11-14	140.69	KME	587744	6940265	11-22 25	11-22	25.05	KMD	586499	6940183
11-14 146	11-14	145.82	KME	587744	6940265	11-22 44	11-22	44.25	KMD	586499	6940183
11-14 152	11-14	151.95	KME	587744	6940265	11-22 109	11-22	109.40	KMD	586499	6940183

Table A18 Cont. Drill Core Sample Locations					
I.D	Drill Hole	Depth (m)	Area	UTM E Collar*	UTM N Collar*
11-22 135	11-22	134.85	KMD	586499	6940183
11-22 149	11-22	149.05	KMD	586499	6940183
11-22 170	11-22	170.20	KMD	586499	6940183
11-22 190	11-22	189.65	KMD	586499	6940183
11-22 230	11-22	230.43	KMD	586499	6940183
11-22 317	11-22	317.00	KMD	586499	6940183
11-23 251	11-23	251.00	KMD	586549	6940101
11-27 207	11-27	207.00	KMD	586485	6939968
11-27 344	11-27	344.00	KMD	586485	6939968
11-29 30	11-29	29.56	KMD	586045	6940012
11-29 90	11-29	90.24	KMD	586045	6940012
11-29 140	11-29	140.15	KMD	586045	6940012
11-29 186	11-29	185.90	KMD	586045	6940012
11-29 220	11-29	220.00	KMD	586045	6940012
11-29 294	11-29	294.00	KMD	586045	6940012
11-29 330	11-29	329.55	KMD	586045	6940012
11-36 392	11-36	392.00	KMD	586310	6939897
11-37 486	11-37	485.65	KMD	586532	6939867
11-37 489	11-37	488.58	KMD	586532	6939867
11-38 225	11-38	224.68	KMD	586693	6940682
11-38 297	11-38	297.27	KMD	586693	6940682
11-38 314	11-38	314.39	KMD	586693	6940682
11-40 533	11-40	532.60	KMD	586449	6939817
11-40 544	11-40	544.00	KMD	586449	6939817
11-41 18	11-41	18.32	KMD	586878	6940116
11-41 56	11-41	55.70	KMD	586878	6940116
11-41 68	11-41	67.54	KMD	586878	6940116
11-41 69	11-41	69.39	KMD	586878	6940116
11-41 73	11-41	72.90	KMD	586878	6940116
11-41 96	11-41	96.13	KMD	586878	6940116
11-41 102	11-41	102.44	KMD	586878	6940116
11-41 106	11-41	106.19	KMD	586878	6940116
11-41 109	11-41	109.10	KMD	586878	6940116
11-41 111	11-41	111.20	KMD	586878	6940116
11-41 131	11-41	131.06	KMD	586878	6940116
11-41 144	11-41	144.29	KMD	586878	6940116
11-41 149	11-41	148.98	KMD	586878	6940116
11-41 159	11-41	159.10	KMD	586878	6940116
11-41 167	11-41	167.26	KMD	586878	6940116
11-41 172	11-41	172.12	KMD	586878	6940116
11-41 180	11-41	180.01	KMD	586878	6940116
11-41 180	11-41	180.47	KMD	586878	6940116
11-41 214	11-41	213.82	KMD	586878	6940116
12-48 300	12-48	300.00	KMD	586675	6940044
12-52 385	12-52	385.00	KMD	586217	6939864
* All UTM Zone 8					

Table A19. Handspecimen Samples

I.D	UTM E*	UTM N*
HS-AI	586962	6940613
HS-AN2	587784	6939184
HS-AS	587176	6939517
HS-BD	586036	6939715
HS-BG	586081	6939930
HS-BH2	586228	6940069
HS-CL	587333	6939760
HS-CT	585046	693904
HS-DA	584438	6938651
HS-EJ	585294	6938915
HS-G	586738	6940342
HS-J1	585820	6939330
HS-J5	585820	6939330

* All UTM Zone 8

Table A20. Stannite-Sphalerite Geothermometry from EPMA

Sample I.D	Stage	FeS mineral	# of Stn analyses	Stn Zn (mol%)	Stn Fe (mol%)	# of Sp analyses	Sp Zn (mol%)	Sp Fe (mol%)	Calculated T (°C)
11-14 105	Sp-1	Po+py	5	1.43	12.65	7	39.39	9.77	282
11-14 105	Sp-1	Po	1	4.36	12.45	6	39.82	9.35	339
11-14 105	Sp-1	Po+Py	1	1.61	12.58	5	39.17	9.93	289
11-14 105	Sp-1	Po	4	1.82	12.44	4	40.36	8.54	287
11-15 142	Sp-2	Po	10	1.61	12.58	3	40.48	8.71	281
11-15 142	Sp-2	Po	7	1.84	12.49	9	39.82	9.30	292
11-15 142	Sp-2	Unknown	1	1.48	12.27	4	39.82	9.14	282
11-15 142	Sp-2	Unknown	7	1.91	12.22	9	38.76	10.07	301
HS-G	Sp-2	Unknown	1	2.49	11.00	1	44.03	4.39	272
HS-G	Sp-2	Unknown	5	3.30	10.75	3	43.43	4.58	289
HS-G	Sp-2	Unknown	4	1.78	11.56	3	40.31	7.89	286
11-14 47	Sp-2	Py	2	1.11	12.68	2	41.67	9.06	264

Calculated based on Shimizu and Shikazona 1985

Table A21. Whole Rock Minor and Trace Elements Data

Sample I.D	Type	Ba (ppm)	Ga (ppm)	Rb (ppm)	Sn (ppm)	Sr (ppm)	V (ppm)	W (ppm)	Zr (ppm)	Y (ppm)	La (ppm)	Ce (ppm)	Nd (ppm)	Mo (ppm)	Cu (ppm)	Pb (ppm)	Zn (ppm)
11-24 107		1096	27	16	241	232	1037	7	347	47	36	63	35	68	75	258	515
11-24 287	**Flt Rck**	1216	12	64	68	108	81	39	420	29	20	44	22	3	218	194	2261
11-24 432		630	6	41	15	109	85	5	128	35	24	36	24	4	234	11	656
HS-CL		101	1	2	0	592	70	0	27	10	1	2	3	0	12	3	10
HS-EJ	**Unaltered MT**	151	5	32	1	594	21	0	33	9	15	29	13	1	10	3	39
11-24 32		91	3	27	7	325	66	0	58	25	32	36	22	2	37	6	7
11-24 97		684	9	72	8	259	510	2	129	34	28	45	26	148	124	42	29
11-24 460		959	9	74	3	552	124	1	116	44	31	39	26	4	33	12	82
HS-AS		2571	9	100	1	41	33	2	83	11	14	42	16	1	12	1	73
HS-CT	**Unaltered CPMC**	6176	21	246	9	507	79	1	162	15	45	80	28	2	83	15	61
11-40 210		688	14	155	5	170	103	2	146	25	26	48	24	1	176	5	30
11-40 398		573	12	132	22	217	497	1	183	41	27	54	30	18	99	4	971
HS-DA	**Unaltered DME**	544	25	133	2	439	85	1	107	17	51	92	37	1	12	4	68
HS-BD		1491	15	109	2	126	119	1	178	18	19	39	17	1	28	8	17
11-12 353		1502	13	149	4	323	135	1	231	28	22	43	24	6	99	21	28
11-12 357		470	1	23	1	583	35	1	306	19	16	24	13	1	18	5	4
11-12 364		699	8	62	3	178	99	1	235	24	21	36	18	6	56	6	10
11-12 365		1489	9	60	2	183	93	1	193	30	21	35	21	6	82	6	25
11-12 368	**Alteration Transect**	559	11	57	3	186	128	1	330	44	28	46	28	10	93	9	16
11-12 369a		778	7	36	14	378	217	1	152	40	27	37	26	14	69	4	25
11-12 369b		319	3	6	37	313	100	1	90	20	14	18	11	5	156	60	173
11-12 369c		871	5	49	3	313	84	1	77	16	12	15	10	4	28	4	96
11-12 372		544	2	23	1	555	17	<0.1	224	10	9	15	7	1	7	42	13
11-12 387		739	4	26	1	1306	147	1	63	41	21	17	16	8	52	19	229
HS-AI	**Wollastonite**	535	4	59	10	465	156	1	164	20	20	35	18	1	13	1	7
11-40 534	**KCS**	3958	7	127	122	245	266	2	184	20	18	34	17	41	24	258	453
11-12 164		878	14	134	17	240	235	2	221	37	31	58	32	16	168	32	119
11-40 119	**KCS**	1397	10	122	66	270	295	2	184	25	23	40	22	17	79	9	700
11-29 51		641	14	201	8	182	174	1	213	28	23	42	23	5	128	11	54
11-40 535	**Marbles**	19	2	0	95	78	27	1	193	8	8	14	8	2	3	16	13
11-12 40	**Stage 3 Min**	41	9	5	120	160	68	1	244	15	17	32	15	4	149	2695	1876
10-04 51		5	6	0	3433	8	9	1	107	5	8	9	3	2	>10000.00	349	>10000.0
11-24 234a	**Stage 1 and 2 Min**	9	4	0	190	25	29	1	446	14	8	15	9	5	4632	188	>10000.0
11-24 234b		22	3	0	136	34	44	8	488	16	22	33	14	5	1930	221	>10000.0
11-24 234c		188	16	11	73	274	171	8	293	33	26	49	27	14	212	19	723
11-24 234d		681	16	64	68	297	218	2	274	46	45	72	38	17	132	18	236

Table A21 Cont. Whole Rock Minor and Trace Elements Data

Sample I.D	Type	Ag (ppb)	Co (ppm)	Mn (ppm)	As (ppm)	Cd (ppm)	Bi (ppm)	Cr (ppm)	Se (ppm)	In (ppm)	Li (ppm)	Ni (ppm)
11-24 107		4144	12	1273	182	5	18	63	10	0	33	93
11-24 287	**Flt Rck**	5245	4	883	125	16	24	27	6	5	44	25
11-24 432		2145	6	562	31	16	1	31	13	0	11	35
HS-CL		43	1	361	1	0	0	2	0	<0.02	1	6
HS-EJ	**Unaltered MT**	24	5	553	3	0	0	15	<0.1	<0.02	21	10
11-24 32		176	4	482	12	0	0	3	7	<0.02	1	29
11-24 97		1510	11	116	87	0	4	7	24	<0.02	2	94
11-24 460		701	5	124	6	2	0	31	9	0	9	53
HS-AS		60	8	626	11	<0.01	0	25	<0.1	0	63	25
HS-CT	**Unaltered CPMC**	122	9	221	0	0	1	90	1	<0.02	44	23
11-40 210		238	13	114	9	0	2	66	4	<0.02	29	79
11-40 398		179	9	161	3	11	1	85	6	0	43	63
HS-DA	**Unaltered DME**	7	14	298	8	0	0	85	0	0	48	32
HS-BD		86	8	122	1	0	0	48	1	<0.02	29	34
11-12 353		1799	8	59	5	1	1	33	22	0	28	50
11-12 357		436	2	146	5	0	0	2	7	<0.02	2	8
11-12 364		1552	13	39	218	0	1	7	16	<0.02	2	66
11-12 365		998	6	58	7	0	1	12	19	<0.02	10	41
11-12 368	**Alteration Transect**	1094	7	47	7	0	1	17	17	<0.02	4	42
11-12 369a		291	5	182	4	1	0	15	16	<0.02	3	86
11-12 369b		1613	4	238	9	5	3	12	10	0	6	40
11-12 369c		244	2	121	2	5	0	7	7	<0.02	3	32
11-12 372		389	1	203	3	0	0	4	2	<0.02	4	4
11-12 387		1402	2	136	8	13	0	15	22	<0.02	4	48
HS-AI	**Wollastonite**	44	1	169	89	0	0	5	<0.1	<0.02	2	7
11-40 534	**KCS**	3748	2	655	35	10	13	5	5	0	3	63
11-12 164		495	11	88	56	2	1	58	20	0	19	92
11-40 119	**KCS**	199	8	86	92	13	0	9	4	0	4	61
11-29 51		359	9	70	5	1	1	51	24	<0.02	28	51
11-40 535	**Marbles**	332	1	1953	7	1	1	1	0	0	1	2
11-12 40	**Stage 3 Min**	31667	7	160	212	34	104	8	36	1	8	34
10-04 51		>100000	36	1496	3	1905	33	4	>100.0	122	4	59
11-24 234a	**Stage 1 and 2 Min**	15081	31	853	2	868	164	15	84	59	13	48
11-24 234b		5649	15	723	3	655	107	12	47	43	16	25
11-24 234c		968	5	277	4	19	7	42	5	1	9	68
11-24 234d		519	5	135	3	6	2	26	5	0	2	49